

Dissertation  
submitted to the  
Combined Faculty of Natural Sciences and Mathematics  
of Heidelberg University, Germany  
for the degree of  
Doctor of Natural Sciences

Put forward by  
M.Sc. Robin G. Tress

born in: Freyung (Germany)

Oral examination: 17-11-2021



ISM dynamics in simulated galaxies: bridging the scales

Referees: Prof. Dr. Ralf S. Klessen  
Prof. Dr. Henrik Beuther



# Abstract

The interstellar medium (ISM) and in particular giant molecular clouds (GMCs) are complex and dynamic entities, shaped by internal and external agents like stellar feedback and the galactic environment in which they reside. The aim of this thesis is to model the ISM to understand the connection of the smallest GMC scales to the large galactic scales and study the role of the environment in regulating their dynamics. We perform high resolution hydrodynamic simulations of the ISM in peculiar and rather extreme galactic configurations where we can stress test the ISM response to these environments. Our ISM model and resolution is fine-tuned to capture all important GMC physics while still retaining the large dynamic range in spatial scales necessary to follow them in the galactic environment.

In the first part of this thesis I focus on the gas dynamics of an M51-like galaxy encounter. I describe how the interaction affects the global ISM and star formation properties and I proceed with an analysis of the cloud population.

In the second part the focus falls on the central barred region of a Milky Way model. I describe the complex gas flows in this extreme environment and analyse the properties of the molecular ISM and the resulting star formation. These simulations are valuable tools to interpret observational data of the region.



# Zusammenfassung

Die interstellare Materie (ISM) und vor allem Molekülwolken (GMCs) sind komplexe und dynamische Einheiten, die von internen und externen Faktoren wie stellarem Feedback und der galaktischen Umgebung in der sie sich befinden, geformt werden. Das Ziel dieser Arbeit ist es, das ISM zu modellieren, um die Verbindung der kleinsten GMC-Skalen mit den großen galaktischen Skalen zu verstehen und die Rolle der Umgebung bei der Regulierung ihrer Dynamik zu untersuchen. Wir führen hochauflösende hydrodynamische Simulationen des ISM in besonderen und extremen galaktischen Konfigurationen durch. In diesen können wir die Verhaltensweise des ISM in solchen Systemen testen. Unser ISM-Modell und unsere Auflösung sind abgestimmt, um alle wichtigen physikalischen Phänomene der Molekülwolken zu erfassen und gleichzeitig dem Lebenszyklus der GMCs in der galaktischen Umgebung zu folgen.

Im ersten Teil dieser Arbeit konzentriere ich mich auf die Gasdynamik einer M51-ähnlichen Galaxienbegegnung. Ich beschreibe, wie sich die Wechselwirkung auf die globalen ISM- und Sternentstehungseigenschaften auswirkt und fahre mit einer Analyse der Wolkenpopulation fort.

Im zweiten Teil liegt der Fokus auf dem zentralen Balkenbereich eines Modells der Milchstrasse. Ich beschreibe die komplexen Gasströmungen in dieser extremen Umgebung und analysiere die Eigenschaften des molekularen ISM und die daraus resultierende Sternentstehung. Diese Simulationen sind wertvolle Werkzeuge, um Beobachtungsdaten der Region zu interpretieren.



# Contents

<b>Abstract</b>	<b>v</b>
<b>Zusammenfassung</b>	<b>vii</b>
<b>Contents</b>	<b>ix</b>
<b>1 Introduction</b>	<b>1</b>
1.1 About this thesis . . . . .	1
1.2 The Interstellar Medium . . . . .	3
1.2.1 Thermal Phases of the ISM . . . . .	4
1.2.2 Giant Molecular Clouds . . . . .	7
1.2.3 Equations of Hydrodynamics . . . . .	14
1.2.4 Numerically solving the Hydro Equations . . . . .	15
1.2.5 Star formation . . . . .	16
1.2.6 Stellar feedback . . . . .	18
1.3 Galactic dynamics . . . . .	21
1.3.1 Bars . . . . .	22
1.3.2 Spiral arms . . . . .	24
1.3.3 galactic encounters . . . . .	26
1.3.4 ISM in a galaxy . . . . .	27
1.4 The Milky Way . . . . .	29
1.5 Scientific goals and methodology . . . . .	32
1.6 Structure of the thesis . . . . .	35
<b>2 Simulations of the star-forming molecular gas in an interacting M51-like galaxy</b>	<b>43</b>
2.1 Statement about my contribution . . . . .	43
<b>3 Simulations of the star-forming molecular gas in an interacting M51-like galaxy: cloud population statistics</b>	<b>71</b>

---

3.1	Statement about my contribution . . . . .	71
<b>4</b>	<b>Simulations of the Milky Way's central molecular zone - I. Gas dynamics</b>	<b>97</b>
4.1	Statement about my contribution . . . . .	97
<b>5</b>	<b>Simulations of the Milky Way's central molecular zone - II. Star formation</b>	<b>133</b>
5.1	Statement about my contribution . . . . .	133
<b>6</b>	<b>Conclusions</b>	<b>153</b>
6.1	Summary . . . . .	153
6.2	Open questions . . . . .	156
6.3	Future steps . . . . .	159
6.3.1	Planned simulations . . . . .	159
6.3.2	planned analysis . . . . .	160
	<b>Acknowledgements</b>	<b>165</b>

# Chapter 1

## Introduction

### 1.1 About this thesis

The study of the Interstellar Medium (ISM) is fundamental in the task of understanding the star formation process. This is however not an easy endeavour since multiple physical processes are at play and several orders of magnitude in spatial scales are deeply interlinked and equally important in the regulation of the ISM. It is part of a larger galactic ecosystem and interactions between gas- and galactic- dynamics are non-trivial yet fundamental. Galaxy encounters and mergers, the presence of spiral arms and bars can all radically affect the kinematics and dynamics of the ISM down to the smallest scales. Properly simulating the ISM and in particular Giant Molecular Clouds (GMCs) in the larger scale galactic context has been an elusive task which is nowadays however becoming achievable due to progress in computing resources. The goal of this dissertation is to better understand the connection between environment and the dynamics of the ISM with particular attention to the cold molecular phase which directly connects to star formation. Our ISM model is therefore fine-tuned to properly follow the processes controlling the life-cycle of GMCs. We perform state-of-the-art hydrodynamic simulations of the ISM in different galactic systems following the dynamics of the gas down to sub-pc scales. We stress test the response of the ISM to particularly interesting and dynamic galactic environments. Specifically, our setup of choice consists of a galaxy encounter on one hand and a galactic bar on the other, both of which build an extreme framework for the evolution of the gas.

As for the interacting galaxy model, we take inspiration from the tidally disturbed M51 system (the Whirlpool galaxy) which we try to roughly reproduce by fine-tuning the initial conditions of the galaxy and the orbital parameters of the merger. We find that despite the great morphological change of the interacting galaxy compared to the isolated case, the encounter cannot substantially affect the ISM phases and the resulting

Star Formation (SF). The tidally induced spiral arms are instead just gathering the gas without triggering new collapse and even in the outer HI disc no new star formation can be induced since it is stripped from the galaxy forming a diffuse tidal tail. We study the GMC population for a given time of the simulation and find similarly that the spiral arms merely group the clouds without greatly affecting their properties. We instead see a much greater systematic shift in GMC properties as we approach the centre where surface densities and shearing forces are high enough to induce a change in their properties. The spiral arms that develop are just not strong enough in this setup to produce an analogous shift.

For our study of the ISM in the presence of a galactic bar, we take the central region of our Milky Way as our real-life prototype. We use an external background gravitational potential to model the presence of the bar, taking particular care to meet observational constraints in order to be able to compare and interpret observed features in our framework. We describe the complex and dynamic life of a gas parcel in the region and contribute towards a better understanding of the 3D structure of the Central Molecular Zone (CMZ) and the gas fluxes in the region. We are able to identify the formation location of observed stellar clusters and assess the positioning of known molecular clouds within this context. Moreover, with these simulations we work towards a better understanding on the modality of how star formation proceeds in the region. We further find that supernova feedback in the CMZ is responsible in driving mass flows towards more central regions, contributing to the buildup of a Circum-Nuclear Disc (CND). This is an important result since it contributes to the feeding process of the Super-Massive Black Hole (SMBH) in the centre.

## 1.2 The Interstellar Medium

The ISM denotes the diffuse matter distributed in a galaxy which is not locked up in stars. Even though it is mostly subdominant in terms of mass, it is absolutely relevant since stars are formed from the gravitational collapse of the densest parts of the ISM. The main constituents are Hydrogen and Helium atoms but in the present-day Universe many other trace elements are present which are fundamental for its thermal evolution. The thermo-dynamical states of the ISM are vast and span several orders of magnitude from temperatures of  $T \sim 10^8$  K and extremely low densities around  $\rho \sim 10^{-28}$  g/cm<sup>3</sup> to the highest densities of pre-stellar cores and extremely low temperatures comparable to the cosmic microwave background. Most of the mass resides however in quite distinct thermal phases. In the colder phases more complex molecules can survive and we are able to detect more than 200 different types of molecules here (Endres et al., 2016).

Other than the gas phase, there exists also a particulate component which is referred to as dust which can survive in the colder phases of the ISM. These particles are mainly formed in atmospheres of red-giant stars and released into the ISM through planetary nebulae. But they can also form during the compression of the ISM by Supernova (SN) shocks (Jones & Tielens, 1994; Waters, 2004). Dust grains are responsible for broad banded absorption of radiation in the ISM and they re-emit the radiation at longer wavelengths in the infrared. Their properties can be deduced by studying the extinction curves in the ISM (e.g. Mathis et al., 1977). The dust is generally composed by elements like Silicate and Graphite and their sizes, ranging between 50 nm and 0.25  $\mu$ m, follow a power law type distribution (e.g. Draine & Lee, 1984; Mathis et al., 1977). In terms of mass it accounts for just  $\sim 1$  %, but it holds almost half of the metals of the ISM and it is therefore chemically a very important component (see Stahler & Palla, 2004, and references therein). In particular it can act as a catalyst of several chemical reactions, most notably the formation of H<sub>2</sub> (Gould & Salpeter, 1963).

The ISM is permeated by radiation referred to as the Interstellar Radiation Field (ISRF) which can interact with the ISM and contribute to its thermal and chemical state. Apart from the cosmic microwave background radiation, it is mainly of stellar origin. It can heat the gas (through photoelectric heating), determine its ionisation and molecular fractions, and as stated earlier be absorbed by the dust and re-emitted in infrared. For photon energies above  $E > 13.6$  eV the UV radiation is able to ionise atomic Hydrogen (HI). This part of the spectrum is mainly produced by massive and young OB stars which are able to keep the surrounding hydrogen ionised in so called HII regions. This part of the radiation, however, is not able to penetrate far into the ISM since it is absorbed on scales  $\lesssim 100$  pc by HI, which has a large volume filling fraction inside the galactic disc

(McKee & Ostriker, 1977) . It could however be important at high galactic altitudes since it could escape the disc through chimneys carved into the HI layer. The UV part of the spectrum at lower energies, which is able to photo-dissociate molecular Hydrogen, penetrates instead much deeper into the ISM since it will be absorbed by the molecular clouds which have a much smaller volume filling fraction. The insides of molecular clouds, are however shielded from this radiation (self-shielding property of  $H_2$ ), allowing high  $H_2$  fractions (Draine & Bertoldi, 1996). Pioneering work in trying to estimate the ISRF in the local environment has to be attributed to Draine (1978); Habing (1968); Mathis et al. (1983).

Another important component of the ISM are cosmic rays. These are high energy relativistic particles generated at strong shock-fronts, as for instance is the case of a shock wave expanding into the ISM driven by a SN event (Ackermann et al., 2013). These particles are charged and as such they follow the magnetic field lines. Any directional information is therefore quickly lost, and they permeate uniformly the medium instead. Their energy spectrum follows a power law which decreases sharply towards higher energies (Aartsen et al., 2013). They play an important role in the energy balance of the ISM. Moreover they contribute to some important chemical reactions in the molecular ISM. Here they can for instance dissociate  $H_2$  which is shielded by the ISRF (Padovani et al., 2009). In these regions they provide the main source of heat (Glassgold & Langer, 1973).

The ISM is permeated by magnetic fields of the order of a few tens of  $\mu\text{G}$ , as revealed by the Zeeman splitting of molecular lines like OH (e.g. Davies, 1974; Fish et al., 2003). Dust grains in the ISM tend to be aligned with the field and therefore polarize transmitted light. This can be detected and is an effective way to reveal magnetic field orientation in the ISM. Magnetic fields are energetically an important component and the flux increases with ISM density (see Han, 2017, and references therein), indicating flux freezing, i.e. that the field is coupled to the gas phase and the flux follows the gas flow.

### 1.2.1 Thermal Phases of the ISM

In this section we describe the thermal state of the ISM approaching the topic from a pedagogical rather than from a purely descriptive point of view.

Considering the heating and cooling processes taking place in the atomic ISM<sup>1</sup> we can distinguish two thermally stable phases at most pressures. This two phase model (Field et al., 1969) comprises a high temperature volume filling HI phase called Warm Neutral Medium (WNM) at  $T \sim 10^4$  K, in pressure equilibrium with a colder, denser, thermally

---

<sup>1</sup>The part of the ISM where hydrogen is found in its atomic rather than molecular or ionised form.

stable atomic phase at  $T \sim 100$  K called Cold Neutral Medium (CNM).

This simple model was soon amended by McKee & Ostriker (1977) by the so-called three phase model. In addition to the WNM and the CNM, most of the volume of the ISM is filled by an even hotter  $T \sim 10^6$  K ionised phase generated by Supernova (SN) called the Hot Ionised Medium (HIM). Technically, this phase is not in thermal equilibrium, but at the densities and temperatures of the HIM cooling times are extremely long and this phase is easily replenished by the SNe before it can cool down again such that as a matter of fact it can still be considered as a stable phase.

Observations reveal that the ionised component of the ISM resides also in a separate phase at temperatures and densities comparable to the WNM (Gaensler et al., 2008; Hoyle & Ellis, 1963; Mierkiewicz et al., 2006; Reynolds et al., 1973). This phase is called Warm Ionised Medium (WIM) and actually  $\sim 90$  % of the ionised gas in the ISM is in this phase. This phase is not to be confused with the HII regions which also harbor ionised gas at similar densities but are considered separate from the WIM (Haffner et al., 2009) due to its different origin.

The CNM is not the coldest and densest phase of the ISM but instead at large column densities the gas is able to shield itself from the ISRF cooling further down and becoming molecular. The molecular phase is therefore organised in giant molecular clouds (see Sec. 1.2.2) surrounded by the CNM. Here the final stages of the star formation process happens such that GMCs can be thought to as the nurseries of stars. Most of the ISM mass is in the form of molecular hydrogen which is, however, extremely difficult to observe directly since  $H_2$  is a symmetric homonuclear diatomic molecule and therefore electric dipole driven ro-vibrational transitions are forbidden. We use therefore other elements as a proxy to trace the molecular phase at given density and temperature regimes. Most notably CO is widely observed, and by assuming a constant CO to  $H_2$  ratio we can estimate the distribution and dynamics of the molecular hydrogen.

This picture of the ISM is extremely useful to contextualise observations and processes of the ISM, but in general it has nowadays been superseded by a more dynamic picture of the ISM. In particular these phases are not static but there is constantly mass transfer between them. Moreover, since reaching a state of equilibrium requires time, at any given instant there is actually a quite substantial fraction of gas out of equilibrium such that the thermal phases are not so distinct but transition smoothly from one into another. Some chemical reactions can have long timescales (such as  $H_2$  formation) and their abundances are therefore sensitive to the dynamical history of the gas (e.g. Glover & Clark, 2012; Glover & Mac Low, 2007b; Krumholz, 2012).

The ISM is therefore quite complex and dynamic in nature. This is nowadays being revealed by observations and studied with numerical simulations which consider not only

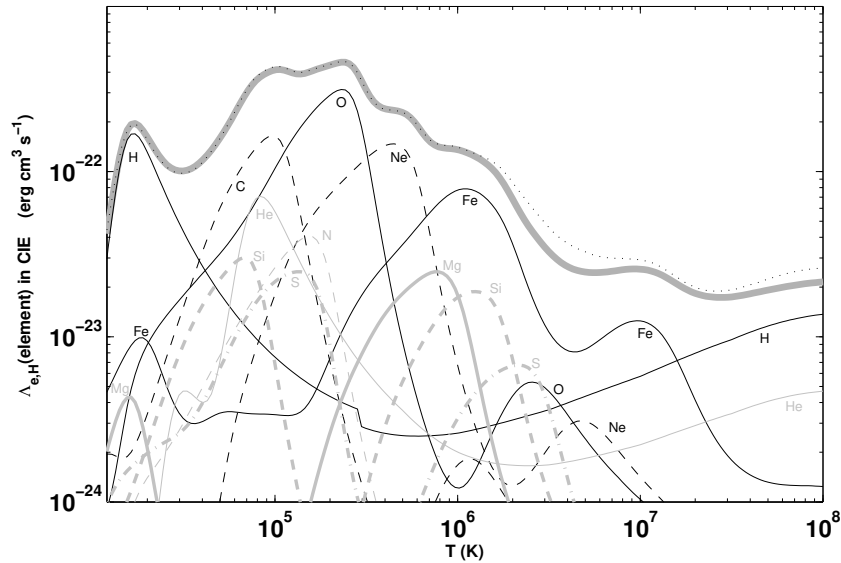


**Figure 1.1.** Cooling efficiency as a function of temperature for the ISM at solar metallicity for  $T > 10^4$  K (taken from Gnat & Ferland, 2012). The contribution of the different elements to the total efficiency are shown.

the thermal and chemical evolution of the system in detail, but also include the environmental and dynamical effects which influence the properties and fractions of gas in the different phases. The field is however still in its infancy and this thesis tries to contribute and contextualise in this regard, especially in relation to the galactic environment.

### Thermal processes in the ISM

Apart from adiabatic heating and cooling, the ISM can change its internal energy by the means of radiative processes. In an optically-thin medium any photon emitted by any radiative process, such as atomic or molecular state transitions, can escape the system and remove internal energy from the gas. Conversely the energy of any absorbed photon can be translated into kinetic energy of the particles and so increase its temperature<sup>2</sup>. When the heating rate equals the cooling rate, the system reaches thermal equilibrium.

At high temperatures, complex molecules cannot survive and the major cooling processes are driven by atomic line transitions. Hydrogen and helium line transitions dominate the cooling between  $10^4$ – $10^5$  K while at higher temperatures, when H and He are fully ionised, the cooling is dominated by atomic line transitions of the metals (see Fig. 1.1). For  $T \gtrsim 10^7$  K even metals are fully ionised and the cooling is now dominated by Bremsstrahlung. For temperatures below the ionisation energy of H ( $T \lesssim 10^4$  K) the chemical processes in the ISM increase vastly in number and complexity, each process contributing to the thermal evolution of a parcel of ISM. The main coolants are however

<sup>2</sup>Of course this is a very crude simplification and the processes at play are vastly more complex.

C and O for  $T \gtrsim 100$  K, and CO for lower temperatures, being the dominant cooling source in the molecular phase of the ISM.

In terms of heating, the adiabatic compression plays an important role and shocks from SNe, stellar winds and jets can increase the gas temperatures substantially. Another distinctive heating source comes from the radiation through processes like photoelectric heating. Here a sufficiently energetic UV photon can hit a dust grain and extract an electron. The energy of the photon is used to free this electron and the surplus energy is transferred into kinetic energy of the free electron, and therefore heat. Other ways to translate the energy of photons into heat is through photo-ionisation or photo-dissociation (mainly of  $\text{H}_2$ ). Moreover, a molecule in an excited state after the absorption of a photon, can redistribute this energy into kinetic energy of the surrounding particles through collisional de-excitation processes (UV pumping). Highly energetic particles such as cosmic rays can also provide a heating source, since they hold a lot of kinetic energy. Finally, the turbulence can heat the gas at the dissipation scale through the turbulent cascade (Minter & Spangler, 1997).

### Formation and destruction of $\text{H}_2$

The formation of  $\text{H}_2$  in the gas phase of the ISM is extremely inefficient due to the low densities. Most of the  $\text{H}_2$  forms on the surface of grains (Gould & Salpeter, 1963; Hollenbach & Salpeter, 1971) where it is easier for H atoms to meet once they are absorbed at the surface.

The dominant process responsible for the dissociation of  $\text{H}_2$ , on the other hand, is photodissociation. The process is line-based and the photons responsible have energies between 11.2–13.6 eV and are known as Lyman-Werner photons. Since this energy falls in a narrow energy range, the dissociation rate is sensitive to self-shielding and the molecular hydrogen becomes sufficiently self-shielded at total gas column densities of  $N \simeq 10^{20} G_0 n^{-1} \text{ cm}^{-2}$  (Draine & Bertoldi, 1996). The dissociation of CO is also line-driven, and  $\text{C}^+$  to CO transitions happen around  $N \simeq 10^{21} \text{ cm}^{-2}$  at solar metallicities.

### 1.2.2 Giant Molecular Clouds

The most relevant for this dissertation is the molecular phase since it is the phase directly preceding star formation. This is the coldest among the ISM phases with temperatures ranging from 20 to 50–100 K. Having the highest densities it has inherently a low volume filling factor and organises itself into relatively distinct structures called Giant Molecular Clouds (GMCs), or sometimes simply molecular clouds (see Fig. 1.2 for a prominent example of a GMC.). The distinction into coherent structures is favoured by the relatively

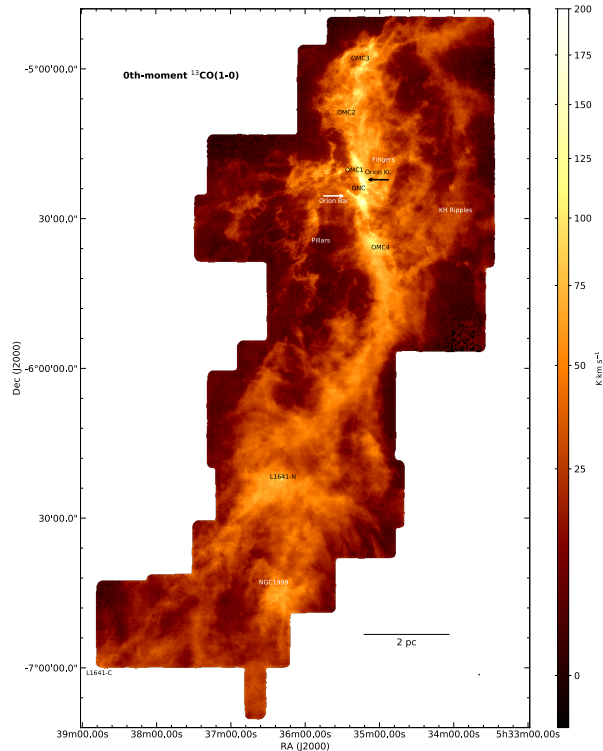


**Figure 1.2.**  $^{13}\text{CO}$  emission map of the famous Orion molecular cloud (Kong et al., 2018)

sharp transition of the ISM from atomic to molecular gas around densities of  $1\text{--}100\text{ cm}^{-3}$  which delineates the boundaries of GMCs. This feature can be attributed to the self-shielding property of  $\text{H}_2$  and  $\text{CO}$  from the ISRF. Therefore, the exact density regime where this transition happens sensibly depends on the UV ISRF strength and ISM metallicity (Dobbs et al., 2008; Glover & Mac Low, 2007a; Gnedin et al., 2009).

### Structure of GMCs

Molecular clouds have sizes from  $\sim 20\text{--}100\text{ pc}$  and masses from  $10^2\text{--}10^7\text{ M}_\odot$  (Heyer et al., 2001; Oka et al., 2001) with a typical cloud mass around  $10^4\text{ M}_\odot$ .

Due to the turbulent nature of the ISM, the structure of GMCs is complex, filamentary and fractal. Filaments are then divided into sub-filaments, with many junctions. Gas can travel along these filaments, efficiently funneling considerable amount of material towards these junction points into one star-forming site. It is therefore believed that these junctions play an important role in massive star formation (e.g. Kumar et al., 2020).

Overdense regions within GMCs are called clumps which are generally gravitationally bound structures. Even denser structures exist referred to as cores or protostellar cores. They have masses of a few solar masses and sizes  $< 10^{-2}\text{ pc}$ . Around densities of  $n_{\text{H}_2} \sim 10^{10}\text{ cm}^{-3}$  the ISM becomes optically thick, so at densities of the protostellar cores the gas

starts to contract adiabatically instead of isothermally. Cores have low, close to thermal internal velocities and are therefore sub- or trans-sonic. These structures will then lead directly to individual or a small group of newborn stars. This is also reflected in the mass distribution of the protostellar cores, which more closely resembles the IMF of stars (Goodwin et al., 2008).

As stated earlier, molecular gas is generally not observable directly. Most of the molecular gas is, however, bright in CO(1 – 0) and assuming a conversion factor  $X_{\text{CO}} = N_{\text{H}_2}/I_{\text{CO}}$  the H<sub>2</sub> column density  $N_{\text{H}_2}$  can be inferred by measuring the CO intensity  $I_{\text{CO}}$ . The  $X_{\text{CO}}$  factor is assumed constant, but there are many uncertainties here (Tielens & Hollenbach, 1985; Wolfire et al., 2010). In the envelopes of GMCs CO is however photo-dissociated while the H<sub>2</sub> column densities are large enough to keep the molecular gas shielded from the ISRF. These more diffuse envelopes are therefore CO dark, and a considerable amount of molecular gas could be hidden here (Smith et al., 2014). The capability of C<sup>+</sup> as a tracer of the molecular CO dark gas is being tested nowadays Glover & Smith (2016). Acknowledging these large uncertainties in identifying H<sub>2</sub>, it becomes clear how important and valuable numerical studies are to understand the actual H<sub>2</sub> dynamics. Post-processing tools are then mostly used on these models to infer the emission of CO(1 – 0) or other observable tracers to see how such simulated systems would look like to an observer.

At even lower column densities, also the molecular hydrogen is now efficiently photodissociated by the ISRF and we find therefore a thick layer of HI surrounding the GMCs, namely the CNM (see Fukui & Kawamura, 2010, and references therein).

In terms of masses, the GMCs can grow quite considerably and harbor a gas mass of up to  $10^7 M_{\odot}$  (e.g. Rosolowsky, 2005; Williams & McKee, 1997). The observed mass function of GMCs, however, is still largely debated and dependant on exact definition of a cloud, but it is generally acknowledged that the mass follows a power-law distribution  $dN/m \propto m^{-\alpha}$  with  $3/2 < \alpha < 2$  and so with most of the mass sitting in the most massive clouds (80 % of the molecular mass sits in clouds with  $M > 10^5 M_{\odot}$  (Stark & Lee, 2006)). There is no evidence for a break in the power-law given the observations of GMCs available to this date, and so there seems to be no characteristic GMC mass (e.g. Heyer & Dame, 2015, and references therein).

The mass distribution within the clouds, instead, indicates that GMCs are highly clumped. Most of the mass is therefore hosted in high density clumps such that the typical density in GMCs is  $n \sim 3 \times 10^3 \text{ cm}^{-3}$ , while the mean density is much less. The observed column-density probability distribution function (PDF) exhibits generally a lognormal shape, and evolved clouds where regions started to collapse to form stars additionally show a power-law tail at the highest column-densities (e.g. Corbelli et al., 2018; Lombardi et al.,

2010; Schneider et al., 2016). The lognormal shape can be explained given the turbulent nature of the molecular ISM. Simulations of isothermal supersonic turbulent boxes do in fact produce lognormal column-density PDFs (e.g. Federrath et al., 2008). The power-law tail, instead, is a product of the runaway gravitational collapse (Kainulainen et al., 2009) which generally starts to dominate around densities of  $5 \times 10^3 \text{ cm}^{-3}$  (Kainulainen et al., 2014).

Regarding the internal velocity of GMCs, Observations show highly supersonic and super-alfvenic velocity dispersions of 2–3 km/s attributed to turbulence and gravitational collapse (e.g. Heyer & Brunt, 2012; Padoan & Nordlund, 1999). Due to the low temperatures of the molecular gas, these velocities correspond to Mach numbers of 10 or larger, the dynamics of GMCs are therefore governed by turbulent motions which dominate over thermal and magnetic energies.

Simulations and observations show that magnetic fields of the order of a few microgauss are present in GMCs but are generally insufficient to stabilize the cloud (Heitsch et al., 2001; Padoan & Nordlund, 1999; Padoan et al., 2001). Nevertheless magnetic fields can be dynamically important and alter how cores fragment (Hennebelle et al., 2011; Peters et al., 2011), change the coupling between stellar feedback and the surrounding gas (Krumholz et al., 2007) and slow down evolution in general (Heitsch et al., 2001). Dust polarization studies show that magnetic field lines are predominantly parallel to the molecular filaments on large scales, but become progressively perpendicular at smaller scales (Girart et al., 2006; Soler et al., 2013, 2017). This can be understood in view of ideal magnetohydrodynamics (MHD) where the field is coupled to the gas and as the cloud initially collapses it does so along the magnetic field lines. At smaller scales and higher densities the collapse then happens also perpendicular to the magnetic field lines and non-ideal MHD effects like ambipolar diffusion start to become important, hence the field lines start to get more and more perpendicular to the filament.

### Cloud formation

A necessary condition for molecular hydrogen formation is the shielding from the ISRF ( $n > 100 \text{ cm}^{-3}$ ). A GMC therefore forms whenever the environmental conditions are favourable to the build-up of high column densities. The main responsible physical processes are cloud-cloud collisions, gravitational-, thermal-, magnetic- instabilities, spiral arm shocks, turbulence and colliding flows.

The coagulation model for GMC formation (Field & Saslaw, 1965; Oort, 1954; Tasker & Tan, 2009) sees small atomic cloudlets formed by the thermal instability to coagulate due to collisions where energy can be dissipated. Clouds can so grow progressively larger until feedback from the new formed stars starts to dissipate the GMC. This process

naturally leads to a power law cloud mass function (Kwan, 1979) and could explain the presence of GMCs in spiral arms where the density is higher and coagulation therefore more frequent. Due to the random collisions between clumps, the formation of counter-rotating clouds can be explained in this picture (Dobbs et al., 2008) as observations show that a considerable fraction of GMCs are indeed counter-rotating with respect to the rotation of the disc. The time required to build up high mass clouds with this model is however prohibitively long ( $> 100$  Myr) and especially for low density environments it cannot explain the presence of the observed massive clouds (e.g. Hughes et al., 2013).

Moreover this picture is rather simplistic as it assumes cloudlets to be quasi-steady objects steadily coalescing to form larger objects. But the real ISM is more complex than that, and cloud formation can be understood in the context of a turbulent ISM. In this sense the clouds are the density peaks of a turbulent flow and the mass function the result of the turbulent cascade (Ballesteros-Paredes et al., 2007; Mac Low & Klessen, 2004). Moreover GMCs tend to continuously accrete mass during their lifetimes (Fukui et al., 2009; Kawamura et al., 2009). In a turbulent ISM framework, the turbulent flow provides further accretion and so continues to drive and maintain the turbulence within the cloud (Goldbaum et al., 2011; Klessen & Hennebelle, 2010).

Converging flows of atomic gas can also produce a GMC as the density increases when the two streams shock (Banerjee et al., 2009; Clark et al., 2012; Hennebelle & Pérault, 1999; Vázquez-Semadeni et al., 2006). Many properties such as velocity structures of the cloud can be explained in this framework but on the other hand this method seems inefficient to build very massive clouds. Converging gas flows can arise simply from the turbulent flow, from large scale instabilities such as the Toomre (1964) instability and the Parker (1966) instability, or from stellar feedback. Expanding shells powered by SNe and wind feedback can create such colliding flows and observations indeed show star formation at the edges of shells (Oey et al., 2005). However, it is unclear if these are actually triggered by the shell or just due to sweeping of pre-existing structures (Pringle et al., 2001). In general it is therefore still unclear how often the conditions for converging flows actually appear in a galaxy.

### Scaling relations

Observations reveal that the properties of GMCs exhibit empirical scaling relations. These could hint towards a fundamental intrinsic dynamical origin underlying these objects responsible for these scaling relations. Understanding them is therefore an important step towards a better grasp of the dynamical state of GMCs.

These relations were first noticed and described by Larson (1981). The first Larson relation describes the connection between the velocity dispersion (or the line-width) and

the sizes of the clouds:

$$\sigma \propto L^\alpha; \quad (1.1)$$

where Larson (1981) identified  $\alpha \simeq 0.38$  while observations with improved sensitivity show  $\alpha \simeq 0.5$  (Solomon et al., 1987). This power-law type relation is scale-free and any emitting region with size  $L$  would lie on the relation, not only GMCs as a whole. The second Larson relation states that clouds are roughly in self-gravitational equilibrium:

$$\frac{2\sigma L^2}{GM} \sim 1; \quad (1.2)$$

and finally the third Larson relation finds an inverse relationship between the mean density  $n$  of the cloud and its size  $L$ :

$$n \propto L^{1.1}. \quad (1.3)$$

This equation directly implies a constant surface density for GMCs.

In a turbulent medium following some kind of Kolmogorov cascade, a power-law type relation like the one described in equation 1.1 is expected (Kritsuk et al., 2013). The first Larson relation could therefore be a symptom of the underlying turbulence of the molecular ISM. If, however, we consider clouds as virialised objects, and acknowledge a constant surface density of the clouds, then the first Larson relation with an exponent of  $\alpha = 0.5$  follows from these assumptions. In the framework first described by Larson (1981), the three relations are therefore not independent, but the first follows from the other two.

It is however debated whether clouds actually have constant surface densities or if this is instead an artefact due to limited sensitivity of the data (Ballesteros-Paredes & Mac Low, 2002) and clouds being selected in similar, solar-neighborhood environmental conditions. If we let go of this assumption, the first Larson relation still follows from the second, but acquires a dependency on the surface density:

$$\sigma/L^{1/2} \propto \Sigma^{1/2}. \quad (1.4)$$

This is known as the Heyer et al. (2009) relation.

Another important caveat to these deductions, is the assumption of virial equilibrium for clouds. GMCs that are collapsing develop virial velocities as well and can therefore be mis-interpreted as structures in gravitational equilibrium (Ballesteros-Paredes et al., 2011; Ibáñez-Mejía et al., 2016). It is therefore still unclear to what extent the second Larson relation is valid or how it is influenced by these biases.

Finally the validity of these relations across the cosmos still has to be tested. How much these relations vary when we observe external galaxies, and more extreme environments such as galactic centres is still under investigation.

### Time scales

The timescales relevant for cloud formation, evolution and destruction are the following: the formation time, the free-fall time and the dissipation time.

The formation time scales are still discussed in literature and depend on the formation mechanism described in section 1.2.2. Observational data initially hinted towards rather long GMC life-times of the order of 100 Myr (Koda et al., 2009; Scoville & Hersch, 1979; Scoville & Wilson, 2004). More recent observations, on the other hand, favour much shorter time-scales between 10–50 Myr (Engargiola et al., 2003; Kawamura et al., 2009; Meidt et al., 2015).

Once the GMC is assembled, the timescale at which we can expect any dynamical evolution is the free-fall time. Given a sphere of density  $\rho$ , if we assume that self-gravity is the only force acting on the cloud (pressure forces are neglected), it will collapse on a time scale of

$$\tau_{\text{ff}} = \sqrt{\frac{3\pi}{32G\rho}}. \quad (1.5)$$

This is the time-scale on which we can expect star formation to happen. However this is not the full story, since if we would assume that the observed molecular mass of the Milky Way would all collapse and form stars according to the free-fall time, we get excessively high star formation rates than those observed. In reality the depletion times are much longer and it is evident that a different time-scale is at play to prevent collapse on the free-fall time. If we assume that clouds are virialised objects, there has to be a contrasting force at play which is counteracting the self-gravity. Magnetic field can introduce a stabilizing effect, but in general its intensity seems to be too low to produce enough support against gravity (Bertram et al., 2012; Crutcher et al., 2010; Padoan & Nordlund, 1999). Also thermal pressures are negligible due to the low temperatures of the molecular gas. Turbulence, on the other hand, can play an important role in this regard since the molecular gas is highly supersonic (e.g. Krumholz & Tan, 2007).

We can achieve low star formation efficiencies per free fall time also without invoking a stabilizing force for the GMCs but instead assuming that stellar feedback is efficient at dispersing the cloud as soon as the first stars start to form. This would then explain the short lifetimes of GMCs and retrieve average star formation efficiencies per free-fall time of 1–10 %.

The main culprits responsible for GMC destruction are internal, like feedback, and external, like galactic shear and turbulence. The timescales depend on the mechanism and the mass of the cloud (Jeffreson & Kruijssen, 2018). If we only account for internal feedback processes to disperse the cloud, we can estimate the minimum star formation efficiency needed to fully disperse the cloud (Rahner et al., 2017, 2019). If the star for-

mation is initially too low the cloud can re-collapse and generate a second generation star formation event. What exactly the most important mechanisms responsible to disperse GMCs are is still debated and will depend on mass of the cloud and galactic environment.

### 1.2.3 Equations of Hydrodynamics

The ISM can be treated as a fluid and its evolution can be described by the equations of compressible, adiabatic, inviscid, ideal Magneto Hydrodynamic (MHD):

$$\frac{\partial \rho}{\partial t} + \nabla \cdot (\rho \mathbf{u}) = 0; \quad (1.6)$$

$$\frac{\partial \mathbf{u}}{\partial t} + \mathbf{u} \cdot \nabla \mathbf{u} = -\frac{\nabla P}{\rho} - \nabla \Phi + \frac{1}{4\pi\rho} (\mathbf{B} \cdot \nabla) \mathbf{B} - \frac{1}{8\pi\rho} \nabla |\mathbf{B}|^2; \quad (1.7)$$

$$\frac{\partial \rho e}{\partial t} + \nabla \cdot \left[ \left( \rho e + P + \frac{1}{2} |\mathbf{B}|^2 \right) \mathbf{u} - \mathbf{B} (\mathbf{u} \cdot \mathbf{B}) \right] = \rho \dot{Q} + \rho \frac{\partial \Phi}{\partial t}; \quad (1.8)$$

$$\frac{\partial \mathbf{B}}{\partial t} + \nabla \times (\mathbf{B} \times \mathbf{u}) = 0; \quad (1.9)$$

$$\nabla \cdot \mathbf{B} = 0, \quad (1.10)$$

where  $\rho$  is the mass density of the fluid,  $\mathbf{u}$  its velocity,  $P$  its pressure,  $\mathbf{B}$  the magnetic field,  $\Phi$  the gravitational potential and  $e$  the total energy per unit mass of the fluid. We have that

$$e = e_{\text{th}} + \Phi + \frac{|\mathbf{u}|^2}{2} + \frac{|\mathbf{B}|^2}{2\rho}, \quad (1.11)$$

where  $e_{\text{th}}$  is the thermal energy per unit mass and can be inferred by assuming an ideal gas equation:

$$P = (\gamma - 1)\rho e_{\text{th}}, \quad (1.12)$$

where  $\gamma$  is the adiabatic index.

Equation 1.6 denotes conservation of mass, 1.7 conservation of momentum and 1.8 conservation of energy. Equation 1.9 is the induction equation in the ideal case and 1.10 denotes the absence of magnetic monopoles.

The last term of the momentum equation 1.7 is the magnetic pressure force, denoting the resistance to compression; while the second-to-last term is the magnetic tension term, denoting the resistance to bending of the magnetic field lines.

In the energy equation 1.8 the term  $\dot{Q}$  indicates the thermal losses and heating processes of the ISM (see section 1.2.1).

### 1.2.4 Numerically solving the Hydro Equations

We briefly describe the main numerical techniques used in astrophysics to solve the hydrodynamic equations. These include grid-based methods, particle methods and moving mesh algorithms.

In grid codes the conserved fluid quantities are discretised on a set of finite volume elements in the integration domain. Forces acting on each grid cell are then computed and the fluxes at the grid interfaces calculated by solving the local Riemann problem. In this way the mass transfer from each cell can be inferred and the fluid quantities updated for the given time-step. Another approach is to discretise the differential equations at the grid points and solving them through finite difference methods.

The grid cells can have a fixed size throughout the domain or instead have a whole hierarchy of different sizes by subdividing cells for regions of interest. These are then called adaptive mesh refinement (AMR) codes and the criteria for refinement can be set by the user and performed on the fly as the conditions change during the simulation time.

Disadvantages of grid-based methods include artefacts that arise along principal grid axes along which the advection is more efficient. Moreover grid codes are generally not Galilean invariant.

Gravity in these codes is approached by solving the Poisson equation in differential form on the discretised map. For regular grids this is easily done in the Fourier domain for which efficient algorithms exist. On an adaptive grid more complex methods have to be used such as multi-grid techniques. The mass can also be discretised and the Poisson equation then solved in its integral form through N-body methods.

Some notable examples of AMR codes are FLASH (Fryxell et al., 2000) and RAMSES (Teyssier, 2002).

A different approach to solve the hydrodynamic equations is presented through particle codes. Here the fluid is divided into discrete and equal mass elements and the continuous fluid quantities are then inferred by smoothing the properties of these elements over a given smoothing kernel. The smoothing radius is adaptive such that it always contains a given number of neighbouring particles and so the continuous nature of the fluid is respected. At each time-step the forces, including pressure forces, can be computed for each particle and advected in time accordingly. This method is known as Smoothed Particle Hydrodynamics (SPH) and some notable examples still widely used in astrophysics are GADGET (Springel, 2005) and GASOLINE (Wadsley et al., 2004).

Such an approach automatically achieves adaptive resolution for regions with higher density, but it is not really possible to define other criteria for local refinement other than density. Due to the Lagrangian nature of the SPH approach, these codes are fully Galilean invariant, and fluid elements are easily traced throughout the simulation whereas

grid codes would require passive tracer particles. However they have the disadvantage that shocks and contact discontinuities are poorly treated (Agertz et al., 2007), although several ingenious approaches exist to mitigate the problem (e.g. Read et al., 2010; Saitoh & Makino, 2013).

For obvious reasons SPH codes synergies well with particle-based methods to solve gravitational forces. Particularly efficient are tree methods where the particles are organised into a hierarchical spatial tree structure. For each particle gravitational forces are computed between the particle and each tree-node. If a given node is close enough to the particle such that the approximation of treating the particles in the node as a single mass breaks down, the node is opened and the same procedure is performed on the next hierarchy of the structure.

The third type of hydro code are moving-mesh codes, the most prominent of which is probably AREPO (Springel, 2010). Here the domain is divided into grid cells by constructing the Voronoi mesh given a set of mesh-generating points. These points then inherit the velocity of the local fluid and are thus able to evolve in time following the flow and the mesh therefore dynamically adapts during the simulation. The fluid equations are then solved on this unstructured grid in a similar manner as for grid codes by computing interface fluxes and solving the Riemann problem in the rest-frame of the interface. The quasi-Lagrangian nature of this approach limits interface fluxes and therefore minimizes advection errors and generally achieves Galilean invariance of the solution. As such it can be viewed as a hybrid method between grid- and particle-based schemes inheriting the advantages of both, compensating the drawbacks. It has good shock and discontinuity treatment, lacks the artefacts arising from a particular grid geometry and inherits the automatic resolution adaptivity of SPH codes while still being able to allow for user defined refinement criteria. A drawback, however, arises from the unstructured geometry of the mesh which can introduce spurious errors known as grid noise. Moreover the implementation of additional physics such as magnetic fields is complicated by the irregular mesh.

Another recent code which tries to combine the strengths of the grid and the SPH world is GIZMO (Hopkins, 2015) which is a meshless Godunov-type method which uses kernel discretization of the volume. In a similar way as the moving-mesh codes, but smoothing the boundaries between cells; fluxes are then not defined at the interfaces but over a larger overlapping volume between the cells.

### 1.2.5 Star formation

Due to the high densities and low temperatures of the molecular gas, the Jeans mass can drop by more than an order of magnitude in GMCs compared to the diffuse atomic

phase. Moreover, the sound speed drops once the gas becomes molecular, leading to an increase in Mach number of the turbulence. Higher Mach numbers imply that high density regions are more easily created, some of which will then likely be gravitationally bound. In other words, GMCs have just the right conditions for SF and are therefore the nurseries of stars.

The star formation process is fast (Elmegreen, 2007) and once the initial collapse is initiated the entire cluster is quickly formed on time-scales less than  $\sim 1$  Myr as revealed by the age spread of young stellar clusters (Palla & Stahler, 1999).

The ISM, and molecular clouds in particular, are governed by supersonic turbulent motions. The turbulence, on one hand, inhibits star formation on large scales, since it can act as a pressure force counterbalancing the self-gravity. But on the other hand, the turbulence promotes star formation locally, since it can induce high density fluctuations. If these are gravitationally bound and the collapse happens before the passage of a new shock can disrupt the overdensity, this will lead to local star formation. It is therefore the large scale supersonic turbulence which controls star formation (Mac Low & Klessen, 2004).

Since stars are born in molecular clouds, it is only reasonable to expect a correlation between  $\text{H}_2$  and SF (Krumholz et al., 2011). On large scales ( $> 100$  pc) this is indeed found, and observations reveal a tight, almost linear correlation between  $\text{H}_2$  and SF surface densities (Bigiel et al., 2008, 2011; Leroy et al., 2008; Schruba et al., 2011). However, molecular gas is just a tracer of SF and not its cause. The correlation between the two and its universal validity, has therefore to be taken with care. In low metallicity environments where  $\text{H}_2$  formation is less efficient, gravitational collapse could for instance be triggered also in atomic gas (Glover & Clark, 2012; Krumholz, 2012).

The linear dependency hints towards a constant molecular gas depletion time, regardless of galactic environment. If the total instead of only molecular gas is considered, the relation becomes super-linear of the type  $\Sigma_{\text{SFR}} \propto \Sigma_{\text{HI}+\text{H}_2}^{1.4 \pm 0.15}$  and is known as the Schmidt-Kennicutt relation (Kennicutt, 1998; Schmidt, 1959). This super-linearity indicates that high-surface density environments are more efficient in turning gas into stars compared to low-surface density regions.

But these star formation relations are valid only on large enough scales of  $L \gtrsim 100$  pc and have to be considered averages of the gas behaviour in these regions. On smaller scales the molecular gas might be dynamically young and still not be forming stars; or the feedback could already have disrupted the cloud such that no molecular gas is detected while star formation tracers have not faded yet.

Empirically it is observed that on scales smaller than a GMC, SF only happens in regions of column densities above  $7.5 \times 10^{21} \text{ cm}^{-2}$  (Molinari et al., 2014), but it is unclear

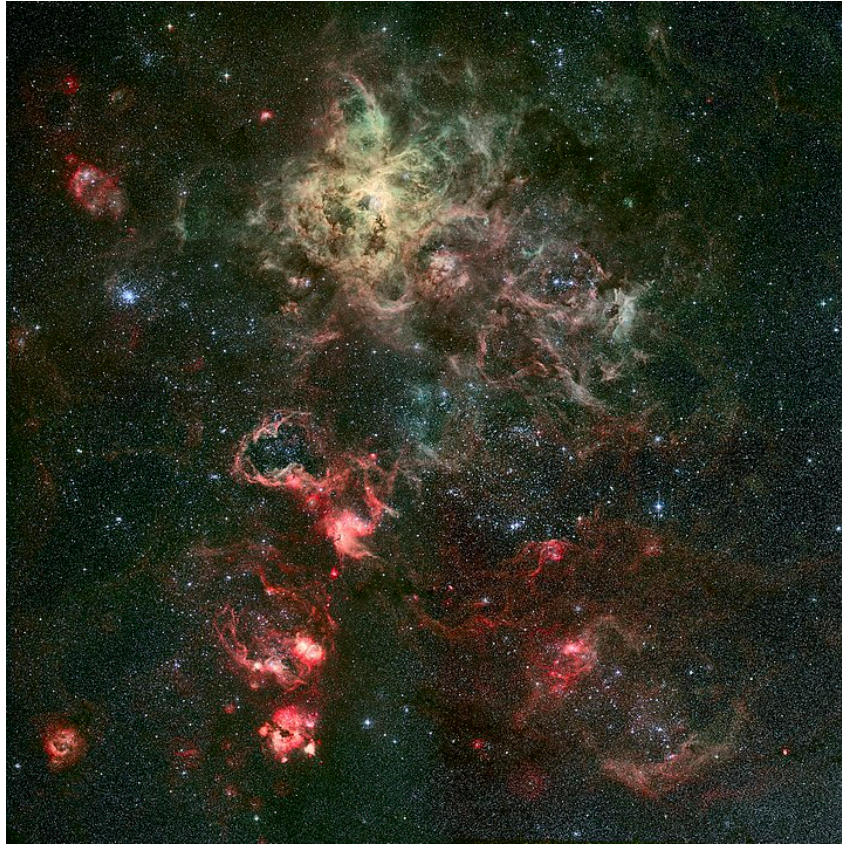


**Figure 1.3.** Optical image of the Tarantula nebula (Credit:ESO/R.Fosbury (ST-ECF)). Notice how the feedback from the young stars are dispersing the surrounding molecular gas from which they formed.

if this is an intrinsic threshold (see e.g. Burkert & Hartmann, 2013; Evans et al., 2014; Lada et al., 2010) and whether this is universally valid. In the central regions of our Galaxy, for instance, there seems to be a deficit of SF relative to the observed dense gas which still needs proper explanation (Kauffmann et al., 2017; Longmore et al., 2013). A possible reason for a given density threshold for SF might come from the need for a high enough column density to allow dust to provide sufficient shielding from the background ISRF (Clark & Glover, 2014).

### 1.2.6 Stellar feedback

The star formation itself profoundly affects the properties of the ISM through energetic feedback processes (see Fig. 1.3). These are important to disperse GMCs and so limit the efficiency of the star formation process per unit mass on cloud scales (see Klessen & Glover, 2016, and references therein). It also drives turbulence in the ISM, regulating star formation on galactic scales as well (see McKee & Ostriker, 2007, and references therein). Moreover, through stellar feedback the metals synthesised in the stellar interiors are being

re-injected into the environment such that feedback regulates the chemical enrichment and evolution of the ISM in a galaxy (e.g. Audouze & Tinsley, 1976, and references therein).

The most energetic type of feedback processes predominantly come from massive OB-type stars and include radiation-, wind- and supernova- feedback.

Young and massive stars have surface temperatures high enough to produce considerable amount of ionising photons ( $h\nu > 13.6$  eV). These will ionise the surrounding gas producing an HII region. In a uniform medium of density  $n$ , a star emitting an ionising photon flux of  $S$  will be able to ionise a sphere of radius

$$R_s = \left( \frac{3S}{4\pi\alpha_B n^2} \right)^{1/3}; \quad (1.13)$$

where  $\alpha_B n^2$  is the recombination rate. This is called the Strömgen (1939) radius. The region will be hot ( $T \simeq 10^4$  K) and therefore overpressurized compared to the molecular surrounding, which leads to an expansion and a generation of a low density cavity surrounded by a dense shell. Ionising radiation is an early-type feedback in the sense that it affects the parental GMC as soon as the massive star formed.

OB stars generate large photon fluxes which are able to drive line-driven winds from their atmospheres. This wind feedback is able to constantly inject mass fluxes of  $10^{-4}$ – $10^{-5}$   $M_\odot$ /yr at high velocity throughout their life-times and is therefore a continuous source of momentum deposited in the surrounding ISM. It therefore powers an expanding wind-driven bubble around young massive stars (Castor et al., 1975; Weaver et al., 1977), shocking the gas and sweeping up the ISM in a cold shell. Also the stellar winds are an early-type of feedback.

Stars more massive than  $\sim 8 M_\odot$  will end their life as an explosive supernova event. This will deposit roughly the mass of the star worth of metal enriched material at high velocity in the surrounding environment producing  $\sim 10^{51}$  erg worth of kinetic energy. This results in a free-expansion phase where the ejected material travels unhindered through the ISM until the swept-up gas is comparable to the mass of the ejecta. This shocks and heats up the interior of the expanding bubble such that it will subsequently evolve adiabatically as a pressure driven blast-wave following the self-similar Sedov-Taylor solution (Sedov, 1959; Taylor, 1950). This phase then transitions to an isothermal expansion phase as soon as the cooling time of the shocked gas is shorter than the expansion timescale. As the bubble continues to expand it loses its internal pressure due to adiabatic cooling such that the last stages of the expansion are purely driven by the momentum of the shell (Ostriker & McKee, 1988). Supernovae are a late type of feedback, in the sense that they will start to act only at late stages of the star formation process when the most massive stars start to die off. The most massive O stars will reach the SN stage after just a few

Myr which is still much shorter than the GMC life-time. SNe are therefore still important ingredients responsible for the dispersion of the parental cloud.

A SN event in a high density medium is inefficient in transferring the initial energy to the surrounding ISM since, due to short cooling times, the momentum building Sedov-Taylor phase is comparatively shorter. Therefore the pre-processing effect of the early feedback is crucial to the effectiveness of the SNe.

Other type of feedback which can become important in certain circumstances include radiation pressure from the most massive and luminous stars, accretion luminosity on protostellar objects and stellar jets, which are high-velocity collimated outflows generated in the presence of magnetised accretion discs. Of course the non-ionising part of the radiation emitted by the stars can also have a significant impact on the ISM, especially the photons with energy sufficient to photo-dissociate molecular hydrogen. This part of the spectrum is responsible to generate the ISRF which was discussed in the previous sections.

The relative importance of these different feedback types for the fate of a GMC are non-trivial, and strongly depend on the natal cloud density and mass. In certain circumstances the feedback might initially not be sufficient in dispersing the gas, such that a recollapse can occur which leads to a second generation star formation event (Rahner et al., 2017, 2019).

## 1.3 Galactic dynamics

The ISM is not evolving in an isolated sterile environment, but is part of a galaxy, and in most of the present day instances it is not the dominating component in terms of mass. Therefore it is important to study the ISM in this context, to understand the many feedback loops and interactions that the gas has with the galactic dynamics.

A stellar system such as a galaxy, is a collisionless system and as such it follows the collisionless Boltzmann equation:

$$\frac{\partial f}{\partial t} + \mathbf{v} \frac{\partial f}{\partial \mathbf{x}} + \dot{\mathbf{v}} \frac{\partial f}{\partial \mathbf{v}} = 0; \quad (1.14)$$

where  $f = f(\mathbf{x}, \mathbf{v}, t)$  is the distribution function of the stellar system which describes the stellar density in phase space at a position  $\mathbf{x}$  and velocity  $\mathbf{v}$  at a given time  $t$ . This equation is then coupled to

$$\dot{\mathbf{v}} = -\nabla \Phi_{\text{tot}}, \quad (1.15)$$

where  $\Phi_{\text{tot}}$  is the gravitational potential, which is given by the Poisson equation

$$\nabla^2 \Phi(\mathbf{x}, t) = 4\pi G \rho(\mathbf{x}, t), \quad (1.16)$$

where  $\rho(\mathbf{x}, t) = \int f d^3\mathbf{v}$  is the mass density of the system. The solution to these three coupled equations fully describes the time evolution of the stellar system.

A star with a given energy and angular momentum evolving in a specific axisymmetric potential performs generally a non-closing rosette orbit. The angular momentum sets the guiding radius  $R_g$  which is the radius of a circular orbit in the given potential having the same angular momentum. Each circular orbit at a given guiding radius has an intrinsic natural radial oscillating frequency when displaced radially in its circular orbit. This is called epicyclic frequency and is defined by

$$\kappa^2(R_g) = \left( R \frac{d\Omega^2}{dR} + 4\Omega^2 \right)_{R_g}, \quad (1.17)$$

where  $\Omega$  is the angular frequency of the circular orbit. If we then consider a perturbation to the axisymmetric potential, having  $m$ -fold rotational symmetry and which rotates at a pattern speed  $\Omega_p$ , we can identify resonances when

$$m(\Omega_p - \Omega) = l\kappa. \quad (1.18)$$

For  $l = 0$  we have corotation, where the guiding radius of corotating orbits has the same angular velocity than the perturbation. For  $l = \pm 1$  we have the inner and outer Lindblad resonance, where the perturbation has a forcing frequency equal to the internal natural frequency of the orbit at the given guiding radius.

Resonances are dynamically important because at these locations there can be energy exchange between stars and the potential (Binney & Tremaine, 1987; Sellwood, 2011).



**Figure 1.4.** Optical image of the NGC1097 barred galaxy (Credit: ESO).

### 1.3.1 Bars

A particularly interesting instance of an  $m$ -fold perturbation to an axisymmetric potential, is the case of  $m = 2$ , i.e. galactic bars. Half of all observed spiral galaxies are barred (Fig. 1.4) and isophotes retrieved from photometry reveal that bars have axis ratios of 3 : 1 (Athanasoula et al., 1990). A key parameter describing bars is the pattern speed, which determines the co-rotation radius. Observations show that bars extend to about 80 % of their co-rotation radius such that the ratio between co-rotation and semi-major axis is  $\sim 1.2 \pm 0.2$  (Elmegreen et al., 1996). Contrary to galactic discs, bars tend to be thick in the vertical direction due to a dynamical instability called "buckling instability" (Athanasoula, 2005; Combes & Sanders, 1981). Barred systems most often also show ring-like structures which can be divided into inner rings having radii of a few hundred parsecs, and outer rings located outside the tip of the bar (Buta, 1986). Moreover, dust lanes running almost radially from the tip of the bar towards the centre are present in most barred galaxies (see Fig. 1.4).

Simulations and dynamical studies show that discs are generally unstable for bar formation. Combined with the fact that simulations show that bars are long lived features, we can so explain the ubiquity of bars in observed targets (Bournaud et al., 2005).

A few mechanisms for bar formation have been proposed. In wave theory bars can be understood as a standing cavity wave where the reflection of the wave happens between the centre and the co-rotation radius. Swing amplification then provides a positive feed-

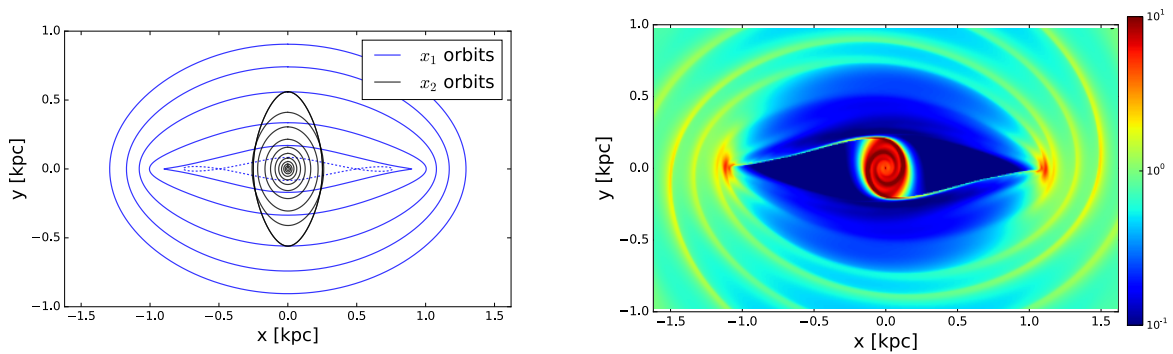


**Figure 1.5.** Different families of closed stellar orbits integrated in a barred potential (left-hand panel). On the right-hand panel I show the behaviour of the gas instead, evolved isothermally in the same barred potential.

back loop (Toomre, 1981). By increasing the central mass of the galaxy, an ILR develops which prevents the wave from travelling all the way to the centre. This cuts the feedback loop and inhibits the instability from forming. This explains the absence of bars in some galaxies with massive bulges.

Bars can also be formed by the effect of orbit trapping where eccentric orbits tend to align themselves in the inner part of galaxies (Lynden-Bell, 1979).

In the presence of bars, closed stellar orbits in the rotating frame of the bar can be of different family type (see Fig. 1.5). The  $x_1$  orbit family are elongated parallel to the bar and constitute its backbone. They rotate in the same direction as the bar and are mostly stable orbits. Some of these  $x_1$  orbits can be self-intersecting, producing a loop around the edges. This property is important when considering the gas kinematic in this region as self-intersecting gas orbits will produce shocks (see Section 1.3.4).

A second important type of closed orbits is the family of  $x_2$  orbits which can exist near the centre of a barred system. Those are mostly stable orbits elongated in the direction perpendicular to the bar. A prerequisite of their existence in a given galactic potential is the presence of an ILR and their radial extent is limited by the strength of the bar. The stronger the bar the smaller the central area where the  $x_2$  orbits can live.

Near co-rotation no stable closed orbits exist and so orbits get more and more chaotic here. This is why the extension of a bar is strongly limited by co-rotation (Contopoulos, 1980).

Bars, which are instabilities of discs, are in turn themselves unstable for a different type of instability: the buckling instability. This is a gravitational instability where small wrinkles in a thin sheet grow exponentially and cause the sheet to buckle and therefore thicken. This is the explanation of why bars are usually much thicker than the disc from



**Figure 1.6.** Optical image of the interacting M51 galaxy. The encounter induces a grand-design two-armed spiral pattern in the galactic disc. (Credits: NASA, ESA, S. Beckwith (STScI) and the Hubble Heritage Team (STScI/AURA))

which they originated and have rather a peanut shape (Combes & Sanders, 1981).

Some galaxies have secondary barred structures at the inner parts of the primary bar (Erwin & Sparke, 2002) with two different pattern speeds.

### 1.3.2 Spiral arms

Spiral arms are ubiquitous in early type galaxies (Fig. 1.6) although their dynamical origin remains debated. Spiral structures in galaxies can be quite variegated but in general we can distinguish grand design spirals where the structure in the observational B band is dominated by (generally) two well distinguished great arms, and flocculent galaxies where the spiral structure is more messy. Only  $\sim 10\%$  of all spirals fall in the category of grand design spirals and typical examples are M51, M81 and M100. Spiral structures in the disc induce shocks in the gas causing gas compression and thus favouring conditions for star formation. Indeed, real systems show enhanced star formation activity and higher molecular gas associated to the arms (e.g. Regan & Wilson, 1993; Rodriguez-Fernandez et al., 2006). With a few exceptions (Buta et al., 1992, find leading and trailing arms in NGC4622), all observed spirals are trailing, i.e. the gas and stars enter the concave edge and leave the convex edge.

The spiral instability of discs must be a dynamical one instead of pure hydrodynamical since it is observed both in the gas as well as in the stellar component. It can therefore

be understood as a gravity wave moving through the disc.

Grand design spirals are thought to be produced either by rotating bars (Buta et al., 2009) or by tidal interactions with a companion galaxy (e.g. Dobbs et al., 2010; Salo & Laurikainen, 1993), while flocculent spirals are probably caused by instabilities. The dynamics of such instabilities are however not fully understood and different theories are competing. The main debate rotates around whether spiral arms are long-lived features which can be understood in density wave theory as being a quasi steady global mode of discs (Bertin & Lin, 1996); or on the other hand short-lived and recurring features, originating from perturbing density fluctuations (e.g. Sellwood, 2000; Toomre, 1990).

Density wave theory requires a dynamically cool disc and hot inner part (Toomre (1964)  $Q \sim 1$  for the disc and  $Q > 2$  for the inner disc). It is technically a standing wave in a cavity where the reflection point is the inner  $Q$  barrier which shields the wave from reaching the ILR where it would be damped. Similarly to the bar instability, the conditions are right for swing amplification to generate a positive feedback loop. Rapid growing modes would quickly disappear, while slow growing modes are limited in amplitude by the dissipative shocks of the gas component. A quasi-steady spiral pattern can so be achieved which can be sustained indefinitely. The theory predicts a single dominant mode and therefore a single pattern speed for spiral arms in disc galaxies.

Even if the long lived spiral arm picture is analytically sound, it requires quite specific conditions and it is therefore unclear how significant this mechanism is in real systems.

The truth is that dynamically cool discs are in general always prone to develop spiral structures. Any disturbance, such as overdensities in the disc, perturbations from minor mergers, grooves in (the phase space of) the disc can induce spiral activity (Goldreich & Lynden-Bell, 1965; Toomre, 1990), and even if these spirals might be short lived, the sheer number of perturbations in real galaxies can easily explain the ubiquity of spirals. Multiple instances of these patterns usually co-exist and therefore in this recurrent spiral picture the spirals exhibit multiple pattern speeds.

Spiral structures can dynamically heat up the disc through wave-particle interactions at the Lindblad resonances where also angular momentum can be transferred between stars and spiral wave. Since these resonances are broader and more frequent in a scenario which allows for multiple pattern speeds, the recurrent spirals are much more efficient in disc heating, angular momentum transport and radial mixing (Sellwood, 2011).

A dynamically hot disc is much less sensitive to spiral instability. Therefore for new phases of spiral structures to arise the presence of gas is essential. Due to its dissipative nature, it can replenish the stellar component with dynamically colder stars and so keep the conditions favourable for spiral activity (Sellwood & Carlberg, 1984).

Simulations do show spiral activity, but they do not provide a clear picture of the

mechanism that originates them. Since observationally then it is difficult to understand the dynamical origin given only a snapshot in time of galaxies, this remains an actively researched topic. In the case of the Milky Way, the recurrent spiral picture seems to be the favorite model (De Simone et al., 2004).

### 1.3.3 galactic encounters

Galactic encounters are frequent in the Universe as revealed by observations of peculiar galaxies, which are galaxy systems disturbed by such encounters; cosmological models and considerations about the number density of galaxies in the local Universe come to a similar conclusion (Conselice, 2006; Toomre, 1977; Tremaine, 1981). Even the Milky Way has undergone several minor mergers during her life-time and will face a major merger with M31 in  $\sim 3$  Gyr (Unavane et al., 1996).

Even though the cross-section of a galaxy might be small, the merger rate is also enhanced by the phenomenon of dynamical friction. Small galaxies orbiting a bigger halo slowly experience orbital decay due to dynamical friction which leads it to fall towards the larger galaxy. This is the dominant mechanism for minor mergers to happen (e.g. Navarro et al., 1995).

Galaxy mergers can be quite violent events. The collision is inelastic and dynamically heats the stellar system enhancing the amount of random orbits, such that a major merger of two disc galaxies will produce an elliptic galaxy (see Vogelsberger et al., 2014). In the case of wet mergers (when at least one of the two galaxies is an early type, see Fig. 1.6) the encounter can induce shocks in the gas, loss of angular momentum and general enhancement of star formation. A typical example are the Antennae galaxies which are undergoing a merger which lead to extreme starburst events. The loss of angular momentum can drive large amount of gas towards the gravitational centre where it leads to a central star burst event which can reach star formation rates as high as  $10^3 M_{\odot}/\text{yr}$ . These extreme starburst events are however inevitably quite short lived, lasting only a few tens of Myr (Larson & Tinsley, 1978).

The best way to investigate galaxy encounters and mergers is through N-body simulations, but the most instructive and educational view of the phenomenon comes from the pioneering work of Toomre & Toomre (1972). Their simple model consisted of studying the dynamics of massless particles orbiting a central mass which would undergo a merger. With these simple assumptions they could describe the key features of observed peculiar galaxies (spiral arms, connecting arms, rings, tails, etc...).

Galactic encounters are an established mechanism to form prominent  $m = 2$  spiral arms in disc galaxies, especially in the case of in-plane prograde interactions and if the encounter is considered minor (Toomre & Toomre, 1972). A near side arm develops

bridging the galaxy to the companion and a counter-arm at the opposite site of the galaxy.

If the companion is more massive, the encounter can lead to bridges between the two galaxies and a long tidal tail develops through which gas can be stripped from the system.

Another interesting group of galaxies forms when a disc galaxy collides head-on with another system. This can trigger radially expanding density waves that trigger star formation as they pass (Lynds & Toomre, 1976). These galaxies then exhibit an outer ring of young stars which is rotating and expanding, a textbook example of such a system is the Cartwheel galaxy (Appleton & Struck-Marcell, 1996). These rings are rather short lived and disappear as soon as the density wave passed.

### 1.3.4 ISM in a galaxy

It transpires from our previous sections that the ISM and the stellar dynamics are two deeply interlinked systems and that a proper understanding of the gas properties cannot ignore the environmental conditions that the complex dynamics of a galaxy sets.

Large scale dynamical features affect the gas properties down to the smallest scales. Spiral arms gather material, shock the gas and trigger molecular cloud formation leading to star formation. But also local properties like galactic shear and midplane pressure forces affect the behaviour of the gas and influence cloud and star formation.

The presence of a bar is particularly interesting when we study the ISM. It is here helpful to recall the stellar dynamics of bars described in section 1.3.1. The dissipation due to the collisional nature of the gas leads the ISM to follow only the stable closed orbits. Therefore close to the centre the gas follows the  $x_2$  orbits creating a disc like (most often it is a ring like) structure. At greater radii, instead, the gas follows the  $x_1$  orbits, elongated in the direction of the bar. However this reasoning breaks down whenever the closed orbits would be self-intersecting or intersecting with other closed orbits. The gas, contrary to the stellar component, is in fact collisional and such a configuration would lead to shock generation in the gas. This is the case for the intermediate region between the inner  $x_2$  and the outer  $x_1$  orbits where the  $x_1$  orbits are looping and self-intersecting. Here the gas develops strong shocks which connect the tip of the bar to the central  $x_2$  ring (see the right-hand panel of Fig. 1.5 where the behaviour of the gas is shown.). The gas flows at high velocity almost radially along these shocks which can be identified with the dust lanes observed in barred galaxies.

In general there can be angular momentum transfer between gas and bar which efficiently drives gas inwards. Momentum transfer stagnates however when the gas reaches the  $x_2$  ring where a considerable amount of gas can accumulate. This is why in many barred galaxies the  $x_2$  ring corresponds with an accumulation of dense molecular gas and

active star formation.

The presence of an ILR is necessary for the existence of the x2 ring (Binney & Tremaine, 1987), and in cases where this is not present, the gas can easily be transported directly to regions close to the central SMBH where it can trigger AGN activity (see Sellwood, 2011, and references therein).

Gas responds strongly to the presence of spiral arm features in the stellar component which induce shock formation in the ISM (Roberts, 1969; Shu et al., 1973; Woodward, 1975). The gas is indeed very sensitive to any perturbation in the stellar disc and even smaller overdensities can result in highly amplified perturbations in the gas. Observationally, molecular gas and SF tracers correlate with spiral arms, and it is thought that the shock generation can be the triggering mechanism for gas compression and thus molecular cloud and star formation (Seigar & James, 2002). But on the other hand the gaseous disc is very susceptible to any kind of perturbation and instabilities such that clouds can form even without the presence of spiral arms. Some observations indeed do not find great differences in the SF between grand-design and flocculent disc galaxies (Eden et al., 2012; Elmegreen & Elmegreen, 1986; Stark et al., 1987) and spiral arms are then not drivers of SF but merely gather the gas that would anyway form stars (Vogel et al., 1988). However cloud-cloud collisions are more frequent in the presence of a spiral structure due to the high density environment and this favours the formation of massive GMC associations (Colombo et al., 2014; Dobbs, 2008) compared to the inter-arm region where instead clouds tend to be stretched apart by the galactic shear. In the inter-arm region clouds tend therefore to have more pronounced CO-dark envelopes compared to the compressive and high density region within a spiral arm where clouds are more shielded from the ISRF (Smith et al., 2014).

Apart from GMCs, spiral arms exhibit substructure in the gas phase known as spurs and feathers. These are feather-like features which extend from the arm at a typical angle from the trailing side. They are generated when substructure is sheared apart as it leaves the spiral arm (Dobbs & Bonnell, 2006). A smooth gas flow through periodic shocks is in general unstable due to resonant forcing and creates similar feather-like structures as the instability develops (Sormani et al., 2017).

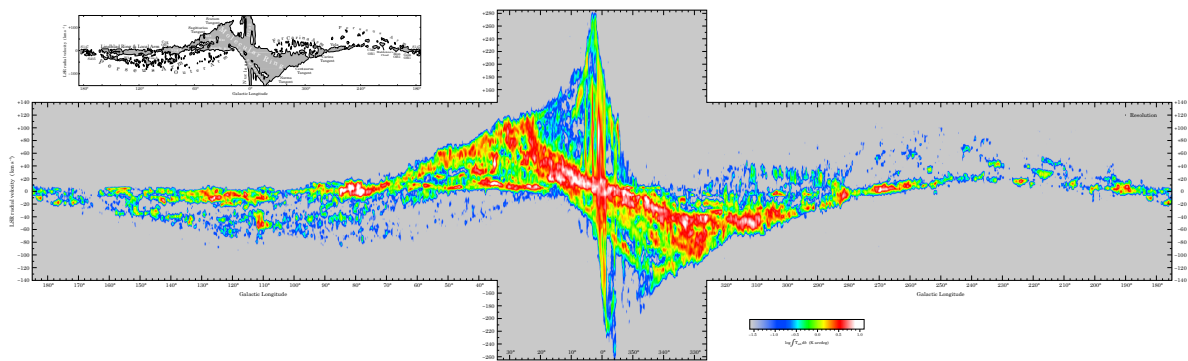


**Figure 1.7.** Longitude-line-of-sight-velocity map of the CO emission of the galactic plane of the MW (Dame et al., 2001). Important features are identified by their names in the upper left box.

## 1.4 The Milky Way

To study the morphology and dynamics of the Milky Way (MW) and in particular the properties of the ISM in the context of the local environment, is a challenging task. Indeed, the problem with the Milky Way is that we lie inside the plane of the galaxy, and therefore it is difficult to disentangle the 3D structure of the components. We therefore have to rely on dynamical models and then interpret the observations in this framework. Of particular utility in this regard are longitude-velocity diagrams where we consider also the line-of-sight velocity of the gas, since these are reflecting the kinematics of the ISM which in turn are highly dependent on the dynamical model of the Milky Way (Fig. 1.7).

We know that the MW is a barred galaxy from deprojections of standard candle stars (e.g. Wegg & Gerhard, 2013). The impact of the bar on the gas kinematics is evident in the l-v diagrams where the gas starts to follow non-circular orbits as the bar becomes more important with respect to the other components. The axis of the bar forms an angle of  $\sim 20^\circ$  with the location of the Sun and therefore the gas has extreme line-of-sight velocities as it flows almost radially along the shock-lanes of the Milky Way induced by the bar. These features are called dust-lanes.

In the light of gas flow in presence of a galactic bar described in section 1.3.4, the Milky Way hosts a ring-like structure of molecular gas in its centre associated to the x2 disc/ring described above, which is known as the Central Molecular Zone (CMZ). The molecular gas peaks therefore in the CMZ and falls off sharply in the region dominated by the dust-lanes. It increases again at Galactocentric radii of 4–6 kpc in a structure known as the molecular ring and then falls off exponentially until 12–13 kpc (Heyer et al., 1998). The HI distribution, on the other hand, extends to much larger radii and can be detected

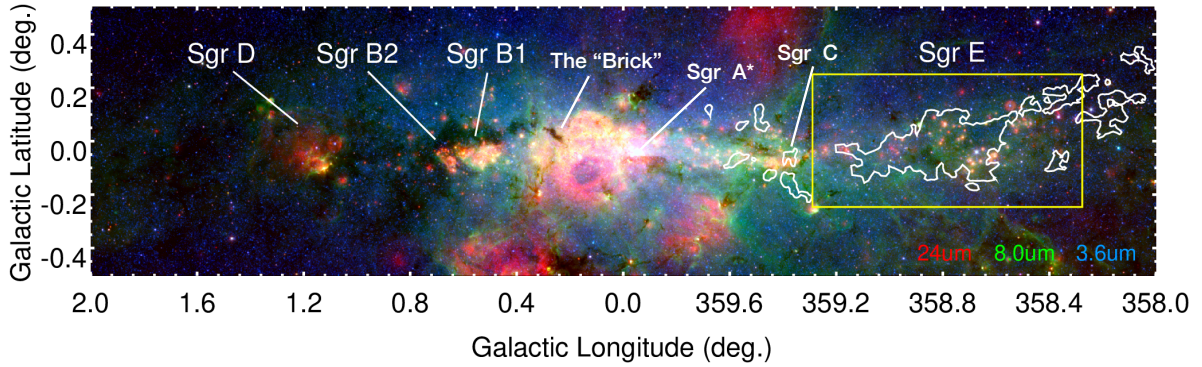


**Figure 1.8.** Infrared view of the CMZ (image adapted from Anderson et al., 2020). Famous GMCs are labelled, as well as the location of the central SMBH, SgrA\*.

up to  $\sim 60$  kpc. It has roughly constant surface density of  $10 M_{\odot} \text{pc}^{-2}$  between 4–12.5 kpc and then declines exponentially. The HI component is also much more extended in the vertical direction and has a scale-height of  $\sim 85$  pc at the Solar radius compared to the scale-height of the molecular gas of only  $\sim 45$  pc. The total mass in the HI component is  $\sim 1.1 \times 10^{10} M_{\odot}$  against the  $\sim 1.2 \times 10^9 M_{\odot}$  for the molecular component (Kalberla & Dedes, 2008; McMillan, 2017).

The MW disc is warped as can be seen in the HI traced at great Galactic radii (Kerr et al., 1957; Levine et al., 2006). Moreover coherent gas ridges seen in the  $l$ - $v$  diagrams suggest the presence of spiral arms in the disc of the MW.

### The CMZ

The CMZ is a particularly interesting place in the Milky Way (Fig. 1.8). Due to the gas transport from the galactic bar we have an accumulation of material in a relatively small region ( $R \sim 200$  pc). This leads to high star formation making this environment an analogue to a high-redshift star-forming galaxy (Kruijssen & Longmore, 2013). The gas is predominantly molecular here and the mean density of  $n \sim 10^4 \text{cm}^{-3}$  is considerably higher relative to solar-neighbourhood conditions (Guesten & Henkel, 1983). Locally, stars are observed to form whenever the density exceeds a given threshold (see Section 1.2.5), resulting a relation between the observed SF and the mass of gas above this density threshold (e.g. Lada et al., 2012). In the CMZ, on the other hand, this relation breaks down, and for the amount of dense gas present, the CMZ is deficient in star formation (Kauffmann et al., 2017; Longmore et al., 2013). The CMZ hosts about 5% in mass of the Milky Ways molecular gas ( $\sim 3 \times 10^7 M_{\odot}$ ), and similarly harbors  $\sim 5\%$  of the star formation (Crocker, 2012). Therefore, even though deficient of SF relative to the dense gas, the CMZ still resides on the Shmidt-Kennicutt relation.

The gas is extreme also in other aspects here. It is highly turbulent with molecular clouds showing velocity dispersion of  $\sigma \simeq 10\text{--}15$  km/s (Bally et al., 1987) and the molecular phase is generally hotter than solar-neighborhood clouds (Ginsburg et al., 2016). Cosmic-ray ionisation rates and the interstellar radiation field intensity is orders of magnitude higher than in the disc of the Milky Way (Clark et al., 2013; Yusef-Zadeh et al., 2007).

The molecular gas is organised into several dozen of prominent GMCs which exhibit a variety of different star formation rates and average densities. A few important examples are Sgr B2 which is the most actively star forming molecular cloud in the CMZ (Gordon et al., 1993), and the *Brick* which is an extremely compact cloud, but hosting virtually no star formation (e.g. Mills et al., 2015). These are believed to follow an x2 orbit forming a ring like structure around the centre of the Milky Way. Some gas is, however, also observed at even smaller Galactic radii, forming a disc-like structure of a few tens of pc surrounding the supermassive black hole of the MW, SgrA\*. This feature goes by the name of *Circum Nuclear Disc* (CND).

The star formation in the CMZ slowly builds up a stellar disc called the *Nuclear Stellar Disc* which is observed to have roughly the same extent than the gas in the CMZ from which it formed (Schönrich et al., 2015).

Above and below the Galactic plane in the centre of the MW, there are two symmetric lobes of hot ionised gas, associated with ionized, atomic and even molecular outflows (Di Teodoro et al., 2020) coming from the region. These are known as the Fermi bubbles (Su et al., 2010) and a possible origin could be AGN activity from SgrA\* (e.g. Guo & Mathews, 2012) or prolonged and intense star formation in the CMZ (e.g. Carretti et al., 2013).

In the picture presented here, the CMZ coincides to the region of x2 orbits, and the dust lanes are directly connected to this ring-like structure. Alternatively Krumholz & Kruijssen (2015) suggested that the inflow from the bar happens further out and is driven inwards via acoustic instabilities to settle in a ring-like structure at the shear minimum when the Galactic rotation curve transitions to solid-body. The necessary instability seems however to be a spurious result (Sormani & Li, 2020) and l-v diagrams of CO emissions seem to be consistent with a direct dynamical connection of the dust lanes with the CMZ. In the framework of Krumholz & Kruijssen (2015), however, it is easier to fit an arbitrary orbit to the observed kinematic data since the gas can follow multiple paths towards the shear minimum as it is not being disturbed by the dissipative action of the shocks colliding at very specific points with the CMZ. Kruijssen et al. (2015) therefore found that a 'pretzel-like' stream could better explain the kinematic data of the GMCs in the CMZ.

## 1.5 Scientific goals and methodology

It is clear that average GMC properties vary with the large-scale galactic environment, but it remains largely unclear how the change in the galactic physical conditions affects the formation and evolution of GMCs.

Numerical simulations are essential in this quest, but it is also extremely difficult to numerically resolve and study GMCs in the context of an entire galaxy due to the large range of spatial scales necessary to include. This starts however to become feasible nowadays given novel numerical techniques and ever improving computing power.

We aim at improving our understanding of the cold molecular gas in galaxies and disentangle the complex interplay between cloud scales and the galactic scales. We study ISM properties in general trying to understand how they are affected by a set of different dynamical environments. Moreover, our aim is to start to resolve with numerical simulations sub-structure in GMCs on galactic scales, such that we can statistically address their properties and draw sensible conclusions regarding the star formation as well as a function of the environment.

Our approach is largely numerical and we develop dedicated hydrodynamic simulations of the ISM in interesting galactic systems. We chose to model two of the most observed targets, namely the interacting galaxy system M51 and the Milky Way. In the latter case a particularly interesting and dynamic environment is the central part of the Galaxy where the bar starts to dominate, and we put particular focus on the CMZ which is an ideal laboratory for GMC dynamics and star formation. With this model we can therefore study the complex dynamics and kinematic of the gas in the presence of a bar and investigate how this complex environment shapes the ISM down to the cloud scales. The M51 galaxy, instead, is an interacting galaxy which exhibits a grand design two arm spiral pattern. For this model we want to study what the effect of a galactic encounter on the ISM, and what is the importance of the spiral arms.

For our Milky Way CMZ model we pay particular attention to observational constraints in order to be compatible with the state-of-the-art models of the Milky Way. This will enable us to confidently interpret observed features in the context of our barred galaxy model. Especially for the Milky Way this is particularly valuable since we lack a sense of the 3d distribution and kinematics of the gas. To achieve agreement with the observed constraints, we refrain from employing a full N-body simulation and ignore the dynamics of the stellar and dark matter component which is instead modelled with a background fixed potential. We then let the simulated ISM evolve in this potential. We adopt this strategy because it is easier to control the parameters and fine-tune it to observational constraints. A true N-body simulation would be more realistic but would

require extensive work to set-up initial conditions which would lead to Milky Way like conditions at a given simulation time. This is outside the scope of our analysis.

In the case of the M51 system, on the other hand, the focus is less in reproducing the observed system in detail as much as to study how the ISM reacts to a galaxy encounter. We therefore take inspiration of a real system but do not pay too much attention on the observational constraints. We can then invest some energies into the setup of the initial conditions and follow the dynamics of the stellar and dark matter component as well with an N-body solver coupled to the hydrodynamic code. To compare the ISM in the interacting case to a more regular environment, we also prepare simulations of the same galaxy in isolation.

We achieve this with high resolution simulations with the moving mesh code AREPO (Springel, 2010) coupled to additional physics necessary to follow GMC formation, evolution and dissipation. A detailed description of the physical ingredients added is described in the following chapters, while here we will remain quite general. Arguably one of the most important aspects about the ISM is its thermal state which deeply depends on the microphysics governing the thermal processes. Of particular importance is the Hydrogen and Carbon chemistry which is extremely relevant for the molecular phase. These species are therefore treated with a non-equilibrium time-dependent chemical network. A proper treatment of the chemical processes here has as a premise a good model of the background UV ISRF which can photodissociate  $\text{H}_2$  and  $\text{CO}$ . This is achieved by assuming a constant background radiation but computing the local attenuation by self-absorption due to the foreground gas, in a non-isotropic manner.

Our work builds upon previous models with a similar setup and resolution, which however did not include star formation and feedback processes in their ISM model (see Smith et al., 2014; Sormani et al., 2018). A particular important addition here is the treatment of the gas self gravity which leads to star formation. The gravitational collapse is a process which covers several orders of magnitude in spatial scales. We can of course not fully follow this down to the smallest scales, so we put particular care into sub-grid modelling these steps. In this regard we use accreting sink particles and use a star formation and evolution model to account for the processes that we cannot resolve. As for the stellar feedback, we only model the supernovae.

The lack of other feedback types and magnetic fields reduces the realism of our simulations, but has other important benefits. We in fact developed this line of research to focus on what the importance of different physical ingredients are structuring the ISM. The best way to approach this is then to incrementally improve the model including new physical processes gradually. Having produced and analysed the models without self-gravity (Smith et al., 2014; Sormani et al., 2018), these models described here are the

next step in this learning process.

We want to stress once again that the focus of this work is to understand the true behaviour of the gas given certain physical conditions, and the focus is less on how these properties would translate in the observational space. Therefore we predominantly analyse the ISM properties of the simulations as produced by the computation and avoid any post-processing step which would translate the simulation data into what an observer might detect. We leave this important task to future work.

## 1.6 Structure of the thesis

The main body of this dissertation is structured as follows: thematically the text can be subdivided into two parts, the first part dedicated to gas dynamics in an interacting M51-like galaxy and the second part where we focus our attention to the CMZ.

In chapter 2 we present the model of the M51-like simulations and study the general properties of the ISM in this simulated system. We put particular emphasis on a comparison between the interacting and the isolated galaxy. In this way we can assess how the tidal interaction and the formation of spiral arms is affecting the ISM. In the following chapter (chapter 3) we then look at the molecular gas in more detail. We select GMCs for a given snapshot time and construct the cloud catalog storing their most important properties. We analyse their properties in general terms as well as relative to their position in the galaxy and with respect to the isolated galaxy. In particular we want to know what type of clouds the physical ingredients and our numerical recipe produce, we discuss if and to what extent the local environment is affecting this, and specifically if the interaction can alter the cloud population.

We then proceed to present and analyse the CMZ simulations. In chapter 4 we present our model and describe the gas flow in general in these simulations. Since they are an upgrade to similar simulations which did not include star formation and stellar feedback, it is of particular interest to explore how the addition of these ingredients is altering the morphology and the general gas flow. We explore if the new model can explain observed features which the previous work could not, for instance the inflow of gas towards more central regions and the tilt of the CMZ. In chapter 5 we then conclude the analysis with a study of the star formation in the region. We try to address questions like the trigger of SF which is thoroughly debated in literature as well as assess the time variability of the SF in the simulation.

We finally summarise our findings and put them in prospective in chapter 6 where we emphasise strengths and limitations of our approach. We point to still open questions that we could address by further analysis or with further follow-up simulations. We conclude by detailing the future research steps planned to tackle these questions and improve our understanding of GMCs as integral part of a galaxy.

## Bibliography

- Aartsen M. G., et al., 2013, *Phys. Rev. D*, 88, 042004
- Ackermann M., et al., 2013, *Science*, 339, 807
- Agertz O., et al., 2007, *MNRAS*, 380, 963
- Anderson L. D., et al., 2020, *ApJ*, 901, 51
- Appleton P. N., Struck-Marcell C., 1996, , 16, 111
- Athanassoula E., 2005, *MNRAS*, 358, 1477
- Athanassoula E., Morin S., Wozniak H., Puy D., Pierce M. J., Lombard J., Bosma A., 1990, *MNRAS*, 245, 130
- Audouze J., Tinsley B. M., 1976, *ARA&A*, 14, 43
- Ballesteros-Paredes J., Mac Low M.-M., 2002, *ApJ*, 570, 734
- Ballesteros-Paredes J., Klessen R. S., Mac Low M. M., Vazquez-Semadeni E., 2007, in Reipurth B., Jewitt D., Keil K., eds, *Protostars and Planets V*. p. 63 ([arXiv:astro-ph/0603357](https://arxiv.org/abs/astro-ph/0603357))
- Ballesteros-Paredes J., Hartmann L. W., Vázquez-Semadeni E., Heitsch F., Zamora-Avilés M. A., 2011, *MNRAS*, 411, 65
- Bally J., Stark A. A., Wilson R. W., Henkel C., 1987, *ApJS*, 65, 13
- Banerjee R., Vázquez-Semadeni E., Hennebelle P., Klessen R. S., 2009, *MNRAS*, 398, 1082
- Bertin G., Lin C. C., 1996, *Spiral structure in galaxies a density wave theory*
- Bertram E., Federrath C., Banerjee R., Klessen R. S., 2012, *MNRAS*, 420, 3163
- Bigiel F., Leroy A., Walter F., Brinks E., de Blok W. J. G., Madore B., Thornley M. D., 2008, *AJ*, 136, 2846
- Bigiel F., et al., 2011, *ApJ*, 730, L13
- Binney J., Tremaine S., 1987, *Galactic dynamics*
- Bournaud F., Combes F., Semelin B., 2005, *MNRAS*, 364, L18
- Burkert A., Hartmann L., 2013, *ApJ*, 773, 48
- Buta R., 1986, *ApJS*, 61, 609
- Buta R., Crocker D. A., Byrd G. G., 1992, *AJ*, 103, 1526
- Buta R. J., Knapen J. H., Elmegreen B. G., Salo H., Laurikainen E., Elmegreen D. M., Puerari I., Block D. L., 2009, *AJ*, 137, 4487
- Carretti E., et al., 2013, *Nature*, 493, 66
- Castor J. I., Abbott D. C., Klein R. I., 1975, *ApJ*, 195, 157
- Clark P. C., Glover S. C. O., 2014, *MNRAS*, 444, 2396
- Clark P. C., Glover S. C. O., Klessen R. S., Bonnell I. A., 2012, *MNRAS*, 424, 2599
- Clark P. C., Glover S. C. O., Ragan S. E., Shetty R., Klessen R. S., 2013, *ApJ*, 768, L34
- Colombo D., et al., 2014, *ApJ*, 784, 3
- Combes F., Sanders R. H., 1981, *A&A*, 96, 164
- Conselice C. J., 2006, *ApJ*, 638, 686
- Contopoulos G., 1980, *A&A*, 81, 198
- Corbelli E., Elmegreen B. G., Braine J., Thilker D., 2018, *A&A*, 617, A125
- Crocker R. M., 2012, in Tuffs R. J., Popescu C. C., eds, Vol. 284, *The Spectral Energy Distribution of Galaxies - SED 2011*. pp 371–378 ([arXiv:1112.6249](https://arxiv.org/abs/1112.6249)), doi:10.1017/S1743921312009441
- Crutcher R. M., Wandelt B., Heiles C., Falgarone E., Troland T. H., 2010, *ApJ*, 725, 466
- Dame T. M., Hartmann D., Thaddeus P., 2001, *ApJ*, 547, 792
- Davies R. D., 1974, in Kerr F. J., Simonson S. C., eds, Vol. 60, *Galactic Radio Astronomy*. p. 275

- De Simone R., Wu X., Tremaine S., 2004, *MNRAS*, 350, 627
- Di Teodoro E. M., McClure-Griffiths N. M., Lockman F. J., Armillotta L., 2020, *Nature*, 584, 364
- Dobbs C. L., 2008, *MNRAS*, 391, 844
- Dobbs C. L., Bonnell I. A., 2006, *MNRAS*, 367, 873
- Dobbs C. L., Glover S. C. O., Clark P. C., Klessen R. S., 2008, *MNRAS*, 389, 1097
- Dobbs C. L., Theis C., Pringle J. E., Bate M. R., 2010, *MNRAS*, 403, 625
- Draine B. T., 1978, *ApJS*, 36, 595
- Draine B. T., Bertoldi F., 1996, *ApJ*, 468, 269
- Draine B. T., Lee H. M., 1984, *ApJ*, 285, 89
- Eden D. J., Moore T. J. T., Plume R., Morgan L. K., 2012, *MNRAS*, 422, 3178
- Elmegreen B. G., 2007, *ApJ*, 668, 1064
- Elmegreen B. G., Elmegreen D. M., 1986, *ApJ*, 311, 554
- Elmegreen B. G., Elmegreen D. M., Chromey F. R., Hasselbacher D. A., Bissell B. A., 1996, *AJ*, 111, 2233
- Endres C. P., Schlemmer S., Schilke P., Stutzki J., Müller H. S. P., 2016, *Journal of Molecular Spectroscopy*, 327, 95
- Engargiola G., Plambeck R. L., Rosolowsky E., Blitz L., 2003, *ApJS*, 149, 343
- Erwin P., Sparke L. S., 2002, *AJ*, 124, 65
- Evans Neal J. I., Heiderman A., Vutisalchavakul N., 2014, *ApJ*, 782, 114
- Federrath C., Klessen R. S., Schmidt W., 2008, *ApJ*, 688, L79
- Field G. B., Saslaw W. C., 1965, *ApJ*, 142, 568
- Field G. B., Goldsmith D. W., Habing H. J., 1969, *ApJ*, 155, L149
- Fish V. L., Reid M. J., Argon A. L., Menten K. M., 2003, *ApJ*, 596, 328
- Fryxell B., et al., 2000, *ApJS*, 131, 273
- Fukui Y., Kawamura A., 2010, *ARA&A*, 48, 547
- Fukui Y., et al., 2009, *ApJ*, 705, 144
- Gaensler B. M., Madsen G. J., Chatterjee S., Mao S. A., 2008, *Publications of the Astronomical Society of Australia*, 25, 184
- Ginsburg A., et al., 2016, *A&A*, 586, A50
- Girart J. M., Rao R., Marrone D. P., 2006, *Science*, 313, 812
- Glassgold A. E., Langer W. D., 1973, *ApJ*, 186, 859
- Glover S. C. O., Clark P. C., 2012, *MNRAS*, 421, 9
- Glover S. C. O., Mac Low M.-M., 2007a, *ApJS*, 169, 239
- Glover S. C. O., Mac Low M.-M., 2007b, *ApJ*, 659, 1317
- Glover S. C. O., Smith R. J., 2016, *MNRAS*, 462, 3011
- Gnat O., Ferland G. J., 2012, *ApJS*, 199, 20
- Gnedin N. Y., Tassis K., Kravtsov A. V., 2009, *ApJ*, 697, 55
- Goldbaum N. J., Krumholz M. R., Matzner C. D., McKee C. F., 2011, *ApJ*, 738, 101
- Goldreich P., Lynden-Bell D., 1965, *MNRAS*, 130, 125
- Goodwin S. P., Nutter D., Kroupa P., Ward-Thompson D., Whitworth A. P., 2008, *A&A*, 477, 823
- Gordon M. A., Berkemann U., Mezger P. G., Zylka R., Haslam C. G. T., Kreysa E., Sievers A., Lemke R., 1993, *A&A*, 280, 208
- Gould R. J., Salpeter E. E., 1963, *ApJ*, 138, 393
- Guesten R., Henkel C., 1983, *A&A*, 125, 136
- Guo F., Mathews W. G., 2012, *ApJ*, 756, 181

- Habing H. J., 1968, , 19, 421
- Haffner L. M., et al., 2009, *Reviews of Modern Physics*, 81, 969
- Han J. L., 2017, *ARA&A*, 55, 111
- Heitsch F., Zweibel E. G., Mac Low M.-M., Li P., Norman M. L., 2001, *ApJ*, 561, 800
- Hennebelle P., Pérault M., 1999, *A&A*, 351, 309
- Hennebelle P., Commerçon B., Joos M., Klessen R. S., Krumholz M., Tan J. C., Teyssier R., 2011, *A&A*, 528, A72
- Heyer M. H., Brunt C. M., 2012, *MNRAS*, 420, 1562
- Heyer M., Dame T. M., 2015, *ARA&A*, 53, 583
- Heyer M. H., Brunt C., Snell R. L., Howe J. E., Schloerb F. P., Carpenter J. M., 1998, *ApJS*, 115, 241
- Heyer M. H., Carpenter J. M., Snell R. L., 2001, *ApJ*, 551, 852
- Heyer M., Krawczyk C., Duval J., Jackson J. M., 2009, *ApJ*, 699, 1092
- Hollenbach D., Salpeter E. E., 1971, *ApJ*, 163, 155
- Hopkins P. F., 2015, *MNRAS*, 450, 53
- Hoyle F., Ellis G. R. A., 1963, *Australian Journal of Physics*, 16, 1
- Hughes A., et al., 2013, *ApJ*, 779, 46
- Ibáñez-Mejía J. C., Mac Low M.-M., Klessen R. S., Baczynski C., 2016, *ApJ*, 824, 41
- Jeffreson S. M. R., Kruijssen J. M. D., 2018, *MNRAS*, 476, 3688
- Jones A. P., Tielens A. G. G. M., 1994, in Tielens A. G. G. M., ed., *The Diffuse Interstellar Bands*. pp 79–83
- Kainulainen J., Beuther H., Henning T., Plume R., 2009, *A&A*, 508, L35
- Kainulainen J., Federrath C., Henning T., 2014, *Science*, 344, 183
- Kalberla P. M. W., Dedes L., 2008, *A&A*, 487, 951
- Kauffmann J., Pillai T., Zhang Q., Menten K. M., Goldsmith P. F., Lu X., Guzmán A. E., 2017, *A&A*, 603, A89
- Kawamura A., et al., 2009, *ApJS*, 184, 1
- Kennicutt Robert C. J., 1998, *ApJ*, 498, 541
- Kerr F. J., Hindman J. V., Carpenter M. S., 1957, *Nature*, 180, 677
- Klessen R. S., Glover S. C. O., 2016, *Saas-Fee Advanced Course*, 43, 85
- Klessen R. S., Hennebelle P., 2010, *A&A*, 520, A17
- Koda J., et al., 2009, *ApJ*, 700, L132
- Kong S., et al., 2018, *ApJS*, 236, 25
- Kritsuk A. G., Lee C. T., Norman M. L., 2013, *MNRAS*, 436, 3247
- Kruijssen J. M. D., Longmore S. N., 2013, *MNRAS*, 435, 2598
- Kruijssen J. M. D., Dale J. E., Longmore S. N., 2015, *MNRAS*, 447, 1059
- Krumholz M. R., 2012, *ApJ*, 759, 9
- Krumholz M. R., Kruijssen J. M. D., 2015, *MNRAS*, 453, 739
- Krumholz M. R., Tan J. C., 2007, *ApJ*, 654, 304
- Krumholz M. R., Stone J. M., Gardiner T. A., 2007, *ApJ*, 671, 518
- Krumholz M. R., Leroy A. K., McKee C. F., 2011, *ApJ*, 731, 25
- Kumar M. S. N., Palmeirim P., Arzoumanian D., Inutsuka S. I., 2020, *A&A*, 642, A87
- Kwan J., 1979, *ApJ*, 229, 567
- Lada C. J., Lombardi M., Alves J. F., 2010, *ApJ*, 724, 687
- Lada C. J., Forbrich J., Lombardi M., Alves J. F., 2012, *ApJ*, 745, 190
- Larson R. B., 1981, *MNRAS*, 194, 809

- Larson R. B., Tinsley B. M., 1978, *ApJ*, 219, 46
- Leroy A. K., Walter F., Brinks E., Bigiel F., de Blok W. J. G., Madore B., Thornley M. D., 2008, *AJ*, 136, 2782
- Levine E. S., Blitz L., Heiles C., 2006, *ApJ*, 643, 881
- Lombardi M., Lada C. J., Alves J., 2010, *A&A*, 512, A67
- Longmore S. N., et al., 2013, *MNRAS*, 429, 987
- Lynden-Bell D., 1979, *MNRAS*, 187, 101
- Lynds R., Toomre A., 1976, *ApJ*, 209, 382
- Mac Low M.-M., Klessen R. S., 2004, *Reviews of Modern Physics*, 76, 125
- Mathis J. S., Rumpl W., Nordsieck K. H., 1977, *ApJ*, 217, 425
- Mathis J. S., Mezger P. G., Panagia N., 1983, *A&A*, 500, 259
- McKee C. F., Ostriker J. P., 1977, *ApJ*, 218, 148
- McKee C. F., Ostriker E. C., 2007, *ARA&A*, 45, 565
- McMillan P. J., 2017, *MNRAS*, 465, 76
- Meidt S. E., et al., 2015, *ApJ*, 806, 72
- Mierkiewicz E. J., Reynolds R. J., Roesler F. L., Harlander J. M., Jaehnig K. P., 2006, *ApJ*, 650, L63
- Mills E. A. C., Butterfield N., Ludovici D. A., Lang C. C., Ott J., Morris M. R., Schmitz S., 2015, *ApJ*, 805, 72
- Minter A. H., Spangler S. R., 1997, *ApJ*, 485, 182
- Molinari S., et al., 2014, in Beuther H., Klessen R. S., Dullemond C. P., Henning T., eds, *Protostars and Planets VI*. p. 125 ([arXiv:1402.6196](https://arxiv.org/abs/1402.6196)), doi:10.2458/azu\_uapress\_9780816531240-ch006
- Navarro J. F., Frenk C. S., White S. D. M., 1995, *MNRAS*, 275, 56
- Oey M. S., Watson A. M., Kern K., Walth G. L., 2005, *AJ*, 129, 393
- Oka T., Hasegawa T., Sato F., Tsuboi M., Miyazaki A., Sugimoto M., 2001, *ApJ*, 562, 348
- Oort J. H., 1954, , 12, 177
- Ostriker J. P., McKee C. F., 1988, *Reviews of Modern Physics*, 60, 1
- Padoan P., Nordlund Å., 1999, *ApJ*, 526, 279
- Padoan P., Goodman A., Draine B. T., Juvela M., Nordlund Å., Rögnvaldsson Ö. E., 2001, *ApJ*, 559, 1005
- Padovani M., Galli D., Glassgold A. E., 2009, *A&A*, 501, 619
- Palla F., Stahler S. W., 1999, *ApJ*, 525, 772
- Parker E. N., 1966, *ApJ*, 145, 811
- Peters T., Banerjee R., Klessen R. S., Mac Low M.-M., 2011, *ApJ*, 729, 72
- Pringle J. E., Allen R. J., Lubow S. H., 2001, *MNRAS*, 327, 663
- Rahner D., Pellegrini E. W., Glover S. C. O., Klessen R. S., 2017, *MNRAS*, 470, 4453
- Rahner D., Pellegrini E. W., Glover S. C. O., Klessen R. S., 2019, *MNRAS*, 483, 2547
- Read J. I., Hayfield T., Agertz O., 2010, *MNRAS*, 405, 1513
- Regan M. W., Wilson C. D., 1993, *AJ*, 105, 499
- Reynolds R. J., Scherb F., Roesler F. L., 1973, *ApJ*, 185, 869
- Roberts W. W., 1969, *ApJ*, 158, 123
- Rodriguez-Fernandez N. J., Braine J., Brouillet N., Combes F., 2006, *A&A*, 453, 77
- Rosolowsky E., 2005, *PASP*, 117, 1403
- Saitoh T. R., Makino J., 2013, *ApJ*, 768, 44
- Salo H., Laurikainen E., 1993, *ApJ*, 410, 586
- Schmidt M., 1959, *ApJ*, 129, 243

- Schneider N., et al., 2016, *A&A*, 587, A74
- Schönrich R., Aumer M., Sale S. E., 2015, *ApJ*, 812, L21
- Schruba A., et al., 2011, *AJ*, 142, 37
- Scoville N. Z., Hersh K., 1979, *ApJ*, 229, 578
- Scoville N. Z., Wilson C. D., 2004, in Lamers H. J. G. L. M., Smith L. J., Nota A., eds, *Astronomical Society of the Pacific Conference Series Vol. 322, The Formation and Evolution of Massive Young Star Clusters*. p. 245
- Sedov L. I., 1959, *Similarity and Dimensional Methods in Mechanics*
- Seigar M. S., James P. A., 2002, *MNRAS*, 337, 1113
- Sellwood J. A., 2000, , 272, 31
- Sellwood J. A., 2011, *MNRAS*, 410, 1637
- Sellwood J. A., Carlberg R. G., 1984, *ApJ*, 282, 61
- Shu F. H., Milione V., Roberts William W. J., 1973, *ApJ*, 183, 819
- Smith R. J., Glover S. C. O., Clark P. C., Klessen R. S., Springel V., 2014, *MNRAS*, 441, 1628
- Soler J. D., Hennebelle P., Martin P. G., Miville-Deschênes M. A., Netterfield C. B., Fissel L. M., 2013, *ApJ*, 774, 128
- Soler J. D., et al., 2017, *A&A*, 603, A64
- Solomon P. M., Rivolo A. R., Barrett J., Yahil A., 1987, *ApJ*, 319, 730
- Sormani M. C., Li Z., 2020, *MNRAS*, 494, 6030
- Sormani M. C., Sobacchi E., Shore S. N., Treß R. G., Klessen R. S., 2017, *MNRAS*, 471, 2932
- Sormani M. C., Treß R. G., Ridley M., Glover S. C. O., Klessen R. S., Binney J., Magorrian J., Smith R., 2018, *MNRAS*, 475, 2383
- Springel V., 2005, *MNRAS*, 364, 1105
- Springel V., 2010, *MNRAS*, 401, 791
- Stahler S. W., Palla F., 2004, *The Formation of Stars*
- Stark A. A., Lee Y., 2006, *ApJ*, 641, L113
- Stark A. A., Elmegreen B. G., Chance D., 1987, *ApJ*, 322, 64
- Strömgren B., 1939, *ApJ*, 89, 526
- Su M., Slatyer T. R., Finkbeiner D. P., 2010, *ApJ*, 724, 1044
- Tasker E. J., Tan J. C., 2009, *ApJ*, 700, 358
- Taylor G., 1950, *Proceedings of the Royal Society of London Series A*, 201, 159
- Teyssier R., 2002, *A&A*, 385, 337
- Tielens A. G. G. M., Hollenbach D., 1985, *ApJ*, 291, 722
- Toomre A., 1964, *ApJ*, 139, 1217
- Toomre A., 1977, in Tinsley B. M., Larson Richard B. Gehret D. C., eds, *Evolution of Galaxies and Stellar Populations*. p. 401
- Toomre A., 1981, in Fall S. M., Lynden-Bell D., eds, *Structure and Evolution of Normal Galaxies*. pp 111–136
- Toomre A., 1990, *Gas-hungry Sc spirals..* pp 292–303
- Toomre A., Toomre J., 1972, *ApJ*, 178, 623
- Tremaine S., 1981, in Fall S. M., Lynden-Bell D., eds, *Structure and Evolution of Normal Galaxies*. pp 67–84
- Unavane M., Wyse R. F. G., Gilmore G., 1996, *MNRAS*, 278, 727
- Vázquez-Semadeni E., Ryu D., Passot T., González R. F., Gazol A., 2006, *ApJ*, 643, 245
- Vogel S. N., Kulkarni S. R., Scoville N. Z., 1988, *Nature*, 334, 402

- 
- Vogelsberger M., et al., 2014, *Nature*, 509, 177
- Wadsley J. W., Stadel J., Quinn T., 2004, , 9, 137
- Waters L. B. F. M., 2004, in Witt A. N., Clayton G. C., Draine B. T., eds, *Astronomical Society of the Pacific Conference Series Vol. 309, Astrophysics of Dust*. p. 229
- Weaver R., McCray R., Castor J., Shapiro P., Moore R., 1977, *ApJ*, 218, 377
- Wegg C., Gerhard O., 2013, *MNRAS*, 435, 1874
- Williams J. P., McKee C. F., 1997, *ApJ*, 476, 166
- Wolfire M. G., Hollenbach D., McKee C. F., 2010, *ApJ*, 716, 1191
- Woodward P. R., 1975, *ApJ*, 195, 61
- Yusef-Zadeh F., Muno M., Wardle M., Lis D. C., 2007, *ApJ*, 656, 847



# Chapter 2

## Simulations of the star-forming molecular gas in an interacting M51-like galaxy

### 2.1 Statement about my contribution

- **Code development:** my contribution was major. The main tasks were the development of the module responsible for supernova feedback and the coupling to the sink particle routine. Minor tasks were related to general debugging and adjustments of the code to conform to our needs.
- **Simulation setup:** my contribution was central. The major tasks were to setup the initial conditions of the galaxy and the interstellar medium, and setting the parameters used by the simulations.
- **Physical model:** my contribution was major but Input from my collaborators was essential. The main tasks were to decide the physical ingredients to include in the model for the interstellar medium and define their parameters.
- **Running the simulations:** my contribution was central. I run autonomously the simulations on the available supercomputers.
- **Analysis:** my contribution was central. The analysis was driven by feedback and input from my collaborators.
- **Figures:** my contribution was central. I produced the figures autonomously, according to the planned analysis and scientific discussion. The process was iterative and input from my collaborators was essential.

- **Writing:** my contribution was central. I produced autonomously most of the text of the manuscript. The process was however iterative with major feedback from my collaborators.
- **Scientific discussion:** most of my collaborators contributed equally to the scientific discussion. However, my contribution was major and never passive.

# Simulations of the star-forming molecular gas in an interacting M51-like galaxy

Robin G. Treß,<sup>1\*</sup> Rowan J. Smith,<sup>2</sup> Mattia C. Sormani,<sup>1</sup> Simon C. O. Glover,<sup>1</sup>  
Ralf S. Klessen,<sup>1,3</sup> Mordecai-Mark Mac Low<sup>4,5</sup> and Paul C. Clark<sup>6</sup>

<sup>1</sup>Universität Heidelberg, Zentrum für Astronomie, Institut für Theoretische Astrophysik, Albert-Ueberle-Str. 2, 69120 Heidelberg, Germany

<sup>2</sup>Jodrell Bank Centre for Astrophysics, School of Physics and Astronomy, University of Manchester, Oxford Road, Manchester M13 9PL, UK

<sup>3</sup>Universität Heidelberg, Interdisziplinäres Zentrum für Wissenschaftliches Rechnen, Im Neuenheimer Feld 205, 69120 Heidelberg, Germany

<sup>4</sup>Department of Astrophysics, American Museum of Natural History, New York, NY 10024, USA

<sup>5</sup>Center for Computational Astrophysics, Flatiron Institute, New York, NY, 10010, USA

<sup>6</sup>School of Physics and Astronomy, Queen's Buildings, The Parade, Cardiff University, Cardiff, CF24 3AA

Accepted 2019 December 17. Received 2019 December 17; in original form 2019 September 20

## ABSTRACT

We present here the first of a series of papers aimed at better understanding the evolution and properties of giant molecular clouds (GMCs) in a galactic context. We perform high resolution, three-dimensional AREPO simulations of an interacting galaxy inspired by the well-observed M51 galaxy. Our fiducial simulations include a non-equilibrium, time-dependent, chemical network that follows the evolution of atomic and molecular hydrogen as well as carbon and oxygen self-consistently. Our calculations also treat gas self-gravity and subsequent star formation (described by sink particles), and coupled supernova feedback. In the densest parts of the simulated interstellar medium (ISM) we reach sub-parsec resolution, granting us the ability to resolve individual GMCs and their formation and destruction self-consistently throughout the galaxy. In this initial work we focus on the general properties of the ISM with a particular focus on the cold star-forming gas. We discuss the role of the interaction with the companion galaxy in generating cold molecular gas and controlling stellar birth. We find that while the interaction drives large-scale gas flows and induces spiral arms in the galaxy, it is of secondary importance in determining gas fractions in the different ISM phases and the overall star-formation rate. The behaviour of the gas on small GMC scales instead is mostly controlled by the self-regulating property of the ISM driven by coupled feedback.

**Key words:** galaxies: ISM – ISM: clouds – ISM: structure – hydrodynamics – stars: formation – ISM: kinematics and dynamics

## 1 INTRODUCTION

In the cold and dense molecular phase of the interstellar medium (ISM), it is much easier to trigger runaway gravitational collapse, which makes giant molecular clouds (GMCs) the preferred birth-site of stars. Key questions in the study of star formation (SF) on galactic scales therefore include how the gas gets to these densities and temperatures, and what controls the amount of cold gas with respect to the other thermal phases of the ISM. A thorough understanding of the properties, evolution and dynamics of the ISM and especially of the cold molecular phase, is a vital step towards

a predictive theory of SF (Mac Low & Klessen 2004; McKee & Ostriker 2007; Klessen & Glover 2016).

The ISM is composed of three main thermal phases: a hot ( $T \sim 10^6$  K) ionised phase produced by mechanical energy input from supernovae and stellar winds; a warm ( $T \sim 10^4$  K) phase that can be further subdivided into largely ionised gas (found e.g. in H II regions around massive stars or the diffuse ionised medium) or largely neutral atomic gas; and a cold phase composed of a mix of atomic and molecular gas (McKee & Ostriker 1977). Although the warm atomic phase is generally close to thermal equilibrium (e.g. Wolfire et al. 1995), the ISM is a rich and dynamic system and perturbations can generate thermal instabilities that lead to runaway cooling and the formation of cold, dense gas clouds. Clouds that are dense and massive enough to shield themselves

\* E-mail: robin.tress@uni-heidelberg.de

from the interstellar radiation field develop high molecular fractions, becoming GMCs. General causes for these perturbations include gravitational instabilities, cloud-cloud collisions of warm atomic gas, and shocks in the turbulent ISM (e.g. Klessen & Hennebelle 2010; Smith et al. 2014; Dobbs et al. 2014, and references therein). Once formed, GMCs may be disrupted by feedback from the stars forming within them (Krumholz et al. 2014) or by external processes such as galactic shear (e.g. Jeffreson & Kruijssen 2018).

Larger-scale processes can play a fundamental role as well: spiral arms and bars can gather together warm gas, triggering the formation of cold clouds and initiating the SF process. The global rotation curve of a galaxy is a central parameter, directly affecting the Toomre  $Q$  parameter and thus the local stability against gravitational collapse of the disc (Li et al. 2005) as well as controlling the local shear experienced by the ISM.

Most noticeably, in the question of what controls SF, galaxy interactions and mergers play a prominent role. Mergers are often associated with bursts of SF (Larson & Tinsley 1978; Lonsdale et al. 1984; Barton et al. 2000; Ellison et al. 2008; Renaud et al. 2014) and the most vigorously star-forming galaxies can all be morphologically interpreted as merging pairs (Sanders & Mirabel 1996). These enhancements in SF may be triggered by the collapse of previously stable gas due to cloud collisions and gas compression in tidally-induced spiral arms (Toomre & Toomre 1972). In addition, mergers can result in a substantial redistribution of the angular momentum of the gas and also in the formation of bars (Mihos & Hernquist 1996), both of which act to drive large-scale gas flows towards the centre of the most massive galaxy, leading to a nuclear starburst.

Simulations (e.g. Cox et al. 2006; Di Matteo et al. 2007; Renaud et al. 2014) show that the SF histories of these interactions exhibit an increase in SF immediately after the pericentric passage of the companion and then again during the coalescence phase with an increase of the SF rate (SFR) of at least a factor of two with respect to the isolated case.

However, the details are case-specific and initial conditions such as orbital parameters, mass ratios, gas fractions and the initial stability of the isolated disc all play an important role (Di Matteo et al. 2007; Cox et al. 2008) such that not every merger is immediately linked to an enhanced SFR. Cox et al. (2008) showed that there is a strong correlation with the mass ratio and found that for high mass differences between the two galaxies it is questionable whether the interaction drives any SF whatsoever, since the tidal disturbance is small. Even for similar masses the merger can, for example, remove a large amount of gas from the galaxy during the first encounter via tidal tails. If this gas cannot fully re-accrete during the coalescence phase, the galaxy will be unable to form significantly more stars than in its isolated state (Di Matteo et al. 2007).

In addition, if the isolated galactic disc is mainly Toomre unstable it will already be collapsing and radially flowing towards the centre. In this case, the disc is maximally star forming and the rate is self-regulated by the energy input of stellar feedback to counterbalance the midplane pressure exerted by the disc (Ostriker & Shetty 2011; Shetty & Ostriker 2012), combined with the energy input from radial infall (Krumholz et al. 2018). If the interaction cannot sig-

nificantly increase the midplane pressure and drive radial inflow, it is unlikely that the SFR will be enhanced.

In recent decades, numerical simulations of the ISM have improved substantially, reaching ever higher resolutions and including more and more physical ingredients. There has been important progress in understanding the relative importance of different physical processes and their direct effect on the ISM phases and thus on the regulation of SF (e.g. Dale et al. 2014; Gatto et al. 2015; Walch et al. 2015; Kim & Ostriker 2017; Peters et al. 2017; Hill et al. 2018; Rahner et al. 2019). However simulations that can resolve scales smaller than entire GMCs rarely include larger galactic scale phenomena<sup>1</sup> and are often carried out using highly idealised setups, such as isolated or colliding clouds or kpc-sized portions of the stratified galactic disc.

Larger-scale simulations typically rely on sub-grid models to follow the SF process, which abstract the complex nature of the ISM on the cloud and sub-cloud scales (e.g. Hopkins et al. 2014; Vogelsberger et al. 2014; Schaye et al. 2015; Pillepich et al. 2018). In these cases, the transition from atomic to molecular gas and the composition of the ISM on the scale of individual GMCs are at best only marginally resolved. In spite of this, these models have proved very successful for developing a general understanding of the dynamics of the ISM in galaxies and its global SF properties. However, their predictive power starts to become questionable on smaller scales and research bridging the gap between these large-scale models and detailed simulations of individual clouds has only recently started to become computationally viable.

The details of how a galaxy encounter affects its cold molecular gas content and the following SF on the level of individual molecular clouds remains an open question. For instance, it has been debated whether the increase of SF during the encounter reflects an increase in the available molecular gas reservoir or whether it follows from a higher SF efficiency with strong arguments favouring both sides (Cox et al. 2006; Krumholz et al. 2012; Pan et al. 2018). Some of the observational studies endorsing the higher efficiency scenario assume a different conversion factor between CO and H<sub>2</sub> with respect to more quiescent galaxies (Daddi et al. 2010) and some numerical studies seem to hint at such a scenario (Renaud et al. 2019). But ultimately these highly interesting questions can only be fully addressed with models capable of properly resolving the molecular phase of the ISM.

In this paper, we study the ISM of a galaxy undergoing a merger with a particular focus on the molecular gas. We try to understand how the encounter affects the gas properties with the help of high-resolution galactic-scale simulations carried out using the AREPO moving-mesh code (Springel 2010). One key goal of our current study is to quantify the relative importance of local feedback and global dynamical processes for regulating the SFR and shaping the molecular phase of the ISM.

We take inspiration for our model from the well-studied interacting galaxy M51 (also known as NGC 5194 or the

<sup>1</sup> Exceptions are dwarf galaxy simulations where the total gas mass is small and more detailed studies are possible (e.g. Hu et al. 2016, 2017; Emerick et al. 2019).

Whirlpool galaxy). M51 is a nearby and almost face-on example of a galaxy currently undergoing a merger, in this case with its smaller neighbour NGC 5195, with a mass ratio around one-half (Schweizer 1977; Mentuch Cooper et al. 2012). Owing to this interaction, it displays a prominent grand-design spiral pattern. Because of this, plus its relative proximity and favourable inclination, it has been the target of many observational studies, of which the most important for our purposes is probably the PdBI Arcsecond Whirlpool Survey (PAWS; Schinnerer et al. 2013), which mapped CO emission on scales down to  $\sim 40$  pc, comparable to the size of individual GMCs.

Our simulations are not the first to attempt to model M51. We follow the lead of Dobbs et al. (2010), who simulated the gas and the stars of a system inspired by the present-day M51 system. However, they used an isothermal equation of state for the gas, preventing them from studying the cold gas distribution or the properties of individual GMCs. More recently, Pettitt et al. (2017) performed smoothed particle hydrodynamics (SPH) simulations of an interacting galaxy morphologically similar to M51 using a more sophisticated thermal treatment. However, the SPH particle mass in their simulations was  $2000 M_{\odot}$ , rendering them unable to resolve all but the largest GMCs. The simulations presented here have considerably higher resolution, down to a few  $M_{\odot}$ , allowing us to resolve a much broader range of GMCs.

Our paper is organised as follows. In Section 2 we describe our model, the numerical methods and the initial conditions of our simulation. We describe the outcome of our simulations in Section 3 with a particular emphasis on the ISM properties and the SFR. We then proceed to analyse the role of the galactic interaction on the ISM phases in Section 4 by comparing simulations of an isolated and an interacting galaxy with the same initial properties. We discuss the limitations and problems of our model in Section 5 and summarise our findings in Section 6.

## 2 METHODS

### 2.1 Numerical code

Our simulations were performed with AREPO (Springel 2010), which is a moving-mesh hydrodynamic code coupled with an  $N$ -body gravity solver.

The fundamental conservation laws needed to describe the evolution of an unmagnetised<sup>2</sup> fluid are conservation of mass, momentum and energy:

$$\frac{\partial \rho}{\partial t} + \nabla \cdot (\rho \mathbf{u}) = 0; \quad (1)$$

$$\frac{\partial \mathbf{u}}{\partial t} + \mathbf{u} \cdot \nabla \mathbf{u} = -\frac{\nabla P}{\rho} - \nabla \Phi; \quad (2)$$

$$\frac{\partial \rho e}{\partial t} + \nabla \cdot [(\rho e + P)\mathbf{u}] = \rho \dot{Q} + \rho \frac{\partial \Phi}{\partial t}. \quad (3)$$

<sup>2</sup> Although the ISM of M51 is known to be magnetised (see e.g. Fletcher et al. 2011), we restrict our attention here to the unmagnetised case for simplicity, and defer any investigation of MHD effects to a future study.

Here  $\rho$  is the mass density,  $\mathbf{u}$  is the velocity field,  $P$  is the thermal pressure,  $\Phi$  is the gravitational potential,  $e = e_{\text{th}} + \Phi + \mathbf{u}^2/2$  is the total energy per unit mass, and  $e_{\text{th}}$  is the thermal energy per unit mass. The term  $\dot{Q}$  hides all the complexity of the chemical and radiative cooling and heating processes described in Section 2.2 below.

To close the system, we use an ideal gas equation of state,

$$P = (\gamma - 1)\rho e_{\text{th}}, \quad (4)$$

where  $\gamma$  is the adiabatic index. We set  $\gamma = 5/3$  throughout the simulation, even in gas which is predominantly molecular. We justify our neglect of the rotational degrees of freedom of the molecular gas by noting that in our simulations, gas with a high molecular fraction is typically too cold to excite the rotational energy levels of  $\text{H}_2$ .

These fluid equations are then solved in 3D on a time-dependent mesh constructed by computing the Voronoi tessellation of the domain given a set of mesh-generating points. By assigning to each mesh-generating point the local velocity of the fluid, the grid can naturally follow the flow and continuously adapt the configuration of the cells which will approximately retain constant mass. As a quasi-Lagrangian scheme, the resolution of AREPO strongly depends on the fluid density. Moreover, instead of inferring the necessary time-step globally based on the Courant criterion, this is done locally and every cell is evolved in time based on its local conditions. The code is therefore able to efficiently deal with problems having a large dynamical range both in space and in time, which is necessary to study a multi-scale problem such as the ISM dynamics of a galaxy.

Other strengths of the AREPO code include its (nearly) Galilean invariance, its good shock treatment, its minimization of advection errors and the lack of an underlying preferential mesh geometry. At every interface between cells, the code finds the flux by solving the Riemann problem in the rest-frame of the interface. Since the cells are moving approximately at the local fluid velocity, these fluxes are kept minimal and advection errors are thus small. Furthermore in this way the solution is independent from the chosen frame of reference and best suited to study problems where there is no preferred flow direction.

To compute the gravitational potential, AREPO uses a tree-based approach adapted from an improved version of GADGET-2 (Springel 2005). The contribution of the gas cells is included by treating each as a point mass located at the centre of the cell, with an associated gravitational softening. This softening changes as the gas cell grows or shrinks, with a lower limit in our simulations of 0.1 pc.

The self-gravity of the gas is mainly important on small scales when local gravitational runaway collapse sets in, leading to SF. On larger scales, the gravity is dominated by the dark matter and the old stellar population of the galaxy. We follow the behaviour of both components by simulating the dynamical evolution of a set of representative dark matter (DM) and star particles, which are assumed to be collisionless, meaning that they only enter into the gravity calculation. The masses and softening lengths chosen for these particles are discussed in Section 2.6 below.

## 2.2 Chemical network

The chemical evolution of the gas is modelled using the NL97 network of [Glover & Clark \(2012\)](#), which combines the network for hydrogen chemistry presented in [Glover & Mac Low \(2007a,b\)](#) with a highly simplified treatment of CO formation and destruction developed by [Nelson & Langer \(1997\)](#). The NL97 network was first implemented in AREPO by [Smith et al. \(2014\)](#) and has subsequently been used in a number of studies with this code (e.g. [Bertram et al. 2015](#); [Sormani et al. 2018](#)). The effects of dust shielding and H<sub>2</sub> and CO self-shielding from the non-ionizing UV part of the interstellar radiation field are modelled using the TREECOL algorithm developed by [Clark et al. \(2012\)](#). The background radiation is taken to be spatially constant at a solar-neighbourhood value ([Draine 1978](#)).

We also solve for the thermal evolution of the gas due to radiative heating and cooling, which we compute simultaneously with the chemical evolution. We use a detailed atomic and molecular cooling function, the latest version of which is described in [Clark et al. \(2019\)](#). Of particular note here is our treatment of the cooling of the gas at high temperatures ( $T \gg 10^4$  K) owing to the effects of permitted atomic transitions, since this is of great importance for modelling the effects of supernova feedback. We treat cooling due to transitions in atomic hydrogen in a fully non-equilibrium fashion using the H and electron abundances computed in our chemical model. For cooling due to transitions in He and metals we use the collisional ionization equilibrium cooling rates tabulated in [Gnat & Ferland \(2012\)](#) instead.

We finally impose a temperature floor of 20 K on the simulated ISM. Without this floor, the code can occasionally produce anomalously low temperatures in cells close to the resolution limit undergoing strong adiabatic cooling, with unfortunate effects on the stability of the code. Since the equilibrium gas temperature is comparable to or larger than 20 K throughout the full range of densities resolved in our simulation (see e.g. the temperature-density plots in the high resolution simulations of individual clouds presented in [Clark et al. 2019](#)), we do not expect the presence of this temperature floor to have any effects on the results of our simulations.

## 2.3 Sink particles

In order to form stars, gas must undergo gravitational collapse and increase its density by many orders of magnitude from typical GMC densities to protostellar densities. Despite AREPO's adaptive capabilities, it is not computationally feasible to simulate the whole of this process in simulations of the scale presented here. We therefore adopt a technique widely used in computational studies of SF and replace the densest gravitationally-bound collapsing regions in the simulation with collisionless sink particles.

Sink particles, hereafter referred to as sinks, are mainly used in high resolution simulations of individual clouds where the SF process can be spatially and temporally resolved reasonably well. Typically galactic-scale simulations cannot resolve the collapse within GMCs, and tend to avoid using accreting sink particles to represent SF. Instead non-accreting star particles are often employed where particles of a given mass representing stars are stochastically cre-

$\rho_c$ (g cm <sup>-3</sup> )	10 <sup>-21</sup>
$r_{\text{acc}}$ (pc)	2.5
Softening length (pc)	2.5
$\epsilon_{\text{SF}}$	0.05
$r_{\text{sc}}$ (pc)	5.0

**Table 1.** Parameters of the sink particles;  $\rho_c$  is the sink density threshold,  $r_{\text{acc}}$  is the accretion radius,  $\epsilon_{\text{SF}}$  is the SF efficiency, and  $r_{\text{sc}}$  is the scatter radius of SNe around the sink. For details see the text.

ated in the densest parts of the ISM (e.g. [Katz 1992](#); [Katz et al. 1996](#); [Stinson et al. 2006](#)). These schemes are often fine-tuned to reproduce the Schmidt-Kennicutt relation ([Schmidt 1959](#); [Kennicutt 1989, 1998](#)); although they tend to produce a healthy matter cycle in the ISM, their power to predict SF is strongly limited. Since our resolution reaches below GMC scales, we use accreting sink particles that we describe here and discuss possible caveats and limitations in Section 5.

Following [Bate et al. \(1995\)](#) and [Federrath et al. \(2010\)](#), sink particles form if within an accretion radius  $r_{\text{acc}}$ , a region above a density threshold  $\rho_c$  satisfies these criteria:

- (i) The gas flow in this region is converging. To establish this, we require not only that the velocity divergence is negative ( $\nabla \cdot \mathbf{v} < 0$ ) but also that the divergence of the acceleration is negative ( $\nabla \cdot \mathbf{a} < 0$ ).
- (ii) The region is located at a local minimum of the potential.
- (iii) The region is not situated within the accretion radius of another sink and also will not move within the accretion radius of a sink in a time less than the local free-fall time.
- (iv) The region is gravitationally bound, i.e.  $U > 2(E_k + E_{\text{th}})$ , where  $U = GM^2/r_{\text{acc}}$  is the gravitational energy of the region within the accretion radius,  $E_k = 1/2 \sum_i m_i \Delta v_i^2$  is the total kinetic energy of all gas particles within the accretion radius with respect to the centre of collapse, and  $E_{\text{th}} = \sum_i m_i e_{\text{th},i}$  is the total internal energy of the same region.

These criteria help to ensure that a region of the gas is only converted into a sink particle if it is truly self-gravitating and collapsing.

If a gas cell satisfies all of the above criteria it is turned into a collisionless sink particle. These are then allowed to accrete mass during the simulation. If a gas cell within  $r_{\text{acc}}$  is denser than the threshold density and the gas is also gravitationally bound to the sink particle, then we move an amount of mass

$$\Delta m = (\rho_{\text{cell}} - \rho_c) V_{\text{cell}} \quad (5)$$

from the cell to the sink, where  $\rho_{\text{cell}}$  is the initial gas density in the cell and  $V_{\text{cell}}$  is its volume. Afterwards the new density of the cell is simply the threshold density  $\rho_c$ . We also update appropriately any other quantities in the cell that depend on the mass, such as the total momentum or kinetic energy. In the case where a given gas cell is located within the accretion radii of multiple sink particles, we place the accreted mass from it onto the sink to which the gas is most strongly bound.

As discussed in more detail in [Springel \(2010\)](#), AREPO makes use of a hierarchical time-stepping scheme in which

individual gas cells and collisionless particles can have different timesteps, meaning that at any given time not every cell and particle is active. Accretion onto a sink particle is allowed only when the sink particle itself and the candidate gas cells are active. In order to ensure that we do not miss accretion from cells that spend only a short time within the sink accretion radius, we make sure that the timestep used to evolve the sinks is the same as the shortest one of the gas cells.

In order to properly follow the hierarchical collapse and correctly resolve the underlying fragmentation, we ensure that the local Jeans length is resolved by at least four resolution elements (Truelove et al. 1997; see also Federrath et al. 2011 for further discussion). In the densest and coldest parts of GMCs, the Jeans length can, however, become prohibitively small. We therefore choose to stop refining for densities above  $\rho_{\text{lim}} = 10^{-21} \text{ g cm}^{-3}$  and we set  $\rho_c = \rho_{\text{lim}}$ . This is a good compromise between excellent resolution in the collapsing regions, and computational performance. The chosen density threshold is also well above the critical density for  $\text{H}_2$  formation (Smith et al. 2014) such that this process is fully captured by the simulation.

The accretion radius is chosen such that at the given threshold density, several cells fall inside  $r_{\text{acc}}$  given the local size of the cells. The gravitational softening length of the collisionless sink particles is set to the same value as  $r_{\text{acc}}$ , as this ensures that the gravitational potential is not altered much due to the infall of mass onto a sink, while at the same time limiting the size of the gravitational acceleration produced within  $r_{\text{acc}}$ , which otherwise would have a detrimental effect on performance. The main parameters that characterise the sink particles used in our study are listed in Table 1.

## 2.4 Feedback

To form molecular clouds we need to capture the proper cooling and chemical evolution of the dense ISM. Our chemical network in conjunction with our model of the self-shielding properties of the molecular gas from the ambient dissociating UV radiation is the key to achieving this.

To capture the disruption of molecular clouds, on the other hand, it is necessary to introduce some feedback mechanism. In principle galactic shear can disperse dense molecular clouds, but in general this is insufficient to produce realistic cloud lifetimes and masses throughout the galactic disc (Jeffreson & Kruijssen 2018). GMCs turn out to be too massive and too long-lived when shear is the only disruptive process.

Supernovae (SNe) randomly distributed with respect to the gas have also been shown to be ineffective at destroying molecular clouds. On the contrary, they help to pile up gas into dense, compact regions, resulting in massive molecular cloud complexes with extremely long lifetimes (Gatto et al. 2015; Walch et al. 2015). Therefore, a feedback mechanism coupled to the SF is needed that disrupts the clouds from within. In our present study, we focus on the effects of clustered SNe forming in locations correlated with the sink particles. We have found that this is an effective way to reproduce reasonable lifetimes for our simulated molecular clouds and to generate a healthy matter cycle in the ISM.

Despite our high resolution, we cannot resolve the formation of individual stars in our simulations. Instead, sinks

represent small stellar clusters formed during an SF event within a cloud. We relate the mass of stars formed to the mass of the sink by assuming that only a fraction  $\epsilon_{\text{SF}} = 0.05$  of the mass accreted actually forms stars, since at the scale at which we form the sinks, the SF process is still quite inefficient (see e.g. Evans et al. 2009). We then attribute a discrete stellar population to the sink based on the method described in Sormani et al. (2017). Given an initial mass function (IMF) we populate a set of discrete mass bins using a Poisson distribution with an appropriately chosen mean for each bin. In this way we ensure that the mass distribution of the stars formed in the simulation follows the desired IMF even when the individual sinks are too small to fully sample the IMF. This method also allows us to account for stars formed from mass accreted at later times.

For each star more massive than  $8 M_{\odot}$  associated with a sink, we generate an SN event at the end of the lifetime of the star, inferred based on their mass from Table 25.6 of Maeder (2009). Since the sink represents an entire group of stars that can interact dynamically, we do not assume that the SN occurs exactly at the location of the sink. Instead, we randomly sample the SN location from a Gaussian distribution centred on the particle and with standard deviation  $r_{\text{sc}} = 5 \text{ pc}$ .

Since the assumed efficiency of SF within the sink is relatively small, most of the mass in the sink represents gas that should be returned to the ISM once stellar feedback starts. The mass that is not locked up in stars is therefore gradually given back to the ISM with every SN event. Each event ejects a total mass of  $M_{\text{ej}} = (M_{\text{sink}} - M_{\text{stars}})/n_{\text{SN}}$ , where  $M_{\text{sink}}$  is the mass of the sink at the time that the supernova occurs,  $M_{\text{stars}}$  is the mass of stars contained within the sink at that time, and  $n_{\text{SN}}$  is the remaining number of SN events that the sink harbors. The mass is distributed uniformly within the energy injection region. The temperature of the injection cells is not altered at this stage.

Once the last massive star has reached the end of its lifetime, the sink has a final mass of  $M_{\text{stars}}$ . At this point, we convert it into a collisionless  $N$ -body particle representing its evolved stellar population. It will then become part of the group of stellar particles that make up the disc and bulge in our simulation. Our base mass resolution for these stellar particles is  $\sim 10^4 M_{\odot}$  (see Section 2.5); in order not to lose resolution in computing gravitational interactions, we switch off accretion onto sink particles that have reached this limiting stellar mass content, and allow instead a new sink to form. In this way, sink particles can be seen as maturing star particles and we retain the ability to follow the dynamical evolution of star clusters to some extent.

Especially in the high resolution simulations, it is not uncommon to have sinks that do not accrete enough mass to form a massive star. In this case we cannot return the gas mass trapped within the sink during an SN event. Instead, after a period of 10 Myr, if the sink still did not manage to create a massive star, we convert it into a normal star particle and return the remaining mass (95%) to the ISM by uniformly adding it to all gas particles in a surrounding sphere of  $R = 100 \text{ pc}$ .

In addition to the type II SNe associated with SF, we also account for type Ia SNe, which are produced by the older stellar population in the galaxy. Based on the inferred SF history of M51 (Eufrazio et al. 2017), we estimate a rate

of one SNIa every 250 years. We create a SN event at this rate<sup>3</sup> at the position of a randomly selected star (not sink) particle of the stellar disc and bulge.

To model the supernova energy injection we use a highly modified version of the algorithm first implemented in AREPO by [Bubel \(2015\)](#). For every SN event, we calculate the radius of a supernova remnant at the end of its Sedov-Taylor phase based on an assumed SN energy of  $10^{51}$  erg and the local mean density  $\bar{n}$ , which for solar metallicity yields ([Blondin et al. 1998](#))

$$R_{\text{ST}} = 19.1 \left( \frac{\bar{n}}{1 \text{ cm}^{-3}} \right)^{-7/17} \text{ pc}, \quad (6)$$

where in our case  $\bar{n}$  is calculated including the contributions from both the ambient gas and also the mass loading of the SN event. We compare this with the radius of the injection region,  $R_{\text{inj}}$ , defined as the size of the smallest sphere around the explosion site that contains 40 grid cells. If  $R_{\text{ST}} > R_{\text{inj}}$ , we inject  $E_{\text{SN}} = 10^{51}$  erg into the injection region in the form of thermal energy and fully ionise the contained gas. If, on the other hand, the Sedov-Taylor phase of the SN remnant is unresolved, then this is a sign that the local density is too high for thermal injection to be reliable. If we were to inject thermal energy in this case, then it would be radiated away too quickly, making it unable to generate a strong shock and deposit the correct amount of kinetic energy into the ISM. This is a numerical effect that can be prevented by directly injecting the correct terminal momentum instead. This has been estimated to be (see e.g. [Martizzi et al. 2015](#); [Gatto et al. 2015](#); [Kim & Ostriker 2015](#))

$$p_{\text{fin}} = 2.6 \times 10^5 n^{-2/17} M_{\odot} \text{ km s}^{-1}, \quad (7)$$

for a SN of energy  $E_{\text{SN}} = 10^{51}$  erg and solar metallicity. We do not change the temperature or the ionization state of the region in this case as this would throw off-balance the energy budget in large unresolved regions.

Momentum injection alone can not produce a hot phase in the ISM. By keeping the injection radius small we minimise the number of occasions on which we must inject momentum rather than thermal energy. On the other hand, taking too small an injection radius leads to unphysically anisotropic momentum injection. We have found through experimentation that defining  $R_{\text{inj}}$  such that a total of 40 grid cells are contained within a sphere of that radius seems to offer the best trade-off between minimizing the number of momentum injection events and minimizing the impact of grid noise and anisotropic expansion on the evolution of the individual remnants. We note that this mixed approach of injecting thermal energy in regions where  $R_{\text{ST}}$  is resolved and momentum in regions where this is not the case is not new. Similar methods have been successfully used by a number of other authors to study the impact of SN feedback on the ISM (see e.g. [Kimm & Cen 2014](#); [Hopkins et al. 2014](#); [Walch et al. 2015](#); [Simpson et al. 2015](#); [Kim & Ostriker 2017](#)).

Finally, we note that SNe are not the only type of feedback associated with SF. For example, stellar winds and radiation from young stars also play an important role in dispersing GMCs, particularly since they act much earlier

<sup>3</sup> SNIa actually follow an exponential distribution in time having the given rate as an average.

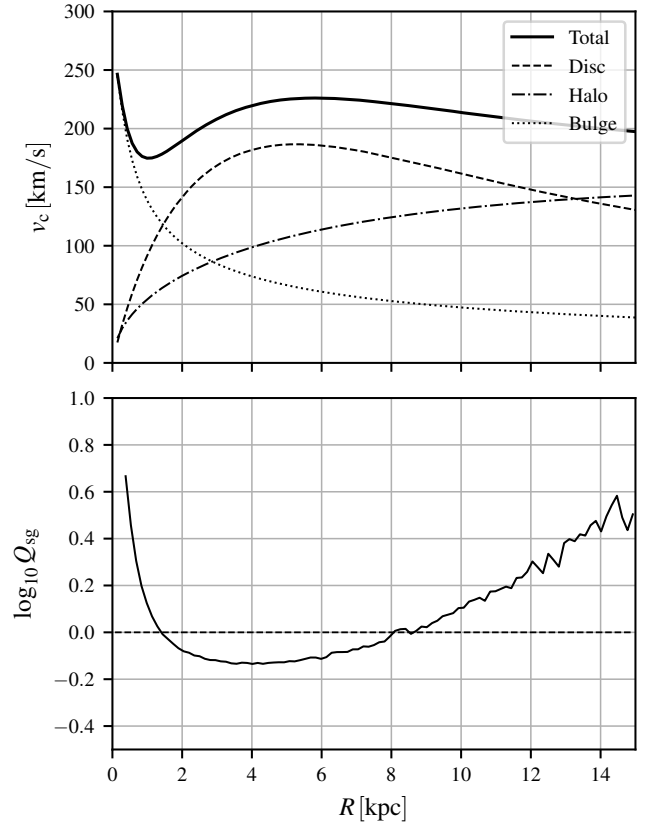


**Figure 1.** *Top:* initial circular velocity curve for the galaxy model. The solid line shows the behaviour for the full galaxy, while the other lines show the contribution of the individual components. *Bottom:* combined star-gas Toomre parameter using the equation derived by [Rafikov \(2001\)](#) for the chosen initial conditions. Everything below the dashed line is Toomre-unstable.

**Table 2.** Parameters of the different galaxy components.

	Mass ( $M_{\odot}$ )	Scale length (kpc)	$h_z$ (kpc)
DM Halo	$6.04 \times 10^{11}$	28.7	-
Bulge	$5.30 \times 10^9$	$9.03 \times 10^{-2}$	-
Stellar disc	$4.77 \times 10^{10}$	2.26	0.3
Gas disc	$5.30 \times 10^9$	2.26	0.3

than SN feedback (e.g. [Dale et al. 2014](#); [Inutsuka et al. 2015](#); [Gatto et al. 2017](#); [Rahner et al. 2018, 2019](#)). However, it remains computationally challenging to include all of these forms of feedback in simulations with the scale and resolution of those presented here. Therefore, in our initial study we restrict our attention to the effects of SN feedback and defer an investigation of other feedback processes to future work.

## 2.5 Initial conditions

We set up a disc galaxy in isolation that consists of four different components: a dark matter halo, a stellar bulge, a stellar disc and a gaseous disc.

The bulge and the halo follow a spheroidal [Hernquist](#)

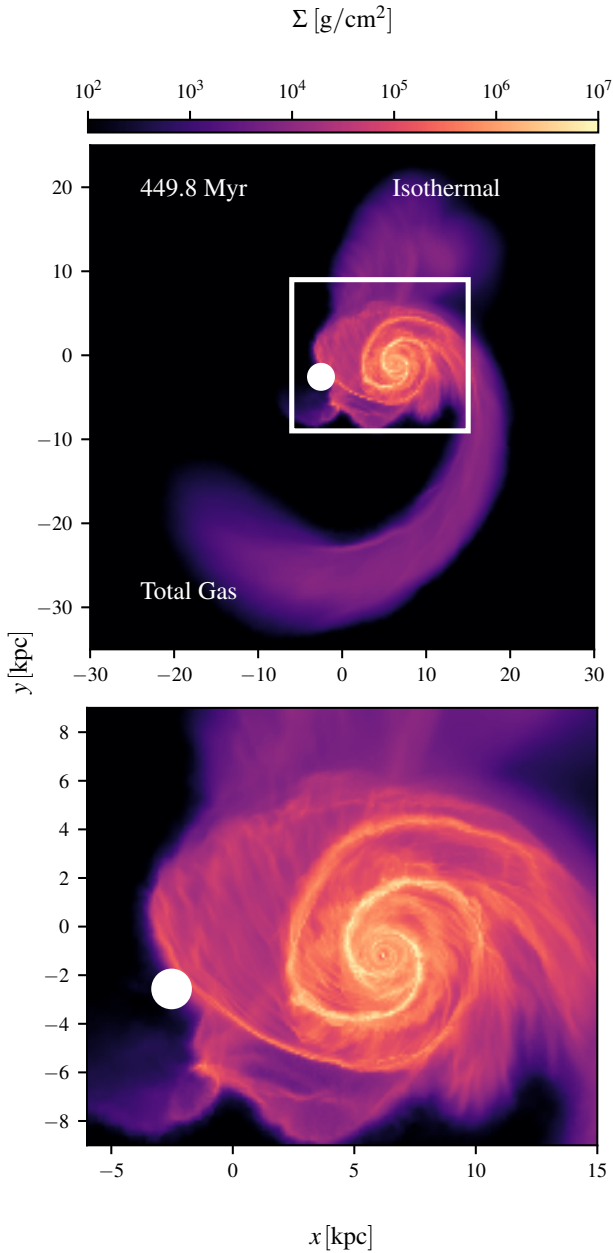


**Figure 2.** Total gas column density map of the isothermal test run at  $t \approx 450$  Myr.

**Table 3.** Initial conditions of the companion galaxy.

position	value (kpc)	velocity	value ( $\text{km s}^{-1}$ )
$x_0$	-21.91	$v_{x_0}$	73.2
$y_0$	-8.44	$v_{y_0}$	-31.2
$z_0$	-4.25	$v_{z_0}$	188.6

(1990) profile

$$\rho_{\text{spheroid}}(r) = \frac{M_{\text{spheroid}}}{2\pi} \frac{a}{r(r+a)^3}, \quad (8)$$

where  $r$  is the spherical radius,  $a$  is the scale-length of the spheroid (the bulge or the halo, depending on which component is considered), and  $M_{\text{spheroid}}$  is its mass.

The stellar and gas disc follow a double exponential density profile

$$\rho_{\text{disc}}(R, z) = \frac{M_{\text{disc}}}{4\pi h_z h_R^2} \text{sech}^2\left(\frac{z}{2h_z}\right) \exp\left(-\frac{R}{h_R}\right), \quad (9)$$

where  $R$  and  $z$  are the cylindrical radius and height, and  $h_z$  and  $h_R$  are the scale-height and scale-length of the disc, respectively.

We generate the initial conditions using the method and software developed by Springel et al. (2005), where the choice of the profile and parameters were cosmologically motivated. The code chooses positions and velocities for the collision-less DM and stellar particles such that the desired equilibrium configuration is established. During setup the gas disc is then created by randomly converting stellar disc particles into gas particles until the desired gas mass fraction is reached. The stellar and gas discs therefore initially follow the same density profile.

We choose parameters of a typical spiral galaxy, summarised in Table 2. The total mass in baryonic matter for the modelled galaxy is chosen to be comparable to the observed baryonic mass of M51a (NGC 5194) which is estimated to be  $(5.8 \pm 0.1) \times 10^{10} M_{\odot}$  (Mentuch Cooper et al. 2012). The scale-length of the disc corresponds approximately to the one listed in Schrubba et al. (2011) with the caveat that the interaction might have affected this observed value. We set the mass of the DM halo under the assumption that its spin parameter is directly connected to the scale-length of the disc by the disc-halo mass ratio and considering the cosmological constraints on this parameter (Hernandez et al. 2007). The choice of the remaining parameters is motivated instead by the desire to produce a velocity curve (Fig. 1) roughly consistent with observations (Sofue 1996; Oikawa & Sofue 2014) and to suppress the formation of a strong bar in the simulations of the isolated galaxy. We finally settle on a typical gas-disc mass fraction of 10 %. At the highest gas resolution this is the borderline value which is still computationally viable, but we have to consider that this is still only about half of the estimated gas mass in M51 (Mentuch Cooper et al. 2012).

To model the interaction with the companion galaxy, we follow the approach and initial conditions presented in Dobbs et al. (2010), hereafter D10. The companion is described as a single collisionless particle with initial position and velocity given in Table 3 (taken from Dobbs et al. 2010, ultimately from Theis & Spinnaker 2003). Since the companion is reduced to a single particle, we assign a very large gravitational softening of  $\epsilon = 3$  kpc to it in order to avoid strong two-body close encounters. This is equivalent to setting the density profile of the galaxy equal to a Plummer sphere with its scale-length equal to the softening length. Given the differences in the model of the main galaxy with respect to D10 we could not reproduce their exact same orbit. However the orbit and the morphological behavior were retrieved by lowering the mass of the particle representing

**Table 4.** Mass resolution and softening length of the different particle types.

	Mass resolution ( $M_{\odot}$ )	Softening (kpc)
Dark matter	$6 \times 10^5$	0.2
Stellar particles	$5 \times 10^4$	0.1
Companion galaxy	$4 \times 10^{10}$	3

the companion galaxy to  $4 \times 10^{10} M_{\odot}$ . Observationally the stellar mass of NGC5195, companion of M51, is estimated by photometry to be  $(2.5 \pm 0.2) \times 10^{10} M_{\odot}$  (Mentuch Cooper et al. 2012) and thus the mass ratio between the two galaxies is about 0.5 (see also Schweizer 1977). Our ratio is much lower than that, but given that we recover the morphological behavior of the encounter, the massive particle that we included to represent the companion should rather be seen as the core of its DM halo, while the outer parts do not affect much the dynamics of the encounter.

All these initial assessments were done by running low resolution isothermal simulations with a sound speed  $c_s = 10 \text{ km s}^{-1}$ . With the final setup we can reproduce the global morphology of the M51 system (see Fig. 2). We obtain the typical two-armed spiral pattern and the relative position of the two galaxies in the plane of the sky. The second passage of the companion induces a large tidal H I tail also seen in observations. Other characteristics that we reproduce are the peculiar kink in the spiral arm pattern towards the companion (see Fig. 2 approximately at position (2.5, -2.5) kpc), and the connecting (only in perspective) arm. All these features were also reproduced in the original work of D10 using SPH.

Finally we set the initial temperature of the gas to  $T = 10^4 \text{ K}$  and consider it to be fully atomic. We assume the ISM to be of solar metallicity throughout. The metallicity of the ISM in the real M51 appears to be slightly super-solar with a small radial metallicity gradient (Croxall et al. 2015), but we do not expect this minor difference to significantly affect our results.

## 2.6 Resolution

The mass resolutions and softening lengths used for the different types of collisionless particles included in our simulation are listed in Table 4.

Given the method described in the previous section, the gas cells start with an initial mass equal to the star particles from which they are drawn. The code is however able to quickly refine them during the first few million years of the simulation until the nominal resolution is reached. For our production simulation we set a target mass resolution for the gas cells of  $300 M_{\odot}$ . In the denser parts of the ISM, however, we reach considerably higher resolutions, down to a few solar masses (see Fig. 3), since we require the local Jeans length to be resolved by at least four resolution elements in all gas with a density  $\rho < \rho_c = 10^{-21} \text{ g cm}^{-3}$ . This requirement generates a differential distribution of cell masses as a function of density and temperature. We reach high spatial resolutions in the star-forming part of the ISM despite a relatively low resolution in the more diffuse phase. For stability reasons, we also try to avoid having neighbour-

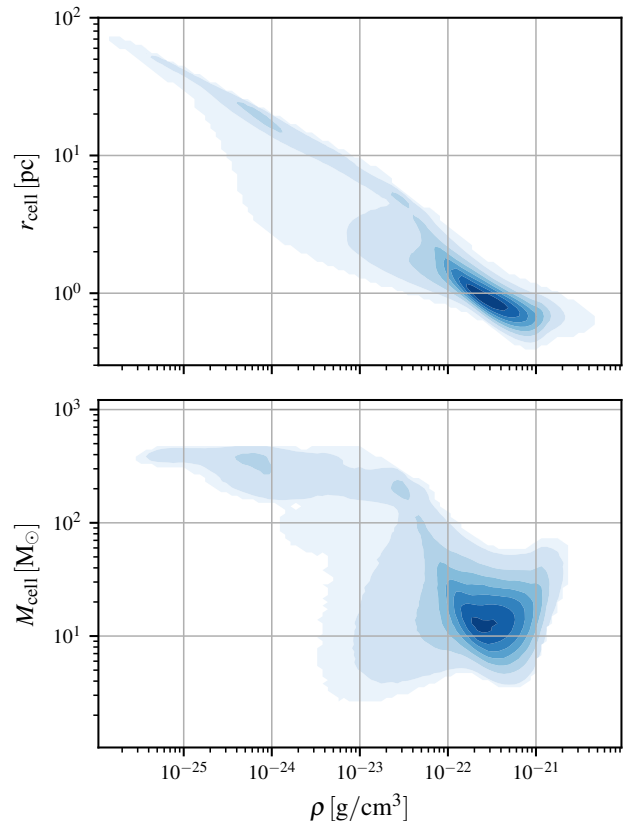


**Figure 3.** *Top:* spatial resolution as a function of local density for the high resolution run.  $r_{\text{cell}}$  is the radius of a sphere with the same volume as the cell. *Bottom:* distribution of cell masses, plotted as a function of density. The colours are linearly related to the total number of cells. Most of the computational effort is spent in the high density regime where the Jeans-length criterion determines the cell masses. Here we reach sub-parsec resolution at densities comparable to the sink formation threshold. The Jeans-length criterion is responsible for the knee in the plots at a density of  $\sim 5 \times 10^{-23} \text{ g cm}^{-3}$ .

ing cells with a large volume difference. If two neighbouring cells approach a volume ratio greater than 8, the larger cell is split. The resulting spatial resolution as a function of the local gas density and the corresponding mass distribution of the cells in the different density regimes is shown in Fig. 3.

To help us to quantify the resolution dependence of our simulations, we have also carried out low resolution runs with a target mass resolution of  $1000 M_{\odot}$ . In these runs, we apply the Jeans-length refinement criterion only up to a limiting density of  $\rho_{\text{lim}} = 0.1 \times \rho_c = 10^{-22} \text{ g cm}^{-3}$ . This will result in a difference of spatial resolutions in the dense gas of about a factor of two with respect to the high resolution case. A comparison between the two simulations for a resolution study is therefore meaningful (see Appendix A).

Since the gas cells have different masses and sizes, we cannot use a unique gravitational softening length. Rather, we use AREPO's adaptive softening option to scale the softening length according to the cell radius, i.e.  $\epsilon_{\text{gas}} = 2r_{\text{cell}}$ ,

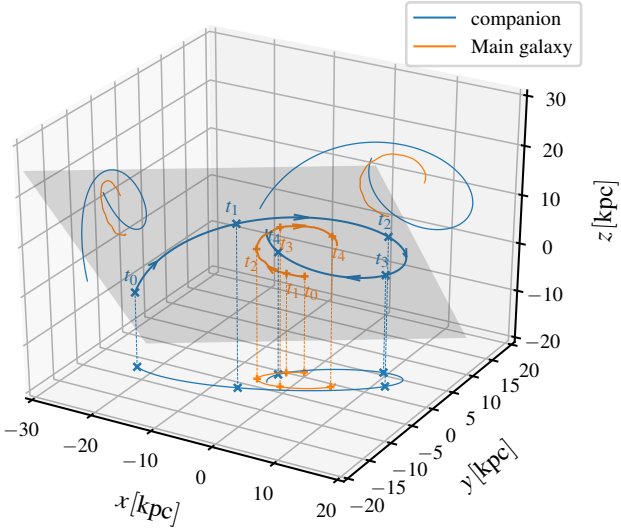


**Figure 4.** Trajectory of the centre of mass of the simulated galaxy (orange line) and its companion (blue line). The shaded area defines the plane of the orbit.

where  $r_{\text{cell}}$  is the radius of a sphere with the same volume as the cell.<sup>4</sup>

If we compare the spatial resolution that we achieve in gas at typical GMC densities (a few times  $10^{-22} \text{ g cm}^{-3}$  and above) with the requirements that were recently shown by Joshi et al. (2019) to be necessary for producing converged molecular fractions in 3D simulations ( $\Delta x \sim 0.2 \text{ pc}$  for  $\text{H}_2$ ,  $\Delta x \sim 0.04 \text{ pc}$  for  $\text{CO}$ ), then we see that the chemical state of our simulations is not completely converged. Although we have more than enough resolution to successfully identify molecular-dominated clouds (the “physical” condition of Joshi et al. 2019), we do not resolve the dense substructure within these clouds in enough detail to ensure that the molecular formation time is shorter than the cell crossing time in the densest cells (the “dynamical” condition of Joshi et al. 2019). Therefore, although the details of the molecular gas distribution in our simulations should be qualitatively correct, some of the quantitative details may still be resolution-dependent (see also Appendix A).

## 2.7 Simulation details

As stated above, our major focus in this study is to address the relative importance of the interaction in shaping the ISM. Therefore we set up two sets of simulations. In one case the galaxy is allowed to interact with a smaller companion galaxy as described in Section 2.5. The same galaxy is evolved in isolation in a comparison set of simulations.

For both setups, we carry out calculations at two different resolutions, as described in Section 2.6. Unless stated otherwise, all the analysis below refers to the high resolution

simulations. The results of the other simulations are summarised in Appendix A, where we discuss how our results depend on the chosen resolution.

For the high resolution simulations we simulate the first  $\sim 40 \text{ Myr}$  at a low base resolution of  $1000 M_{\odot}$  per cell and without requiring the Jeans length to be resolved. We then switch to a base resolution of  $300 M_{\odot}$  per cell and finally at  $\sim 80 \text{ Myr}$  we switch on the requirement for the Jeans length as described in Section 2.6 as well, reaching our nominal resolution as illustrated in Fig. 3. With this gradual increment in resolution we can overcome the strong initial collapse due to the cooling of the atomic disc without investing too much computational power into this initial transition phase.

## 3 RESULTS

We start in this section by giving a general description of the outcome of the simulations, with a focus on the properties of the ISM and the SFR. We then look at how the interaction affects the total mass fractions in the different ISM phases and try to understand how the galaxy encounter influences the cold molecular gas reservoir which is available for SF.

### 3.1 A qualitative description of the simulation

We follow the system for about 400 Myr. This is the time when the relative position and morphology of the galaxy most closely resemble the observed M51 system. We show the trajectories of the main galaxy and its companion in Fig. 4, while the evolution of the system in time can be followed looking at Fig. 5. The companion galaxy moves on a highly eccentric orbit in front of the face-on disc relative to the observer and reaches its pericentric passage  $\sim 110 \text{ Myr}$  after the start of the simulation. The companion then continues its orbit behind the disc of the galaxy at  $\sim 270 \text{ Myr}$ . At the final snapshot the companion has a positive line-of-sight velocity with respect to the observer and is just emerging from behind the face-on disc of the main galaxy. At this point the distance between the two centres of mass is about  $\sim 12 \text{ kpc}$ . Even though we stop the simulation at this time, the two galaxies will merge completely within the next orbit of the companion (e.g. Dobbs et al. 2010).

The interaction is responsible for the development of a typical two-armed tidally induced spiral pattern in the disc (Toomre & Toomre 1972). These arms are particularly pronounced in molecular gas and are the loci of intense SF (see Fig. 6). Due to the close passage, the outer parts of one of the arms are flung out, creating an extended tidal tail similar to what is seen in 21 cm observations of M51 (see e.g. Rots et al. 1990). This tidal tail is predominantly atomic as we can see in the bottom panel of Fig. 6.

Due to gravitational instabilities the warm gas is pushed out of its thermal equilibrium and rapidly cools from its initial temperature of  $T = 10^4 \text{ K}$ . Part of it becomes molecular and builds up large and dense GMC associations. In the isolated galaxy simulation these are distributed in a flocculent style pattern, while in the interacting case they are mainly assembled inside the tidally induced spiral arm structure (Fig. 7). The clouds formed are filamentary, with complex substructure (Fig. 8), due to turbulence induced by a combination of SN feedback, galactic shear, and self gravity. See

<sup>4</sup> As AREPO endeavours to prevent its grid cells from becoming highly distorted, most are quasi-spherical and so this radius is an accurate way of characterizing the size of the cells.

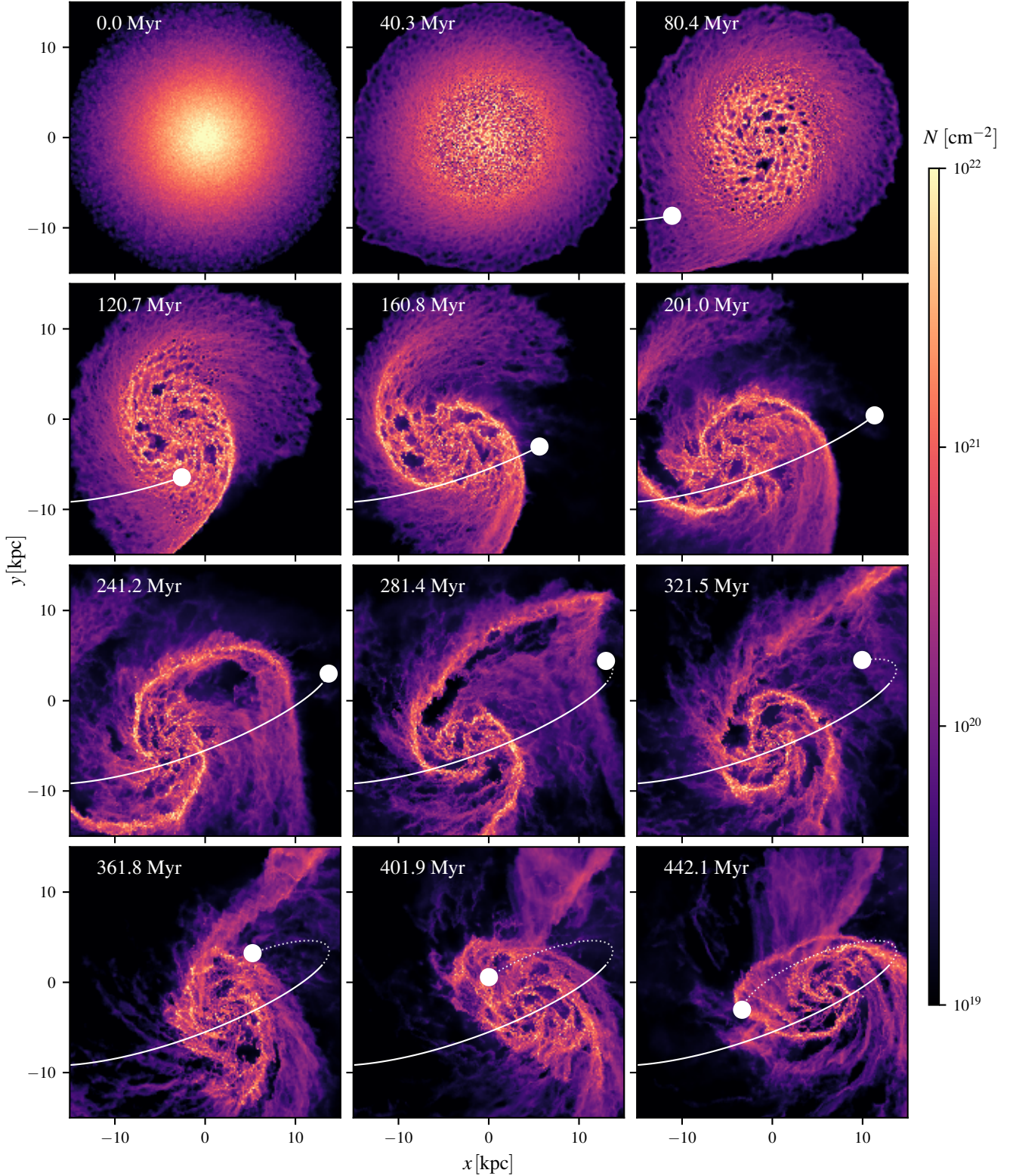


**Figure 5.** Total gas column density projections at different times for the interacting simulation. The location of the companion (*white filled circle*) and its trajectory (*white solid and dotted line*) are plotted in each panel. Notice how the interaction triggers a two-armed spiral structure. When the companion is behind the disc of the main galaxy the trajectory is plotted with a dotted line. The simulated galaxy and its companion in the last panel at  $t = 428.9$  Myr are in a configuration similar to the observed M51 galaxy. The morphological changes induced by feedback can be clearly seen by comparing the last panel to the isothermal model shown in Fig. 2.

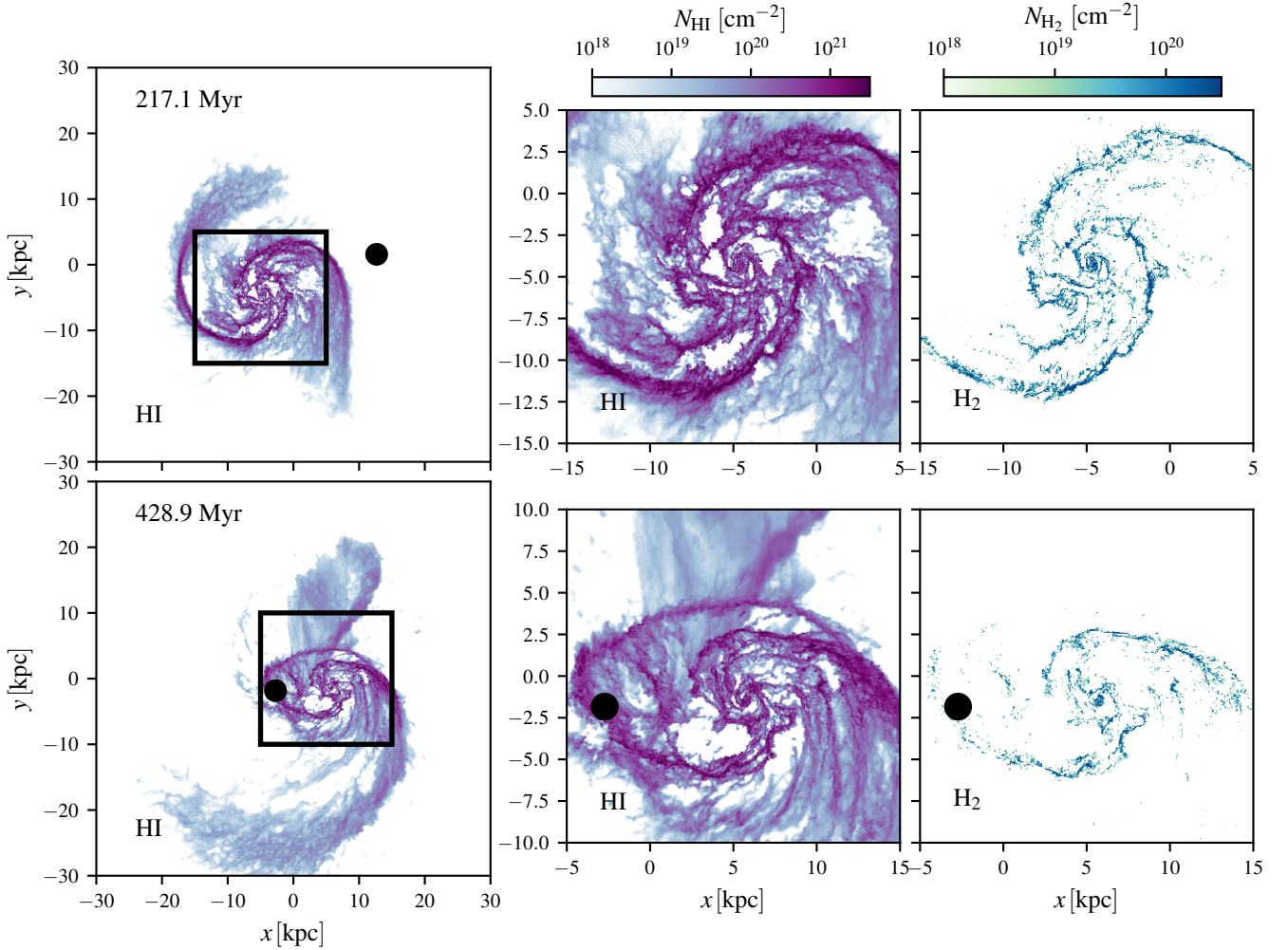


**Figure 6.** Column density maps of the interacting simulation at two different times. The left-hand panel shows maps of the H I column density at  $t = 217.1$  Myr and  $428.9$  Myr. The remaining panels show a zoomed-in view of the H I (*central panels*) and H<sub>2</sub> (*right-hand panels*) column density in the central 20 kpc of the galaxy at the same two output times. The grand design spiral arm pattern induced by the companion galaxy is clearly visible, especially in the upper panels. The pattern is much more pronounced in molecular gas. The bottom panels correspond to a configuration similar to the observed M51 galaxy. Also of note is the large tidal tail that has been ejected from the galaxy due to the close encounter with the companion, which is visible in the H I column density map but not in the H<sub>2</sub> column density map. The black dot indicates the position of the companion.

Smith et al. (2019) for a discussion of the relative importance of the galactic potential with respect to the SN feedback in shaping the filamentary properties of clouds in a similar setup to the one used here. A detailed analysis of the GMCs in this M51-like galaxy simulation is deferred to a future study.

The ultraviolet component of the interstellar radiation field cannot penetrate these clouds and the pressure can thus drop quite substantially due to runaway cooling down to the temperature floor of 20 K. This favours local collapse, which leads to intense SF. These newly-formed stars are responsible for clustered SN feedback that disrupts the parental clouds, creates large expanding superbubbles, and drives turbulence in the ISM. This favours a self-regulating matter cycle of the ISM (see e.g. Mac Low & Klessen 2004; Klessen & Glover 2016) whose properties converge to a roughly steady state after  $\sim 100$  Myr in the isolated case

(see next paragraph). Only the slow depletion of gas affects this equilibrium.

Since we lack early feedback such as winds or ionizing radiation, the earliest SNe exploding in each star-forming region are predominantly located in high density environments. In general, the momentum deposited by these SNe can create low density bubbles in which further SNe explode, with the combined effect of the clustered SNe eventually destroying the cloud. However, we encounter a few cases where this does not occur, so the SNe cannot completely disrupt the cloud. These pathological clouds continue to accrete mass onto sinks for a substantial amount of time, leading to extremely compact and massive clusters. We will come back to this point in Section 5.

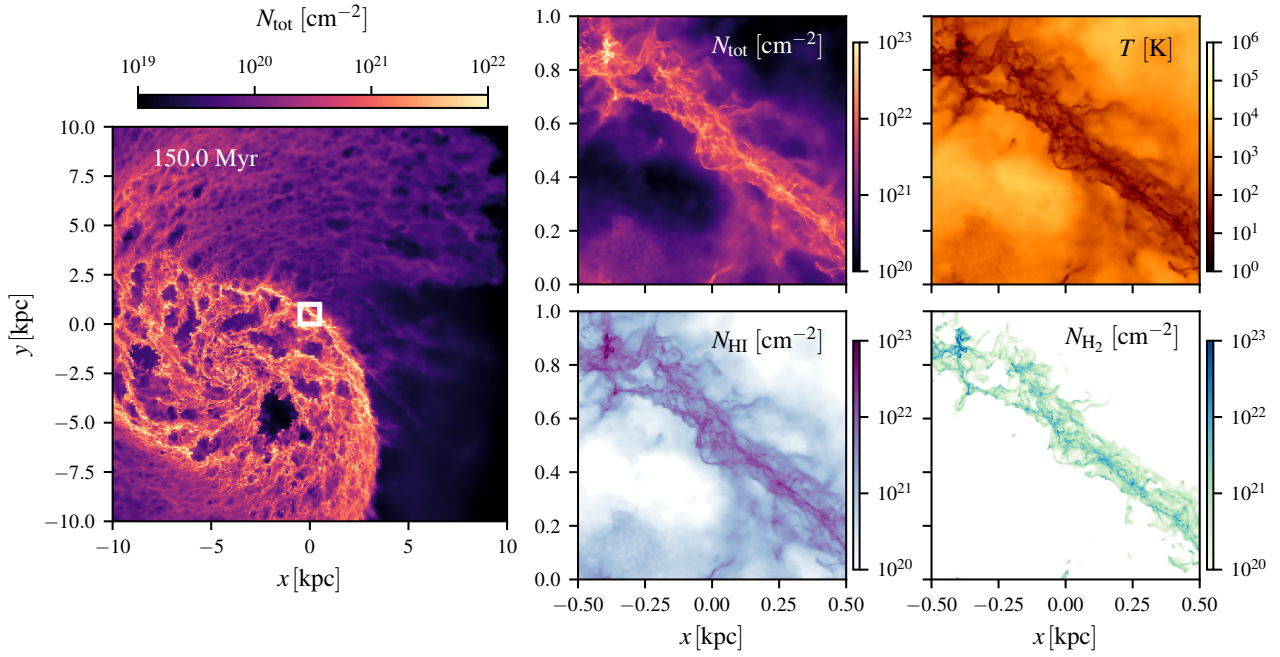


**Figure 7.** Total gas column density (*top left*), mass-averaged temperature along the line of sight (*top right*), H I column density (*bottom left*) and H<sub>2</sub> column density (*bottom right*) of a (1 × 1) kpc patch (*white square*) within the spiral arm of the interacting galaxy.

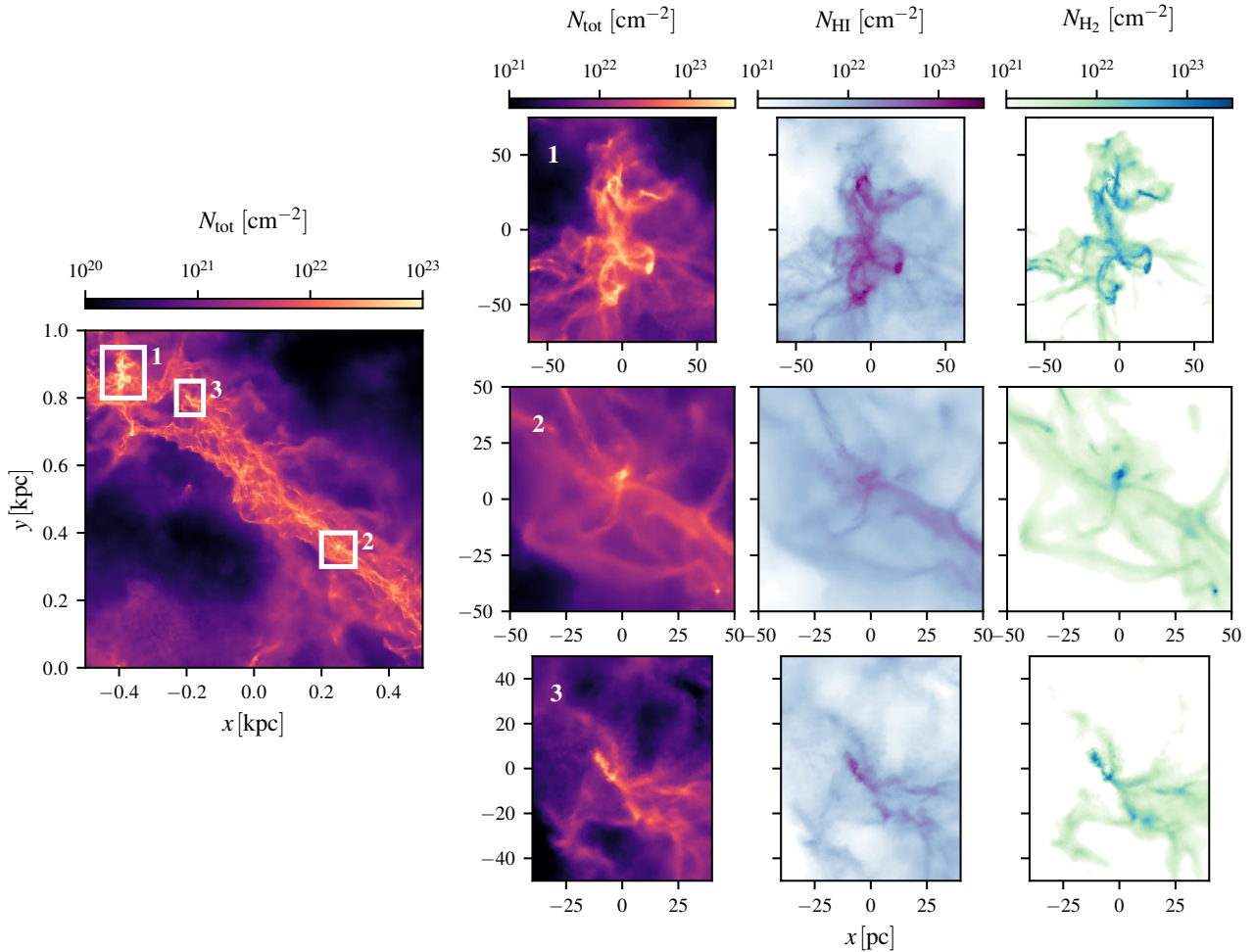


**Figure 8.** We further zoom in on a few selected GMCs of the spiral arm portion shown in Fig. 7. We show the total (*left*), H I (*centre*) and H<sub>2</sub> column density maps for the selected regions.

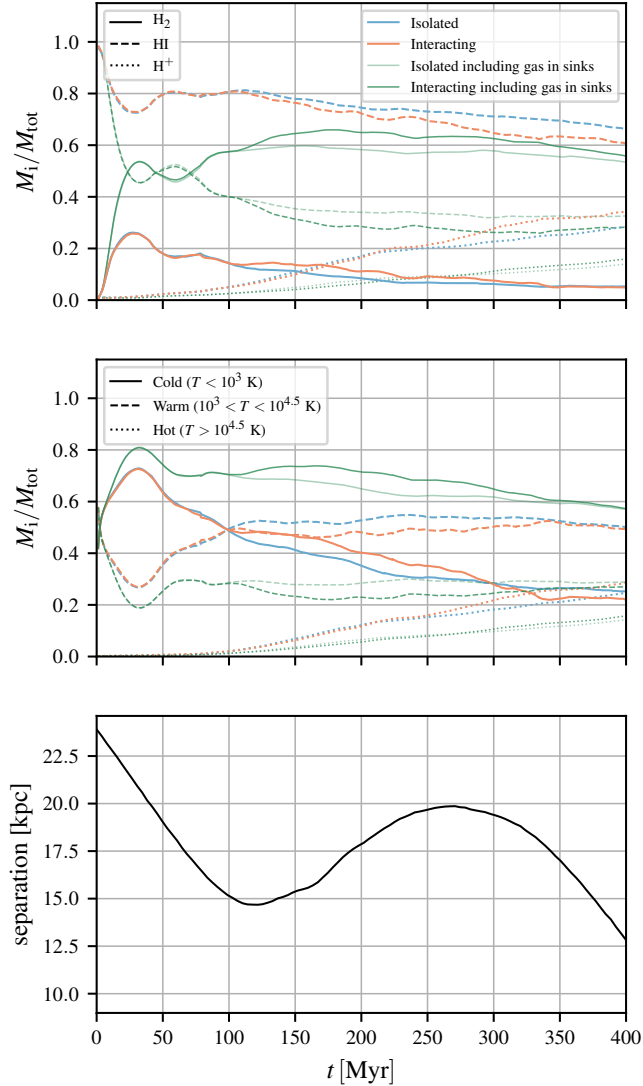


**Figure 9.** *Top:* Molecular (solid line), atomic (dashed line) and ionised (dotted line) mass fraction as a function of time. *Middle:* Cold gas at  $T < 10^3$  K (solid line), warm gas at  $10^3 < T < 10^{4.5}$  K (dashed line) and hot gas at  $T > 10^{4.5}$  K mass fractions as a function of time. The interacting simulation is given in orange while the isolated one is depicted in blue. Here the gas trapped in sinks is not considered, but if we assume this gas to be cold and fully molecular the fractions change and are presented in green instead. *Bottom:* separation between the main galaxy’s centre of mass and the companion as a function of time.

### 3.2 Thermal phases of the ISM

Sink particles are formed in the densest collapsing parts of the cold ISM. As described in Section 2.5, this removes dense cold gas from the hydrodynamic simulation and locks it into collisionless particles. Only part of this gas is directly converted into stars, while the rest is temporarily trapped inside the sink and will be returned to the gas phase after the associated SNe occur. This prompts the question of how to account for this material when examining the distribution of gas across the different phases of the ISM, since we do not have any information about the density, temperature,

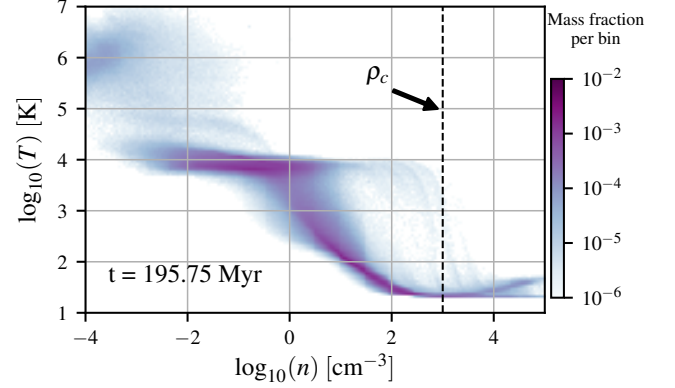


**Figure 10.** Density-temperature phase diagram of the gas phase in the interacting simulation. The colour indicates the total gas mass fraction in the given  $(n, T)$  bin. The vertical dashed line indicates the density threshold for sink particle formation.

or chemical composition of the trapped gas. One reasonable assumption would be that it is cold and fully molecular. However, this is likely an oversimplification; the real thermodynamical state of the gas could differ, especially if the stellar population within the sink in an advanced state of evolution and feedback has started to affect its contents. Nevertheless, this assumption does at least offer an upper limit on the cold molecular gas fraction in the simulations. Alternatively, by not including the gas in sinks at all, we instead recover a lower limit on the cold molecular gas fraction. This approach has the advantage that the state of the gas included in the analysis emerges self-consistently from the simulation and no additional assumptions have to be made. In our thermal analysis of the ISM phases, we have chosen the latter option and hence do not account for the trapped gas; the absolute value of the PDF and molecular fractions will be affected by this. However, this is the case for both isolated and interacting simulations, so a comparison between the two is consistent and the effect of the interaction can still be effectively studied. Finally, note that in some of the analysis later in the paper, we do attempt to account for the trapped material, making the assumption that it is cold and molecular.

After an initial transition phase, shown in Fig. 9, the ISM in the simulated galaxy develops a three-phase thermal structure with a sharp lower limit of 20 K due to the imposed temperature floor (see Fig.’s 10 and 11). An upper limit of roughly 70% of the gas mass is in the cold ( $T < 10^3$  K) phase, assuming the gas in the sink particles is primarily cold (Fig. 9), a fraction rather higher than the 50% found in the Milky Way (Ferrière 2001). This is perhaps appropriate for this actively star-forming galaxy.

Most of the remaining gas mass is in the warm stable phase around  $T = 10^4$  K with less than 10 % in the hot phase peaking at  $10^6$  K, generated by SN feedback and strong shocks. Note however that our resolution prescription (Section 2.6) is tuned to have the highest resolution in the dense part of the ISM at GMC scales, so it is likely that the fraction of gas in the hot diffuse phase where spatial resolution is small is not numerically converged. Numerical diffusion across interfaces in unresolved regions between hot

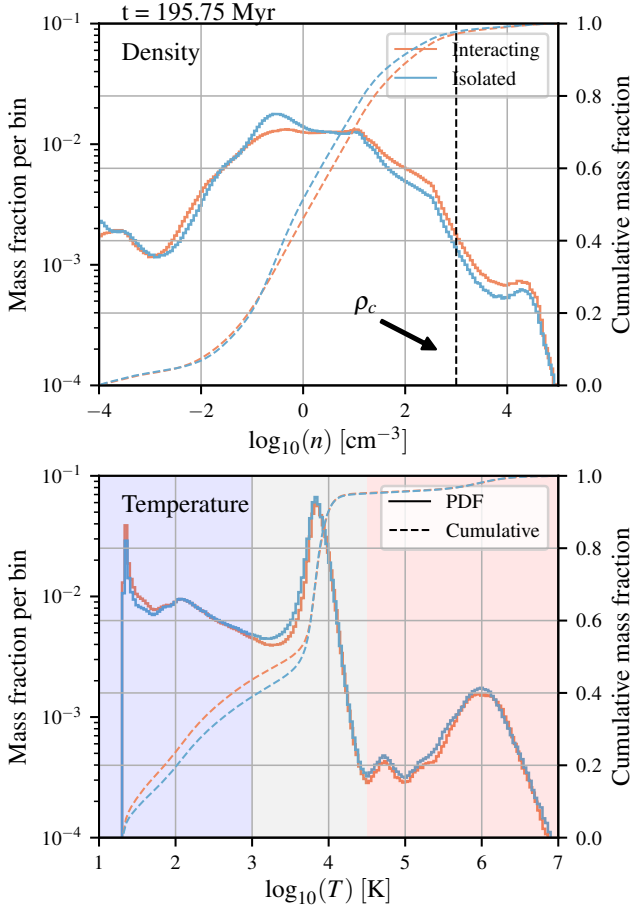


**Figure 11.** Mass-weighted density (*left panel*) and temperature PDF (*right panel*) of the gas phase in the simulations. The dashed line represents the cumulative density and temperature PDF respectively, i.e. the mass fraction with density/temperature below a given value. The blue line represents the isolated galaxy run while the orange shows the interacting simulation at the same time. The coloured regions in the temperature PDF indicate our definition of the cold/warm/hot phases (see text). Note that there is very little difference in the two cases highlighting how the interaction has little effect on the thermal phases of the ISM.

and warm gas tends to favor cooling, thus under-predicting hot gas fractions. Moreover, a higher number of SN events with an unresolved Sedov-Taylor expansion implies a lower production rate of hot gas since momentum energy injection is unable to contribute to the hot phase. For an indication of the actual trend of the hot phase fraction as a function of resolution see Appendix A.

The density PDF (upper panel of Fig. 11) exhibits a roughly log-normal profile as expected in a turbulent supersonic medium (e.g. Vázquez-Semadeni 1994; Wada & Norman 2001). We however do not see the gravity-induced power law tail for densities higher than  $10^4 \text{ cm}^{-3}$  (e.g. Klessen 2000; Kainulainen et al. 2009; Elmegreen 2011; Girichidis et al. 2014; Corbelli et al. 2018) as this regime lies above the sink particle density threshold and so the density distribution in this regime is strongly affected by accretion onto the sinks.

In Fig. 12 we show the temperature of the gas in a slice

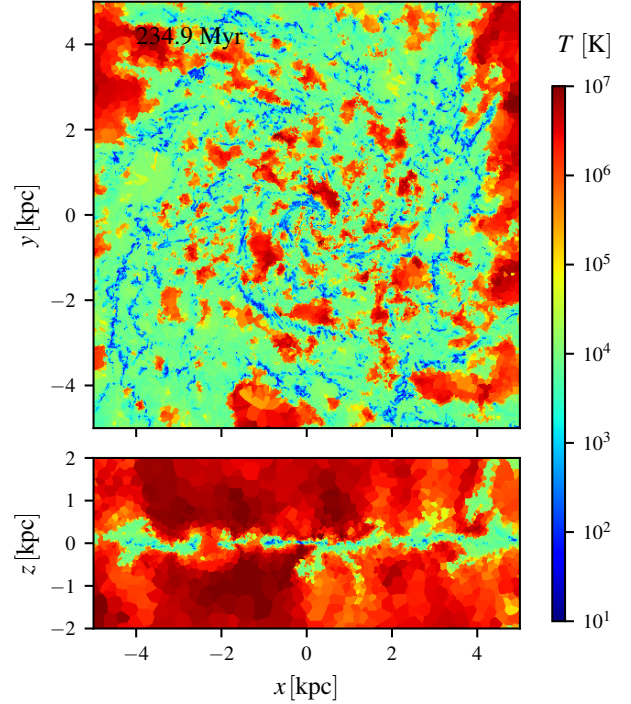


**Figure 12.** Temperature distribution in a slice in the  $z = 0$  plane (*top*) and  $y = 0$  plane (*bottom*) for the isolated simulation.

through the mid-plane of the central 5 kpc of the isolated galaxy. We can see that the cold phase is organised into GMC structures with a relatively low volume filling factor. These clouds are embedded in the warm phase at  $T = 10^4 \text{ K}$  while the clustered feedback coming from the sink particles drives superbubbles generating outflows producing the volume-filling hot phase, which permeates most of the volume above and below the disc.

Figure 13 shows that only the densest and coldest parts of the ISM ( $n > 10^2 \text{ cm}^{-3}$  and  $T \approx 20 \text{ K}$ ) are fully molecular and CO-bright. Because no CO is found below  $n \lesssim 100 \text{ cm}^{-3}$  the molecular gas in the transition zone between  $\sim 10$  and  $10^4 \text{ K}$  is CO-dark.

In the top right panel of Fig. 13 there are parts of the temperature-density phase space populated with high CO fractions but very little  $\text{H}_2$ . These are rapidly evolving SN shells where the simple model of CO chemistry used in our simulations does not capture the correct behaviour of the CO. The NL97 network used in our simulations assumes that photodissociation is the dominant destruction process for CO. In most of the ISM, this is a good assumption, but it breaks down in dense gas heated to high temperatures by strong shocks, where we would expect collisional dissociation of CO to dominate. Fortunately, this limitation of the NL97 network is highly unlikely to have a significant effect on the dynamical behaviour of the gas, since the cooling in these conditions is dominated by atomic line cooling and is hence insensitive to the CO content. In addition, the actual fraction of mass in this region of density-temperature space is small, as Figure 10 makes clear.

As expected given the microscopic cross-section for collisional ionization of hydrogen, gas with a temperature

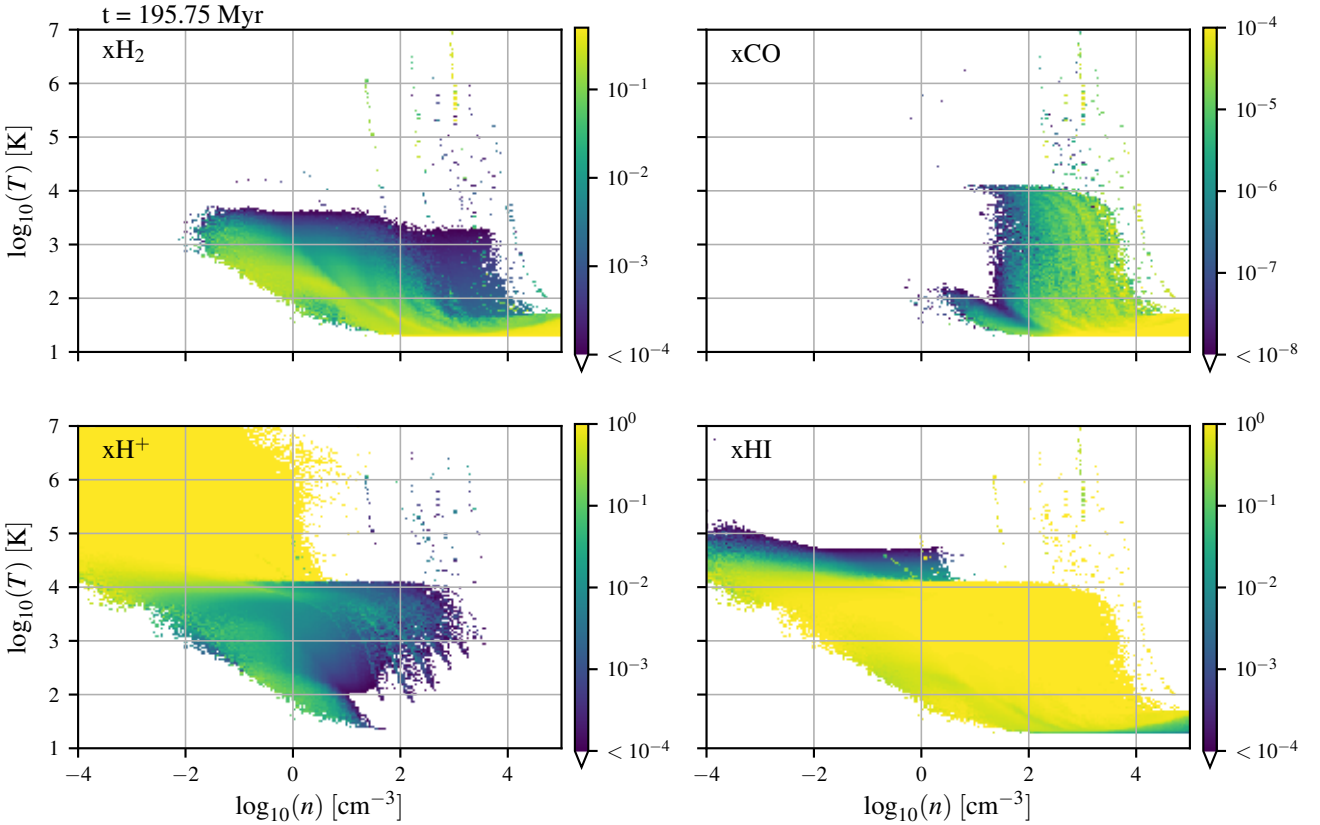


**Figure 13.** Mass-weighted average of the chemical abundance relative to the number of hydrogen nuclei in a given density–temperature bin for molecular hydrogen (*top left*), CO (*top right*),  $H^+$  (*bottom left*) and atomic hydrogen (*bottom right*). Note that for molecular hydrogen, a fraction of 0.5 corresponds to fully molecular gas.

$T \gg 10^4$  K is fully ionised. The atomic gas, on the other hand, lives in a wide region of the density–temperature phase space. A considerable fraction of the atomic gas is found at temperatures  $T \sim 10^4$  K or  $T \sim 100$  K, corresponding to the warm neutral medium (WNM) or cold neutral medium (CNM), respectively. However, there is also a substantial amount of atomic hydrogen in the transition region between these two thermally stable regimes (see also Figure 10), as is observed in the Milky Way (Heiles 2001). It should also be noted that as our simulations do not include the local effects of ionizing radiation from young stars, we underestimate the ionization rate in warm ( $T \sim 10^4$  K) low density gas, particularly far above or below the galactic midplane. Therefore, in our simulations this material remains largely atomic, while in a more realistic simulation it would be more highly ionised. As we are primarily interested in the behaviour of the dense gas and the SFR in our simulated galaxies, this should not have a significant impact on our results.

In Fig. 11 we also compare the density and temperature distributions of the ISM in the interacting galaxy to the isolated one. We notice that the interaction increases only marginally the amount of cold gas and the ISM phases are in general not affected by the merger. In Fig. 9 where we show the time evolution of the gas mass in the different thermal/chemical phases for the two simulations, we see that after  $\sim 100$  Myr, when the companion reaches its point

of closest approach to the galaxy, the tidally-induced two-armed spiral pattern starts to develop and this correlates with an increase in cold molecular gas. However this difference is relatively small, amounting to only a few percent throughout the simulation time. Secular changes in the gas fractions as gas is consumed in SF are far larger.

### 3.3 Column density power spectrum

The power spectrum of the column density of the ISM exhibits a power law profile whose parameters are related to the properties of the turbulence experienced by the gas. Therefore the power spectrum is an important statistical diagnostic tool to study the turbulence. In galaxy observations a characteristic change of slope is often seen at a scale of a few hundred parsecs and interpreted as the scale where the gas changes from a three dimensional regime of turbulence within the disc midplane to motions in two dimensions for scales larger than the scale-height (Dutta et al. 2009; Puerari et al. 2010). Simulations seem to confirm this scenario (Bournaud et al. 2010).

To investigate this in our simulations, we compute Fourier transforms of the column density  $\Sigma$ :

$$F(k_x, k_y) = \int_x \int_y \Sigma(x, y) e^{-i(k_x x + k_y y)} dx dy, \quad (10)$$

where  $k_x$  and  $k_y$  are the spatial frequencies associated to  $x$

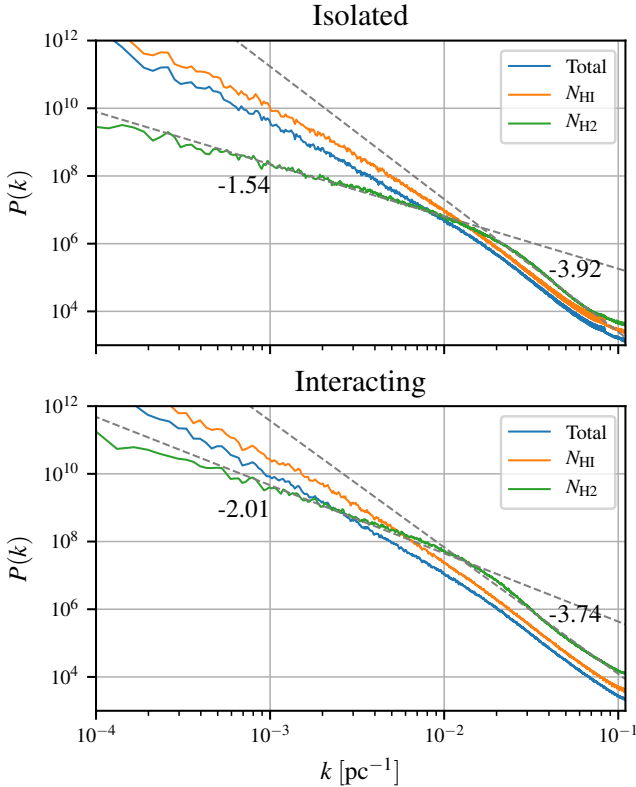


**Figure 14.** Power spectrum of the column density of the isolated (*top*) and the interacting (*bottom*) galaxy at  $t = 430$  Myr. We plot the power spectrum of the total (*blue line*), H I (*orange line*) and H<sub>2</sub> (*green line*) column densities. The different regimes of the molecular component have been fitted with a power law (*dashed line*) where we annotated the resulting exponents.

and  $y$ . The 1D power spectrum is then simply obtained by azimuthal averaging  $P(k_x, k_y) = |F(k_x, k_y)|^2$  over frequencies having equal  $k = \sqrt{k_x^2 + k_y^2}$ .

In Fig. 14 we show the power spectrum of the total, H I and H<sub>2</sub> column densities for the isolated and the interacting simulation. We note the change of slope in the molecular hydrogen case at scales of about 50 pc while in the atomic case the change of slope is less pronounced. These scales are comparable to the scale-height of our discs and we suggest therefore that this is an indication of the aforementioned change of turbulence regime. Similar slopes are for instance inferred in M33 by Combes et al. (2012) which also exhibits a much greater change in slope for the molecular than for the atomic case (see their Fig. 8).

It is interesting to notice that the interaction does not change this general trend and affects the slopes only marginally especially in the atomic case. Moreover the change of slope in the molecular phase is more pronounced at larger scales where the interaction is able to drive the formation of spiral arms and generally change the morphology of the gas, while at smaller scales the two profiles are comparable.

### 3.4 Star Formation

Gravitational collapse occurs in GMCs where densities are highest and the ISM is cold enough to trigger runaway collapse leading to SF. We therefore expect a similar behaviour of the SFR to that of the cold molecular gas that we described in the previous section.

We show the SFR as a function of time for the isolated and interacting runs in Fig. 15. Around  $t = 80$  Myr we turn on the full refinement scheme and previously stable gas becomes unstable due to better resolved collapse. This explains the spike in SF noticeable just after the onset of our highest resolution scheme. In less than 20 Myr the ISM self-regulation brings this value back down to previous levels. SF increases after the point of closest separation, when the spiral arms start to develop ( $t \approx 110$  Myr). However, the difference between the isolated and interacting runs is small and at the end of the simulation the difference in the total mass of stars formed in the two simulations is less than 10% (see Fig. 16).

At  $t = 418$  Myr, the time at which our simulation is at an equivalent evolutionary phase to M51, we find an SFR of  $4 M_{\odot} \text{ yr}^{-1}$  which is comparable to the observed value of  $4.6 M_{\odot} \text{ yr}^{-1}$  (Pineda et al. 2018). However if we consider that we started with a galaxy that had only half of the gas mass of M51a, we conclude that our depletion times are most likely too short by a factor of about two. This may reflect the lack of early feedback that can shut off SF earlier in the evolution of a newborn star cluster than SNe alone.

We did not include any type of hot circumgalactic coronal gas from which the disc could replenish its gas reservoir, nor did we simulate other types of gas inflow. Therefore, even though we include a mass return from the sink particles, we are slowly depleting the gas available to SF (see Fig. 17). This is also reflected in the measured SFR in Fig. 15, where we see a slow but steady decline in SF at later stages of the simulation.

To have an idea of where the SF is taking place, we look at how it correlates with the local gas column density. Observationally the gas surface density is connected to the SFR by a simple power law  $\Sigma_{\text{SFR}} \propto \Sigma_{\text{gas}}^{\alpha}$  where  $\alpha \approx 1.4$  known as the Schmidt-Kennicutt relationship (Schmidt 1959; Kennicutt 1989, 1998). An even narrower relationship with an exponent close to unity can be observed if only the molecular gas is considered (Bigiel et al. 2008). Although this relation does not seem to be as universally applicable and in several instances can exhibit a large scatter (Shetty et al. 2014a,b), it has been extensively used in the literature to connect large-scale galaxy properties directly to the local SF by abstracting the complexity of the SF process to a simple power law.

To see whether and how this relation develops in our simulations in Fig. 18 we convolve the H<sub>2</sub> column density and the SFR surface density map with a Gaussian function of variable standard deviations  $\sigma$  and then cross-correlate the two quantities. We find that the observed slope and scaling is well reproduced for  $\sigma = 100$  pc. This smoothing is reasonable, as we do not expect molecular gas and SF to remain correlated down to arbitrarily small scales within galaxies (Schruba et al. 2010; Kruijssen et al. 2018), and a recent study has shown that the scale on which this decorrelation occurs is around 100–200 pc for a range of different

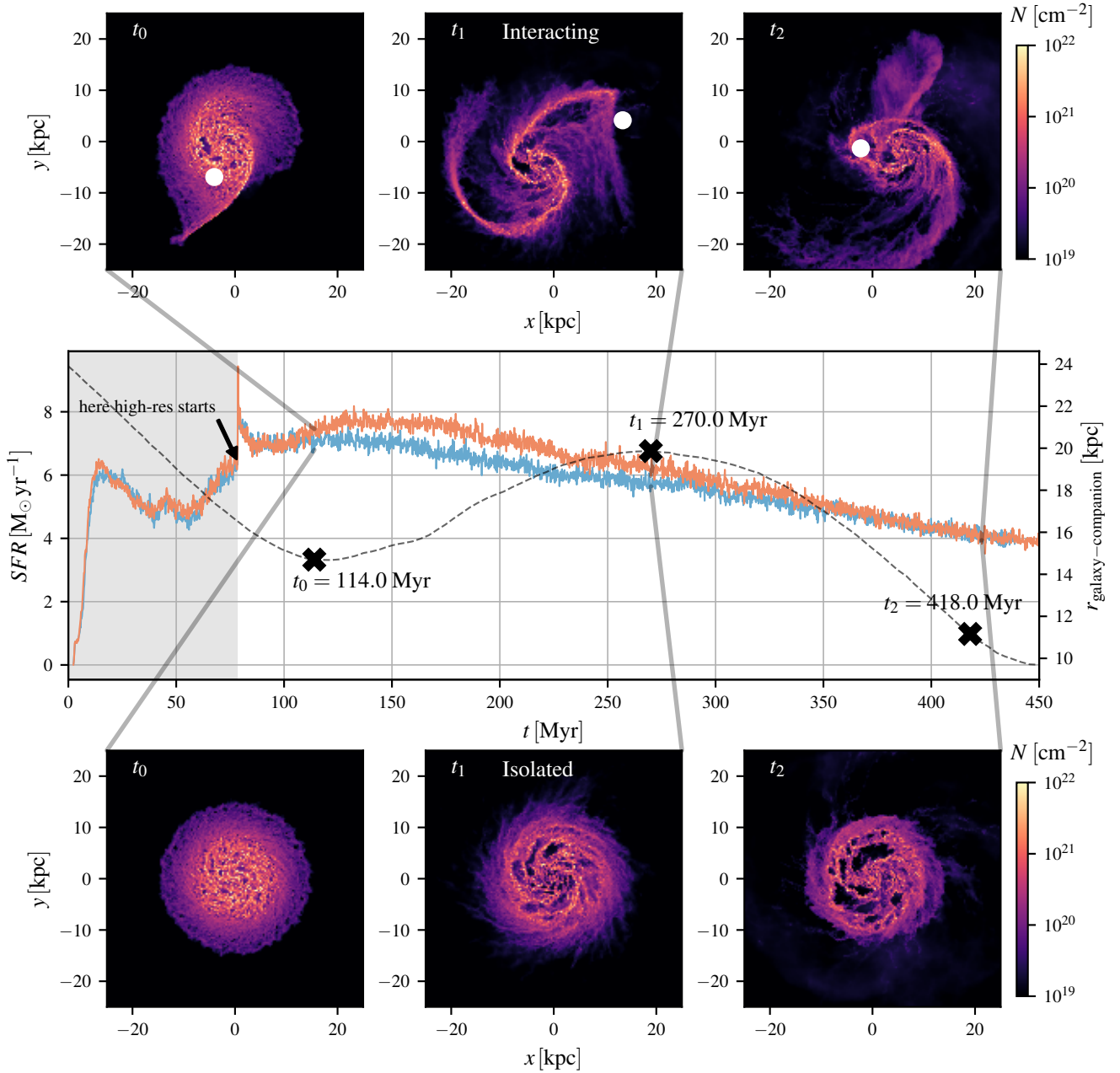


**Figure 15.** SFR as a function of time for the *Isolated* (blue) and *Interacting* (orange) runs, respectively. The black dotted line shows the separation of the centre of mass between the main galaxy and the companion for the interacting case. Three representative times are chosen (black crosses) for which we show the morphology of the interacting simulation (*top three panels*) and isolated simulation (*bottom three panels*). Despite the clear differences in the morphology of the galaxies in the two simulations, the SFR is surprisingly similar. This shows that the interaction has little effect on the SFR. The interaction merely dictates the morphology of the star-forming regions, but the intensity is controlled by the self-regulated feedback within the ISM.

galaxies (Chevance et al. 2019). The mean SFR for every  $H_2$  column density bin (orange line of Fig. 18), however, follows a slightly steeper power law with higher rates for higher surface density regimes with respect to the observed one. This connects to the low depletion times that we observe in our simulations (see next paragraph).

We do not see a significant change in the slope, scaling and broadening of the relation if we consider the isolated galaxy simulation instead. This is an indication that the

mechanism that controls SF is similar in the two instances and the relation emerges due to the local dynamics of the collapse, something that the galactic-scale interaction seems to have little impact on.

Morphologically, however, the two galaxies differ substantially and accordingly so does the distribution of the star-forming regions that are correlated with the molecular gas. The isolated galaxy remains flocculent throughout the simulation; frequently SF occurs at the edges of ex-

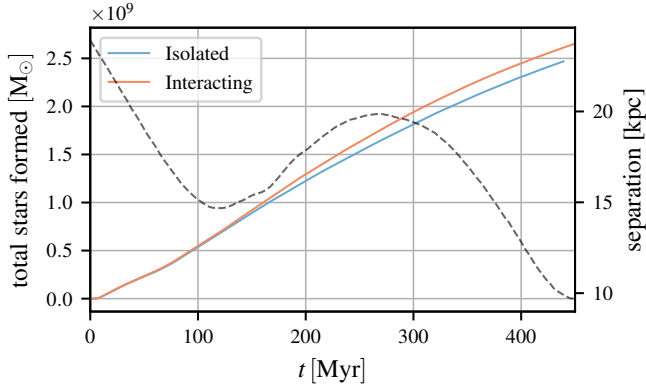


**Figure 16.** Cumulative SFR as a function of time, i.e. total amount of stars formed up to a given time  $t$ . The isolated galaxy is plotted in blue and the interacting one in orange. As in Fig. 15 we also show the separation of the galaxy and its companion for the interacting simulation (*dotted line*).

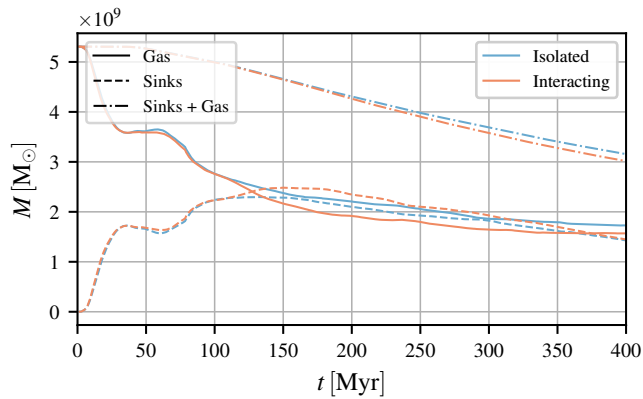


**Figure 17.** Gas mass (*solid line*) as a function of time for the interacting (*orange*) and isolated (*blue*) simulation. Part of the gas is locked into sink particles (*dashed line*) and will be returned to the gas phase over time, but part will be lost to stars contributing to a global steady depletion of gas. The dash-dotted line therefore shows the sum of the mass in sinks plus gas mass.

panding superbubbles, which compress the gas and facilitate GMC formation. The interacting simulation instead develops strong spiral arms that correlate with SF (see Fig. 19). Since no new SF is generated during the encounter, it seems that the interaction is only grouping the GMCs and the associated SF into spiral arms as opposed to these structures being the trigger for new collapse.

#### 4 DISCUSSION

Given the findings of the previous two sections, we see that the interaction, for the type of encounter considered here, is not able to significantly change the structure of the ISM in terms of thermal phases and chemical state (see Figs. 9, 11). This is reflected in the almost identical SF history experienced by the two galaxies (Figs. 15, 16).

Major galaxy interactions are generally associated with enhanced SFRs (Larson & Tinsley 1978; Lonsdale et al.

1984; Barton et al. 2000; Ellison et al. 2008; Renaud et al. 2019). Outliers are however possible and the details are strongly dependent on the orbital parameters of the encounter and the stability of the isolated disc (Di Matteo et al. 2007). This is actually in line with the inferred SF history of the M51 galaxy which lacks the fingerprint of enhanced SF activity but had a roughly constant rate of  $5 M_{\odot} \text{yr}^{-1}$  during the past few gigayears which even declined somewhat in the past 100 Myr (Eufrazio et al. 2017). This is roughly what we see also for the simulated system (Fig. 15).

Most simulated mergers, however, show the peak of the SFR during the coalescence phase (Cox et al. 2006; Di Matteo et al. 2007; Renaud et al. 2014), which could be associated with a different behaviour of the ISM due to more extreme galaxy conditions. This phase is not followed by our model, so it is possible that the bulk of the SF is yet to come.

The strength of the SF burst decreases for smaller mass ratios between the two galaxies and can be negligible when the tidal disturbance is small, as in the case of minor mergers (Cox et al. 2008). Even though our nominal mass ratio turns out rather low, based on dynamical considerations we have argued that our simulated companion galaxy de facto represents just its core (see Section 2.5) and that the actual mass ratio is closer to the observed one of M51. If this statement is erroneous, on the other hand, the lack of enhanced SF is not an exception, but rather the normal behaviour for mergers in this mass regime in agreement with Cox et al. (2008). A better treatment of the mass distribution of the companion galaxy, instead of treating it as a simple point mass, will shed light on this.

Di Matteo et al. (2007) suggested that in some cases the close encounter can eject considerable amounts of gas into the diffuse tidal tail, which then cannot fully re-accrete at later stages of the merger, thereby explaining the lack of enhanced SF. Our simulation also develops such a diffuse atomic tidal tail (bottom panel of Fig. 6). It could therefore be that this is removing significant amounts of gas from the pool available to SF while still increasing the SFR in more central regions.

From Fig. 20, where we plot cumulative masses as a function of radius for the two simulations, we can see that this is however not the case. Almost 20% of the total mass of the interacting galaxy is at  $R \gtrsim 10$  kpc and thus in the tidal tail, however in the isolated case a similar mass fraction is in the part of the disc that is mainly atomic and not star forming. Therefore it is unlikely that the interaction is effective at removing gas which would otherwise have been available for SF.

We conclude that the two galaxies have essentially the same amount of gas available for SF throughout the simulation. This is also seen in Fig. 21, where we show the depletion times of the different ISM components versus time and notice that between the interacting and the isolated simulation there is only a marginal difference during their evolution. Globally, the interaction is not able to change the relation between the available gas and the SFR, which explains also why the inferred Schmidt-Kennicutt relations for the two cases are the same.

As suggested in Fig. 20, we do not see a significant mass flow to the very centre, as the mass profiles up to  $\sim 2.5$  kpc are similar in the two simulations. Other studies found that

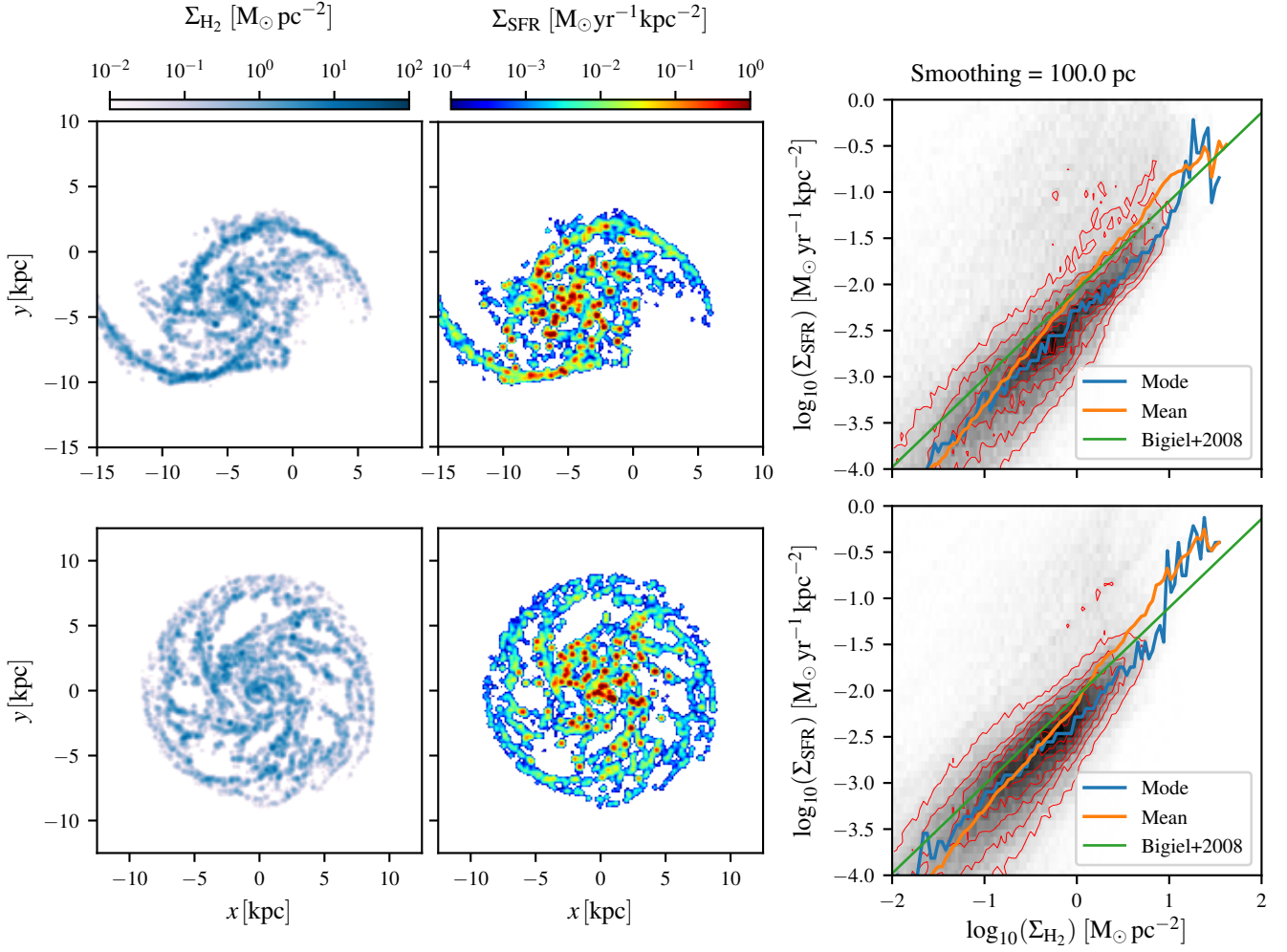


**Figure 18.** H<sub>2</sub> column density map convolved with a Gaussian function with standard deviation  $\sigma = 100$  pc (left) at a time of  $\sim 200$  Myr. SFR surface density map convolved with the same kernel (centre). On the right we show the Schmidt-Kennicutt type relation based on the two maps. The green line is the observed relation taken from Bigiel et al. (2008), the orange line describes the mean while the blue line is the mode of the SFR distribution in each surface density bin. The top row indicates the interacting simulation while on the bottom we show the isolated one.

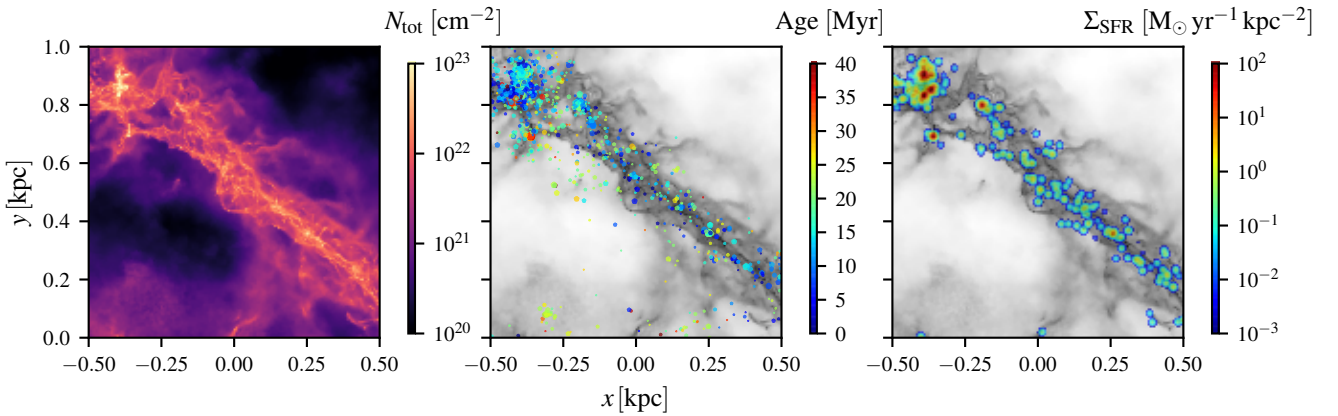


**Figure 19.** For the region shown in Fig. 7 we show the location of the sink particles formed, coloured by their age (central panel) and the SFR surface density convolved with a Gaussian aperture of  $\sigma = 5$  pc averaged over the past 4 Myr.

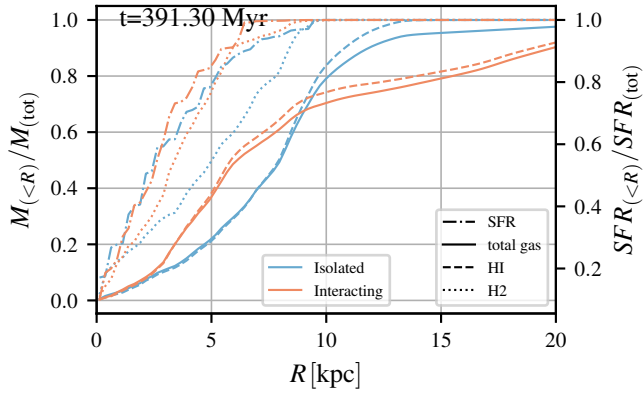


**Figure 20.** Cumulative total/H I/H<sub>2</sub> gas mass distribution (*solid, dashed and dotted lines*) as a function of galactocentric radius normalised to the total mass in each component for the isolated (*blue*) and interacting galaxy (*orange*) at a simulation time around 400 Myr. We also show the normalised cumulative SFR as a function of galactocentric radius for the two simulations (*dot-dashed line*).

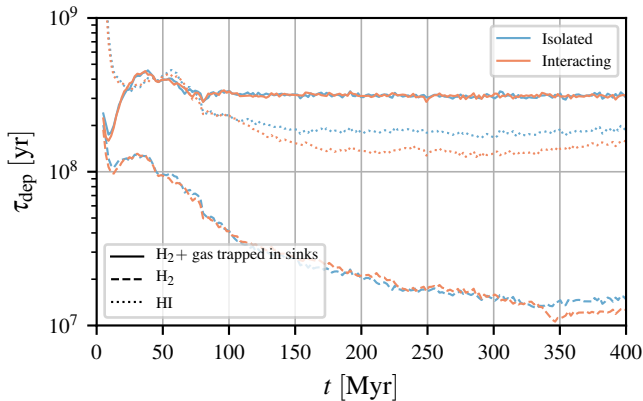


**Figure 21.** Depletion times ( $\tau_{\text{dep}} = M_i/SFR$ ) as a function of time for the isolated (*blue*) and interacting (*orange*) simulation. The H I (*dotted line*) and H<sub>2</sub> (*dashed line*) depletion times are shown. Since a lot of gas is trapped into sink particles, the H<sub>2</sub> depletion time is a lower limit. Considering all of the gas in the sink particles as molecular, we can sum it with the H<sub>2</sub> gas (*solid line*) to get an upper limit on the molecular gas depletion time.

galaxy interactions drive large gas flows towards the central regions and therefore drive a nuclear star burst (Torrey et al. 2012; Moreno et al. 2015). This is not reproduced in our high resolution simulations for this specific merger system, and so the SF rate remains low.

The interaction is, however, able to redistribute the gas mass within the disc for more intermediate radii as we can notice from Fig. 22, where we plot the radial surface density profiles. As a matter of fact, in the interacting case roughly 60% of the mass is within the central  $\sim 6$  kpc while the same radius contains only 30% in the isolated disc (Fig. 20). Such a strong difference between the two is absent if we look at the cumulative SFR profile (dot-dashed line in Fig. 20). This indicates that the interaction studied here is able to produce changes to the SF efficiency locally. This can also

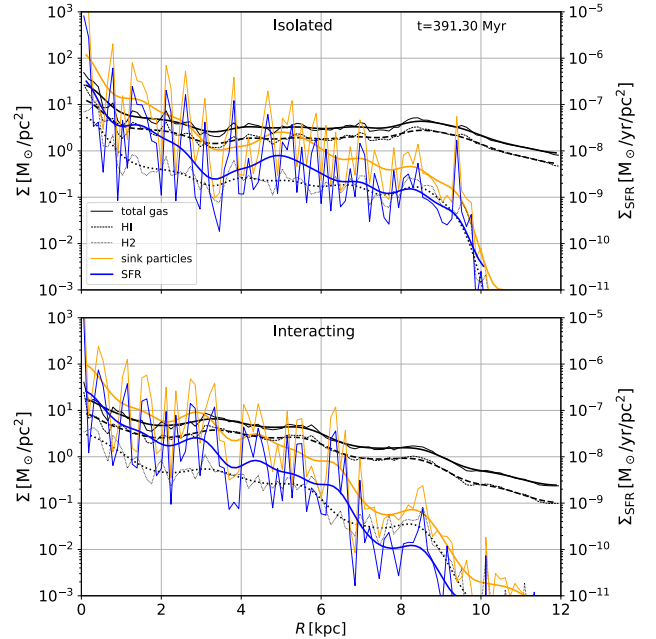


**Figure 22.** Surface density as a function of radius for the isolated (*top*) and the interacting simulation (*bottom*) at a simulation time of  $\sim 400$  Myr. The total gas (*solid black line*), H I (*dashed line*) and H<sub>2</sub> (*dotted line*) surface densities are shown. We also show the distribution of sink particles (*orange line*) and the SFR surface density (*blue line*). Due to the high radial variability for some of the quantities, we also plotted (*thicker lines*) the same quantities convolved with a Gaussian filter to better show the radial profile.

be appreciated in Fig. 23 where we plot depletion times as a function of radius. We see here that variations of the order of a few are possible. These differences are significant as they are greater than just the temporal fluctuations of the local depletion times.

The question arises then as to what is controlling the ISM phases and the SFR if the interaction is ineffective in doing so. The isolated disc collapses and generates GMCs leading to SF in the central 8–10 kpc which is the region that is initially marginally Toomre unstable (Fig. 1). Once the collapse started, a self-regulating equilibrium is generated where the energy input from the stellar feedback acts to counterbalance the forces responsible for cooling the gas to GMC levels to be available for SF again. The disc is essentially maximally star forming in the sense that in the Toomre unstable regions there is no gas reservoir that is not available for SF. Stars form at a rate set by the requirement that feedback balance the vertical pressure in the disc (Ostriker et al. 2010; Ostriker & Shetty 2011). The interaction is not able to increase the SFR since no new gas is added and all of the available gas is already available for SF. If the encounter is then not able to considerably change the conditions that control the turnover time of molecular gas, such as midplane pressure, SFR is unaltered.

These conclusions are case specific for the type of interaction studied here. If for instance the companion galaxy had a non-negligible ISM fraction, direct collision of the two gas discs could have led to local collapse in the Toomre sta-

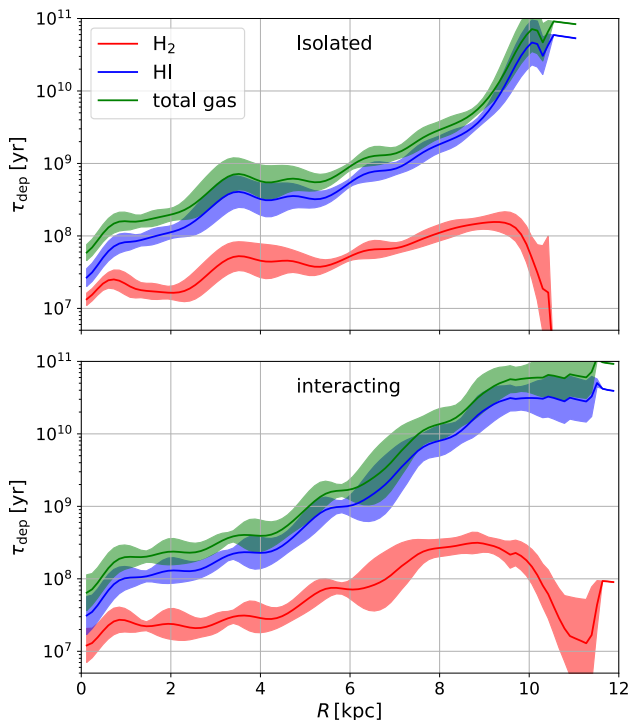


**Figure 23.** Depletion times of the total (green), molecular (red) and atomic (blue) gas as a function of radius for the isolated (top) and interacting (bottom) galaxy. The depletion times are calculated for a simulation time around 400 Myr and averaged over a time period of  $\sim 20$  Myr. The shaded area is a one sigma deviation from that average.

ble part of the isolated disc, resulting thus in an enhanced SFR.

Moreover, if the mass ratio between the two galaxies were greater, we might have seen a more pronounced mass flow towards the centre, more compression in the tidal tail, and an increase of midplane pressure, all factors that could lead to higher SFRs, either by changing the available amount of gas or by increasing the SF efficiency. Exploring these issues will require a more extensive parameter study of galaxy interactions, which is out of the scope of the study presented here.

## 5 CAVEATS

The ISM is dynamically complex, and so our simulations are inevitably a simplification compared to the true behaviour of the ISM in a galaxy. In particular, there are several important physical processes that are not included in our current model. These include magnetic fields and early stellar feedback such as ionizing radiation and winds.

Early feedback is responsible for clearing out the surrounding gas so that when SNe explode, every SN event can deposit a much higher energy into the ISM than in the case of SNe being directly injected into the high-density molecular phase. In our simulations it is often the initial SN that takes over the role of early feedback of clearing out the surroundings and preparing the region for the later SNe to disrupt

the cloud. Although the specific details of this disruption are likely sensitive to the specific feedback implementation, the sole fact of having a mechanism to self-consistently disrupt clouds from within ensures that the ISM is self-regulated by the internal feedback and so a healthy matter-cycle is achieved. These simulations are therefore well suited to address questions regarding the global life cycle of the ISM or the formation and early stages of GMCs.

In a few cases, however, we find that the initial SNe explode in such a dense environment that they cannot efficiently pre-process the surrounding ISM for later SNe to be effective. Instead, in these cases the injected energy is quickly radiated away and the bubble re-collapses before further SNe can pressurise its interior and drive further expansion. Consequently, SF cannot be halted by feedback but instead continues for an unphysically long period of time, generating extremely massive star clusters and long-lived GMCs. While some models predict re-collapse of massive clouds and subsequent SF cycles (see e.g. [Rahner et al. 2017, 2018, 2019](#)), in our simulations this is largely a numerical artefact.

If for some dynamical reason these massive clusters decouple from the parental cloud<sup>5</sup>, the SNe associated with the cluster can deposit their energy much more efficiently into the ISM. Since the cluster is unphysically massive, it also produces a large number of SNe. The resulting superbubble can therefore be extremely large and have a significant impact on the morphology of the entire galaxy. This is probably a major reason for the spiral arms being much less defined in the interacting simulations compared to the isothermal runs (compare Fig. 2 and Fig. 6 for instance).

Early feedback is also responsible for shutting down SF much earlier in the life of a young GMC than in the case of SNe alone (see e.g. [Gatto et al. 2017; Kannan et al. 2018; Fujimoto et al. 2019](#)). The absence of early feedback may therefore lead us to overestimating the SFR. To some extent this has been corrected for by our assumption of the local SF efficiency within the individual sink particles (Section 2.5). Moreover, even if our SFRs are overestimated in some cases, the effect should be comparably strong in both simulations, meaning that the trend that we see in Fig. 15 should be similar and our conclusions should not change.

Our neglect of magnetic fields means that we are missing a source of stabilizing pressure against collapse and cloud formation. The compression of gas into spiral arms due to the galactic interaction could potentially be a trigger to overcome this additional pressure force and initiate cloud formation. In this case the interaction with the companion could have a more dramatic effect on the cold molecular phase than in the simulations presented in this paper. This should be investigated in dedicated studies.

## 6 CONCLUSIONS

We have performed high resolution AREPO simulations of a massive spiral galaxy interacting with a smaller companion. The properties of the galaxies and the orbital parameters

<sup>5</sup> The gas is collisional while the stars are collisionless, so it is not unusual for the two components to decouple, for instance during cloud collisions.

of the encounter were chosen to roughly reproduce an M51-like system. For comparison purposes, we also modelled the evolution of the spiral galaxy in the absence of the interaction. Our simulations reach sub-parsec spatial resolution in dense molecular gas throughout the galaxy. We include the major physical ingredients thought to play key roles in the formation and destruction of GMCs to get a healthy life-cycle of the molecular gas in the galaxy. These include a time-dependent, non-equilibrium chemical network able to follow hydrogen and CO chemistry, local shielding from the molecule-dissociating part of the interstellar radiation field, sink particle formation to follow local centres of collapse and model stellar birth, and coupled SN feedback.

The isolated galaxy stays mostly flocculent throughout the simulation while in the case of the interaction a strong two-armed spiral pattern develops, along with an extended atomic tidal tail similar to the one observed for M51a. The final morphology and configuration closely resembles the M51 system, although our feedback prescription created strong superbubbles disrupting the otherwise clean spiral pattern much more than in the real case.

The ISM in the simulations settles into a typical three-phase medium with the cold molecular gas organised into dense GMCs associated with intense SF. Atomic gas makes up the cold neutral medium as well as the warm  $T \sim 10^4$  K phase into which the molecular cloud complexes are embedded. Supernova explosions coupled to recent SF activity are responsible for creating large superbubbles disrupting surrounding clouds and generating the hot ionised volume filling phase. The ISM properties roughly converge to an equilibrium state after an initial transition phase and only vary slowly after this due to gas depletion.

A lower limit of  $\sim 10\%$  and an upper limit of  $\sim 60\%$  of the gas mass is molecular, depending on what one assumes regarding the chemical state of gas trapped inside sink particles. We find an SFR of  $4.0 M_{\odot} \text{ yr}^{-1}$  at a time corresponding to the current evolutionary phase of M51, in good agreement with the measured value of  $4.6 M_{\odot} \text{ yr}^{-1}$ . Due to lack of early feedback, however, our depletion times are too low by a factor of at least two considering that we started with a less massive ISM disc.

With this study we tried to further understand how the interaction of two galaxies can affect the ISM and the resulting SFR. Galaxy interactions are frequently invoked to induce star-bursts and to produce a general increase in SFRs. In the case analysed here, however, we find that other factors such as the initial disc stability and local feedback are more important than the interaction itself for controlling the ISM properties. While morphologically very different from each other, we find that the ISM phases of the two simulations are only marginally affected by the interaction, resulting in an almost identical SF history for the two cases. The galaxy interaction is *not* the trigger of strong star-bursts in the disc for our simulations. The M51 system is therefore a prototypical example of a merger event where SF is not controlled by the interaction but rather by pre-existing galaxy conditions and the self-regulating nature of the ISM. This is also supported by the observations that suggest a roughly constant SF rate during the past several  $10^8$  years.

In the two scenarios simulated, the total gas accessible to SF is roughly the same. The interaction can not remove gas from the pool available to SF by shooting it into the dif-

fuse tidal tail, as that mainly comes from an already stable part of the isolated disc. Nor is it compressing previously stable gas in the outskirts of the disc enough to trigger additional SF there. The global depletion times are therefore very similar in the two simulations. Locally, however, the interaction modifies the radial profile of the gas, making the galaxy more compact for intermediate radii and inducing local changes in the depletion times.

In the isolated galaxy, collapse is triggered in the Toomre unstable part of the disc. In this region the ISM is maximally star forming in the sense that there is no locked-up gas that is not accessible to SF, and the rate is self-regulated by feedback from young stellar populations injecting energy into the system to counterbalance the mid-plane pressure. Since the interaction cannot drastically change the latter, the ISM changes only slightly. On the other hand, the outer regions of the disc, which were stable in the isolated case, are unable to form stars even in the interacting simulation since the encounter ejects most of this gas into the extended atomic tidal tail.

We conclude that SFR and the balance of the gas between the different phases is set by self-regulation in response to stellar feedback, and the effect of the interaction is limited here to inducing changes in the morphology of the galaxy, grouping the already present molecular gas and associated SF into dense spiral arms.

## ACKNOWLEDGEMENTS

We would like to thank the referee, Frederic Bournaud, for his suggestions which improved the manuscript. We gratefully acknowledge Mattis Magg, Ondrej Jaura, Eric Pellegrini and Ana Duarte Cabral Peretto for insightful comments and discussions. We further thank Rüdiger Pakmor and Volker Springel for letting us use their code. MCS, RGT, SCOG, and RSK acknowledge support from the Deutsche Forschungsgemeinschaft via the Collaborative Research Centre (SFB 881) “The Milky Way System” (sub-projects B1, B2, and B8) and the Priority Program SPP 1573 “Physics of the Interstellar Medium” (grant numbers KL 1358/18.1, KL 1358/19.2, and GL 668/2-1). RGT also thanks the AMNH and the Kade foundation for its support and hospitality in the early stages of this project. RSK furthermore thanks the European Research Council for funding in the ERC Advanced Grant STARLIGHT (project number 339177). RJS gratefully acknowledges an STFC Ernest Rutherford fellowship (grant ST/N00485X/1) and HPC from the Durham DiRAC supercomputing facility (grants ST/P002293/1, ST/R002371/1, ST/S002502/1, and ST/R000832/1). The authors acknowledge support by the state of Baden-Württemberg through bwHPC and the German Research Foundation (DFG) through grant INST 35/1134-1 FUGG. M-MML acknowledges partial support from US NSF grant AST-1815461, and the hospitality of the Institut für Theoretische Astrophysik during writing of this paper. PCC acknowledges support from the Science and Technology Facilities Council (under grant ST/N00706/1). PCC also acknowledges StarFormMapper, a project that has received funding from the European Union’s Horizon 2020 Research and Innovation Programme, under grant agreement no. 687528.

## REFERENCES

- Barton E. J., Geller M. J., Kenyon S. J., 2000, *ApJ*, **530**, 660
- Bate M. R., Bonnell I. A., Price N. M., 1995, *MNRAS*, **277**, 362
- Bertram E., Glover S. C. O., Clark P. C., Klessen R. S., 2015, *MNRAS*, **451**, 3679
- Bigiel F., Leroy A., Walter F., Brinks E., de Blok W. J. G., Madore B., Thornley M. D., 2008, *AJ*, **136**, 2846
- Blondin J. M., Wright E. B., Borkowski K. J., Reynolds S. P., 1998, *ApJ*, **500**, 342
- Bournaud F., Elmegreen B. G., Teyssier R., Block D. L., Puerari I., 2010, *MNRAS*, **409**, 1088
- Bubel A.-P., 2015, Master's thesis, Ruprecht-Karls-Universität Heidelberg, doi:10.5281/zenodo.49764
- Chevance M., et al., 2019, *MNRAS*, in press
- Clark P. C., Glover S. C. O., Klessen R. S., 2012, *MNRAS*, **420**, 745
- Clark P. C., Glover S. C. O., Ragan S. E., Duarte-Cabral A., 2019, *MNRAS*, **486**, 4622
- Combes F., et al., 2012, *A&A*, **539**, A67
- Corbelli E., Elmegreen B. G., Braine J., Thilker D., 2018, *A&A*, **617**, A125
- Cox T. J., Jonsson P., Primack J. R., Somerville R. S., 2006, *MNRAS*, **373**, 1013
- Cox T. J., Jonsson P., Somerville R. S., Primack J. R., Dekel A., 2008, *MNRAS*, **384**, 386
- Croxall K. V., Pogge R. W., Berg D. A., Skillman E. D., Moustakas J., 2015, *ApJ*, **808**, 42
- Daddi E., et al., 2010, *ApJ*, **714**, L118
- Dale J. E., Ngoumou J., Ercolano B., Bonnell I. A., 2014, *MNRAS*, **442**, 694
- Di Matteo P., Combes F., Melchior A.-L., Semelin B., 2007, *A&A*, **468**, 61
- Dobbs C. L., Theis C., Pringle J. E., Bate M. R., 2010, *MNRAS*, **403**, 625
- Dobbs C. L., et al., 2014, *Protostars and Planets VI*, pp 3–26
- Draine B. T., 1978, *ApJS*, **36**, 595
- Dutta P., Begum A., Bharadwaj S., Chengalur J. N., 2009, *MNRAS*, **398**, 887
- Ellison S. L., Patton D. R., Simard L., McConnachie A. W., 2008, *AJ*, **135**, 1877
- Elmegreen B. G., 2011, *ApJ*, **737**, 10
- Emerick A., Bryan G. L., Mac Low M.-M., 2019, *MNRAS*, **482**, 1304
- Eufrazio R. T., et al., 2017, *ApJ*, **851**, 10
- Evans Neal J. I., et al., 2009, *ApJS*, **181**, 321
- Federrath C., Banerjee R., Clark P. C., Klessen R. S., 2010, *ApJ*, **713**, 269
- Federrath C., Sur S., Schleicher D. R. G., Banerjee R., Klessen R. S., 2011, *ApJ*, **731**, 62
- Ferrière K. M., 2001, *Rev. Mod. Phys.*, **73**, 1031
- Fletcher A., Beck R., Shukurov A., Berkhuijsen E. M., Horellou C., 2011, *MNRAS*, **412**, 2396
- Fujimoto Y., Chevance M., Haydon D. T., Krumholz M. R., Kruijssen J. M. D., 2019, *MNRAS*, **487**, 1717
- Gatto A., et al., 2015, *MNRAS*, **449**, 1057
- Gatto A., et al., 2017, *MNRAS*, **466**, 1903
- Girichidis P., Konstantin L., Whitworth A. P., Klessen R. S., 2014, *ApJ*, **781**, 91
- Glover S. C. O., Clark P. C., 2012, *MNRAS*, **421**, 116
- Glover S. C. O., Mac Low M.-M., 2007a, *ApJS*, **169**, 239
- Glover S. C. O., Mac Low M.-M., 2007b, *ApJ*, **659**, 1317
- Gnat O., Ferland G. J., 2012, *ApJS*, **199**, 20
- Heiles C., 2001, *ApJ*, **551**, L105
- Hernandez X., Park C., Cervantes-Sodi B., Choi Y.-Y., 2007, *MNRAS*, **375**, 163
- Hernquist L., 1990, *ApJ*, **356**, 359
- Hill A. S., Mac Low M.-M., Gatto A., Ibáñez-Mejía J. C., 2018, *ApJ*, **862**, 55
- Hopkins P. F., Kereš D., Oñorbe J., Faucher-Giguère C.-A., Quataert E., Murray N., Bullock J. S., 2014, *MNRAS*, **445**, 581
- Hu C.-Y., Naab T., Walch S., Glover S. C. O., Clark P. C., 2016, *MNRAS*, **458**, 3528
- Hu C.-Y., Naab T., Glover S. C. O., Walch S., Clark P. C., 2017, *MNRAS*, **471**, 2151
- Inutsuka S.-i., Inoue T., Iwasaki K., Hosokawa T., 2015, *A&A*, **580**, A49
- Jefferson S. M. R., Kruijssen J. M. D., 2018, *MNRAS*, **476**, 3688
- Joshi P. R., Walch S., Seifried D., Glover S. C. O., Clarke S. D., Weis M., 2019, *MNRAS*, **484**, 1735
- Kainulainen J., Beuther H., Henning T., Plume R., 2009, *A&A*, **508**, L35
- Kannan R., Marinacci F., Simpson C. M., Glover S. C. O., Hernquist L., 2018, arXiv e-prints 1812.01614,
- Katz N., 1992, *ApJ*, **391**, 502
- Katz N., Weinberg D. H., Hernquist L., 1996, *ApJS*, **105**, 19
- Kennicutt Jr. R. C., 1989, *ApJ*, **344**, 685
- Kennicutt Jr. R. C., 1998, *ApJ*, **498**, 541
- Kim C.-G., Ostriker E. C., 2015, *ApJ*, **802**, 99
- Kim C.-G., Ostriker E. C., 2017, *ApJ*, **846**, 133
- Kimm T., Cen R., 2014, *ApJ*, **788**, 121
- Klessen R. S., 2000, *ApJ*, **535**, 869
- Klessen R. S., Glover S. C. O., 2016, in Gnedin N. Y., Glover S. C. O., Klessen R. S., Springel V., eds, *Saas-Fee Advanced Course Vol. 43, Star Formation in Galaxy Evolution: Connecting Numerical Models to Reality*. Springer-Verlag, Berlin Heidelberg, p. 85, doi:10.1007/978-3-662-47890-5\_2
- Klessen R. S., Hennebelle P., 2010, *A&A*, **520**, A17
- Kruijssen J. M. D., Schrubba A., Hygate A. P. S., Hu C.-Y., Haydon D. T., Longmore S. N., 2018, *MNRAS*, **479**, 1866
- Krumholz M. R., Dekel A., McKee C. F., 2012, *ApJ*, **745**, 69
- Krumholz M. R., et al., 2014, in Beuther H., Klessen R. S., Dullemond C. P., Henning T., eds, *Protostars and Planets VI*. U. of Arizona Press, Tucson, pp 243–266
- Krumholz M. R., Burkhardt B., Forbes J. C., Crocker R. M., 2018, *MNRAS*, **477**, 2716
- Larson R. B., Tinsley B. M., 1978, *ApJ*, **219**, 46
- Li Y., Mac Low M.-M., Klessen R. S., 2005, *ApJ*, **626**, 823
- Lonsdale C. J., Persson S. E., Matthews K., 1984, *ApJ*, **287**, 95
- Mac Low M.-M., Klessen R. S., 2004, *Rev. Mod. Phys.*, **76**, 125
- Maeder A., 2009, *Physics, Formation and Evolution of Rotating Stars*. Springer, Berlin Heidelberg, doi:10.1007/978-3-540-76949-1
- Martizzi D., Faucher-Giguère C.-A., Quataert E., 2015, *MNRAS*, **450**, 504
- McKee C. F., Ostriker J. P., 1977, *ApJ*, **218**, 148
- McKee C. F., Ostriker E. C., 2007, *ARA&A*, **45**, 565
- Mentuch Cooper E., et al., 2012, *ApJ*, **755**, 165
- Mihos J. C., Hernquist L., 1996, *ApJ*, **464**, 641
- Moreno J., Torrey P., Ellison S. L., Patton D. R., Bluck A. F. L., Bansal G., Hernquist L., 2015, *MNRAS*, **448**, 1107
- Nelson R. P., Langer W. D., 1997, *ApJ*, **482**, 796
- Oikawa S., Sofue Y., 2014, *PASJ*, **66**, 77
- Ostriker E. C., Shetty R., 2011, *ApJ*, **731**, 41
- Ostriker E. C., McKee C. F., Leroy A. K., 2010, *ApJ*, **721**, 975
- Pan H.-A., et al., 2018, *ApJ*, **868**, 132
- Peters T., et al., 2017, *MNRAS*, **466**, 3293
- Pettitt A. R., Tasker E. J., Wadsley J. W., Keller B. W., Benincasa S. M., 2017, *MNRAS*, **468**, 4189
- Pillepich A., et al., 2018, *MNRAS*, **473**, 4077
- Pineda J. L., et al., 2018, *ApJ*, **869**, L30
- Puerari I., Block D. L., Elmegreen B. G., Bournaud F., 2010, in Block D. L., Freeman K. C., Puerari I., eds, *Galaxies and their Masks*. p. 121 (arXiv:1008.1044), doi:10.1007/978-1-4419-7317-7\_10

- Rafikov R. R., 2001, *MNRAS*, **323**, 445
- Rahner D., Pellegrini E. W., Glover S. C. O., Klessen R. S., 2017, *MNRAS*, **470**, 4453
- Rahner D., Pellegrini E. W., Glover S. C. O., Klessen R. S., 2018, *MNRAS*, **473**, L11
- Rahner D., Pellegrini E. W., Glover S. C. O., Klessen R. S., 2019, *MNRAS*, **483**, 2547
- Renaud F., Bournaud F., Kraljic K., Duc P.-A., 2014, *MNRAS*, **442**, L33
- Renaud F., Bournaud F., Agertz O., Kraljic K., Schinnerer E., Bolatto A., Daddi E., Hughes A., 2019, *A&A*, **625**, A65
- Rots A. H., Bosma A., van der Hulst J. M., Athanassoula E., Crane P. C., 1990, *AJ*, **100**, 387
- Sanders D. B., Mirabel I. F., 1996, *ARA&A*, **34**, 749
- Schaye J., et al., 2015, *MNRAS*, **446**, 521
- Schinnerer E., et al., 2013, *ApJ*, **779**, 42
- Schmidt M., 1959, *ApJ*, **129**, 243
- Schruba A., Leroy A. K., Walter F., Sandstrom K., Rosolowsky E., 2010, *ApJ*, **722**, 1699
- Schruba A., et al., 2011, *AJ*, **142**, 37
- Schweizer F., 1977, *ApJ*, **211**, 324
- Shetty R., Ostriker E. C., 2012, *ApJ*, **754**, 2
- Shetty R., Kelly B. C., Rahman N., Bigiel F., Bolatto A. D., Clark P. C., Klessen R. S., Konstantin L. K., 2014a, *MNRAS*, **437**, L61
- Shetty R., Clark P. C., Klessen R. S., 2014b, *MNRAS*, **442**, 2208
- Simpson C. M., Bryan G. L., Hummels C., Ostriker J. P., 2015, *ApJ*, **809**, 69
- Smith R. J., Glover S. C. O., Clark P. C., Klessen R. S., Springel V., 2014, *MNRAS*, **441**, 1628
- Smith R. J., et al., 2019, *MNRAS*, in press
- Sofue Y., 1996, *ApJ*, **458**, 120
- Sormani M. C., Treß R. G., Klessen R. S., Glover S. C. O., 2017, *MNRAS*, **466**, 407
- Sormani M. C., Treß R. G., Ridley M., Glover S. C. O., Klessen R. S., Binney J., Magorrian J., Smith R., 2018, *MNRAS*, **475**, 2383
- Springel V., 2005, *MNRAS*, **364**, 1105
- Springel V., 2010, *MNRAS*, **401**, 791
- Springel V., Di Matteo T., Hernquist L., 2005, *MNRAS*, **361**, 776
- Stinson G., Seth A., Katz N., Wadsley J., Governato F., Quinn T., 2006, *MNRAS*, **373**, 1074
- Theis C., Spinnaker C., 2003, *Ap&SS*, **284**, 495
- Toomre A., Toomre J., 1972, *ApJ*, **178**, 623
- Torrey P., Cox T. J., Kewley L., Hernquist L., 2012, *ApJ*, **746**, 108
- Truelove J. K., Klein R. I., McKee C. F., Holliman II J. H., Howell L. H., Greenough J. A., 1997, *ApJ*, **489**, L179
- Vázquez-Semadeni E., 1994, *ApJ*, **423**, 681
- Vogelsberger M., et al., 2014, *MNRAS*, **444**, 1518
- Wada K., Norman C. A., 2001, *ApJ*, **547**, 172
- Walch S., et al., 2015, *MNRAS*, **454**, 238
- Wolfire M. G., Hollenbach D., McKee C. F., Tielens A. G. G. M., Bakes E. L. O., 1995, *ApJ*, **443**, 152

## APPENDIX A: RESOLUTION STUDY

Here we check how robust our results are as a function of the resolution. As described in Section 2.6 we run the simulations at two different resolutions (1000  $M_{\odot}$  and 300  $M_{\odot}$  per cell) and we stop the Jeans refinement at one order of magnitude lower densities for the low resolution case. In Fig. A1 we compare the SF and the ISM properties between the two cases. By looking at the SFRs we see that our main finding is rather resolution independent: the difference in stars formed between the isolated and the interacting case

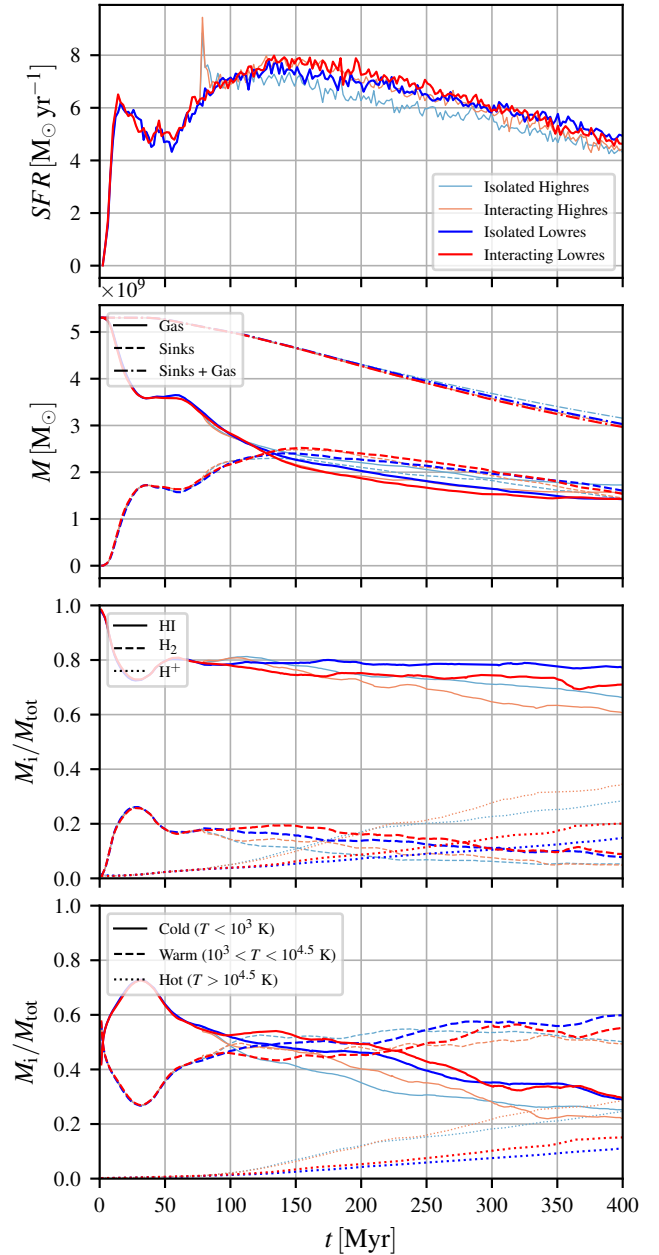


**Figure A1.** Comparison between the simulations at high and low resolution. Throughout the panels the simulations at high-resolution are shown in orange (interacting) and light-blue (isolated) while the isolated simulation at low-resolution is shown in blue and the interacting low-resolution simulation in red. In the top panel we compare the SF rates, in the second from top panel we depict the total gas mass (solid line), the mass in sink particles (dashed line) and the total mass of the two combined (dash-dotted line) as a function of time. The second to last panel shows the H I (solid line), H<sub>2</sub> (dashed line) and H<sup>+</sup> (dotted line) fractions as a function of time for the different runs. Finally we plot the cold ( $T < 10^3$  K), warm ( $10^3 < T < 10^{4.5}$  K) and hot ( $T > 10^{4.5}$  K) gas fractions in the bottom panel.

stays fairly low. Even the magnitude of the SFR is comparable between the low and the high resolution runs. Given the model used, this is an indication of numerical convergence, although even higher resolution is needed to give a complete interpretation. Unfortunately this is computationally out of reach at the moment as our high resolution runs were already stretching the limits of feasibility (each simulation at  $300 M_{\odot}$  per cell required a few months to run with approximately 512 cores).

The second panel shows the mass in sinks and the mass of gas in the simulations as a function of time. Once again, given our physical prescription, the behaviour seems numerically converged. The sinks formed in the low resolution simulation are in general more massive, but less numerous such that their total mass is similar to the high resolution case.

In the last two panels we look at the ISM. We do not account for the gas mass inside sink particles here since we are interested in comparing the properties of the actual simulated ISM. We note that in this case there is a quantitative difference between the simulations. In particular in the high resolution case more supernovae are actually resolved and the sharper interfaces between hot and cold gas cool less, so higher fractions of the hot ionised phase are reached at the expense of the warm phase. The difference in the molecular phase, on the other hand, is smaller between the two different resolutions. At lower resolutions the substructure of clouds is poorly resolved and GMCs are rather big blobs and as such better shielded from the surrounding interstellar radiation field. This allows for higher molecular fractions in the low resolution case.

Despite these quantitative differences, the impact of the interacting galaxy on the ISM properties stays unchanged and the picture described in the main text holds independently of resolution. The magnitude of the difference in the ISM phases induced by the interaction is the same for the simulations at different resolution and stays contained to less than 10 % throughout the computation in both cases.

This paper has been typeset from a  $\text{T}_{\text{E}}\text{X}/\text{L}^{\text{A}}\text{T}_{\text{E}}\text{X}$  file prepared by the author.



# Chapter 3

## Simulations of the star-forming molecular gas in an interacting M51-like galaxy: cloud population statistics

### 3.1 Statement about my contribution

- **Simulations:** this publication relies on the same simulation data produced for the publication presented in Chapter 2. The workload regarding code development, simulation setup, running the simulations and physical model is therefore shared between the two scientific papers.
- **Analysis:** my contribution was central. The analysis was driven by feedback and input from my collaborators.
- **Figures:** my contribution was central. I produced the figures autonomously, according to the planned analysis and scientific discussion. The process was iterative and input from my collaborators was essential.
- **Writing:** my contribution was central. I produced autonomously most of the text of the manuscript. The process was however iterative with major feedback from my collaborators.
- **Scientific discussion:** most of my collaborators contributed equally to the scientific discussion. However, my contribution was major and never passive.

# Simulations of the star-forming molecular gas in an interacting M51-like galaxy: cloud population statistics

Robin G. Treß,<sup>1\*</sup> Mattia C. Sormani,<sup>1</sup> Rowan J. Smith,<sup>2</sup> Simon C. O. Glover,<sup>1</sup>  
Ralf S. Klessen,<sup>1,3</sup> Mordecai-Mark Mac Low,<sup>4,5</sup> Paul Clark,<sup>6</sup> and Ana Duarte-Cabral<sup>6</sup>

<sup>1</sup>Universität Heidelberg, Zentrum für Astronomie, Institut für theoretische Astrophysik, Albert-Ueberle-Str. 2, 69120 Heidelberg, Germany

<sup>2</sup>Jodrell Bank Centre for Astrophysics, Department of Physics and Astronomy, University of Manchester, Oxford Road, Manchester M13 9PL, UK

<sup>3</sup>Universität Heidelberg, Interdisziplinäres Zentrum für Wissenschaftliches Rechnen, Im Neuenheimer Feld 205, 69120 Heidelberg, Germany

<sup>4</sup>Department of Astrophysics, American Museum of Natural History, 79th Street at Central Park West, New York, NY 10024, USA

<sup>5</sup>Center for Computational Astrophysics, Flatiron Institute, 162 Fifth Avenue, New York, NY 10010, USA

<sup>6</sup>School of Physics and Astronomy, Queen's Buildings, The Parade, Cardiff University, Cardiff, CF24 3AA, UK

Accepted 2021 June 09. Received 2021 June 08; in original form 2020 December 14

## ABSTRACT

To investigate how molecular clouds react to different environmental conditions at a galactic scale, we present a catalogue of giant molecular clouds resolved down to masses of  $\sim 10 M_{\odot}$  from a simulation of the entire disc of an interacting M51-like galaxy and a comparable isolated galaxy. Our model includes time-dependent gas chemistry, sink particles for star formation and supernova feedback, meaning we are not reliant on star formation recipes based on threshold densities and can follow the physics of the cold molecular phase. We extract giant molecular clouds from the simulations and analyse their properties. In the disc of our simulated galaxies, spiral arms seem to act merely as snowplows, gathering gas and clouds without dramatically affecting their properties. In the centre of the galaxy, on the other hand, environmental conditions lead to larger, more massive clouds. While the galaxy interaction has little effect on cloud masses and sizes, it does promote the formation of counter-rotating clouds. We find that the identified clouds seem to be largely gravitationally unbound at first glance, but a closer analysis of the hierarchical structure of the molecular interstellar medium shows that there is a large range of virial parameters with a smooth transition from unbound to mostly bound for the densest structures. The common observation that clouds appear to be virialised entities may therefore be due to CO bright emission highlighting a specific level in this hierarchical binding sequence. The small fraction of gravitationally bound structures found suggests that low galactic star formation efficiencies may be set by the process of cloud formation and initial collapse.

**Key words:** galaxies: ISM – ISM: clouds – ISM: structure – hydrodynamics – stars: formation – ISM: kinematics and dynamics

## 1 INTRODUCTION

Understanding the formation and dynamical evolution of the molecular phase in the interstellar medium (ISM) of galaxies is of fundamental importance for the study of star formation and galactic evolution, since it is within this phase that essentially all star formation occurs. Cooling in the molecular phase is efficient, and so it has low temperatures ( $T < 100$  K), and consequently a high density and low volume filling factor. A substantial fraction of the cold molecular phase is associated with giant molecular clouds (GMCs), as seen in

CO observations of our own Galaxy and others. The dynamical state of the molecular phase is still far from fully understood and, in particular, a comprehensive picture of GMCs in a galactic context is missing. The nature of the dynamical processes that shape the ISM can be revealed by a statistical analysis of star-forming molecular gas; the study of GMC properties and their connection with the local galactic environment therefore remains an active research topic.

A major point of debate is centred on the dynamical state of GMCs. It is still discussed whether they are in (or close to) virial equilibrium, or whether they are freely collapsing gravitationally bound objects instead. If they are merely emergent structures in the ISM turbulent cascade,

\* E-mail: robin.tress@uni-heidelberg.de

on the other hand, their properties would be set by the Mach number rather than a requirement of virial equilibrium (e.g. Krumholz & McKee 2005; Hennebelle & Chabrier 2011; Padoan & Nordlund 2011; Federrath & Klessen 2012; Burkhardt 2018). Furthermore, the importance of environmental conditions for their dynamical state remains a central question. Empirical scaling relations of GMC properties have given us important hints in this regard, but their interpretation can be affected by observational biases (Ballesteros-Paredes & Mac Low 2002).

Three important scaling relations were first described by Larson (1981): first, a power-law relation between the velocity dispersion  $\sigma$  (as measured from the linewidth) and the size  $R$  of a CO-emitting region; second, an almost one-to-one relation between the observed masses and inferred virial masses of GMCs; and, third, a constant mass surface density of the analysed clouds.

The validity of these scaling relations has been challenged both in the local environment and in extragalactic targets with different environmental conditions. Most observations do find a correlation between the size and the linewidth, but there seems to be no agreement for the power-law exponent and all observations find large uncertainties in the slope (Imara et al. 2020; Duarte-Cabral et al. 2020). Moreover the third Larson relation is likely to be an artefact produced by the limited dynamical range of early observations of column density, and the sample of observed clouds being located in similar environmental conditions. Several studies have indeed confirmed that surface densities of GMCs can span over two orders of magnitude (Heyer et al. 2009; Hughes et al. 2010, 2013; Leroy et al. 2015; Duarte-Cabral et al. 2020) though other surveys still find confirmation of the third Larson relation (Lombardi et al. 2010).

If we assume that GMCs are virialised objects (i.e. that the second Larson relation holds), then the first Larson relation  $\sigma \propto R^{1/2}$  naturally follows, which implies that the first two Larson relations are in fact not independent. However, if we acknowledge that the mass surface density varies among GMCs, then the constant of proportionality of the linewidth-size relation has a dependency on the surface density  $\Sigma$ . This correction to the first Larson law is summarised in the Heyer (2009) relation

$$\sigma/R^{1/2} \propto \Sigma^{1/2}. \quad (1)$$

While the dependence on  $\Sigma$  is generally acknowledged, GMCs seem to lie above the line predicted for clouds in self-gravitating virial equilibrium. Clouds in free-fall collapse naturally develop velocity dispersions that are close to, but slightly larger than, the virial equilibrium values (Ballesteros-Paredes et al. 2011), and these velocities have the same functional dependence on  $\Sigma$ . Therefore, while clouds internal motions are normally assumed to oppose gravitational collapse, this interpretation is not unique, as inward collapse motions give a similar signature. The set of molecular clouds formed in the self-gravitating MHD simulations of Ibáñez-Mejía et al. (2016), for instance, are mainly gravitationally bound but still recover the observed velocity dispersion relations.

We also have to consider that GMCs are not isolated objects, and their environment could play an important role in confining the clouds. The tendency of observed clouds

to be mainly gravitationally unbound when a virial analysis is performed could be explained by an external pressure confining force which, when considered, retrieves virial stability (Field et al. 2011; Duarte-Cabral & Dobbs 2017). This would give the size-linewidth scaling relation an additional dependency on external pressure and prove the importance of galactic environment for GMC dynamics.

But again, it is not obvious that virialised structures should be expected from a turbulent gas flow. For instance, the energies of colliding streams that generate molecular structures (Ballesteros-Paredes et al. 1999) may be unrelated to the gravitational energy of the gas involved, since the former will be driven by external galactic phenomena. However, given the short dynamical times of the ISM these structures could virialise quickly. Moreover the energies within the turbulent cascade are not completely unrelated to the mass of GMCs but to some extent coupled through feedback processes.

Conditions leading to cloud formation could in general promote structures that are preferentially gravitationally unbound (Dobbs et al. 2011). This could justify the low star formation efficiency of the dense ISM (Kauffmann et al. 2013) without having to invoke internal feedback processes to disperse the cloud (e.g. Federrath 2015).

The universality of GMC properties and their environmental dependence is crucial to resolve these controversies and to understand the dynamics regulating the molecular gas. Retrieving cloud statistics for extragalactic sources is technically challenging, but now achievable in the ALMA era. The first Larson relation in its original form is retrieved in NGC300 (Faesi et al. 2018), but in the case of M51, no or only a weak size-linewidth correlation was found with large scatter (Colombo et al. 2014). Hughes et al. (2013) also find differences in cloud properties among M33, M51 and the LMC. These studies suggest that GMC properties are unlikely to be universal, and must hide a more complex dependence on other factors.

In the case of the Milky Way we now have a set of excellent molecular gas tracer surveys (e.g. SEDIGISM, Schuller et al. 2017; CHIMPS, Rigby et al. 2019; COHRS, Dempsey et al. 2013) but no agreement is reached for the first Larson and the Heyer relation. The trends are observed, but the scatter is large, and different surveys reach different conclusions for the exponents. Within the disc no strong variations of GMC properties in relation to the position in the disc are observed (Duarte-Cabral et al. 2020).

In external galaxies, on the other hand, there can be significant differences depending on the positions of the clouds. Braine et al. (2018) find a radial dependence of properties in M33, confirmed by dedicated simulations (Dobbs et al. 2019), and link the variation to global galactic properties such as mass surface density rather than to local feedback processes. In contrast, differences found between arm and inter-arm clouds in M51 are often attributed to stellar feedback and the presence of galactic spirals (Colombo et al. 2014). The centres of galaxies seem to be a particularly interesting location for cloud dynamics.

Sun et al. (2020) find that in 70 nearby galaxies the GMCs in the central regions (and in particular in barred galaxies) have higher velocity dispersion. They also see a moderate difference in surface density, velocity dispersion, turbulent pressure and virial parameters between arm and

inter-arm clouds, but the scatter is large. In our own Galaxy, clouds in the centre seem to exhibit larger line-widths suggesting larger turbulent driving which [Shetty et al. \(2012\)](#) suggest could be due to larger star formation, environmental densities and pressures with respect to the local ISM.

Interactions and galaxy mergers could also potentially affect the properties of the cold molecular gas. [Pettitt et al. \(2018\)](#) find that clouds in a simulated interacting galaxy are generally more massive and have higher velocity dispersion than in an isolated one. As the tidal interaction induces the formation of spiral arms, the smaller clumps seen in the isolated disc cluster when they enter the arm to form larger mainly unbound clouds.

One major barrier to disentangling the contrasting results of different GMC studies is the definition of a GMC itself. Thanks to the self-shielding property of  $\text{H}_2$ , the molecular phase of the ISM organises itself into structures with relatively sharp boundaries in terms of density, temperature and chemical state. This has led many authors to study the molecular ISM in terms of distinct clouds. Of course this is an oversimplification, and the real molecular phase exhibits a rich and complex morphology as the GMCs interact, merge, aggregate and dissipate.

Nevertheless, it remains useful to be able to partition the molecular phase into discrete structures. Many different segmentation schemes have been developed, each having their own strengths and weaknesses (e.g. [Stutzki & Güsten 1990](#); [Williams et al. 1995](#); [Rosolowsky & Leroy 2006](#)). One must bear in mind that the definition of such structures cannot be unique and universal due to the complexity of the molecular ISM. Defining cloud boundaries can vary with the algorithmic approach used and can be artificial when trying to examine the global structure of the molecular phase. Scaling relations such as the first Larson relation in its original form are scale invariant and as such less sensitive to cloud definition. But properties like the cloud mass or virial parameter strongly depend on the cloud definition, which could produce artefacts and spurious results. Even with a consistent use of a specific cloud identification method, bias could arise in different ways, for example because of different environmental conditions. These could lead to crowding, which is a difficult problem for any segmentation method. Moreover resolution is key for these schemes and different beam sizes would lead to different structure identifications.

This problem is acknowledged in the literature, and we argue that despite the usefulness of defining discrete objects, these studies need to be augmented with a more general method, such as an analysis of the hierarchical structure of the ISM that describes molecular gas properties as a function of iso-(column)density levels (as suggested for instance by [Hughes et al. 2013](#)). This would not put particular emphasis on special scales and be less dependent on resolution and environmental conditions. Together with a cloud finding method this would give the most descriptive view of the molecular phase.

In this work, we aim to improve our general comprehension of GMCs by performing simulations of the molecular gas in an interacting M51-like galaxy and studying cloud statistics. We identify and study individual clouds but we also use a dendrogram analysis ([Rosolowsky et al. 2008](#); [Goodman et al. 2009](#); [Colombo et al. 2015](#)) to identify structure at all levels. We focus in particular on the variation of cloud

population properties in different environments and on the comparison of an interacting to an isolated galaxy. In Section 2 we summarize the galaxy models we use from [Tress et al. \(2020a\)](#) and describe the dendrogram analysis and how we identify clouds. In Section 3 we present the derived properties of our identified structures. We further discuss their dependence on galactic location and environment in Section 4, discuss the implications of missing physics in our simulations in Section 5 and we summarize and conclude in Section 6.

## 2 METHODS

### 2.1 Setup and simulations

An in-depth description of the setup and the simulation details can be found in [Tress et al. \(2020a\)](#). Here we briefly summarise the most important features which are relevant for a clear and self-contained understanding of this manuscript.

The simulations were performed in order to study how the dense molecular phase of the ISM responds to galactic-scale events such as a galaxy interaction. We took the M51 galaxy system as a template and our initial conditions were chosen so that at the end of the simulations we roughly reproduce the properties of this interacting galaxy. The model of the main galaxy comprises a dark matter halo, a stellar bulge and disc, and a gaseous disc. All these components and their mutual gravitational interactions are self-consistently evolved by the code throughout the simulation. The companion galaxy, on the other hand, is represented by a single massive collisionless particle.

We use the AREPO code ([Springel 2010](#)) to evolve the system in time, finding gravitational forces by solving the Poisson equation and, for the gas, solving the unmagnetised, hydrodynamic equations, including the energy equation. We include the major physical ingredients thought responsible for shaping and controlling the life-cycle of GMCs. In particular, we include a non-equilibrium chemical network which is able to trace the hydrogen chemistry as well as a simple treatment for the formation and destruction of CO ([Glover & Clark 2012](#)). To do so we require information about the local non-ionizing UV interstellar radiation field that can photo-dissociate  $\text{H}_2$  and CO. We assume a constant background radiation field and estimate the local shielding by computing for each cell the foreground column densities of the gas with the TREECOL algorithm ([Clark et al. 2012](#)). Radiative and chemical heating and cooling of the gas is followed as described in [Clark et al. \(2019\)](#).

Jeans unstable regions inside GMCs will gravitationally collapse leading to star formation. We abstract the late stages of collapse by employing accreting sink particles that are described in detail in [Tress et al. \(2020a\)](#). Briefly, on each hydrodynamical timestep, we flag as candidates for sink particle formation all active cells<sup>1</sup> that are above a pre-chosen density threshold, taken in these simulations to be  $\rho_{\text{th}} = 10^{-21} \text{ g cm}^{-3}$ . In order to actually form a sink, however,

<sup>1</sup> By default, AREPO uses a hierarchical time-stepping scheme and so only a subset of cells are updated on any given timestep. Cells that are updated on the current timestep are termed active cells.

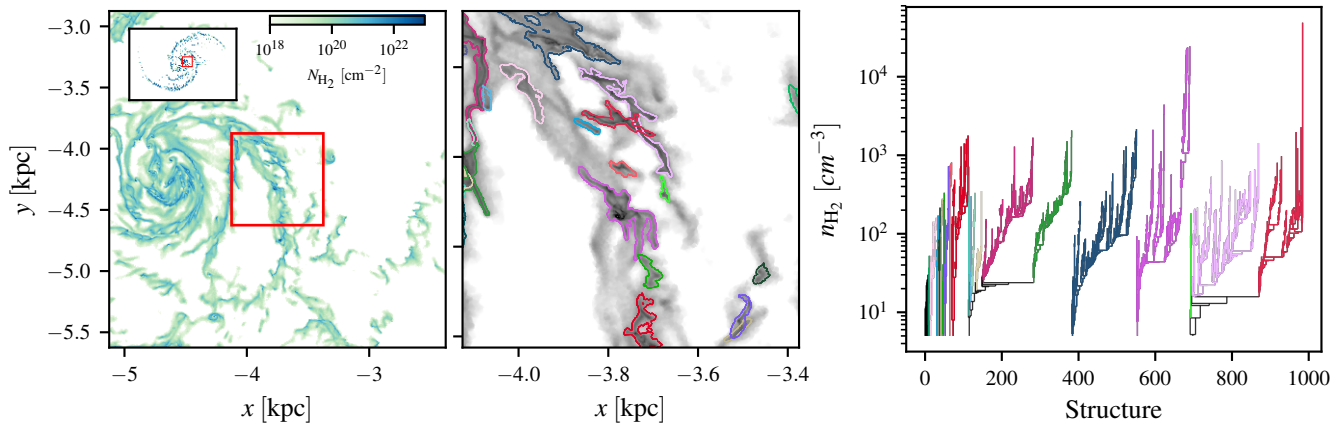


**Figure 1.** A region of the simulations in which we applied the cloud-finding method. In the left-hand panel we show the selected region (*red rectangle*) in the larger galactic context. The region of the left-hand panel is shown in reference to the whole galaxy in the small box in the top-left corner of the left panel. The dendrogram decomposition of this region is shown in the *right-hand panel*. SCIMES then performs the segmentation and each different structure found is highlighted with a different colour. The location of these structures in the region studied is shown in the middle panel.

**Table 1.** Average and median properties of the cloud population of the interacting simulation at  $t = 217$  Myr.

	Mass ( $M_{\odot}$ )	Size (pc)	$\sigma_{1D}$ ( $\text{km s}^{-1}$ )	$\alpha_{\text{vir}}$	$j$ ( $\text{km s}^{-1} \text{pc}$ )
Average	$6.45 \times 10^4$	17.4	5.09	22.1	$1.13 \times 10^2$
Median	$1.99 \times 10^4$	16.0	2.56	6.46	27.7

the candidate cells must pass a series of additional checks: they must be at a local minimum in the gravitational potential, the gas surrounding them must be gravitationally bound and converging, and they must not lie within the accretion radius of an existing sink particle. Cells that pass all of these checks are converted to collisionless sink particles with the same mass and momentum. Cells that have densities  $\rho > \rho_{\text{th}}$  but that lie within the accretion radius of an existing sink particle cannot form new sink particles. Instead, we check to see whether the gas in the cell is gravitationally bound to the sink. If it is, we remove enough mass from the cell to reduce its density to  $\rho_{\text{th}}$  and add this mass to the sink. Cells that lie within the accretion radius of multiple sinks give their gas to the sink to which they are most strongly bound. In the simulations analyzed in this paper, we adopt a sink accretion radius  $r_{\text{acc}} = 2.5$  pc and use the same value for the gravitational softening length of the sink. The gravitational softening length of the gas cells is adjusted adaptively as described in [Springel \(2010\)](#) so that it always roughly matches the cell size.

We assume that 5% of the accreted gas is converted into stars. This mass is then used to populate a Kroupa initial mass function ([Kroupa 2001](#)) using the method described in [Sormani et al. \(2017\)](#). Based on the number of massive stars formed, we can attribute feedback coming from the sink particle, which represents a small young stellar cluster. We consider only SN feedback, neglecting ionization, stellar winds, or protostellar jets. At the end of the life-time of each massive star we create an SN event around the sink. This injects energy as well as returning the part of the sink mass that was not involved in the SF back into the ISM.

In terms of resolution we set a base mass for the gas

cells of  $300 M_{\odot}$  but require that the Jeans length is always resolved by a minimum of four cells. This means that a cell will be refined if it has a mass greater than twice its base mass, or if the Jeans length is smaller than four times the cell diameter, whichever condition is more stringent. This grants us sub-parsec resolution inside of the GMCs and highest mass resolutions of about  $10 M_{\odot}$  (see Figure 3 of [Tress et al. 2020a](#)).

The same physical setup, but with a sink particle formation density threshold of  $\rho_{\text{th}} = 10^{-20} \text{ g cm}^{-3}$  was successfully used in [Tress et al. \(2020b\)](#) and [Sormani et al. \(2020\)](#) to study gas dynamics and star formation in the Central Molecular Zone of our Galaxy.

Along with the interacting M51-like galaxy, we also performed a simulation of the system in isolation. The same simulation was used to address the effect of the galactic encounter on the ISM properties by [Tress et al. \(2020a\)](#).

## 2.2 Cloud identification

To identify clouds in our simulations, we make use of the dendrogram-based scheme SCIMES ([Colombo et al. 2015](#)). In its most general form, a dendrogram is a tree diagram indicating the hierarchical relationship between objects. Dendrograms are used in many different fields of science, with their use in astronomy being popularised by [Rosolowsky et al. \(2008\)](#) and [Goodman et al. \(2009\)](#). Here, we use them to represent the relationship between different isodensity contours in the molecular ISM. Local density maxima are identified as the leaves of the dendrogram (i.e. structures at the top of the tree that enclose no further substructures). Isodensity contours corresponding to lower density values enclose multiple leaves and are called branches of the dendrogram. To construct our dendrogram, we use a set of  $\text{H}_2$  isodensity contours that starts at a minimum density of  $n_{\text{H}_2, \text{min}} = 1 \text{ cm}^{-3}$  and that has a spacing of  $\Delta n_{\text{H}_2} = 5 \text{ cm}^{-3}$  between contours. An example of the resulting dendrogram decomposition of a small sub-region of the simulation is shown in the right-hand panel of Figure 1.

ID	$M_{\text{cloud}}$ ( $M_{\odot}$ )	Volume ( $\text{pc}^3$ )	$M_{\text{sink gas}}$ ( $M_{\odot}$ )	$\alpha_{\text{vir}}$	$(x, y, z)$ (kpc)	$(v_x, v_y, v_z)$ ( $\text{km s}^{-1}$ )	$(\sigma_x, \sigma_y, \sigma_z)$ ( $\text{km s}^{-1}$ )	$(\sigma_{\text{rot},x}, \sigma_{\text{rot},y}, \sigma_{\text{rot},z})$ ( $\text{km s}^{-1}$ )	$(j_x, j_y, j_z)$ ( $\text{km s}^{-1} \text{ pc}$ )	$\Omega$ ( $\text{Myr}^{-1}$ )	Location
1320	$5.8 \cdot 10^3$	$7.7 \cdot 10^3$	–	50.4	(-5.990, -8.738, 6.850)	(196.1, -140.8, 73.3)	(3.2, 4.3, 3.1)	(0.8, 0.4, 1.8)	(-23.4, 1.3, -8.8)	$2.9 \cdot 10^{-1}$	I
1755	$3.7 \cdot 10^4$	$6.7 \cdot 10^4$	$5.1 \cdot 10^3$	13.7	(-4.861, -11.306, 6.851)	(218.8, 9.4, 78.8)	(3.8, 3.3, 3.3)	(1.2, 1.3, 2.1)	(-34.8, 23.6, 47.2)	$4.7 \cdot 10^{-1}$	I
1459	$2.4 \cdot 10^4$	$2.7 \cdot 10^4$	$4.7 \cdot 10^3$	9.5	(-5.666, 1.382, 7.330)	(-179.8, -128.6, 52.4)	(1.9, 3.3, 3.0)	(1.2, 0.1, 1.3)	(10.9, 24.6, 11.9)	$5.0 \cdot 10^{-1}$	A
2152	$7.0 \cdot 10^4$	$3.5 \cdot 10^4$	–	45.3	(-3.711, -9.993, 6.880)	(207.1, 47.1, 100.7)	(10.0, 10.5, 6.3)	(5.8, 6.5, 2.0)	(-101.5, 20.2, 193.7)	$1.7 \cdot 10^{-1}$	A
655	$5.2 \cdot 10^4$	$3.3 \cdot 10^4$	–	7.3	(-8.100, -9.641, 6.803)	(141.3, -197.2, 68.5)	(2.7, 3.7, 3.1)	(0.7, 0.9, 3.3)	(115.9, -70.9, 6.2)	$2.2 \cdot 10^{-1}$	I
1226	$4.8 \cdot 10^4$	$4.2 \cdot 10^4$	$3.3 \cdot 10^4$	2.5	(-6.331, 0.895, 7.386)	(-172.6, -159.1, 52.5)	(2.8, 2.2, 1.6)	(1.6, 0.9, 1.0)	(-11.6, 37.6, -49.2)	$7.8 \cdot 10^{-1}$	A
184	$9.7 \cdot 10^3$	$9.9 \cdot 10^3$	–	2.1	(-12.684, -10.532, 6.033)	(126.5, -215.3, 99.2)	(0.5, 0.8, 1.2)	(0.1, 0.3, 0.3)	(-2.2, -1.7, 2.0)	$8.7 \cdot 10^{-1}$	A
2504	$1.3 \cdot 10^4$	$9.1 \cdot 10^3$	–	38.4	(-2.335, -2.124, 7.276)	(-143.2, 181.3, 96.6)	(3.9, 4.9, 4.7)	(2.4, 2.6, 1.8)	(-9.8, 15.0, 33.5)	$1.3 \cdot 10^{-1}$	A
1634	$2.5 \cdot 10^4$	$2.3 \cdot 10^4$	$2.3 \cdot 10^4$	6.5	(-5.255, 1.280, 7.768)	(-152.1, -90.9, 49.3)	(2.9, 2.9, 3.3)	(0.9, 0.7, 1.3)	(-10.3, 14.1, 0.7)	$3.6 \cdot 10^{-1}$	A
1651	$2.7 \cdot 10^4$	$2.3 \cdot 10^4$	–	1.0	(-5.185, 1.347, 7.729)	(-156.6, -91.8, 43.6)	(1.0, 0.7, 1.0)	(0.4, 0.3, 0.1)	(0.2, 2.3, -7.4)	$1.4 \cdot 10^0$	A
1887	$1.4 \cdot 10^4$	$1.3 \cdot 10^4$	$4.1 \cdot 10^3$	4.0	(-4.382, -10.684, 6.766)	(212.0, 61.7, 96.0)	(1.1, 0.9, 2.4)	(0.3, 0.6, 1.3)	(6.7, 14.4, -6.5)	$4.8 \cdot 10^{-1}$	A
524	$3.2 \cdot 10^5$	$2.0 \cdot 10^5$	$1.2 \cdot 10^5$	3.8	(-8.517, -12.011, 6.462)	(179.2, -98.0, 74.0)	(6.2, 5.4, 2.4)	(1.2, 3.2, 0.9)	(-1.1, -7.7, 212.2)	$8.1 \cdot 10^{-1}$	A
1664	$2.9 \cdot 10^4$	$2.1 \cdot 10^4$	$3.7 \cdot 10^3$	0.8	(-5.132, 1.379, 7.772)	(-157.1, -87.4, 44.4)	(0.7, 1.0, 1.1)	(0.1, 0.3, 0.2)	(-4.6, -1.2, 5.7)	$9.5 \cdot 10^{-1}$	A
2173	$7.8 \cdot 10^4$	$6.5 \cdot 10^4$	–	7.6	(-3.661, -7.873, 7.036)	(246.3, -19.9, 84.1)	(3.3, 4.5, 2.5)	(2.6, 1.5, 3.3)	(-96.9, -92.1, 67.1)	$4.4 \cdot 10^{-1}$	I
826	$3.4 \cdot 10^3$	$3.4 \cdot 10^3$	–	19.0	(-7.567, -11.220, 6.470)	(219.4, -61.1, 117.8)	(1.9, 2.6, 0.8)	(0.4, 0.3, 0.2)	(-1.0, -2.5, 1.5)	$6.6 \cdot 10^{-1}$	I
1378	$1.3 \cdot 10^4$	$1.3 \cdot 10^4$	–	7.5	(-5.857, -8.609, 6.883)	(204.8, -135.4, 77.8)	(1.6, 2.6, 1.0)	(0.1, 0.1, 0.1)	(0.8, 0.4, 1.8)	$1.6 \cdot 10^0$	I
464	$1.6 \cdot 10^4$	$1.3 \cdot 10^4$	–	24.1	(-8.854, -2.928, 6.884)	(-83.3, -274.9, 72.2)	(4.5, 2.6, 3.9)	(0.7, 0.2, 2.3)	(-7.2, 34.6, -3.4)	$3.6 \cdot 10^{-1}$	I
243	$2.5 \cdot 10^4$	$2.3 \cdot 10^4$	–	12.5	(-12.152, -10.708, 5.971)	(118.4, -182.5, 76.3)	(2.6, 3.4, 3.2)	(1.7, 0.8, 0.5)	(-20.9, 35.2, 19.3)	$6.6 \cdot 10^{-1}$	A
3121	$3.7 \cdot 10^4$	$3.6 \cdot 10^4$	$1.1 \cdot 10^4$	3.3	(1.228, 3.166, 8.774)	(-105.1, 109.8, 73.7)	(1.4, 1.6, 2.7)	(1.4, 1.5, 1.5)	(30.7, -16.0, -17.8)	$2.3 \cdot 10^{-1}$	A
2857	$2.5 \cdot 10^5$	$1.8 \cdot 10^5$	$7.7 \cdot 10^4$	3.6	(-1.200, 3.117, 8.541)	(-152.3, 35.9, 72.4)	(3.1, 5.2, 4.2)	(0.3, 3.6, 1.3)	(-230.0, -61.5, 153.2)	$7.5 \cdot 10^{-1}$	A
3228	$1.1 \cdot 10^4$	$1.1 \cdot 10^4$	–	16.7	(3.253, 2.583, 9.165)	(-72.4, 163.3, 89.3)	(1.6, 3.0, 3.2)	(1.2, 0.7, 0.5)	(16.1, 21.1, 13.2)	$8.0 \cdot 10^{-1}$	A
360	$3.6 \cdot 10^3$	$2.0 \cdot 10^3$	–	21.3	(-10.205, -11.180, 6.065)	(191.6, -136.6, 99.3)	(2.1, 1.7, 2.9)	(0.3, 1.9, 1.1)	(7.8, 1.6, -7.6)	$1.3 \cdot 10^{-1}$	A
307	$7.9 \cdot 10^3$	$1.4 \cdot 10^4$	–	3.6	(-11.512, -11.342, 6.458)	(152.2, -196.5, 89.3)	(1.1, 1.0, 0.8)	(0.1, 0.4, 0.4)	(5.0, 0.6, -0.1)	$7.8 \cdot 10^{-1}$	A
2008	$1.5 \cdot 10^4$	$1.7 \cdot 10^4$	–	36.7	(-3.997, 2.281, 7.716)	(-193.2, -46.5, 63.6)	(1.4, 6.7, 2.5)	(1.1, 1.2, 0.9)	(8.0, -1.8, 17.9)	$3.2 \cdot 10^{-1}$	A
464	$1.6 \cdot 10^4$	$1.3 \cdot 10^4$	–	24.1	(-8.854, -2.928, 6.884)	(-83.3, -274.9, 72.2)	(4.5, 2.6, 3.9)	(0.7, 0.2, 2.3)	(-7.2, 34.6, -3.4)	$3.6 \cdot 10^{-1}$	I
1174	$3.8 \cdot 10^4$	$2.2 \cdot 10^4$	–	1.8	(-6.483, 0.556, 7.342)	(-145.3, -180.3, 46.5)	(1.3, 1.6, 1.5)	(1.1, 0.3, 0.6)	(11.2, -13.5, 30.3)	$5.7 \cdot 10^{-1}$	A
2636	$1.0 \cdot 10^4$	$1.2 \cdot 10^4$	–	14.4	(-1.836, -3.859, 7.087)	(-22.2, 153.3, 82.4)	(2.0, 3.2, 1.3)	(0.3, 0.2, 0.5)	(5.6, 2.4, -2.1)	$8.7 \cdot 10^{-1}$	A
357	$2.7 \cdot 10^4$	$2.5 \cdot 10^4$	–	7.0	(-10.320, -11.178, 5.924)	(184.9, -129.5, 102.2)	(0.9, 3.2, 2.4)	(0.8, 2.2, 1.6)	(21.5, 21.8, 14.0)	$2.2 \cdot 10^{-1}$	A
544	$3.2 \cdot 10^4$	$2.4 \cdot 10^4$	$1.6 \cdot 10^4$	2.0	(-8.447, -9.545, 6.876)	(130.8, -228.7, 76.5)	(1.9, 1.6, 1.7)	(0.9, 0.7, 1.0)	(-12.7, -13.3, 23.3)	$6.0 \cdot 10^{-1}$	I
1783	$1.4 \cdot 10^4$	$2.3 \cdot 10^4$	–	23.0	(-4.724, -11.095, 6.835)	(193.0, 22.8, 52.4)	(3.5, 1.3, 4.0)	(0.4, 0.3, 0.2)	(-2.1, -8.9, 2.8)	$1.1 \cdot 10^0$	A
1896	$1.4 \cdot 10^3$	$1.1 \cdot 10^2$	–	93.6	(-4.326, -7.866, 6.956)	(238.8, -38.9, 62.5)	(4.8, 4.8, 4.8)	(3.6, 1.0, 3.0)	(0.9, -7.0, -0.1)	$1.8 \cdot 10^{-2}$	I
1083	$5.3 \cdot 10^5$	$6.6 \cdot 10^5$	$2.3 \cdot 10^4$	39.9	(-6.701, -6.396, 6.848)	(189.5, -177.3, 98.3)	(11.8, 22.2, 4.5)	(5.6, 12.7, 2.2)	(151.9, -269.1, 1815.6)	$5.9 \cdot 10^{-1}$	A
1495	$3.0 \cdot 10^4$	$5.6 \cdot 10^4$	–	20.8	(-5.602, -3.857, 7.127)	(-46.7, -207.7, 59.6)	(4.6, 4.0, 2.3)	(2.3, 1.1, 0.6)	(15.3, -7.1, 85.2)	$5.3 \cdot 10^{-1}$	C
2332	$1.1 \cdot 10^4$	$1.2 \cdot 10^4$	–	20.6	(-3.099, -5.857, 7.140)	(52.8, 93.2, 83.5)	(4.8, 1.5, 0.8)	(0.4, 0.7, 0.3)	(0.4, -2.9, 10.5)	$6.7 \cdot 10^{-1}$	A
1650	$1.9 \cdot 10^4$	$1.2 \cdot 10^4$	–	21.2	(-5.188, -10.636, 6.648)	(210.2, 55.8, 126.1)	(2.3, 6.2, 1.7)	(2.2, 2.5, 0.4)	(5.8, 4.2, -42.4)	$2.3 \cdot 10^{-1}$	A
1092	$5.2 \cdot 10^4$	$2.8 \cdot 10^4$	$3.3 \cdot 10^4$	10.0	(-6.681, -3.248, 7.046)	(-54.0, -212.0, 51.7)	(4.4, 5.4, 4.9)	(1.2, 1.7, 1.3)	(12.0, -28.9, -51.0)	$5.7 \cdot 10^{-1}$	A
146	$1.0 \cdot 10^4$	$1.4 \cdot 10^4$	–	37.8	(-13.100, -10.330, 6.136)	(113.5, -234.8, 96.2)	(4.9, 1.4, 3.9)	(2.9, 1.4, 2.4)	(-8.5, -33.9, -5.8)	$1.3 \cdot 10^{-1}$	A
7	$8.7 \cdot 10^3$	$8.3 \cdot 10^3$	–	13.8	(-17.271, -2.892, 4.895)	(-49.6, -232.1, 80.4)	(2.8, 2.4, 1.4)	(0.9, 1.0, 0.4)	(-4.9, 0.3, -10.3)	$3.5 \cdot 10^{-1}$	A
2668	$3.7 \cdot 10^4$	$2.1 \cdot 10^4$	–	5.1	(-1.714, -8.157, 7.040)	(165.5, 183.2, 87.0)	(3.0, 1.7, 2.4)	(1.4, 0.7, 1.3)	(24.7, 19.4, 9.1)	$4.5 \cdot 10^{-1}$	A
1168	$2.9 \cdot 10^4$	$1.3 \cdot 10^4$	–	8.8	(-6.491, -12.081, 6.616)	(196.4, -60.3, 74.6)	(1.1, 5.1, 1.0)	(1.8, 3.6, 1.0)	(11.6, 4.9, 36.9)	$1.4 \cdot 10^{-1}$	A

Table 2: Properties of a sub-sample of the molecular clouds found in the interacting simulated galaxy. In order from left to right we show the clouds identification number, mass, volume, mass of gas which is trapped in sink particles contained within the cloud if present, virial parameter, centre of mass position, velocity of the centre of mass, velocity dispersion, velocity dispersion coming from rotation, specific angular momentum, angular velocity and the type of cloud where A, I, C indicate clouds associated with the arms, inter-arms and centre respectively. The complete catalogue is provided in machine readable form as supplemental material.

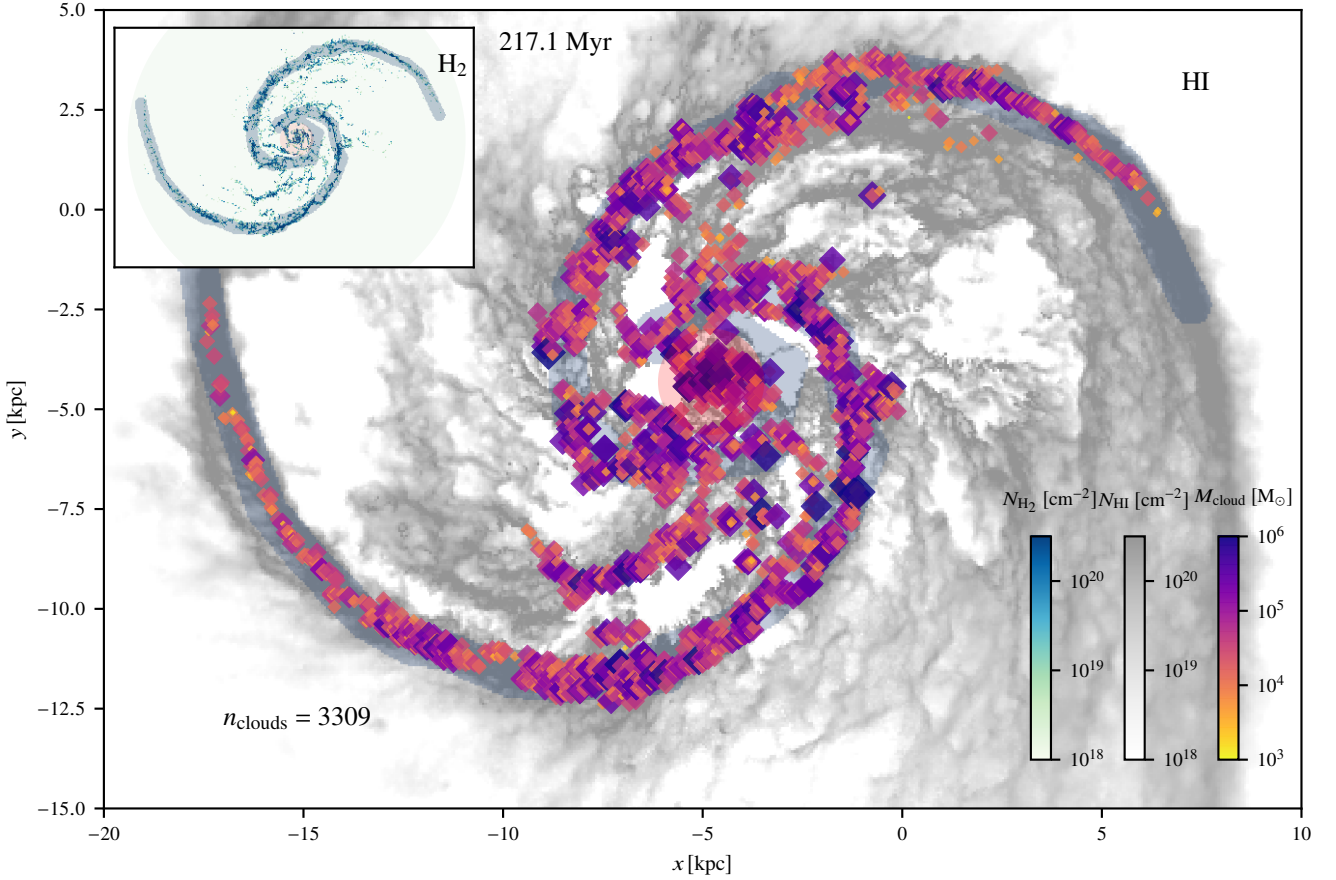


**Figure 2.** Positions of all the clouds found by the algorithm. The colour and the size of each marker is logarithmically related to the mass of the cloud. We also show the background HI column density (*gray-scale colour map*). On the *top left insert* we show the molecular hydrogen column density map. Clouds can be associated with spiral arms, (*dark blue shaded region*), with the inter-arm region (*unshaded region*) or with the nucleus (*red shaded region*).

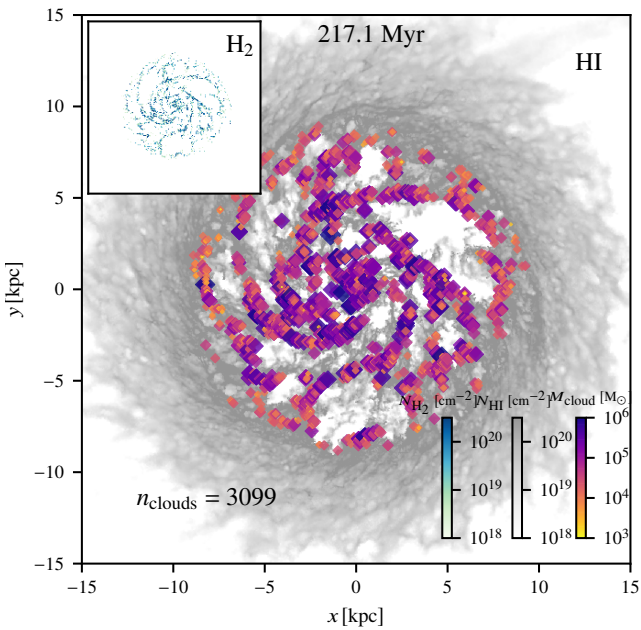


**Figure 3.** Same as Figure 2 but for the isolated galaxy.

Given the dendrogram decomposition of the  $H_2$  density field, we then use the SCIMES algorithm to segment it into a set of discrete structures. SCIMES is a spectral clustering technique that groups the leaves of the dendrogram into clusters according to their similarity, as assessed by a set of user-supplied similarity criteria. In the present case, we use the volume and the mass of structures in the dendrogram as input properties for SCIMES. This means that in general if there is an abrupt change in mass and volume while walking the dendrogram, the code will identify this location in the graph as the point at which to perform the segmentation.

In the dendrogram shown in Figure 1, the different clusters identified by SCIMES are highlighted with different colours. We identify each of these clusters as a distinct molecular cloud. The locations of these clouds in the  $x$ - $y$  plane are shown in the middle panel of Figure 1, overlaid on a projection of the  $H_2$  column density in this sub-region of the galaxy. We see that the clouds identified by SCIMES correspond to regions with high  $H_2$  column densities, as one would expect. In addition, we also see that there is a spatially extended distribution of low column density  $H_2$  surrounding many of the clouds that is not associated by SCIMES with a particular molecular cloud. This mostly corresponds to cold, neutral atomic gas with a low but non-zero  $H_2$  fraction. These envelopes surrounding GMCs were identified as

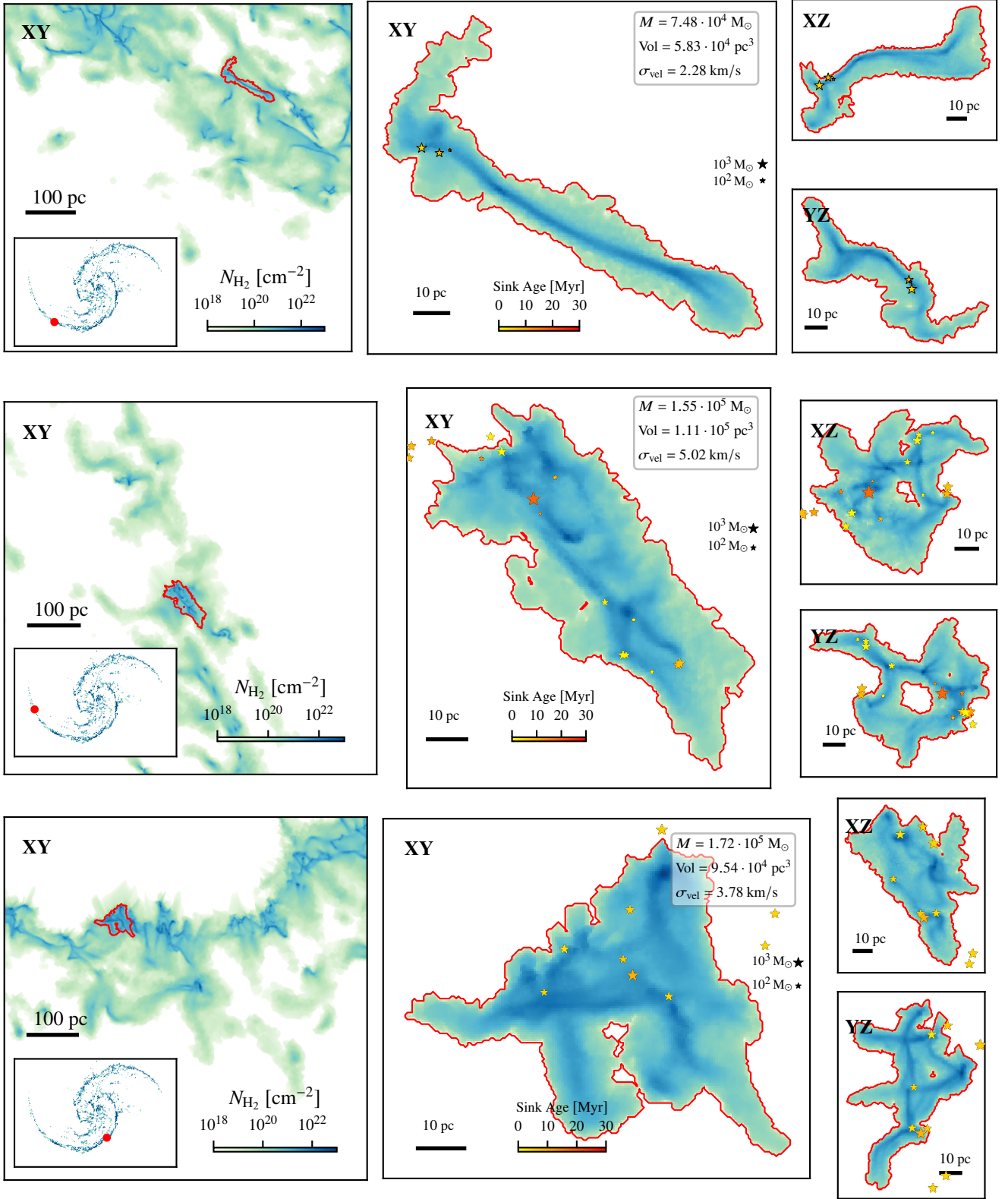


**Figure 4.** Examples of clouds identified by SCIMES. On the left we show the  $H_2$  column density map of the region from which the cloud was extracted. The inset shows the location of the region in the larger galactic context. The red isodensity contour identifies the cloud found by the algorithm. On the right we show the same cloud in the XY, XZ and YZ planes. We also indicate the locations of the sink particles using symbols colored by the sink age and with sizes related to the stellar mass.

being largely CO dark in analogous high resolution simulations (Smith et al. 2014).

We tried to vary the parameters for the dendrogram construction and for SCIMES in a given region of the simulated galaxy to test the sensitivity of the cloud properties against the choice of those parameters. We found that the structures identified and their mass distribution is relatively insensitive to small variations of the density spacing between contours for the dendrogram construction around our chosen value of  $\Delta n_{\text{H}_2} = 5 \text{ cm}^{-3}$ . If instead the spacing increases too much, the algorithm has a tendency to merge structures which were identified as separate with a finer spacing. Small variations in the minimum density generally have a small impact on the mass of some identified clouds as the algorithm is prone to include (or exclude) lower density contours. By adopting a too small minimum density, however, the algorithm will sometimes fail to properly segment clouds in the spiral arm and identify the entire arm as a single cloud. We found that a change in the properties used by SCIMES to assess similarity of dendrogram branches (using only volume, or only mass) can result in a great difference in structures identified, but a visual inspection of the clouds found suggests that a combination of mass and volume comes closest to how a user would proceed with the segmentation by hand. We notice that the definition of clouds is used in this work only in relative terms, and as long as the definition is consistently used throughout the domain, a comparison of cloud properties between regions is justified. Caution is instead advised when comparing the results from studies that used different criteria (parameters) in their cloud identification.

One complication in our cloud identification method is that both SCIMES and the software used to construct the dendrogram (ASTRODENDRO) are only able to operate using isodensity contours defined on a regular grid. We therefore have to regrid the AREPO output, which is defined on an unstructured Voronoi mesh, onto a regular 3D Cartesian mesh. In order to retain all of the details of the simulation in the high density gas, the grid size needs to be smaller than the smallest native resolution. Since the smallest cells have sizes below 0.1 pc (see Tress et al. 2020a, Figure 3), this proved to be computationally impractical owing to the extremely large size of the resulting grid. We therefore compromised by using a grid cell size of 0.5 pc, which is small enough to capture the structure of the molecular clouds, while requiring more than an order of magnitude less memory than a 0.1 pc grid. In addition, rather than representing the entire galaxy using a single grid, we instead sub-divided it into a series of  $(500 \text{ pc})^3$  regions which could then be processed serially using SCIMES. In order to avoid missing clouds located close to the boundary of a region, we overlapped each region by 125 pc with each of its neighbouring regions. For each region we only retain clouds with centre of mass within the original  $(500 \text{ pc})^3$  box. In this way we avoid double-counting.

We store the total density,  $\text{H}_2$  density, and the velocity of the grid points associated with each cloud found with this method. We also determine and save the following properties: cloud ID, total gas mass, volume, mass of gas in any sink particles contained within the cloud, virial parameter, position and velocity of the centre of mass, velocity dispersion, velocity dispersion arising from rotation, specific angular momentum, and angular velocity. For a definition of these quantities see the relevant sections.

Molecular hydrogen is typically undetectable in real galaxies, with CO emission being the most widely used observational proxy for it. However, we do not use CO to identify our clouds and instead rely on the actual  $\text{H}_2$  densities. There are two main reasons for this choice. First, although our resolution is extremely high by the standards of galactic-scale simulations, it is still not high enough to yield numerically converged values for the CO distribution. At typical GMC densities, most of the cells in the simulation have sizes of  $\sim 0.5$  pc or larger, roughly an order of magnitude larger than the value of  $\sim 0.05$  pc that Joshi et al. (2019) find is necessary to obtain fully converged values for the CO distribution in simulations of turbulent molecular clouds. Second, our primary interest in this study is the morphology and dynamics of the entire molecular phase, i.e. all of the gas located in  $\text{H}_2$  dominated regions, rather than just the subset of it which is rich in CO. In future work, we intend to compare the properties of clouds identified using CO emission with the properties of clouds identified using  $\text{H}_2$  densities. However, this lies outside of the scope of our current study.

We also do not convolve the cubes with a Gaussian beam but instead use the native resolution to find structures. This limits any direct comparison to observations but gives us insight into the actual properties of the molecular gas.

### 2.3 Cloud catalogue

We compiled a cloud catalogue for the interacting simulation at  $t = 217$  Myr. The choice of this snapshot was rather arbitrary, but we also took samples of clouds at different times in the simulation and we do not find substantial difference in our results (see Appendix A). To see what the role of the galaxy interaction is in determining cloud properties, we also performed the cloud search algorithm on the same galaxy in isolation at the same simulation time.

Figure 2 shows the positions of all clouds identified by our algorithm in the interacting galaxy while Figure 3 shows the isolated case. A total of 3309 and 3099 clouds were identified in the interacting and isolated galaxy respectively. We summarise the global properties of the cloud population for the interacting simulation in Table 1.

Based on their positions, the clouds in the interacting simulation were assigned either to the spiral arms, to the inter-arm regions, or to the centre. The centre is defined as the area with  $R < 1.3$  kpc. To define the spiral arm region we perform a Fourier transformation on the  $\text{H}_2$  column density in different radial bins. A similar method was used by Pettitt et al. (2020) where only the  $m = 2$  mode was retained to determine the position of the arms. Due to the more complex structure of the spirals here, we retain also higher harmonics in order to be able to better trace the density peaks. The  $m = 2$  mode is dominant in the outer parts of the disc but some radial bins exhibit a multi-arm structure. For these bins we then only consider the continuation of the two-armed spiral pattern from the outer disc. Clouds are then assigned to the spiral arms if they lie within 500 pc of this spiral arm spine (blue shaded region of Figure 2). The largest agglomeration of molecular gas in the inter-arm region (around  $(-6, -8)$  kpc in Figure 2) could be interpreted as an additional arm, but has no counterpart in the stellar component. It is rather an over-density detaching from the spiral arm where the gas

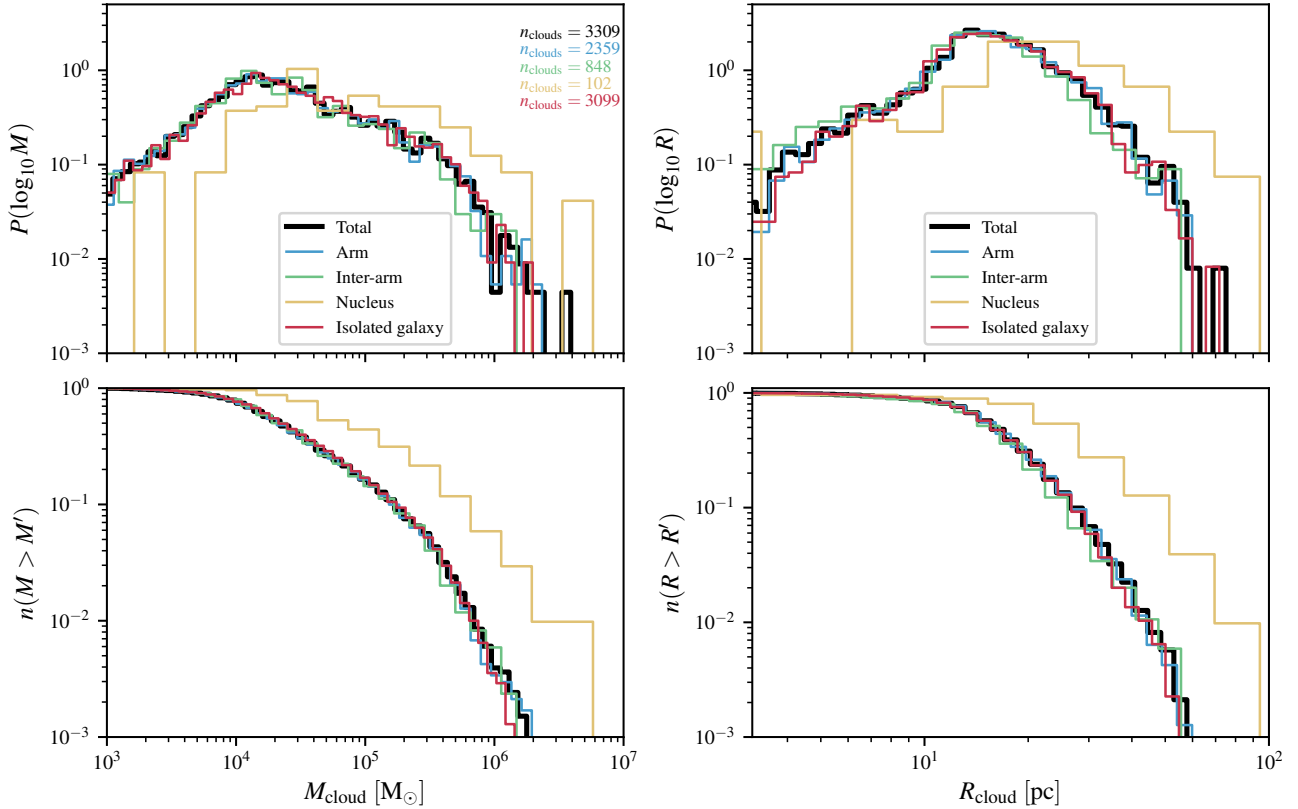


**Figure 5.** In the top panels we show the probability distribution function of the mass (*left*) and size (*right*) of the GMC population. The solid black line refers to the complete set of clouds, while the cloud population associated with spiral arms, inter-arm region, nucleus and the isolated galaxy are highlighted in different colours (see legend in the top panels). The size distribution of the simulated GMC catalogue  $R_{\text{cloud}}$  is computed from the clouds' volumes by assuming spherical shapes. The complementary cumulative distribution is shown in the bottom panels, where  $n(M > M')$  ( $n(R > R')$ ) denotes the fraction of clouds with mass (size) greater than a given value.

accumulated a few tens of megayears earlier, so we attribute it to the inter-arm region.

The total gas mass in molecular clouds in the interacting galaxy is  $M_{\text{tot}} = 2.1 \times 10^8 M_{\odot}$  and the GMCs contain a total of  $M_{\text{H}_2, \text{tot}} = 9.9 \times 10^7 M_{\odot}$  of molecular hydrogen, not counting the mass trapped in sink particles. A total  $\text{H}_2$  gas mass of  $4.3 \times 10^7 M_{\odot}$  was not attributed to any GMC by the algorithm.

In Table 2 we show the properties of a sub-sample of the clouds identified and in Figure 4 some examples of the clouds at different locations in the interacting galaxy, as well as the position of the sink particles associated with the clouds. Even though we are far from resolving GMCs down to core scales, our resolution is high enough to show the complex and filamentary substructure of the clouds. A typical cloud of mass  $2 \times 10^4 M_{\odot}$  is resolved by  $\gtrsim 10^3$  AREPO cells, we therefore believe that a detailed study of their properties is appropriate and gives us important insight to their dynamics.

### 3 CLOUD PROPERTIES

#### 3.1 Masses

In Figure 5 we show the mass distribution of the clouds. To ensure that our analysis only considers well-resolved clouds,

we exclude clouds found by SCIMES with masses lower than  $10^3 M_{\odot}$ . The native mass resolution of the simulation at GMC densities is around  $10 M_{\odot}$ , so all of the clouds identified that we keep for our analysis are resolved with around 100 or more AREPO resolution elements and the bulk of GMCs with more than  $10^3$ .

The most massive clouds found at this resolution have a mass of  $\approx 10^{6.5} M_{\odot}$ . This is considerably lower than the most massive structures identified by Colombo et al. (2014) from CO observations of the M51 system whose clouds reach masses up to  $10^{7.5} M_{\odot}$ . Our resolution is relatively high compared to their beam-size and the cloud finding algorithm is therefore able to pick out and segment smaller structures.

The mass distribution in Figure 5 peaks at around  $10^4 M_{\odot}$ . This is a regime where the GMCs in our simulation are reasonably well resolved, so this peak is of considerable interest and may be an emerging property for simulations of clouds given the physics included in these models. However, the cloud-finding algorithm could potentially introduce bias here.

In Figure 2 we show the positions of the clouds coloured by their mass. Figures 2 and 5 show no evident difference between the cloud distribution of the arm and inter-arm regions. Clouds in the nucleus, however, are generally more massive and have a shallower mass distribution than the rest of the galaxy. Even the isolated galaxy exhibits a cloud pop-

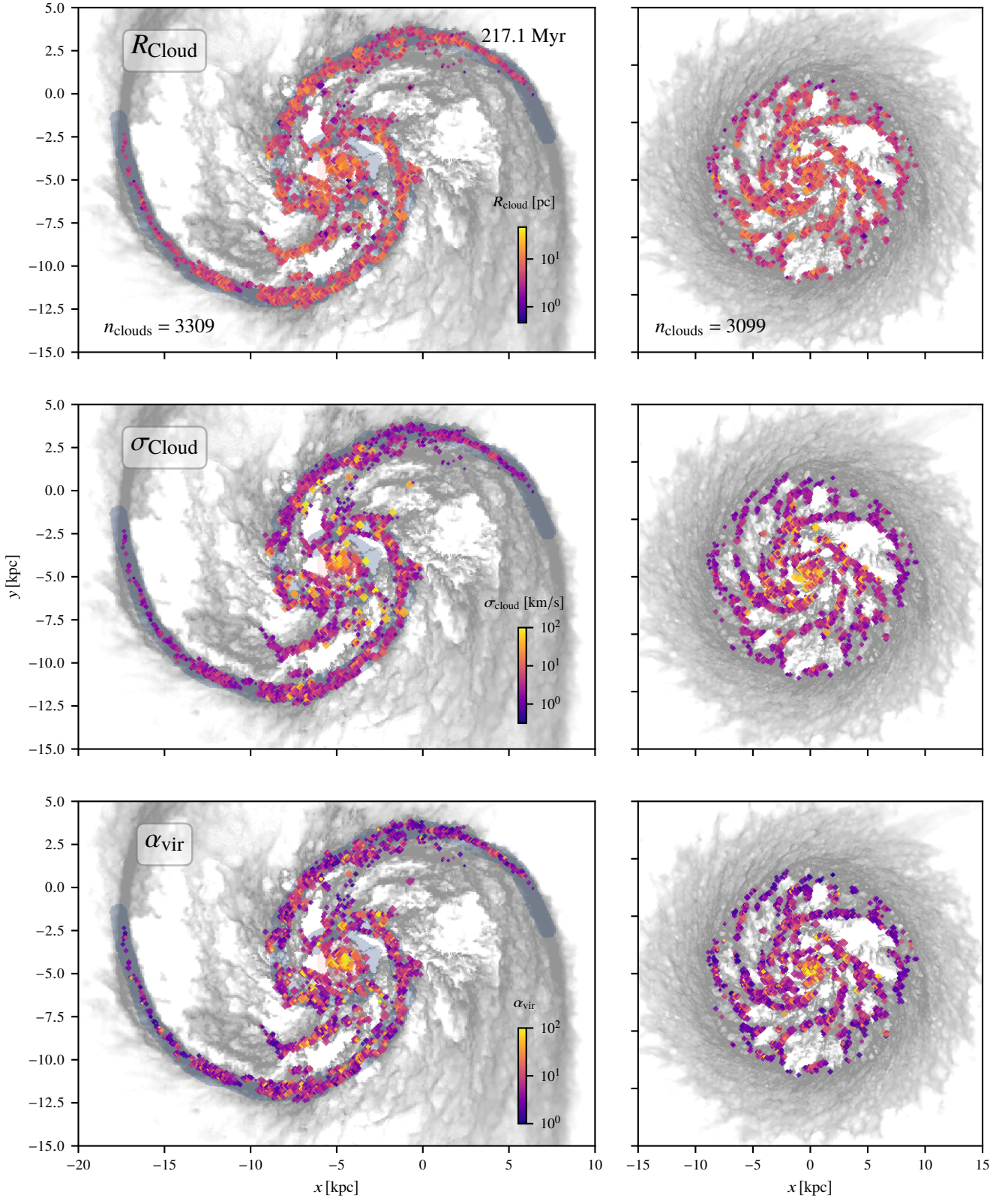


**Figure 6.** Identified clouds coloured based on their effective radius (*top panel*), their velocity dispersion (*middle panel*) and virial parameter (*bottom panel*). The marker size is related to the cloud mass as in Figure 2. We show the interacting galaxy on the left and the isolated case at the same simulation time on the right.

ulation that appears indistinguishable from the interacting one.

The absolute values of these distribution functions have to be viewed with some caution, as a considerable amount of gas could be trapped in sink particles. This is not included when computing the mass of GMCs as this would imply strong sub-grid assumptions on the thermodynamic and chemical state of this gas. The mass distribution is therefore most useful in relative terms, for comparing clouds in different regions within this framework.

### 3.2 Sizes

The effective radius of a specific cloud is computed by assuming the cloud to be spherical:

$$R_{\text{cloud}} = \left( \frac{3}{4\pi} V_{\text{cloud}} \right)^{1/3}, \quad (2)$$

where  $V_{\text{cloud}}$  is the total volume of the cloud. This is of course an over-simplification and in many instances might not represent the actual extension of the cloud, as GMCs can be represented by extremely elongated filaments or might contain holes in their distribution. Nonetheless this simple definition is useful to detect correlations given a statistically large sample of clouds.

From Figure 5 we see that the effective radius of our cloud population peaks at  $\sim 20$  pc. There is no evident difference in size of clouds in the arm and clouds of the inter-arm region while GMCs in the nucleus clearly seem to belong to a different population. Here the large shearing forces are able to considerably stretch the clouds, thus producing a population whose clouds are generally a bit bigger. This would produce an imprint on shapes of clouds and we would expect larger aspect ratios of nuclear GMCs. On the other hand shear would be expected to efficiently disrupt large clouds, and we plan therefore to revisit the geometry of structures in an upcoming work to then tie it to the local shear and test these possibilities. We will see in the following sections that nuclear clouds stand out in velocity dispersion and virial parameter as well. This then fits in this picture as the high shear promotes higher velocity dispersion and could support larger clouds against collapse.

In Figure 6 we show the spatial distribution of clouds in the galaxy coloured respectively by their size, velocity dispersion and virial parameter. The difference of central clouds compared to disc clouds is distinguishable here as well.

### 3.3 Velocity dispersion

We calculate the velocity dispersion

$$\sigma = \left( \frac{\sum_i (\mathbf{v}_i - \mathbf{v}_{\text{com}})^2 m_i}{\sum_i m_i} \right)^{1/2}, \quad (3)$$

where  $\mathbf{v}_i$  and  $m_i$  are the velocities and masses of the Voronoi cells of the cloud and  $\mathbf{v}_{\text{com}}$  is the velocity of its centre of mass. The sum is extended over all cells within a cloud. We then derive the 1D velocity dispersion:

$$\sigma_{1D} = \left( \frac{\sigma_x^2 + \sigma_y^2 + \sigma_z^2}{3} \right)^{1/2}. \quad (4)$$

This is closer to what is accessible with observations where we can only measure the velocity dispersion along the line-of-sight. We show the velocity dispersion distribution of the cloud population in Figure 7. We see here a bimodal distribution of the velocity dispersion; the secondary peak is a set of clouds with very high velocity dispersion. This is associated with the pathological clouds that are produced by the simulation, which are long-lived clouds that SNe can not disrupt due to the lack of early feedback (see Section 5 here and section 5 of Tress et al. 2020a). These objects are long lived and can grow considerably in mass since the feedback cannot halt the collapse, therefore generating massive stellar clusters. They are instead disrupted by cloud collisions eventually. Similar objects appear quite commonly in analogous galaxy scale ISM simulations (e.g. Tasker & Tan 2009; Li et al. 2018; Armillotta et al. 2019).

This calculation includes all motions of the gas in the cloud, including both turbulence and rotation. To see how important rotation is in comparison to random motions, we estimate a rotational velocity dispersion  $\sigma_{\text{rot}}$  by computing the angular momentum  $\mathbf{L}$  of the clouds (see Section 3.5) and finding the velocity dispersion of an analogous mass distribution that would rotate as a solid body having the inferred angular momentum. Specifically

$$\sigma_{\text{rot}} = \left( \frac{\sum_i m_i \mathbf{v}_{\text{rot},i}^2}{\sum_i m_i} \right)^{1/2}, \quad (5)$$

where  $\mathbf{v}_{\text{rot},i} = \mathbf{R}_i \times \boldsymbol{\Omega}$  is the solid body velocity of the cell.  $\mathbf{R}_i$  is the position vector of the Voronoi cells of the cloud with respect to the centre of mass and  $\boldsymbol{\Omega} = \mathbb{I}^{-1} \mathbf{L}$  is the angular velocity of the cloud with inertial tensor  $\mathbb{I}$ .

We show the ratio between the rotational velocity dispersion and the total velocity dispersion  $\sigma_{\text{rot}}/\sigma_{1D}$  in Figure 8. We will discuss the rotation of our cloud sample in detail in Section 3.5.

### 3.4 Virial parameter

The virial parameter of a cloud is defined as

$$\alpha_{\text{vir}} = \frac{5\sigma_{1D}^2 R_{\text{cloud}}}{GM}, \quad (6)$$

(see Bertoldi & McKee 1992). This parameter is used as an indication of whether a cloud is collapsing or dissolving. In particular  $\alpha_{\text{vir}} \propto E_{\text{kin}}/E_{\text{pot}}$ , the ratio of kinetic to potential energy. It can be shown that a Bonnor-Ebert sphere has  $\alpha_{\text{vir}} = 2.06$ , therefore this value is the critical value for stability of non-magnetised clouds and clouds with  $\alpha_{\text{vir}} \lesssim 2$  are considered to be collapsing. There are issues with this definition, for instance, that clouds in free fall would generally develop velocities from the collapse that raise their  $E_{\text{kin}}$  and bring the value of  $\alpha_{\text{vir}}$  closer to unity, making the cloud appear to be stable even though it clearly is not (Ibáñez-Mejía et al. 2016; Ballesteros-Paredes et al. 2018). Moreover the definition assumes spherical symmetry for the clouds which is clearly an oversimplification (see Figure 4). A stability analysis of GMCs can therefore not solely rely on this parameter. The mass used here  $M = M_{\text{cloud}} + M_{\text{sink gas}}$  (see Table 2) includes the mass in sink particles within the GMC as well, as they contribute to the local gravitational energy and can influence the stability of the region.

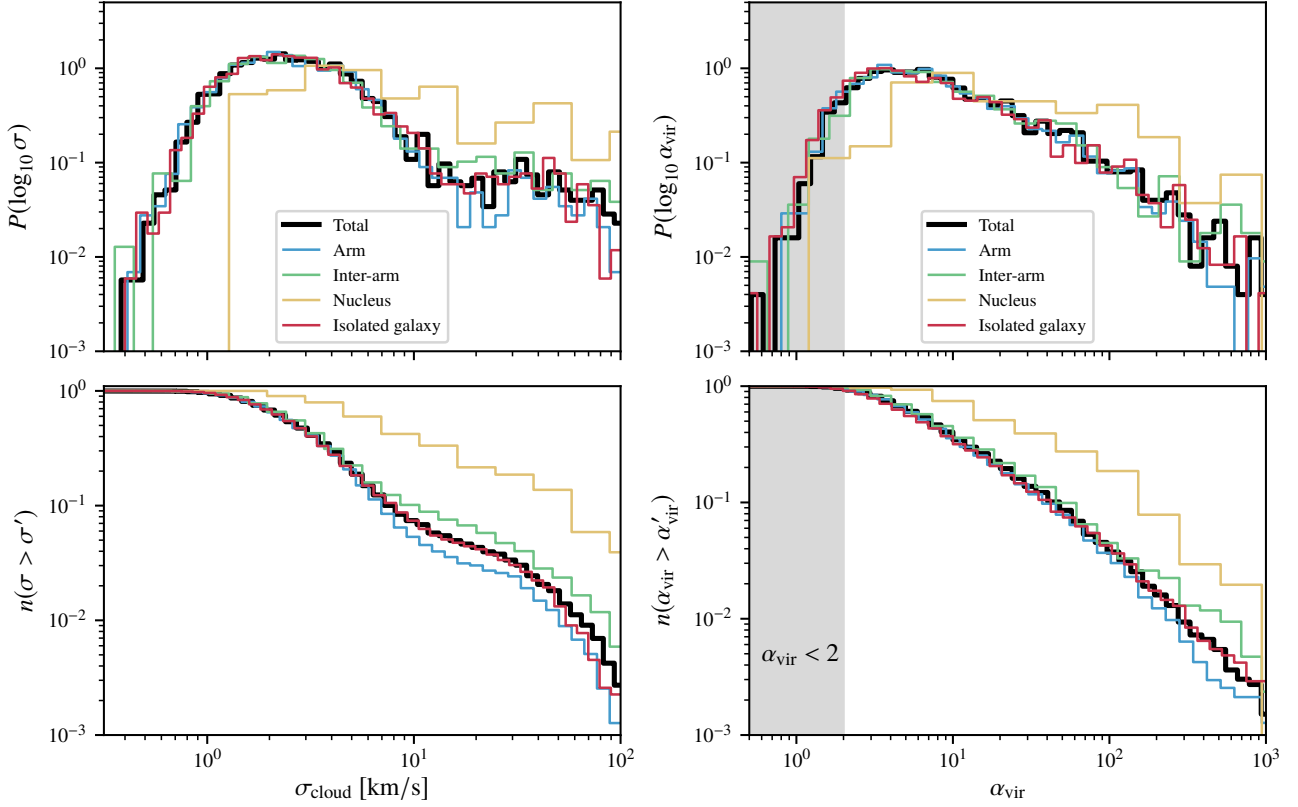


**Figure 7.** Velocity dispersion and virial parameter distributions of the simulated GMC catalog;  $\sigma_{\text{cloud}}$  is the 1D velocity dispersion of the cloud by assuming isotropic motions. The different cloud populations are depicted in different colours, consistent with our other figures. The cumulative distribution is shown in the bottom panel. The different cloud populations are depicted in different colours, consistent with our other figures. The cumulative distribution is shown in the bottom panel. The *gray band* is the region where  $\alpha_{\text{vir}} < 2$ , where the virial analysis suggests that the structures are collapsing. Note that the majority of the clouds are close to the critical value, and gravitationally unbound GMCs are clearly favoured.

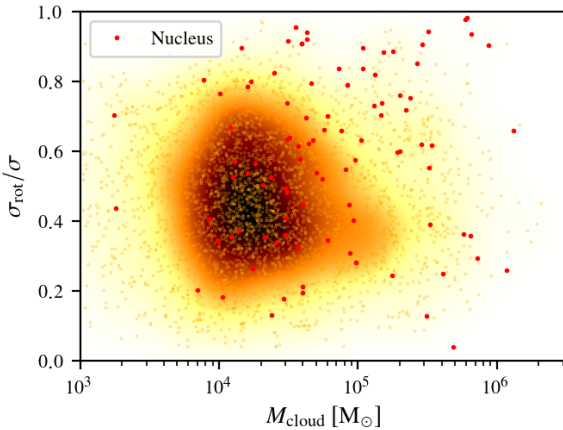


**Figure 8.** Distribution of the ratio between the velocity dispersion coming from rotation ( $\sigma_{\text{rot}}$ ) and the total velocity dispersion ( $\sigma$ ) for the GMCs against their masses. A  $\sigma_{\text{rot}}/\sigma$  value of 1 corresponds to clouds whose only contribution to the velocity dispersion is given by rigid body rotation (see Equation 5) while the random motions are negligible, while a value approaching 0 corresponds to clouds that exhibit little rotation compared to their turbulence. The GMCs of the nucleus are shown in red. With the *gold-brown color-map* we show the resulting kernel density estimation distribution.

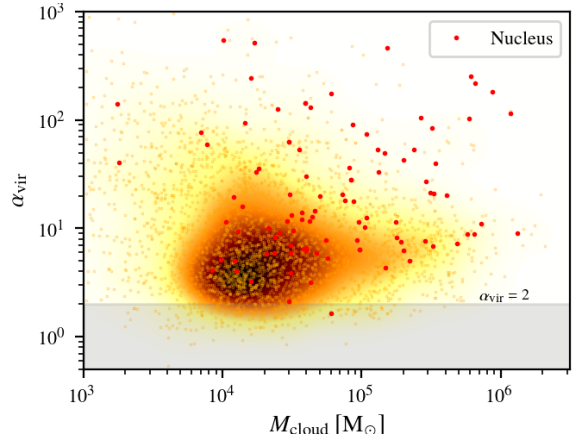


**Figure 9.** Mass-virial parameter distribution of the clouds in the interacting galaxy. In the *gray-shaded region* clouds are considered to be gravitationally bound and collapsing by a simple virial analysis, while clouds above the critical value of  $\alpha_{\text{vir}} = 2$  are normally considered to be unbound. The GMCs of the nucleus are shown in red. With the *gold-brown color-map* we show the resulting kernel density estimation distribution.

The virial parameter distribution of the cloud populations in the different regions is shown in the right panel

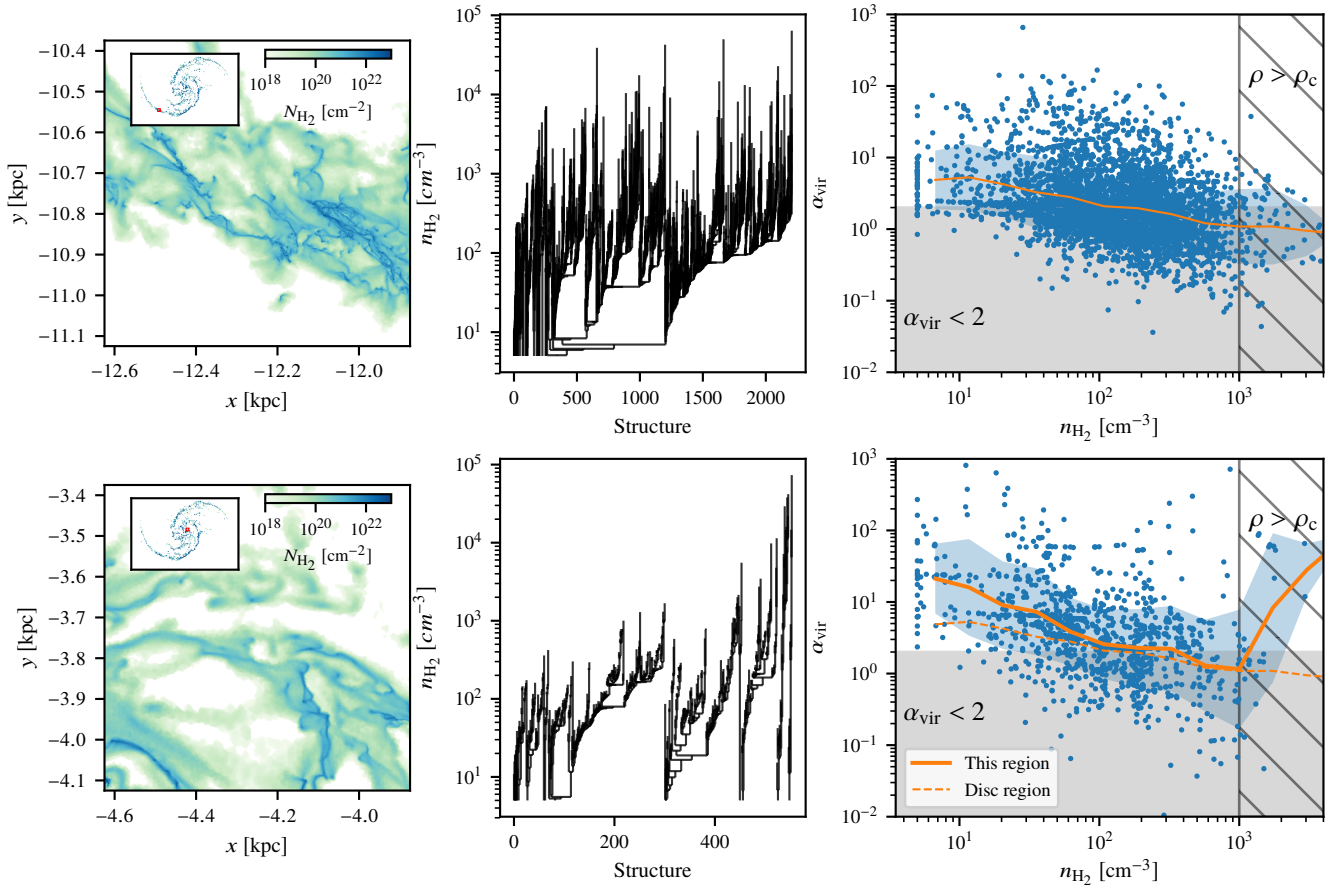


**Figure 10.** The virial parameter of structures defined by various molecular iso-density surfaces as a function of molecular density for two different regions in the simulated interacting galaxy, one far out in a spiral arm (*top*) and one close to the nucleus (*bottom*). We derive the position-space dendrogram (*middle panel*) of the region shown in the left panel; for each structure of the dendrogram, we show its virial parameter as a point in the right panel at the density threshold of the structure. The orange line is the binned average of the data and the blue band the  $\pm 1\sigma$  deviation from that. For comparison, in the bottom panel we also show (*dashed line*) the running average of the region shown in the top panel. The grey band defines collapsing structures based on a virial analysis, while the hatched region shows where the density exceeds the threshold for sink particle creation.

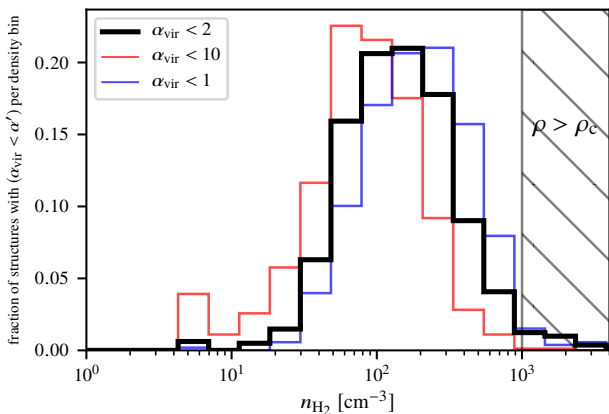


**Figure 11.** Here we walked the dendrogram of a given region and analysed the lowest structures in the hierarchy of the dendrogram (i.e. least dense) with  $\alpha_{\text{vir}} < \alpha'$ , only containing structures which fulfill the same criterion (see Figure 13 to visualise how these structures look like). In this graph we show the density distribution for such structures. The black line is the distribution for such structures with  $\alpha_{\text{vir}} < 2$  which is commonly accepted to denote gravitationally bound and collapsing regions.

of Figure 7 while the dependence of  $\alpha_{\text{vir}}$  with the clouds mass is shown in Figure 9. Compared to observed structures (Kauffmann et al. 2013), the simulated GMCs exhibit relatively high virial parameters for their masses, indicating that most of the molecular gas here is gravitationally unbound. Comparable galaxy scale ISM simulations tend likewise to produce predominantly unbound structures (e.g. Dobbs et al. 2011).

How can we explain this apparent disagreement with observation? As explained in Section 1, the definition of a GMC is relatively arbitrary and tends to pick out just a few isodensity levels in the hierarchical structure of the molecular ISM. To get a clearer picture of the dynamical state of the entirety of the cold phase, we analyse the virial parameter of all the dendrogram structures of a particular region. In Figure 10 we show  $\alpha_{\text{vir}}$  of each structure as a function of its threshold density in the dendrogram. In this way we do not favour a specific iso-density surface and can investigate at what typical density the structures transition from a sub-critical state.

We show the results for two regions of the interacting galaxy: the binned average of  $\alpha_{\text{vir}}$  decreases as the density increases. This is, of course, unsurprising, since it is expected

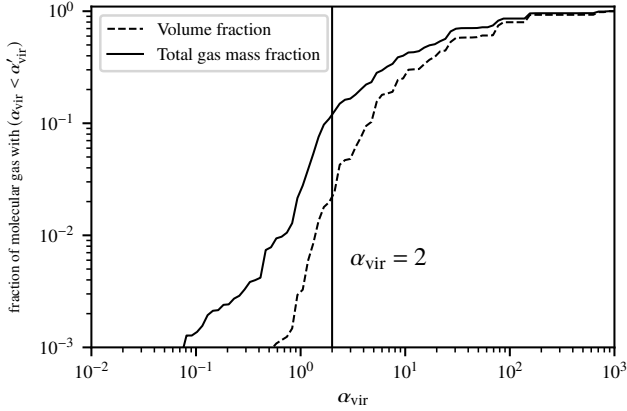


**Figure 12.** Volume and total gas mass fractions of structures lowest in the hierarchy of the dendrogram (i.e. least dense) and containing only structures with a virial parameter lower than a given value. These fractions are computed against the total volume/gas mass of the molecular gas, i.e. the gas with  $n_{\text{H}_2} > 1 \text{ cm}^{-3}$  which is the ISM considered for the dendrogram construction. The vertical line emphasises  $\alpha_{\text{vir}} = 2$ , indicating structures which are generally collapsing. About 10 % of the mass and a few percent of the volume is occupied by molecular gas in this condition.

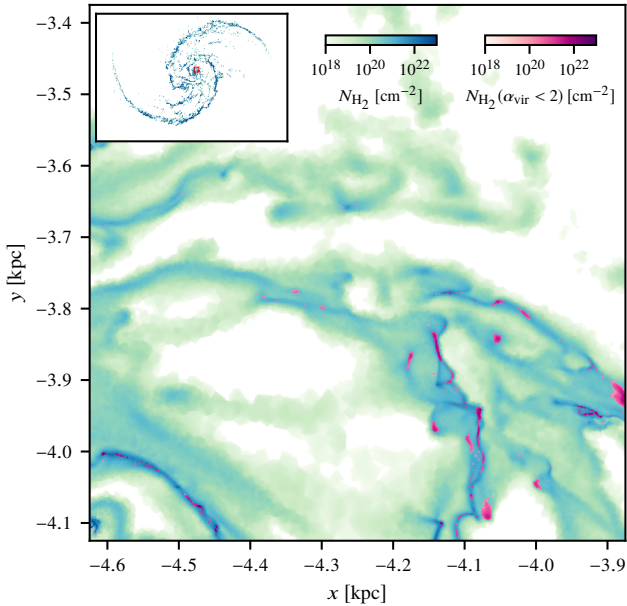


**Figure 13.**  $\text{H}_2$  column densities of a given region in the interacting galaxy. The location of the region is shown in the top-left insert. We constructed and analysed the dendrogram of this region and highlight with a red colormap all the structures lowest in the hierarchy of the dendrogram (i.e. least dense) and containing only structures with  $\alpha_{\text{vir}} < 2$ .

that collapse occurs more easily in higher density regions. The density where the average value of the virial parameter falls below the critical line is  $n_{\text{H}_2} \sim 10^2 \text{ cm}^{-3}$ . We have to highlight, however, that the scatter of  $\alpha_{\text{vir}}$  is considerable and it is possible to find highly unbound structures even at higher densities.

At densities exceeding the sink particle formation den-

sity threshold, gas only survives if it is highly gravitationally unbound or did not have enough time to be swallowed by a sink particle. This explains why the data points in this area are scarcer and seem to break from the general decreasing trend. It is, however, still interesting to see that even at those densities highly sub-critical structures exist.

One caveat is that we did this analysis for only a few regions. Visual inspection of other such regions, however, suggests similar behaviour. It remains an interesting exercise to study systematically the behaviour of  $\alpha_{\text{vir}}$  as a function of galactic environment.

The bottom panel of Figure 10 shows the virial parameter density dependence for a region close to the galactic centre. Comparing the trend of  $\alpha_{\text{vir}}$  to the region farther out in the galaxy disc (top panel), we notice that generally the distribution is shallower and shifted to higher values. This would be expected for a more turbulent and shear dominated region. We leave a more thorough systematic investigation of this statement for future work.

Having a clearer view now of  $\alpha_{\text{vir}}$  of the molecular gas in all density regimes, we can see that the picture of GMCs being objects in virial equilibrium is rather simplistic; the real ISM might exhibit a more complex structure and variety in internal energies. So why is it that clouds are observationally often found to be close to virialised? One reason is because even collapsing clouds develop velocities that make them look like they are virialised; another reason is survival bias: clouds with too extreme virial parameters are short-lived. A third reason is selection bias: since we only observe regions where CO becomes bright, we miss the envelopes of clouds, which lower the clouds' virial parameters. This last point explains the difference of the simulated clouds to observed populations, as we select GMCs using the actual  $\text{H}_2$  density and therefore include even the CO dark gravitationally unbound envelopes. A similar conclusion was reached by Duarte-Cabral & Dobbs (2016) where clouds from the simulation of Dobbs (2015) were analysed in  $\text{H}_2$  and CO, finding that CO traces only the more gravitationally bound parts of clouds. At densities around  $n_{\text{H}_2} \approx 10^2 \text{ cm}^{-3}$  where molecular hydrogen becomes CO bright (Clark et al. 2019), we agree with the observations in finding that the average structure has  $\alpha_{\text{vir}} \approx 2$  (see Figure 11). But this should not be confused for a distinctive feature of molecular clouds, but rather a coincidence among the large range of  $\alpha_{\text{vir}}$  among structures selected at different densities (Beaumont et al. 2013).

Relative to the total molecular gas, the mass and volume fraction of super-critical structures is comparatively low (see Figure 12 and Figure 13). Given the physical conditions simulated here, we find therefore that most structures are gravitationally unbound and only a small percentage of the molecular gas is bound. For the region displayed in the top panel of Figure 10 the volume(mass) fraction of bound gas is 0.033(0.15) while for the region in the bottom panel it is 0.012(0.061). Since only gravitationally bound and collapsing structures could lead to star formation, the low fractions of super-critical molecular gas imply a necessarily low SFE. This is observed in the simulation (see Figure 21 of Tress et al. (2020a), where depletion times of the molecular gas are  $\sim 5 \times 10^8 \text{ yr}$ ) as well as in galaxy observations in general. This suggests therefore that the low galactic SFE is set at the cloud scale.

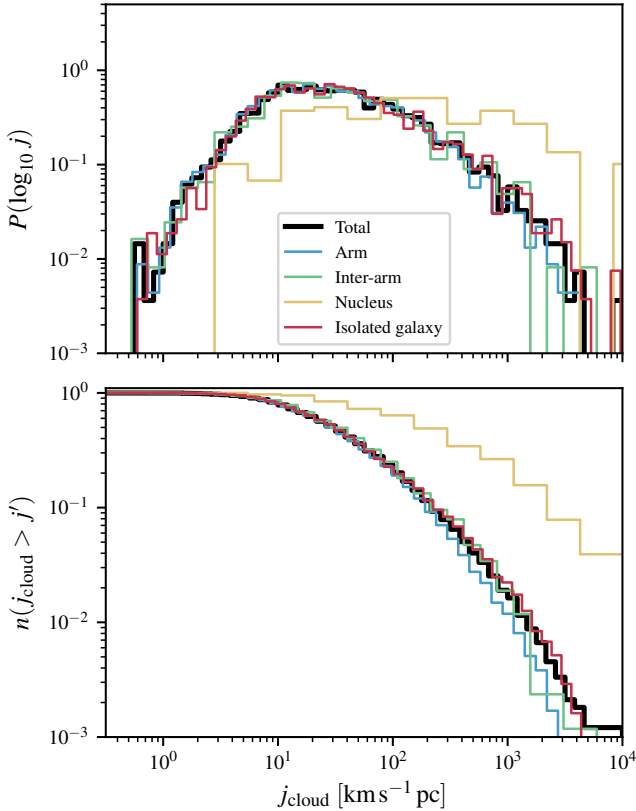


**Figure 14.** Distribution of specific angular momenta  $j_{\text{cloud}}$  of the simulated GMC catalog. The different cloud populations are depicted in different colours, consistent with our other figures. The cumulative distribution is shown in the bottom panel.

### 3.5 Rotation

It has long been suggested that GMCs rotate (Kutner et al. 1977; Blitz 1993; Phillips 1999), but it is still unclear whether cloud rotation is dynamically important. Observations suggest that rotational energy is only a small fraction compared to gravitational energy of clouds and so cannot provide any meaningful support against collapse (Rosolowsky et al. 2003; Braine et al. 2018, 2020). In general, rotational periods seem to always exceed estimated cloud life-times. Environmental variations can however be significant. Clouds in M51 have, for instance, been observed to have three times the specific angular momentum compared to clouds in M33 (Braine et al. 2020).

The origin of this rotation is also under debate. Most clouds are found to have angular momentum vectors aligned with the plane of the galaxy, supporting the idea that the spin of GMCs is imparted from the galactic rotation curve. Moreover the preferred direction being prograde with the disc rotation, it is believed that it is the orbital rotation that dictates spin direction. In particular in a differentially rotating disc the shear generated by a rising rotation curve will produce prograde clouds by gravitational contraction (Mestel 1966). Of course local turbulence (generated for instance by feedback) has no preferred direction and spinning eddies can be generated regardless of the angular momentum of the disc. The interaction of the ISM with spiral shocks, on the other hand, can establish systematic retrograde vor-

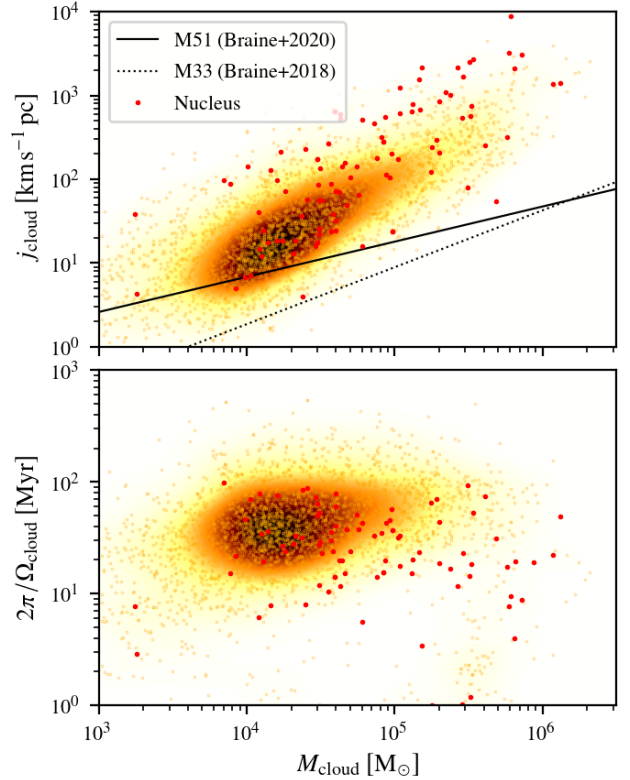


**Figure 15.** *top panel:* Mass-specific angular momentum distribution of the clouds in the interacting galaxy. We show the fits to the observations of M51 and M33 galaxies for comparison. *bottom panel:* mass-rotation period distribution of the GMCs. The clouds of the nucleus are highlighted in red. With the gold-brown color-map we show the resulting kernel density estimation distributions.

ticity generation (Chernin & Efremov 1995). This has been invoked to explain the higher fraction of retrograde clouds in the spiral arms of M51 (Braine et al. 2020). In the Milky Way and in external galaxies about 30–40% of clouds are actually counter-rotating such that the simple top-down formation scenario of clouds cannot solely account for cloud formation (see also Imara & Blitz 2011; Imara et al. 2011).

We compute the specific angular momentum  $j_{\text{cloud}} = |\mathbf{L}|/M_{\text{cloud}}$  of the clouds in our catalogue where  $\mathbf{L} = \sum_i m_i \mathbf{r}_i \times \mathbf{v}_i$  is the angular momentum computed over the grid cells contained within the cloud with respect to their centre of mass. We show the distribution of  $j_{\text{cloud}}$  in Figure 14. The clouds in our simulated galaxy have a typical value of  $j_{\text{cloud}} \approx 20 \text{ km s}^{-1} \text{ pc}$  and reach peak values up to  $10^4 \text{ km s}^{-1} \text{ pc}$ . Again there is no evident difference between the clouds of the arm and the inter-arm region, and also the isolated galaxy produces a comparable distribution.

Only the clouds of the central region clearly exhibit a different distribution; here clouds are generally fast rotators and their typical specific angular momentum is more than an order of magnitude greater than disc clouds. Here shearing forces are higher and changes in the galactic rotation velocity curve are significant for scales comparable to the size of a molecular cloud. During gravitational collapse this high shear is then directly translated into rotation of the GMC.

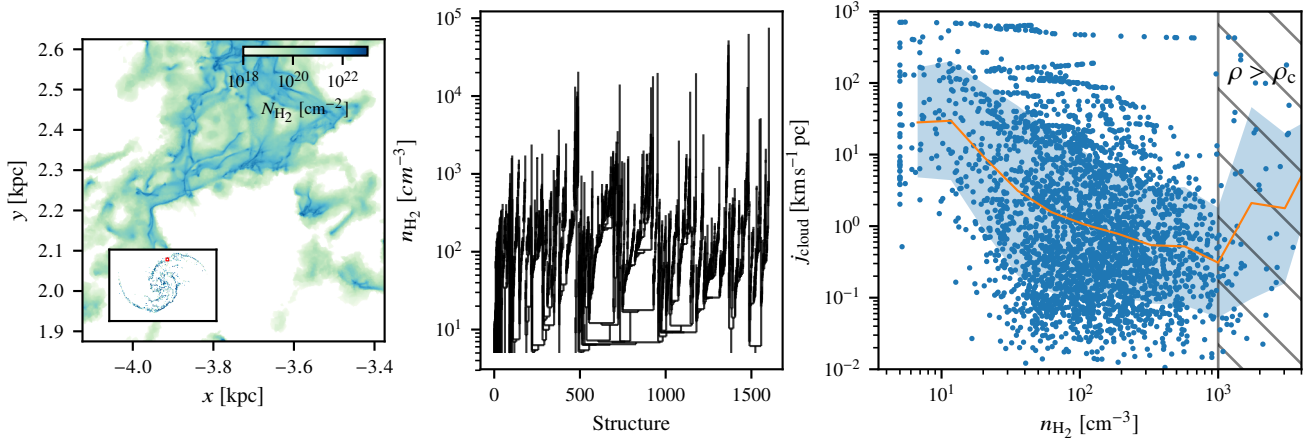


**Figure 16.** Similar to Figure 10 but here we explore the specific angular momentum of isodensity contours.

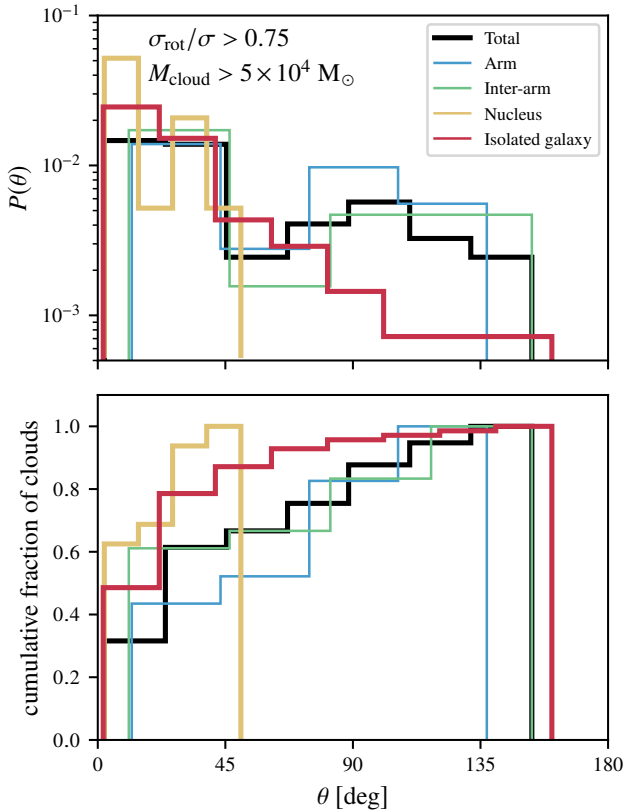


**Figure 17.** Distribution of the angle between the angular momentum vector of the clouds and the whole galaxy. We only selected rotation dominated clouds with  $\sigma_{\text{rot}}/\sigma > 0.75$  and excluded low mass ( $M_{\text{cloud}} < 5 \times 10^4 M_{\odot}$ ) clouds for which the local turbulence is likely responsible for their rotation. A value of 0 denotes clouds completely co-rotating with the galactic disc, while counter-rotating clouds will have  $\theta = 180^\circ$ . The different cloud populations are depicted in different colours, consistent with other figures. The cumulative distribution is shown in the bottom panel.

To compare the energies in rotational modes compared to the general velocity dispersion of clouds, in Figure 8 we show the rotational to total velocity dispersion ratio  $\sigma_{\text{rot}}/\sigma$  (see Section 3.3 for the definition of  $\sigma_{\text{rot}}$ ). On average the

rotational velocities constitute about 40 % of the total velocity dispersion, but in extreme cases all of the velocity dispersion comes from rotation. This is, to be sure, in part a consequence of the insufficient resolution to properly resolve the turbulent cascade within clouds, which results in an excessive power in large scale rotational modes. On the other hand, though, some of our extreme clouds suffer from inefficient feedback which is unable to disrupt the GMC. The massive sink particles that tend to form in such a situation create long-lived, centrally peaked gravitational fields that are prone to form rotating discs due to dissipation, even though the bulk of our clouds do not suffer from such a problem.

If GMCs really are the emerging structures of the turbulent cascade, then it is actually not surprising to find that cloud rotation is significant compared to other internal motions. In particular, it is expected from a direct energy cascade that the most power resides in the largest modes.

We investigate in Figure 15 how the rotation correlates with the mass of the cloud and we see a power-law trend of the specific angular momentum of clouds with increasing masses. The increase in  $j_{\text{cloud}}$  with mass is consistent with a roughly constant angular velocity of the clouds with mass (bottom panel of Figure 15). This is suggestive of a top-down formation scenario of GMCs where local shear from the rotation curve plays a major role in driving the rotation as opposed to a bottom-up agglomeration of small clouds in a turbulent medium where instead larger clouds would have a lower chance of having a net rotation.

Observations show positive exponents as well, but compared to M51, our simulation produces a steeper dependence and in general higher values of rotation. We also tried to detach the specific angular momentum from the definition of a GMC and instead in Figure 16 we inspected  $j_{\text{cloud}}$  of iso-density contours as a function of  $n_{\text{H}_2}$  in a region of the interacting galaxy. There is a general trend of increasing specific angular momentum at lower iso-density levels. This comes plausibly from the large scale shear generated by the rotation curve of the galaxy. A few hierarchical structures in the region shown have high  $j_{\text{cloud}}$  all the way to the highest density level, i.e. the rotation is dominated by a massive and dense accretion disc-like structure. This can be seen in Fig-

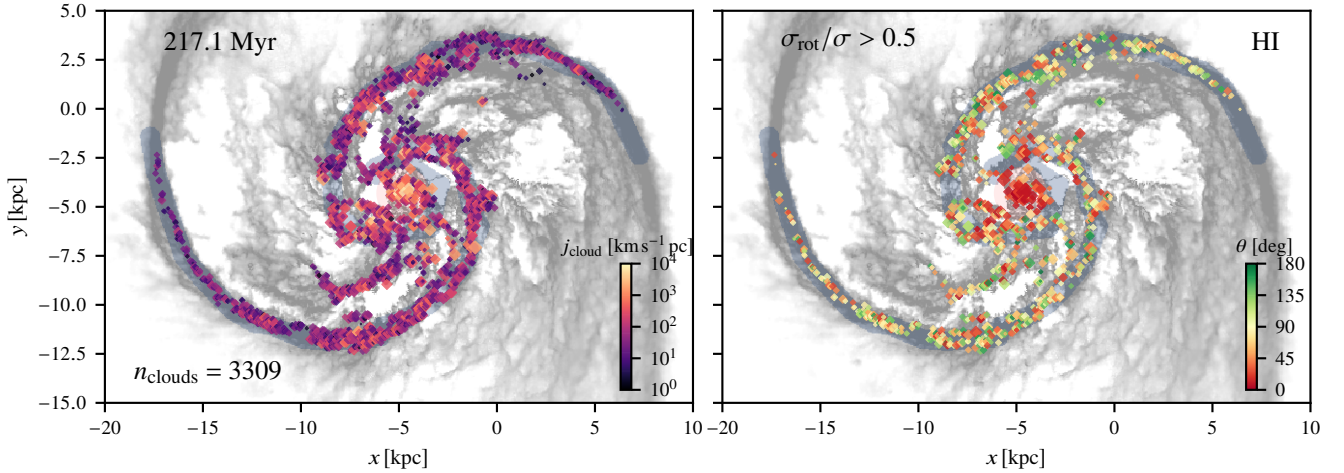


**Figure 18.** Positions of the GMCs as identified by the cloud-finding algorithm coloured by their specific angular momentum (*left hand side panel*) and their inclination with respect to the inclination of the disc (*right hand side panel*). Here green clouds are counter-rotating and red clouds are co-rotating with the galaxy. On the right hand side panel we only show clouds with a substantial rotation component, i.e.  $\sigma_{\text{rot}}/\sigma > 0.5$ .

ure 16 from the entries with almost constant  $j_{\text{cloud}} \sim 10^3 \text{ km s}^{-1} \text{ pc}$  at all density levels.

To study the direction of GMC rotation in our simulations, we selected clouds that had a substantial rotation contribution to their total velocity dispersion, i.e. clouds with  $\sigma_{\text{rot}}/\sigma > 0.5$ , to eliminate the noise of turbulence dominated clouds and slow rotators. Moreover we excluded clouds with low masses ( $M_{\text{cloud}} < 5 \times 10^4 M_{\odot}$ ) for which the local turbulence is more important in regulating their rotation than the galactic shear. In Figure 17 we show the distribution of the angles between the angular momentum vector of those clouds and the galaxy. We find that the majority of the clouds are co-rotating with the disc, but the distribution is quite flat with a considerable fraction of retrograde and perpendicular clouds. It is interesting to notice that the interacting galaxy produces a higher fraction of counter-rotating clouds ( $\sim 30\%$ ) compared to the isolated case ( $\sim 10\%$ ). Braine et al. (2020) found a higher retrograde cloud fraction in the arms of the observed M51 galaxy connecting the origin of the counter-rotation to spiral arm passage. Here, however, there is no apparent increase in counter-rotating clouds in the arms (see also Figure 18). A possible contribution to the increase of counter-rotating clouds is the warp in the disc that the companion galaxy induces as the orbital plane of the two galaxies does not coincide with the plane of the disc. The angular momentum from the encounter could perhaps cascade down to GMC scales and contribute to their rotation direction.

The interaction alters the inclination of GMCs mostly in the outskirts of the galaxy where the forces are greatest, while towards the centre the population stays predominantly co-rotating (see Figure 18). Moreover, in this region shearing forces are greatest so it is not surprising that here turbulence is unable to produce strongly counter-rotating structures.

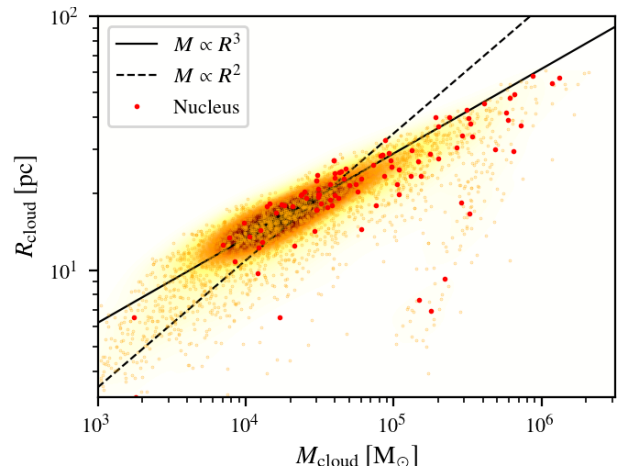


**Figure 19.** Mass-size distribution of the cloud population for the interacting simulated galaxy. The clouds of the nucleus are highlighted in red. With the gold-brown color-map we show the kernel density estimation distribution given the mass and size values of GMCs. The clouds follow a nearly constant density distribution (*solid line*) rather than a constant column-density (*dashed line*).

### 3.6 Scaling relations

We analyse here the emerging scaling relations of our simulations. In Figure 19 we show the mass-size relation where the mass and the size of the GMCs are defined as described in Section 3.1 and 3.2. Larson (1981) first found a relation of the type  $M \propto R^2$  that suggested that clouds may have constant mass surface density. This, however, was most likely an observational bias. For our cloud catalogue we find that GMCs span a wide range in surface densities (see Figure 20) and the relation that we find is rather suggestive of a  $M \propto R^3$  type relation, i.e. constant volume density rather than constant surface density.

We have to stress however that this is likely an artificial result arising from the cloud finding algorithm, which

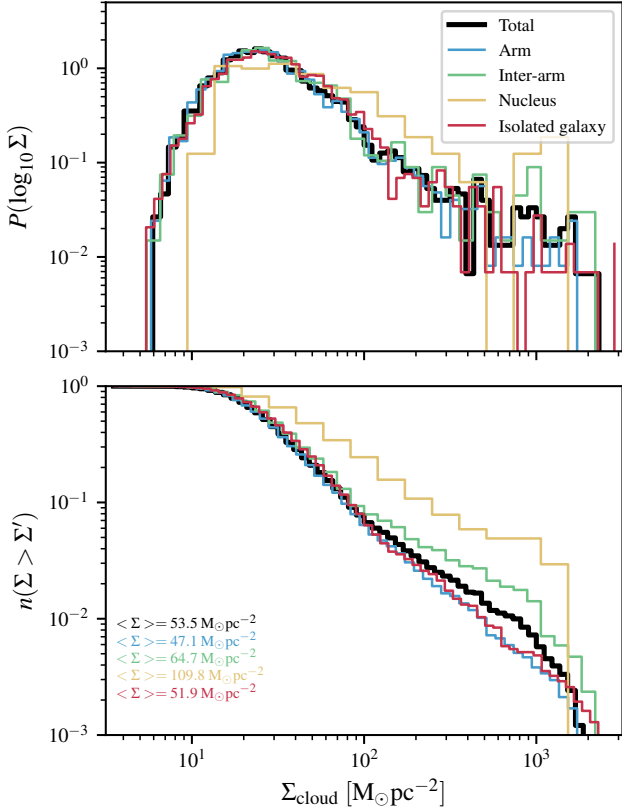


**Figure 20.** Surface density distribution of the simulated GMC catalog. Here the surface density is derived from the clouds masses  $M$  and their size  $R$  according to  $\Sigma = M/(\pi R^2)$ . The different cloud populations are depicted in different colours, consistent with our other figures. The cumulative distribution is shown in the bottom panel.

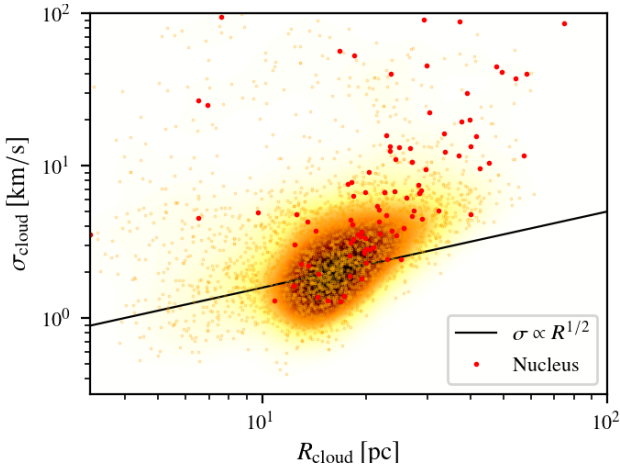


**Figure 21.** Size-velocity dispersion distribution of the clouds in the interacting galaxy. Symbols and colors are analogous to Figure 19. The *solid line* shows  $\sigma_{\text{cloud}} \propto R_{\text{cloud}}^{1/2}$  dependency, typical of virialised structures at constant column density.

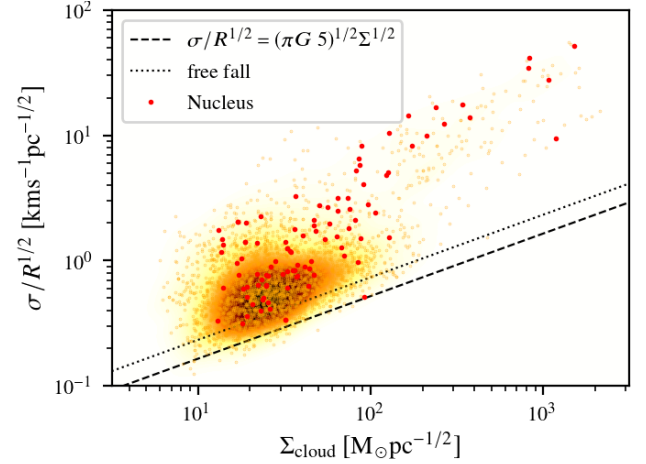


**Figure 22.** Heyer et al. (2009) relation for the interacting galaxy cloud population. Symbols and colors are analogous to Figure 19. The *dashed line* indicates clouds at virial equilibrium while the dotted line assumes clouds in free fall.

assumes a given volume density threshold to start evaluating the dendrogram as described by Ballesteros-Paredes et al. (2012). The average density that the mass-size relation suggests is  $\rho \sim 7 \times 10^{-23} \text{ g cm}^{-3}$  which corresponds approximately to  $n_{\text{H}_2} \sim 10 \text{ cm}^{-3}$ . This is close enough to the threshold density of  $n_{\text{H}_2, \text{min}} = 1 \text{ cm}^{-3}$  used by SCIMES such that we cannot rule out a bias from the cloud finding method.

In Figure 21 we show the emerging size-velocity dispersion relation. Clouds in virial equilibrium at constant surface densities would follow a power-law type relation with an exponent of  $1/2$ . We find a steeper slope for the extracted simulated clouds and large scatter. If the third Larson relation (i.e. constant surface density) does not hold, a dependence of the form  $\sigma \propto \Sigma^{1/2}$  is introduced as well in the first Larson relation (see Heyer et al. 2009). This is often invoked to explain the large scatter of observed size-linewidth relation of some regions. For the synthetic cloud catalogue we see a great variety in  $\Sigma_{\text{cloud}}$  and, if we include the surface density dependence, we do approximately retrieve the observed slope for the bulk of our GMCs (Figure 22). Other numerical studies of GMCs in a galactic environment come to similar conclusions (see for instance Nickerson et al. 2019, in particular their Figure 14).

Moreover, we saw in Section 3.4 that the picture of GMCs as virialised objects is rather simplistic and it is therefore misleading to derive scaling relations based on this assumption. The exponents in the size-linewidth power-law relation can vary widely for different targets and, for instance, in M51 no or a weak relation of the linewidth with clouds sizes is observed Colombo et al. (2014). A similar power-law relation can also emerge from a turbulent medium, with the slope determined by the inertial cascade (Kritsuk et al. 2013).

The structures identified in our simulated galaxies seem mostly gravitationally unbound (see Figure 7 and 9) and this is reflected in the bulk of our identified GMCs lying above the Heyer relation (Figure 22). Even so, the slope remains close to that inferred for virialised structures. This indicates that gravitationally-driven turbulence is likely substantially

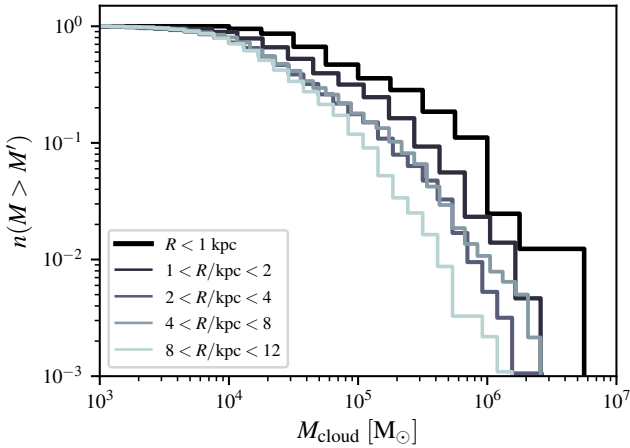


**Figure 23.** Cumulative mass distribution of the cloud catalogue for different radial bins.

contributing to the velocity structure in the clouds, as such motions can mimic virialisation.

For a subset of clouds, to which also the nuclear GMCs belong, the slope is considerably steeper than the Heyer relation slope. Here other factors are most likely dominant in driving the turbulence in the clouds, such as galactic shear.

#### 4 CLOUDS IN THE GALACTIC ENVIRONMENT

Spiral arms have always been seen as a major trigger for SF as most molecular gas and SF tracers are observed to be correlated with these galactic scale structures. Correlation does not imply causality however, and it has been shown in some instances that spiral arms can act as a snowplow rather than as a trigger (Tress et al. 2020a; Kim et al. 2020). In this sense other galactic parameters such as gas fractions, surface densities and local shear are more important in setting the molecular gas properties. The presence of spiral arms will then just change the distribution of GMCs within the disc without significantly affecting their general properties. This has been evident by the analysis of the general structure of the molecular gas and the SF of these simulations in a previous paper (Tress et al. 2020a), and is emerging from our study of the GMCs in these simulations as well.

The distribution functions of mass, size, velocity dispersion and specific angular momentum of the cloud populations of the arms are virtually indistinguishable from those of the inter-arm clouds. Duarte-Cabral & Dobbs (2016) find that the bulk properties of clouds in their galaxy simulations are also similar for the arm and inter-arm regions, but the tails of some distributions show differences. We also see that, excluding central GMCs, the most massive clouds are associated with the spiral arms (see the tail of the mass distribution in Figure 5), but are still statistically in agreement with belonging to the same distribution if we consider Poisson noise.

Moreover the galaxy interaction itself seems to be of little importance in shaping GMCs, as their properties are very similar to those in the galaxy in isolation. Pettitt et al. (2018) find that for an interacting galaxy comparable to the

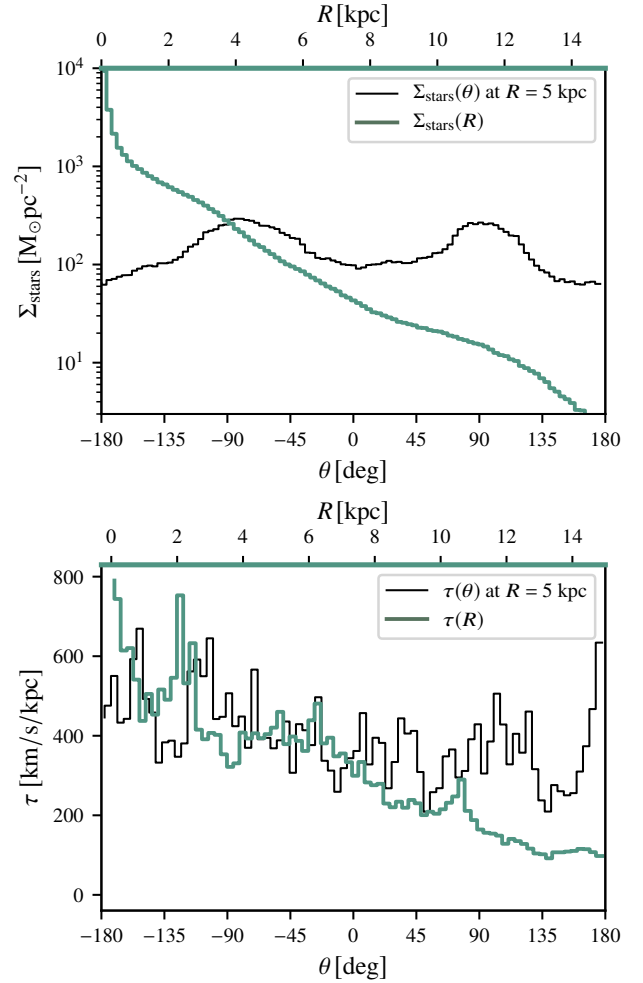


**Figure 24.** Stellar surface density (*top panel*) and mass-weighted average of the shear, as defined in the main text, (*bottom panel*) of the interacting galaxy as a function of galactic radius (*green line*) and as a function of azimuthal angle at  $R = 5$  kpc (*black line*).

one presented here, more massive clouds are produced in association with the spiral arms if compared to an isolated galaxy simulation. Their resolution, however, is insufficient to resolve sub-structures in GMCs and here we see that the large GMC structures associated with the arms can be subdivided into a variety of smaller clouds that still follow the same mass function as for the rest of the disc. Moreover Pettitt et al. (2020) find no change in global cloud properties when performing disc galaxy simulations with different grand design spirals. This would then be an indication that our results are case specific but could be valid to some extent for a different morphology of the spiral arms as well.

The interaction could however have some importance in determining the rotation direction of clouds, as we observe more retrograde clouds in the interacting simulation. In general some GMC properties could depend more strongly on galactic environment than others, and in particular rotation and aspect ratios are sensitive to the local shear (Jeffreson et al. 2020). Changes induced by the galaxy interaction are then more evident for those parameters than, for instance, for cloud masses.

In contrast to our findings, observations of the M51 system show a difference in the GMC population of spiral arms and inter-arm regions (Colombo et al. 2014). The difference is mainly evident in the masses, where clouds in the arms are generally more massive than inter-arm clouds. The authors attribute this difference to the action of the spiral arms on cloud formation and evolution. We note, however, that the available resolution of the data was considerably lower than what we used to identify clouds. This shows also in the much smaller typical mass of clouds in our simulation compared to the observed ones. The smoothing of the data will blend separate structures into one, which results in more massive objects in a crowded region like a spiral arm. This could explain the disagreement with our results. We plan to perform synthetic observations to compare the extracted clouds more closely with the observations in a follow-up study.

The central regions of the simulated galaxy, on the other hand, seem to produce clouds that evidently belong to a separate GMC population. Galaxy centres are extreme environments, with high surface densities and extreme shearing forces from the differential rotation. It is therefore not surprising that this is reflected in the evolution of GMCs. We see in Figure 23 that there is a progressive shift towards more massive clouds for smaller galactic radii. Comparing this to Figure 5 we can see that in our simulations these environmental conditions are not sufficiently different between arm and inter-arm region to affect the formation and evolution of GMCs, but change progressively as we approach more central regions. We can see in Figure 24 that indeed the stellar surface density variation as a function of galactic radius is much higher than for the arm and inter-arm regions. A similar conclusion can be reached by looking at the shear. We define the local shear of the galaxy in two dimensions by using projected quantities. We use the parameter

$$\tau^2 = \left( \frac{\partial v_x}{\partial y} + \frac{\partial v_y}{\partial x} \right)^2 + \left( \frac{\partial v_x}{\partial x} - \frac{\partial v_y}{\partial y} \right)^2, \quad (7)$$

which is the magnitude of the eigenvalues of the traceless part of the strain tensor which gives a description of the local shear. Here  $v_i$  is the mass weighted mean velocity in the plane of the galaxy. In the bottom panel of Figure 24 we show the mass weighted average of  $\tau$  in each radial(angular) bin as a function of galactic radius  $R$ (azimuthal angle  $\theta$ ). Contrary to the stellar surface density, the variation of the shear as a function of  $\theta$  at a given  $R$  is comparable to the radial variation. However, there is no strong correlation with the spiral arms as in the inter-arm regions large shear can arise from SN driven bubbles. There is instead a clear trend of increasing shear with decreasing  $R$  owing to the galactic rotation. This supports our thesis that the shear plays a greater role in determining the properties of clouds than the morphological presence of a spiral arm. Future work should investigate the correlation of cloud properties not to special places in the galaxy, but to the local physical conditions such as shear, mid-plane pressure and surface densities (see for instance Jeffreson & Kruijssen 2018).

## 5 CAVEATS

We use this section to discuss the possible implications of the physical ingredients that were not accounted for in the simulations. These are early stellar feedback (such as ionising radiation and stellar winds) and magnetic fields.

SN feedback alone can produce an ISM with reasonable mass and volume fractions in the different thermal phases (Gatto et al. 2015) such that we do not expect the large-scale behaviour of the gas to change significantly if early feedback would be included. As we approach cloud scales and GMC dynamics, however, the effect of early feedback can become substantial (Geen et al. 2015). We observe this in our simulations with the presence of what we call "pathological" clouds, which are massive, long-lived and often rapidly-rotating dense agglomerations of gas which cannot be disrupted by SN feedback alone. With a proper preconditioning of the ISM by early feedback these clouds would evolve differently. But even for more well-behaved clouds in our simulations, the evolution could differ substantially if winds and ionising radiation would have been considered (Rogers & Pittard 2013), in particular for later stages in the lifetime of the cloud. A general trend to be expected is for clouds to have shorter life-times. This could affect clouds during their passage through spiral arms and contribute to a difference in cloud statistics in the arm compared to the interarm region. A massive cloud that in our simulations would survive spiral arm passage and could then be found in the interarm region, with early feedback the same cloud would potentially have been disrupted earlier.

Magnetic fields can also have an effect on the cloud population which may depend significantly on the environment. In general the magnetic field is stronger in the presence of spiral arms (Beck 2015; Shanahan et al. 2019; Reissl et al. 2020) and so it could be the driver for inducing a difference in cloud population statistics here. The effect of the magnetic fields varies however for different gas density regimes and the influence is stronger for the diffuse atomic than for the molecular phase (Soler et al. 2020, 2021). We therefore do not expect large differences in the dynamics of the dense gas (Padoan & Nordlund 1999; Crutcher et al. 2010; Bertram et al. 2012) although they will affect certain observational signatures.

We stress that this work is intended as a numerical experiment and not an attempt to faithfully reproduce the natural world. It is rather a useful exercise to learn how the system reacts to certain conditions and physical ingredients. By comparing to real observational data and assessing similarities and differences it gives insight to what elements play fundamental roles in determining observed properties. A simulation which would include all of the physics would have limited scientific advantage as it would obscure the effect of individual physical ingredient on the phenomenon under study. We plan to gradually include further physical processes to explore their effect in a series of future projects. The results presented here will then represent a baseline to compare to.

## 6 CONCLUSIONS AND SUMMARY

We used the set of simulations presented in Tress et al. (2020a) to study the nature of the cold molecular ISM in the

context of an interacting galaxy. These were galaxy scale calculations performed with the hydrodynamic moving-mesh code AREPO. They include important GMC physics such as a time-dependent chemical network that follows  $\text{H}_2$  and CO formation and destruction, star formation through sink particles, and SN feedback. They reach sub-parsec resolution in the densest parts of the ISM on scales of an entire galaxy, which is self-consistently evolved throughout the entire time-frame of the interaction. These simulations are therefore particularly useful to study the influence and the effect that galaxy dynamics has on the properties of the molecular phase of the ISM. We focused in particular on the statistical analysis of the emerging GMC population.

We constructed the dendrogram of the three-dimensional molecular gas distribution. We then used the python package SCIMES to extract molecular clouds at different density levels from a fixed point in time of the simulation. We presented the properties of the structures found in different environments, including their masses, sizes, velocity dispersions, virial parameters, and rotation.

We can summarise our conclusions as follows:

- Despite the interacting galaxy developing prominent spiral arm structures in our model, it does not display the difference in mass function of GMCs of the arm compared to the inter-arm region found in observations. We do, however, see clear differences in molecular cloud properties in the central region of the galaxy, where environmental variables such as shear and surface density have substantially higher values. Our high-resolution maps used to identify clouds enable us to disentangle individual structures in crowded regions such as spiral arms. In contrast, observations at lower resolution and projection effects tend to merge multiple structures, thus introducing bias in the analysis. Our simulations therefore suggest that the structure and dynamics of the molecular ISM is determined by environmental factors such as local shear and mid-plane gravitational forces and surface densities. If the spiral arm cannot significantly alter these conditions, the molecular gas properties remain invariant.

- The cold molecular phase of the ISM is a highly dynamic environment, and GMCs, which are the emerging structures of this phase, reflect this. They exhibit a large range of virial parameters  $\alpha_{\text{vir}}$ , as is expected for a turbulent medium where the energy injection mechanism is not fully coupled to the gravitational energy of the gas. The picture of molecular clouds being virialised objects is therefore misleading and likely the result of observational and selection biases, as a more dynamic and rich picture emerges if we consider the CO dark envelopes of GMCs as well. We show that, at densities where clouds tend to become CO bright, the average structure shows  $\alpha_{\text{vir}} \sim 1$ , but considering molecular structures at different density levels we can instead find a large spread in  $\alpha_{\text{vir}}$ . Virial analysis shows that only about 10 % of the total mass of molecular gas is in a gravitationally bound state that only contains bound structures. The low star formation efficiency of the ISM may well result largely from this low fraction.

- We find in our simulations that clouds do not have near constant surface density  $\Sigma$ , as would be suggested by Larson’s scaling relations, but rather span several orders of magnitude in  $\Sigma$ , similar to the findings of more recent observa-

tions that probe larger dynamic ranges (e.g. Hughes et al. 2013; Leroy et al. 2015; Duarte-Cabral et al. 2020).

- In our model we find clouds where rotation makes a substantial contribution to their total velocity dispersion. Most of them are prograde with respect to the disc, suggesting that the large scale galactic rotation provides angular momentum at cloud formation through local shear. We find that the interaction with a companion galaxy alters the fraction of prograde clouds, suggesting that some of the orbital angular momentum of the companion cascades down to GMC formation.

## ACKNOWLEDGEMENTS

The authors are grateful to the anonymous referee whose comments helped to considerably improve the manuscript. The authors acknowledge support from the Deutsche Forschungsgemeinschaft (DFG) via the Collaborative Research Center (SFB 881, Project-ID 138713538) “The Milky Way System” (sub-projects A1, B1, B2 and B8) and from the Heidelberg cluster of excellence (EXC 2181 - 390900948) “STRUCTURES: A unifying approach to emergent phenomena in the physical world, mathematics, and complex data”, funded by the German Excellence Strategy. They also acknowledge funding from the European Research Council in the ERC Synergy Grant “ECOGAL – Understanding our Galactic ecosystem: From the disk of the Milky Way to the formation sites of stars and planets” (project ID 855130). The project made use of computing resources provided by the state of Baden-Württemberg through bwHPC and the German Research Foundation (DFG) through grant INST 35/1134-1 FUGG. Data are stored at SDS@hd supported by the Ministry of Science, Research and the Arts Baden-Württemberg (MWK) and the German Research Foundation (DFG) through grant INST 35/1314-1 FUGG. RJS gratefully acknowledges an STFC Ernest Rutherford fellowship (grant ST/N00485X/1) and HPC from the Durham DiRAC supercomputing facility (grants ST/P002293/1, ST/R002371/1, ST/S002502/1, and ST/R000832/1). M-MML was partly supported by US NSF grant AST18-15461. ADC acknowledges support from the Royal Society through a University Research Fellowship (URF/R1/191609). This research made use of ASTRO-DENDRO, a Python package to compute dendrograms of Astronomical data (<http://www.dendrograms.org/>) and of SCIMES, a Python package to find relevant structures into dendrograms of molecular gas emission using the spectral clustering approach.

## DATA AVAILABILITY

The data underlying this article will be shared on reasonable request to the corresponding author. The properties of the cloud population in the case of the interacting and isolated galaxy are available as online supplementary material.

## REFERENCES

Armillaotta L., Krumholz M. R., Di Teodoro E. M., McClure-Griffiths N. M., 2019, *MNRAS*, **490**, 4401

- Ballesteros-Paredes J., Mac Low M.-M., 2002, *ApJ*, **570**, 734
- Ballesteros-Paredes J., Hartmann L., Vázquez-Semadeni E., 1999, *ApJ*, **527**, 285
- Ballesteros-Paredes J., Hartmann L. W., Vázquez-Semadeni E., Heitsch F., Zamora-Avilés M. A., 2011, *MNRAS*, **411**, 65
- Ballesteros-Paredes J., D'Alessio P., Hartmann L., 2012, *MNRAS*, **427**, 2562
- Ballesteros-Paredes J., Vázquez-Semadeni E., Palau A., Klessen R. S., 2018, *MNRAS*, **479**, 2112
- Beaumont C. N., Offner S. S. R., Shetty R., Glover S. C. O., Goodman A. A., 2013, *ApJ*, **777**, 173
- Beck R., 2015, *A&ARv*, **24**, 4
- Bertoldi F., McKee C. F., 1992, *ApJ*, **395**, 140
- Bertram E., Federrath C., Banerjee R., Klessen R. S., 2012, *MNRAS*, **420**, 3163
- Blitz L., 1993, in Levy E. H., Lunine J. I., eds, *Protostars and Planets III*. p. 125
- Braine J., Rosolowsky E., Gratier P., Corbelli E., Schuster K. F., 2018, *A&A*, **612**, A51
- Braine J., Hughes A., Rosolowsky E., Gratier P., Colombo D., Meidt S., Schinnerer E., 2020, *A&A*, **633**, A17
- Burkhart B., 2018, *ApJ*, **863**, 118
- Chernin A. D., Efremov Y. N., 1995, *MNRAS*, **275**, 209
- Clark P. C., Glover S. C. O., Klessen R. S., 2012, *MNRAS*, **420**, 745
- Clark P. C., Glover S. C. O., Ragan S. E., Duarte-Cabral A., 2019, *MNRAS*, **486**, 4622
- Colombo D., et al., 2014, *ApJ*, **784**, 3
- Colombo D., Rosolowsky E., Ginsburg A., Duarte-Cabral A., Hughes A., 2015, *MNRAS*, **454**, 2067
- Crutcher R. M., Wandelt B., Heiles C., Falgarone E., Troland T. H., 2010, *ApJ*, **725**, 466
- Dempsey J. T., Thomas H. S., Currie M. J., 2013, *ApJS*, **209**, 8
- Dobbs C. L., 2015, *MNRAS*, **447**, 3390
- Dobbs C. L., Burkert A., Pringle J. E., 2011, *MNRAS*, **413**, 2935
- Dobbs C. L., Rosolowsky E., Pettitt A. R., Braine J., Corbelli E., Sun J., 2019, *MNRAS*, **485**, 4997
- Duarte-Cabral A., Dobbs C. L., 2016, *MNRAS*, **458**, 3667
- Duarte-Cabral A., Dobbs C. L., 2017, *MNRAS*, **470**, 4261
- Duarte-Cabral A., et al., 2020, *MNRAS*,
- Faesi C. M., Lada C. J., Forbrich J., 2018, *ApJ*, **857**, 19
- Federrath C., 2015, *MNRAS*, **450**, 4035
- Federrath C., Klessen R. S., 2012, *ApJ*, **761**, 156
- Field G. B., Blackman E. G., Keto E. R., 2011, *MNRAS*, **416**, 710
- Gatto A., et al., 2015, *MNRAS*, **449**, 1057
- Geen S., Rosdahl J., Blaizot J., Devriendt J., Slyz A., 2015, *MNRAS*, **448**, 3248
- Glover S. C. O., Clark P. C., 2012, *MNRAS*, **421**, 116
- Goodman A. A., Rosolowsky E. W., Borkin M. A., Foster J. B., Halle M., Kauffmann J., Pineda J. E., 2009, *Nature*, **457**, 63
- Hennebelle P., Chabrier G., 2011, *ApJ*, **743**, L29
- Heyer M., Krawczyk C., Duval J., Jackson J. M., 2009, *ApJ*, **699**, 1092
- Hughes A., et al., 2010, *MNRAS*, **406**, 2065
- Hughes A., et al., 2013, *ApJ*, **779**, 46
- Ibáñez-Mejía J. C., Mac Low M.-M., Klessen R. S., Baczynski C., 2016, *ApJ*, **824**, 41
- Imara N., Blitz L., 2011, *ApJ*, **732**, 78
- Imara N., Bigiel F., Blitz L., 2011, *ApJ*, **732**, 79
- Imara N., De Looze I., Faesi C. M., Cormier D., 2020, *ApJ*, **895**, 21
- Jefferson S. M. R., Kruijssen J. M. D., 2018, *MNRAS*, **476**, 3688
- Jefferson S. M. R., Kruijssen J. M. D., Keller B. W., Chevance M., Glover S. C. O., 2020, *MNRAS*, **498**, 385
- Joshi P. R., Walch S., Seifried D., Glover S. C. O., Clarke S. D., Weis M., 2019, *MNRAS*, **484**, 1735
- Kauffmann J., Pillai T., Goldsmith P. F., 2013, *ApJ*, **779**, 185
- Kim W.-T., Kim C.-G., Ostriker E. C., 2020, *ApJ*, **898**, 35
- Kritsuk A. G., Lee C. T., Norman M. L., 2013, *MNRAS*, **436**, 3247
- Kroupa P., 2001, *MNRAS*, **322**, 231
- Krumholz M. R., McKee C. F., 2005, *ApJ*, **630**, 250
- Kutner M. L., Tucker K. D., Chin G., Thaddeus P., 1977, *ApJ*, **215**, 521
- Larson R. B., 1981, *MNRAS*, **194**, 809
- Leroy A. K., et al., 2015, *ApJ*, **801**, 25
- Li Q., Tan J. C., Christie D., Bisbas T. G., Wu B., 2018, *PASJ*, **70**, S56
- Lombardi M., Alves J., Lada C. J., 2010, *A&A*, **519**, L7
- Mestel L., 1966, *MNRAS*, **131**, 307
- Nickerson S., Teyssier R., Rosdahl J., 2019, *MNRAS*, **484**, 1238
- Padoan P., Nordlund Å., 1999, *ApJ*, **526**, 279
- Padoan P., Nordlund Å., 2011, *ApJ*, **730**, 40
- Pettitt A. R., Egusa F., Dobbs C. L., Tasker E. J., Fujimoto Y., Habe A., 2018, *MNRAS*, **480**, 3356
- Pettitt A. R., Dobbs C. L., Baba J., Colombo D., Duarte-Cabral A., Egusa F., Habe A., 2020, *MNRAS*, **498**, 1159
- Phillips J. P., 1999, *A&AS*, **134**, 241
- Reissl S., et al., 2020, *A&A*, **642**, A201
- Rigby A. J., et al., 2019, *A&A*, **632**, A58
- Rogers H., Pittard J. M., 2013, *MNRAS*, **431**, 1337
- Rosolowsky E., Leroy A., 2006, *PASP*, **118**, 590
- Rosolowsky E., Engargiola G., Plambeck R., Blitz L., 2003, *ApJ*, **599**, 258
- Rosolowsky E. W., Pineda J. E., Kauffmann J., Goodman A. A., 2008, *ApJ*, **679**, 1338
- Schuller F., et al., 2017, *A&A*, **601**, A124
- Shanahan R., et al., 2019, *ApJ*, **887**, L7
- Shetty R., Beaumont C. N., Burton M. G., Kelly B. C., Klessen R. S., 2012, *MNRAS*, **425**, 720
- Smith R. J., Glover S. C. O., Clark P. C., Klessen R. S., Springel V., 2014, *MNRAS*, **441**, 1628
- Soler J. D., et al., 2020, *A&A*, **642**, A163
- Soler et al., 2021, arXiv e-prints, p. arXiv:2106.13206
- Sormani M. C., Treß R. G., Klessen R. S., Glover S. C. O., 2017, *MNRAS*, **466**, 407
- Sormani M. C., Tress R. G., Glover S. C. O., Klessen R. S., Battersby C. D., Clark P. C., Hatchfield H. P., Smith R. J., 2020, *MNRAS*, **497**, 5024
- Springel V., 2010, *MNRAS*, **401**, 791
- Stutzki J., Güsten R., 1990, *ApJ*, **356**, 513
- Sun J., et al., 2020, *ApJ*, **901**, L8
- Tasker E. J., Tan J. C., 2009, *ApJ*, **700**, 358
- Tress R. G., Smith R. J., Sormani M. C., Glover S. C. O., Klessen R. S., Mac Low M.-M., Clark P. C., 2020a, *MNRAS*, **492**, 2973
- Tress R. G., Sormani M. C., Glover S. C. O., Klessen R. S., Battersby C. D., Clark P. C., Hatchfield H. P., Smith R. J., 2020b, *MNRAS*, **499**, 4455
- Williams J. P., Blitz L., Stark A. A., 1995, *ApJ*, **451**, 252

## APPENDIX A: DIFFERENT TIMES

Compiling a cloud catalogue for a given snapshot is computationally expensive enough that we could not afford to extract the clouds for every simulation snapshot. This raises the question, however, whether our results are valid throughout the evolution of the galaxy. It could be argued, for instance, that the spiral arms of the galaxy at the time chosen for the main analysis are dynamically young and still in the process of developing. The gas could then not have had enough time to leave the freshly formed arms which could be the cause for the small difference in cloud properties between arm and inter-arm regions that we observed

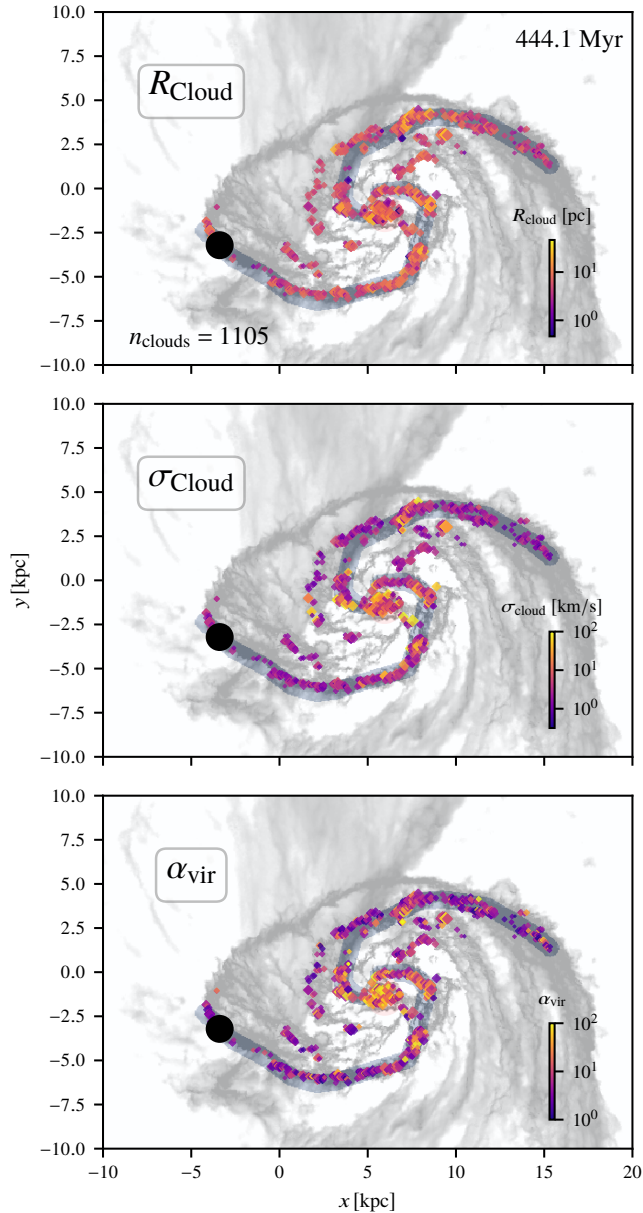


**Figure A1.** Same as Figure 6 but for the interacting galaxy simulation at a later time. The position of the companion galaxy, which is modelled as a single massive particle, is shown as the big black filled circle in the three panels.

and described in the main body of this work. This might be especially valid for the outer parts of the disc where the rotation periods are long. To address this we extracted here the clouds of a second snapshot at a later stage of the simulation ( $t = 444.1$  Myr). The configuration of the simulated galaxy and the companion at this time corresponds to the one of the M51 system which our model was designed to roughly reproduce. We defined the spiral arm, inter-arm region and nucleus in the same way as described in the main text (see Section 2.3).

We show in Figure A1 the locations of the clouds found coloured by their size, velocity dispersion and virial parameter overlaid to the HI column density of the galaxy. Moreover in Figure A2 we look at the mass distribution of the clouds.

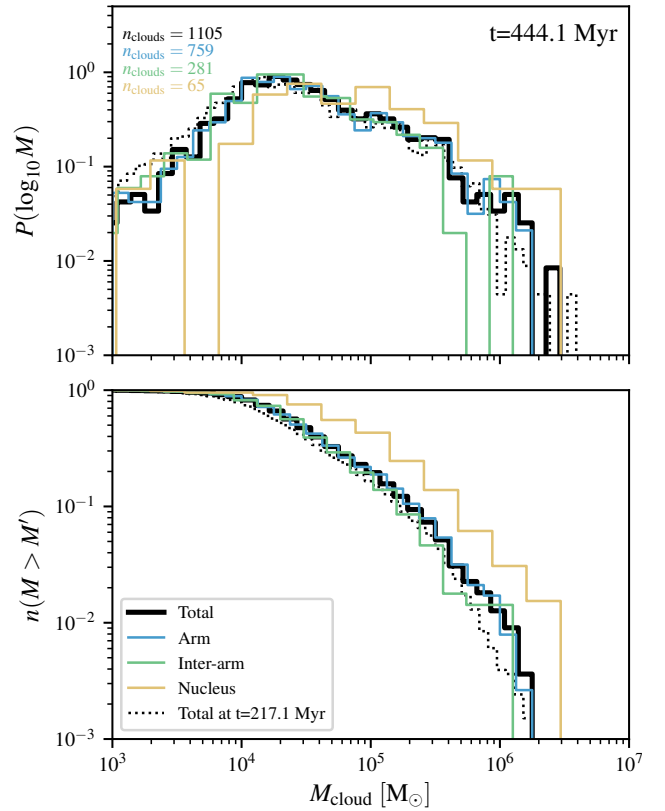


**Figure A2.** Similar to Figure 5 we show here the mass distribution of the clouds identified in the interacting galaxy at a simulation time of  $t = 444.1$  Myr. We show the structures attributed to the centre, the arm and the inter-arm region as well as the total mass distribution of the cloud catalogue at this time (solid black line). For comparison we also show the mass distribution of the clouds identified at an earlier time snapshot, used and described in the main text of this work (dotted black line).

A total of 1167 clouds were found, a considerable smaller amount with respect to the snapshot at  $t = 217.1$  Myr. This is to be attributed to the gas depletion due to the intense SF as well as a slightly higher number of massive clouds compared to earlier times.

If we compare the solid to the dotted line in Figure A2 we see indeed a small deviation at the high-mass end, suggesting that the interaction scenario might slightly favour more massive clouds as the merger progresses. The difference, however, is relatively small.

In the main text we argued that the spiral arms were acting more as a snow-plow rather than triggering new cloud formation. In this sense they mainly collected the clouds from the inter-arm regions without substantially affecting their properties. The same conclusion can be drawn from this snapshot as the cloud population of the inter-arm is very similar to the arm clouds. Only the central regions seem to be systematically of higher mass.

We also selected a few random patches of the interacting galaxy at different times and identified the clouds there. We compared the key properties of those clouds found to the cloud catalogue of the main snapshot analysed. No major differences were detected in the cloud populations. No major changes were expected as the galactic conditions and

the star formation differed only slightly during the time period considered (see Figure 15 of [Tress et al. \(2020a\)](#)). This confirms that our conclusions are not the result of a particular choice of time, but are general for the type of galaxy and environmental conditions.

This paper has been typeset from a  $\text{\TeX}/\text{\LaTeX}$  file prepared by the author.



# Chapter 4

## Simulations of the Milky Way's central molecular zone - I. Gas dynamics

### 4.1 Statement about my contribution

For this scientific publication my contribution was equal to that of Dr. Mattia Sormani, the second author of the publication.

- **Code development:** my contribution was central. As this model uses the same code and ISM model as the one used for my publication presented in Chapter 2, the workload can be attributed equally to the two projects.
- **Simulation setup:** my contribution was central and equal to that of Dr. Mattia Sormani. The main tasks consisted of setting up the initial conditions and parameters of the simulation, running tests and performing preliminary analysis to check the soundness of our setup.
- **Physical model:** my contribution was important, but this part of the project was mainly lead by Dr. Mattia Sormani who is the local expert of the Milky Way Bar and the Central Molecular Zone. The main task was to fine tune the parameters of the gravitational potential of the bar. My contribution was more substantial for the task of deciding on the parameters and physics of our ISM model.
- **Running the simulations:** I mostly run autonomously the final production simulations on the available supercomputers. Support and feedback from Dr. Mattia Sormani was substantial however.

- **Analysis:** my contribution was central and equal to that of Dr. Mattia Sormani. Feedback from and discussion with our other collaborators was important as an iterative process during the analysis step as well as during the revision phase.
- **Figures:** my contribution was central. I produced most of the figures in the publication with major help and feedback from Dr. Mattia Sormani. I gave substantial feedback for the figures produced by Dr. Sormani instead.
- **Writing:** I have written large parts of the manuscript and gave feedback and contributions to the parts written by Dr. Mattia Sormani instead. The process was iterative and driven by feedback from our other collaborators.
- **Scientific discussion:** most collaborators contributed equally to the discussions, but Dr. Sormani and myself led the discussions and often proposed possible research directions which were usually first considered in private meetings and then debated with our other collaborators.

# Simulations of the Milky Way’s central molecular zone - I. Gas dynamics

Robin G. Tress<sup>1</sup>, Mattia C. Sormani<sup>1</sup>, Simon C.O. Glover<sup>1</sup>, Ralf S. Klessen<sup>1,2</sup>,  
Cara D. Battersby<sup>3</sup>, Paul C. Clark<sup>4</sup>, H Perry Hatchfield<sup>3</sup> and Rowan J. Smith<sup>5</sup>

<sup>1</sup>Universität Heidelberg, Zentrum für Astronomie, Institut für theoretische Astrophysik, Albert-Ueberle-Str. 2, 69120 Heidelberg, Germany

<sup>2</sup>Universität Heidelberg, Interdisziplinäres Zentrum für Wissenschaftliches Rechnen, Im Neuenheimer Feld 205, 69120 Heidelberg, Germany

<sup>3</sup>University of Connecticut, Department of Physics, 196 Auditorium Road, Unit 3046, Storrs, CT 06269, USA

<sup>4</sup>School of Physics and Astronomy, Queen’s Buildings, The Parade, Cardiff University, Cardiff, CF24 3AA, UK

<sup>5</sup>Jodrell Bank Centre for Astrophysics, School of Physics and Astronomy, University of Manchester, Oxford Road, Manchester M13 9PL, UK

## ABSTRACT

We use hydrodynamical simulations to study the Milky Way’s central molecular zone (CMZ). The simulations include a non-equilibrium chemical network, the gas self-gravity, star formation and supernova feedback. We resolve the structure of the interstellar medium at sub-parsec resolution while also capturing the interaction between the CMZ and the bar-driven large-scale flow out to  $R \sim 5$  kpc. Our main findings are as follows: (1) The distinction between inner ( $R \lesssim 120$  pc) and outer ( $120 \lesssim R \lesssim 450$  pc) CMZ that is sometimes proposed in the literature is unnecessary. Instead, the CMZ is best described as single structure, namely a star-forming ring with outer radius  $R \simeq 200$  pc which includes the 1.3° complex and which is directly interacting with the dust lanes that mediate the bar-driven inflow. (2) This accretion can induce a significant tilt of the CMZ out of the plane. A tilted CMZ might provide an alternative explanation to the  $\infty$ -shaped structure identified in Herschel data by Molinari et al. 2011. (3) The bar in our simulation efficiently drives an inflow from the Galactic disc ( $R \simeq 3$  kpc) down to the CMZ ( $R \simeq 200$  pc) of the order of  $1 M_{\odot} \text{ yr}^{-1}$ , consistent with observational determinations. (4) Supernova feedback can drive an inflow from the CMZ inwards towards the circumnuclear disc of the order of  $\sim 0.03 M_{\odot} \text{ yr}^{-1}$ . (5) We give a new interpretation for the 3D placement of the 20 and 50 km s<sup>-1</sup> clouds, according to which they are close ( $R \lesssim 30$  pc) to the Galactic centre, but are also connected to the larger-scale streams at  $R \gtrsim 100$  pc.

**Key words:** Galaxy: centre - Galaxy: kinematics and dynamics - ISM: kinematics and dynamics - ISM: clouds - ISM: evolution - stars: formation

## 1 INTRODUCTION

The central molecular zone (CMZ) is a concentration of molecular gas in the innermost few hundred parsecs ( $R \lesssim 200$  pc) of our Galaxy. This accumulation of gas is believed to be created and fed from the outside by the Galactic bar, which drives an inflow of gas from large radii ( $R \simeq 3$  kpc) inwards along the disc of the order of  $\sim 1 M_{\odot} \text{ yr}^{-1}$  (Sormani & Barnes 2019). The CMZ is the Milky Way (MW) counterpart of the star-forming nuclear rings commonly found at the centre of external barred galaxies such as NGC 1300 (see for example the atlas of nuclear rings of Comerón et al. 2010).

The CMZ has a total gas mass of approximately  $5 \times 10^7 M_{\odot}$  (Dahmen et al. 1998), which amounts to roughly 5% of all the molecular gas in the Galaxy. The distribution of molecular gas in the CMZ is highly asymmetric with respect to the Galactic centre, with about 3/4 of the gas seen in <sup>13</sup>CO and CS residing at  $l > 0$ , and only 1/4 at  $l < 0$  (Bally et al. 1988). Our previous simulations

have shown that such an asymmetry develops spontaneously when gas flows in a barred potential, even in the absence of stellar and/or other type of feedback: the highly non-axisymmetric potential of the bar drives large-scale turbulent flows, giving rise to fluctuations comparable to the observed asymmetry (Sormani et al. 2018).

The conditions in the CMZ are extreme. The CMZ has average densities (Longmore et al. 2017; Mills et al. 2018), temperatures (Immer et al. 2016; Ginsburg et al. 2016; Krieger et al. 2017; Oka et al. 2019), velocity dispersions (Shetty et al. 2012; Federrath et al. 2016) and estimated magnetic field strengths (Chuss et al. 2003; Crocker et al. 2010; Morris 2015; Mangilli et al. 2019) several orders of magnitudes higher than in the Galactic disc.

The inner Galaxy also hosts several high-energy processes. The most spectacular example is the presence of the Fermi Bubbles, two giant gamma-ray lobes extending  $\sim 8$  kpc above and below the Galactic centre (Su et al. 2010). These are part of a mul-

tipphase Galactic outflow that has been detected across most of the electromagnetic spectrum and that comprises most of the known interstellar gas phases including hot ionised ( $T \sim 10^6$  K, Kataoka et al. 2013; Ponti et al. 2019; Nakashima et al. 2019), warm ionised ( $T \sim 10^4$ - $10^5$  K, Fox et al. 2015; Bordoloi et al. 2017), cool atomic ( $T \sim 10^3$ - $10^4$  K, McClure-Griffiths et al. 2013; Di Teodoro et al. 2018) and cool molecular ( $T \sim 100$  K, Di Teodoro et al. 2020) gas.

Star formation and gas dynamics in the CMZ have been the subject of intense study during the past decade, which has produced vast advancements both on the observational (e.g. Molinari et al. 2011; Jones et al. 2012; Immer et al. 2012, 2016; Ginsburg et al. 2016; Henshaw et al. 2016b; Longmore et al. 2017; Krieger et al. 2017; Kauffmann et al. 2017b,a; Mills et al. 2018; Mangilli et al. 2019; Oka et al. 2019) and theoretical (e.g. Sormani et al. 2015a,c; Kruijssen et al. 2015; Krumholz & Kruijssen 2015; Krumholz et al. 2017; Ridley et al. 2017; Kruijssen et al. 2019a; Dale et al. 2019; Sormani et al. 2018, 2019; Armillotta et al. 2019, 2020; Li et al. 2020) sides. Despite these advancements, many important open questions remain.

In the current study and in a companion paper (Sormani et al. 2020, hereafter Paper II) we use high-resolution hydrodynamical simulations with sub-parsec resolution that include a non-equilibrium time-dependent chemical network, star formation and stellar feedback in order to address some of these questions. This paper focuses on describing the numerical methods and on the gas dynamics, while Paper II focuses on star formation.

Open questions that we address in the current work include:

- (i) Is gas in the CMZ on  $x_2$  orbits? (see Section 6.1)
- (ii) Is gas deposited by the bar-driven inflow onto an “outer CMZ” at  $R \simeq 450$  pc, or almost directly on the CMZ at  $R \lesssim 200$  pc? Is there an “outer CMZ” which is physically distinct from an “inner CMZ”? (see Section 6.2)
- (iii) What is the *dynamical* origin of the  $\infty$ -shape discovered by Molinari et al. (2011)? Is the CMZ disc tilted out of the Galactic plane? (see Section 6.4)
- (iv) How is gas transported from the CMZ inwards to the central few parsecs? (see Section 5.2)
- (v) Are the 20 and 50 km s<sup>-1</sup> clouds very close ( $R \leq 20$  pc) to SgrA\* or further out ( $R = 50$ -100 pc)? (see Section 6.3)

The paper is structured as follows. In Section 2 we describe our numerical methods and the differences between the present and our previous simulations. In Section 3 we give a brief overview of the overall gas dynamics and morphology. In Section 4 we discuss the thermal and chemical properties of our simulated ISM. In Section 5 we discuss inflows and outflows. In Section 6 we discuss the implications of our results for the open questions raised above. We sum up in Section 7.

## 2 NUMERICAL METHODS

The simulations presented here are similar to those we previously discussed in Sormani et al. (2018, 2019), with the following differences: (i) inclusion of the gas self-gravity; (ii) inclusion of a sub-grid prescription for star formation and stellar feedback. Besides that, we employ exactly the same externally imposed rotating barred potential, the same chemical/thermal treatment of the gas, and the same initial conditions as in Sormani et al. (2019). In Section 2.1 we give a brief overview that provides the minimum background necessary to read the remainder of this paper, while in Sections 2.2-2.7 we describe our numerical methods in more detail.

### 2.1 Overview

We use the moving-mesh code AREPO (Springel 2010; Weinberger et al. 2020). A more detailed description of the strengths of this code in the context of modelling the multi-phase nature of the interstellar medium on galactic scales can be found for example in Sect 2.1 of Tress et al. (2020). The simulations are three-dimensional and unmagnetised, and include a live chemical network that keeps track of hydrogen and carbon chemistry (see Section 2.3). The simulations comprise interstellar gas in the whole inner disc ( $R \leq 5$  kpc) of the MW. This allows us to model the CMZ in the context of the larger-scale flow, which is important since the CMZ strongly interacts with its surrounding through the bar inflow (Sormani et al. 2018). The gas is assumed to flow in a multi-component external rotating barred potential  $\Phi_{\text{ext}}(\mathbf{x}, t)$  which is constructed to fit the properties of the MW. This potential is identical to that used in Sormani et al. (2019) and is described in detail in the appendix of that paper.

The gas self-gravity is included. The process of star formation and stellar feedback processes are modelled as follows (see Sections 2.4 and 2.5 for more details):

- (i) When a high density region collapses and the resolution limit is reached, a sink particle (hereafter referred to simply as “sink”) is created to replace the gas in this region. The sink does not represent an individual star, but a small cluster which contains both gas and stars.
- (ii) Once a sink is created, a stellar population is assigned to it by drawing from an IMF according to the Poisson stochastic method described in Sormani et al. (2017).
- (iii) The sinks are allowed to accrete mass at later times. Their stellar population is updated every time mass is accreted.
- (iv) For each massive star ( $M \geq 8 M_{\odot}$ ) assigned to the sink, we produce a supernova (SN) event with a time delay which depends on the stellar progenitor mass. Each SN event injects energy/momentum into the ISM and gives back to the environment part of the gas “locked-up” in the sink. SN feedback is the only type of feedback included in the simulation.
- (v) When all the SNe in a sink have exploded and all its gas content has been given back to the environment, the sink is converted into a collisionless N-body particle with a mass equal to the stellar mass of the sink. This N-body particle will continue to exist indefinitely in the simulation and will affect it through its gravitational potential.

For simplicity, we ignore magnetic fields. Thus our simulations are unable to capture dynamical effects that may arise as a consequence of the strong and highly ordered magnetic field that is present in the CMZ (Chuss et al. 2003; Crocker et al. 2010; Morris 2015; Mangilli et al. 2019), which could for example induce radial mass and angular momentum transport (Balbus & Hawley 1998), drive Galactic outflows (Pakmor & Springel 2013), shape the properties and structure of molecular clouds (Pillai et al. 2015; Girichidis et al. 2018) and affect the star formation rate (Mac Low & Klessen 2004; Krumholz & Federrath 2019).

When making projections onto the plane of the Sky, we assume an angle between the Sun-Galactic centre line and the bar major axis of  $\phi = 20^\circ$ , as in our previous papers (Sormani et al. 2018, 2019).

## 2.2 Equations solved by the code

The code solves the equations of fluid dynamics:

$$\frac{\partial \rho}{\partial t} + \nabla \cdot (\rho \mathbf{v}) = 0, \quad (1)$$

$$\frac{\partial (\rho \mathbf{v})}{\partial t} + \nabla \cdot (\rho \mathbf{v} \otimes \mathbf{v} + P \mathbf{I}) = -\rho \nabla \Phi, \quad (2)$$

$$\frac{\partial (\rho e)}{\partial t} + \nabla \cdot [(\rho e + P) \mathbf{v}] = \dot{Q} + \rho \frac{\partial \Phi}{\partial t}, \quad (3)$$

where  $\rho$  is the gas density,  $\mathbf{v}$  is the velocity,  $P$  is the thermal pressure,  $\mathbf{I}$  is the identity matrix,  $e = e_{\text{therm}} + \Phi + \mathbf{v}^2/2$  is the energy per unit mass,  $e_{\text{therm}}$  is the thermal energy per unit mass. We adopt the equation of state of an ideal gas,  $P = (\gamma - 1)\rho e_{\text{therm}}$ , where  $\gamma = 5/3$  is the adiabatic index.

The term  $\dot{Q}$  in Eq. (3) contains the changes to the internal energy of the gas due to radiative, chemical and feedback processes ( $\dot{Q} = 0$  for an adiabatic gas). The following processes contribute to  $\dot{Q}$ : (i) the cooling function, which is part of the chemical network (Section 2.3) and which depends on the instantaneous chemical composition of the gas (Glover et al. 2010; Glover & Clark 2012); (ii) heat released and absorbed by those chemical processes that occur in the interstellar medium and are tracked by our chemical network (Section 2.3), such as the formation of  $\text{H}_2$  on dust grains; (iii) the averaged interstellar radiation field and cosmic ray ionisation rate, which represent external heating sources (Section 2.3); (iv) the SN feedback, which injects energy into the ISM if the Sedov-Taylor phase is resolved (see Section 2.5)

The term  $\Phi$  represents the sum of the externally imposed gravitational potential and of the self-gravity of the gas, sinks and N-body particles:

$$\Phi = \Phi_{\text{ext}} + \Phi_{\text{sg}}. \quad (4)$$

The code calculates  $\Phi_{\text{sg}}$  by solving Poisson’s equation at each timestep:

$$\nabla^2 \Phi_{\text{sg}} = 4\pi G \rho. \quad (5)$$

AREPO solves Poisson’s equation by using a tree-based approach adapted from an improved version of GADGET-2 (Springel 2005). In this approach each gas cell is treated as a point mass located at the centre of the cell with an associated gravitational softening. The gas softening length  $\epsilon_{\text{gas}}$  is adaptive and depends on the cell size according to  $\epsilon_{\text{gas}} = 2r_{\text{cell}}$ , where  $r_{\text{cell}}$  is the radius of a sphere with the same volume as the cell. AREPO ensures that the gas cells remain quasi-spherical and so this radius is an accurate way of characterising the size of the cells. The lower limit of the softening length is set at  $\epsilon_{\text{gas},\text{min}} = 0.1$  pc. The softening length of the sinks (which is the same as for N-body particles) is constant and is reported in Table 1.

## 2.3 Chemistry of the gas

We account for the chemical evolution of the gas using an updated version of the NL97 chemical network from Glover & Clark (2012), which itself was based on the work of Glover & Mac Low (2007a,b) and Nelson & Langer (1997). With this network, we solve for the non-equilibrium abundances of H,  $\text{H}_2$ ,  $\text{H}^+$ ,  $\text{C}^+$ , O, CO and free electrons. This network is the same used in Sormani et al. (2018) and we refer to their Section 3.4 for a more extensive description of it.

One of the key parameters of the network is the strength of the spatially averaged interstellar radiation field (ISRF). This is set to

the standard value  $G_0$  measured in the solar neighbourhood (Draine 1978) diminished by a local attenuation factor which depends on the amount of gas present within 30 pc of each computational cell. This attenuation factor is introduced to account for the effects of dust extinction and  $\text{H}_2$  self-shielding and is calculated using the TRECOL algorithm described in Clark et al. (2012). The cosmic ray ionisation rate (CRIR) is fixed to  $\zeta_{\text{H}} = 3 \times 10^{-17} \text{ s}^{-1}$  (Goldsmith & Langer 1978). The values adopted for the strength of the ISRF and the size of the CRIR correspond to the ‘low’ simulation of Sormani et al. (2018). While absorption studies of  $\text{H}_3^+$  (Le Petit et al. 2016; Oka et al. 2019) and the elevated molecular gas temperatures (Clark et al. 2013; Ginsburg et al. 2016) indicate that both the ISRF and the CRIR are almost certainly higher than this in the CMZ, we have chosen these values in order to facilitate comparison with the previous simulation in Sormani et al. (2019), allowing us to isolate the effects of self-gravity and SN feedback on the star formation process, which as mentioned above are the only differences between Sormani et al. (2019) and the simulation presented here. The main effects of a higher CRIR would be to decrease the amount of molecular gas and to make the gas warmer. In particular, since cosmic rays can penetrate much further than UV photons into high-column density regions, they can heat the interior of molecular clouds (Clark et al. 2013). However, we have shown in Sormani et al. (2018) that the strength of the ISRF/CRIR makes little difference to the large-scale dynamics. Indeed, even if the ISRF field is a factor of a 1000 higher than in the solar neighbourhood, the thermal sound speed of the molecular gas never comes close to the values of  $c_s = 5\text{--}10 \text{ km s}^{-1}$  which would be needed to significantly affect the dynamics of the gas (Sormani et al. 2015a). The effects of varying the strengths of the ISRF/CRIR in combination with the inclusion of self-gravity will be explored in future work. Finally, we impose a temperature floor  $T_{\text{floor}} = 20$  K on the simulated ISM. Without this floor, the code occasionally produces anomalously low temperatures in cells close to the resolution limit undergoing strong adiabatic cooling, causing it to crash.

## 2.4 Sink particles

The sink particles implementation used here is identical to that in Tress et al. (2020). We therefore give only a brief description here and refer to their Section 2.3 for more details.

Accreting ‘sink particles’ have been used mainly in small-scale simulations of *individual* molecular clouds, in which the SF process can be spatially and temporally resolved reasonably well, in order to replace collapsing high-density region when the resolution limit is reached (e.g. Bate et al. 1995; Federrath et al. 2010). In larger, galactic-scale simulations, in which the SF process is resolved less well, non-accreting stochastic ‘star particles’ are instead more often employed (e.g. Katz 1992; Katz et al. 1996; Stinson et al. 2006). The former approach requires higher resolution but is more predictive, and allows one to assess the star formation efficiency and the mass distribution of fragments in a robust and quantitative way (Federrath et al. 2010). The latter approach can be used to produce a healthy ISM matter cycle in lower-resolution simulations, but its predictive power is more limited, being often fine-tuned to reproduce the Schmidt-Kennicutt relation (Schmidt 1959; Kennicutt 1998), rather than ‘predicting’ it.

Our simulations are in an intermediate regime. While we are able to resolve individual molecular clouds very well (see Section 2.6 and Figure 3), we do not have the resolution to follow the formation of individual stars. In this intermediate regime, we choose to use sink particles, so that we can take advantage of their superior

predictive power. However, in our simulations each sink represents a small stellar cluster rather than an individual star. We assume that only a fraction  $\epsilon_{\text{SF}} = 5\%$  of the mass accreted actually forms stars, while the rest is “locked-up” as gas in the sinks until SN feedback (see Section 2.5) gives it back to the environment. This is necessary for two important reasons. First, our resolution is not sufficient to fully resolve the turbulent cascade within individual molecular clouds or the generation of the associated density sub-structure. Because of this, the density of a Voronoi cell within a molecular cloud should properly be thought of as representing the mean density of the gas associated with the region of space represented by the cell. Not all of the gas within that region of space will actually be at that density, and hence not all of the gas will be immediately available for star formation. Second, our simulations neglect a number of physical effects (e.g. magnetic field, protostellar outflows) that are known to make star formation less efficient (see e.g. Federrath 2015). Because of this, the adoption of an efficiency of  $\epsilon_{\text{SF}} = 100\%$  would actually be less realistic than our choice of a smaller value and would result in an unrealistically high star formation rate. We note that although the choice of  $\epsilon_{\text{SF}} = 5\%$  is somewhat arbitrary, at our current resolution it does yield a depletion time for the CMZ in fairly good agreement with the observationally determined value (see Paper II). Moreover, our choice yields a star formation efficiency per free-fall time  $\epsilon_{\text{ff}} \simeq 1\%$ , in good agreement with most observational determinations of this value (see e.g. Krumholz et al. 2012; Evans et al. 2014; Barnes et al. 2017; Utomo et al. 2018).

Following Federrath et al. (2010), a sink particle is created if a region within an accretion radius  $r_{\text{acc}}$  and above a density threshold  $\rho_c$  simultaneously satisfies all the following criteria:

- (i) The gas flow is locally converging. To establish this, we require not only that the velocity divergence is negative ( $\nabla \cdot \mathbf{v} < 0$ ), but also that the divergence of the acceleration is negative ( $\nabla \cdot \mathbf{a} < 0$ ).
- (ii) The region is located at a local minimum of the potential  $\Phi$ .
- (iii) The region is not situated within the accretion radius of another sink and also will not move within the accretion radius of a sink in a time smaller than the local free-fall time.
- (iv) The region is gravitationally bound, i.e.  $U > 2(E_k + E_{\text{th}})$ , where  $U = GM^2/r_{\text{acc}}$  is the gravitational energy of the region within the accretion radius,  $E_k = 1/2 \sum_i m_i \Delta v_i^2$  is the total kinetic energy of all gas particles within the accretion radius with respect to the centre of collapse,  $E_{\text{th}} = \sum_i m_i e_{\text{th},i}$  is the total internal energy of the same region, the sum is extended over all cells within the region, and  $m_i$  and  $e_{\text{th},i}$  are the mass and the internal energy per unit mass of the single cells respectively.

These criteria help to ensure that a region is only converted into a sink if it is truly self-gravitating and collapsing. Sink particles are collisionless, so they do not exert/feel pressure forces and interact with gas particles only through gravity. The softening length of the sink particles is reported in Table 1.

Sink particles accrete mass during the simulation. If a gas cell is (i) denser than the threshold density  $\rho_c$ ; (ii) within the accretion radius  $r_{\text{acc}}$  of the sink particle and (iii) gravitationally bound to it, then we move an amount of mass

$$\Delta m = (\rho_{\text{cell}} - \rho_c) V_{\text{cell}} \quad (6)$$

from the cell to the sink, where  $\rho_{\text{cell}}$  is the initial gas density in the cell and  $V_{\text{cell}}$  is its volume. Afterwards the new density of the cell is simply the threshold density  $\rho_c$ . We also update appropriately any other quantities in the cell that depend on the mass, such as the total momentum or kinetic energy. In the case where a given gas cell is located within the accretion radii of multiple sink particles,

parameter	units	value
$\rho_c$	$\text{g cm}^{-3}$	$10^{-20}$
$r_{\text{acc}}$	pc	1.0
$r_{\text{soft}}$	pc	1.0
$\epsilon_{\text{SF}}$		0.05
$r_{\text{sc}}$	pc	5.0

**Table 1.** Parameters of the sink particles.  $\rho_c$  is the density threshold,  $r_{\text{acc}}$  is the accretion radius,  $r_{\text{soft}}$  is the softening length,  $\epsilon_{\text{SF}}$  is the SF efficiency, and  $r_{\text{sc}}$  is the scatter radius of SNe around the sink.

we place the accreted mass from it onto the sink to which the gas is most strongly bound.

Ideally, we would like to have the threshold density  $\rho_c$  as large as possible, but in practice this is set by what we can afford in terms of computational resources. In order to properly follow the hierarchical collapse and correctly follow the underlying fragmentation, we need to ensure that the local Jeans length is resolved by at least four resolution elements (Truelove et al. 1997; see also Federrath et al. 2011 for further discussion). If the threshold density  $\rho_c$  is too high, the Jeans length can become prohibitively small. In this first set of simulation we choose set the threshold density at  $\rho_c = 10^{-20} \text{ g cm}^{-3}$ , and stop refining for densities above this threshold (see Section 2.6). This is a good compromise between resolution in the collapsing regions, and computational performance. The chosen density threshold allows us to resolve star formation at the average densities of the CMZ.

The accretion radius is chosen such that at the given threshold density  $\rho_c$ , several cells fall inside  $r_{\text{acc}}$  given the local size of the cells. The gravitational softening length of the collisionless sink particles is set to the same value as  $r_{\text{acc}}$ , as this ensures that the gravitational potential is not altered much due to the infall of mass onto a sink, while at the same time limiting the size of the gravitational acceleration produced within  $r_{\text{acc}}$ , which otherwise would have a detrimental effect on performance. The main parameters that characterise the sink particles used in our study are listed in Table 1.

The top panel 1 illustrates the typical mass distribution of the sinks at the time of their formation (thick lines) and the instantaneous mass distribution at a representative time (thin lines). The figure shows that the sinks have on average higher masses in the CMZ compared to the Galactic disc (see Figure 4 for the definition of CMZ and disc). The bottom panel in the figure shows a histogram of the sink lifetimes.

The typical accretion histories of a representative sample of our sinks are shown in Figure 2. This figure shows that most of the accretion takes place during the first few Myr, when the sink is still immersed in the collapsing gas cloud from which it originated (see also discussion in Klessen & Burkert 2000). Accretion usually stops when the gas and sink decouple at later times (due to feedback and to gas and sinks following different equations of motion, see discussion in Section 3.3 of Paper II).

## 2.5 Stellar feedback

The only type of feedback included in our simulation is type II supernova (SN) feedback. The implementation used here is identical to that described in Section 2.4 of Tress et al. (2020), to which we refer for a more detailed description.

Once a sink is created, it must be “populated” with stars. We attribute a discrete stellar population to the sink sampling from a Kroupa (2001) initial mass function (IMF) using the method de-

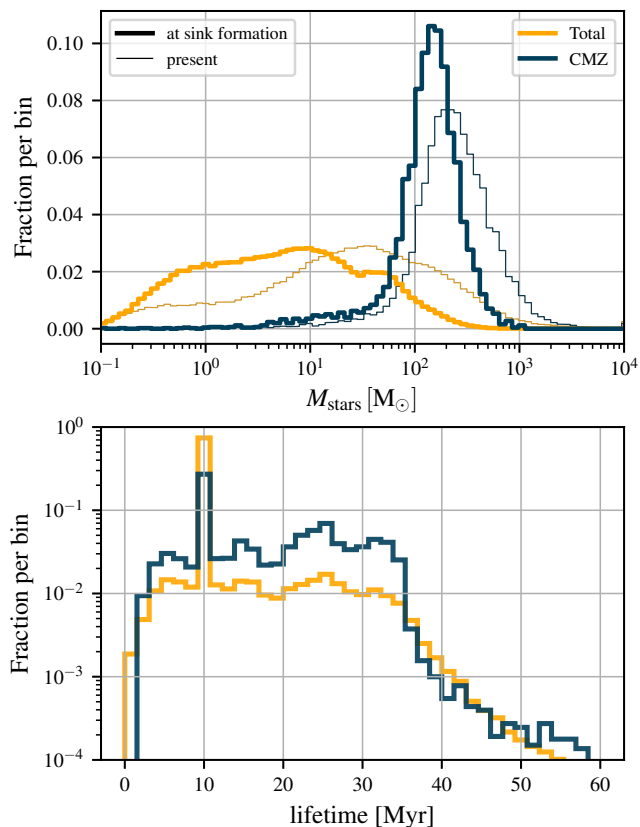


**Figure 1.** *Top panel:* mass distribution of the stellar mass of sink particles found at a representative snapshot in the simulations. We show the mass distribution at their formation (*thick lines*) and at the current time of the snapshot (*thin lines*) where the mass increased due to accretion. *Bottom panel:* distribution of the life-times of the sink particles in the simulation. The peak at 10 Myr is due to sink particles that failed to generate massive stars and are then converted to a passive star particle (see Section 2.5). Blue and yellow indicate sinks in the CMZ and disc respectively (see Section 3.1 and Figure 4 for definitions of CMZ and disc used in the analysis).

scribed in Sormani et al. (2017). According to this method, we draw the IMF according to a Poisson distribution such that the average stellar mass attributed to a sink is  $\epsilon_{\text{SF}} M_{\text{sink}}$ , where  $M_{\text{sink}}$  is the mass of the sink and  $\epsilon_{\text{SF}}$  its SF efficiency (see Table 1). This approach ensures that, globally, the mass distribution of stars in the simulation follows the IMF. The same procedure is repeated every time a mass  $\Delta M_{\text{sink}}$  is accreted onto the sink, by drawing an IMF according to a Poisson distribution with average stellar mass  $\Delta M_{\text{sink}} \epsilon_{\text{SF}}$ . Our method ensures that the final stellar population of the sink (including the stars formed from mass accreted at later times) is independent of the particular accretion history of the sink.

For each star more massive than  $8 M_{\odot}$  associated with the sink, we generate a SN event at the end of the lifetime of the star, which are calculated based on their mass from Table 25.6 of Maeder (2009). Since the sink represents an entire group of stars that can interact dynamically, we do not assume that the SN occurs exactly at the location of the sink. Instead, we randomly sample the SN location from a Gaussian distribution centred on the particle and with standard deviation  $r_{\text{sc}} = 5$  pc.

Since the assumed efficiency of SF within the sink is relatively small, most of the mass in the sink represents gas that should be

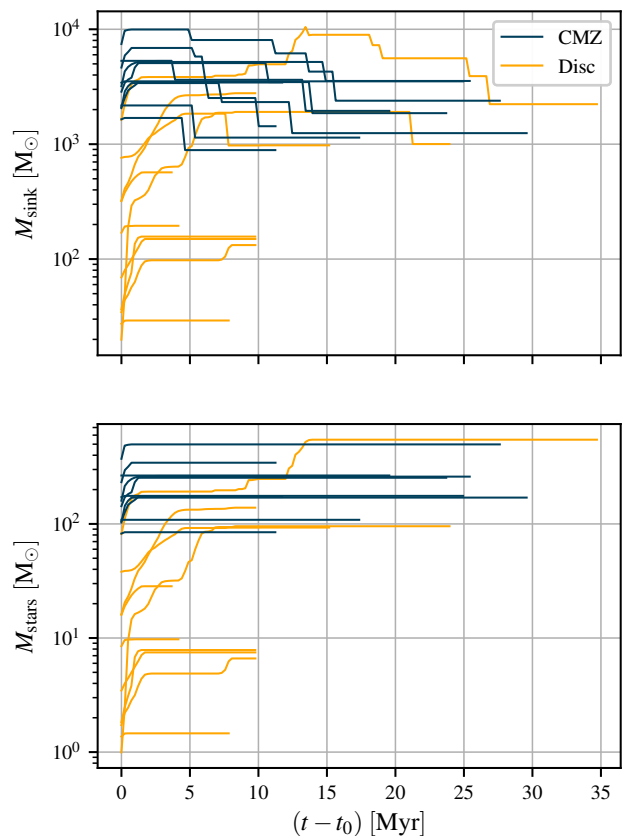


**Figure 2.** Accretion history for a sample of randomly selected sink particles in our simulation. *Top panel:* total mass of the sink (gas + stars) as a function of time for randomly selected sinks (i) in the CMZ (blue lines) and (ii) in the disc (orange lines).  $t_0$  denotes the sink formation time. Each increase in the mass corresponds to an accretion event, while each decrease corresponds to a SN explosion (which frees some of the gas locked-up in the sink). *Bottom panel:* total stellar mass as a function of time for the same sample of sinks shown in the top panel. The stellar mass does not decrease when a SN event occurs, contrary to the total mass, which decreases because gas is given back to the environment. This figure shows that (a) most of the accretion usually takes place during the first few Myr, when the sinks and the collapsing gas cloud from which they originated have not yet decoupled (see also discussion in Section 3.3 of Paper II), and (b) the sink formation mass is on average higher in the CMZ than in the disc (see also Figure 1). The typical lifetimes of the sinks can also be read off this figure: sinks without massive stars (and therefore without any associated SN) event die after  $t = 10$  Myr, while sinks with massive stars die after the last SN event has taken place (see Section 2.5 for more details).

eventually returned to the ISM. The “gaseous” mass locked-up in the sink is therefore gradually given back to the ISM with every SN event. Each event ejects a gas mass of  $M_{\text{ej}} = (M_{\text{sink}} - M_{\text{stars}})/n_{\text{SN}}$ , where  $M_{\text{sink}}$  is the mass of the sink at the time that the supernova occurs,  $M_{\text{stars}}$  is the mass of stars contained within the sink at that time, and  $n_{\text{SN}}$  is the remaining number of SN events that the sink harbors. The mass is distributed uniformly within the energy injection region. The temperature of the injection cells is not altered at this stage.

Once the last massive star has reached the end of its lifetime, the sink has a final mass of  $M_{\text{stars}}$ . At this point, we convert it into a collisionless  $N$ -body particle representing its evolved stellar population. It will then continue to exist until the end of the simulation

as a collisionless particle which interacts with the gas only through gravity.

It is not uncommon to have sinks that do not accrete enough mass to form a massive star. In this case we cannot return the gas mass trapped within the sink during an SN event. Instead, after a period of 10 Myr, if the sink still did not manage to create a massive star, we convert it into a collisionless N-body particle and return the remaining mass (95%) to the ISM by uniformly adding it to all gas particles in a surrounding sphere of  $R = 100$  pc. This is necessary because since gas and stars follow different equations of motion they will eventually decouple (stars are collisionless so that they do not feel pressure forces, while gas is collisional; see also Section 3.3 of Paper II). Typical lifetimes of the sinks can be read off Figure 1.

To model the supernova energy/momentum injection of each SN event, we calculate the radius of a supernova remnant at the end of its Sedov-Taylor phase based on an assumed SN energy of  $10^{51}$  erg and the local mean density  $\bar{n}$ , which for solar metallicity is (Blondin et al. 1998)

$$R_{\text{ST}} = 19.1 \left( \frac{\bar{n}}{1 \text{ cm}^{-3}} \right)^{-7/17} \text{ pc}, \quad (7)$$

where in our case  $\bar{n}$  is calculated including the contributions from both the ambient gas and also the mass loading of the SN event. We compare this with the radius of the injection region,  $R_{\text{inj}}$ , defined as the size of the smallest sphere around the explosion site that contains 40 grid cells. If  $R_{\text{ST}} > R_{\text{inj}}$ , the Sedov-Taylor phase is resolved and we inject  $E_{\text{SN}} = 10^{51}$  erg into the injection region in the form of thermal energy and fully ionise the contained gas. If, on the other hand, the Sedov-Taylor phase of the SN remnant is unresolved, thermal energy would be radiated away too quickly, making it unable to generate a strong shock and deposit the correct amount of kinetic energy into the ISM. In this case, as is common practice in numerical simulations, we inject directly an amount of momentum given by (see e.g. Martizzi et al. 2015; Gatto et al. 2015; Kim & Ostriker 2015)

$$p_{\text{fin}} = 2.6 \times 10^5 \bar{n}^{-2/17} M_{\odot} \text{ km s}^{-1}, \quad (8)$$

for a SN of energy  $E_{\text{SN}} = 10^{51}$  erg and solar metallicity. We do not change the temperature or the ionisation state of the region in this case as this would throw off-balance the energy budget in large unresolved regions. Since we lack early feedback, the initial SN of a star-forming region will be injected into a high density medium in which the Sedov-Taylor phase is often unresolved. Therefore most of the SNe in the simulation inject momentum, with only around 15% injecting thermal energy.

Momentum injection alone cannot produce a hot phase in the ISM. By keeping the injection radius small we minimise the number of occasions on which we must inject momentum rather than thermal energy. On the other hand, we cannot take too small an injection radius since this would lead to anisotropic momentum injection due to the small number of cells amongst which to distribute the momentum. Even though SNe are observed to be anisotropic in some instances (e.g. Wang & Wheeler 2008), we have no reason to expect that the artificial anisotropy introduced by taking a very small accretion radius will resemble this real physical anisotropy. We therefore prefer to minimise the numerical noise that such a low cell count would introduce. We have found through experimentation that defining  $R_{\text{inj}}$  such that a total of 40 grid cells are contained within a sphere of that radius seems to offer the best trade-off between minimising the number of momentum injection events and minimising the impact of grid noise and anisotropic expansion on

the evolution of the individual remnants. We note that this mixed approach of injecting thermal energy in regions where  $R_{\text{ST}}$  is resolved and momentum in regions where this is not the case is not new. Similar methods have been successfully used by a number of other authors to study the impact of SN feedback on the ISM (see e.g. Kimm & Cen 2014; Hopkins et al. 2014; Walch et al. 2015; Simpson et al. 2015; Kim & Ostriker 2017).

Finally, we mention that SN is not the only type of feedback associated with SF. For example, stellar winds and radiation from young stars also play an important role in dispersing GMCs, particularly since they act much earlier than SN feedback (e.g. Dale et al. 2014; Inutsuka et al. 2015; Offner & Arce 2015; Rosen et al. 2016; Gatto et al. 2017; Rahner et al. 2018, 2019; Kruijssen et al. 2019b; Chevance et al. 2020). However, it remains computationally challenging to include all of these forms of feedback in simulations with the scale and resolution of those presented here. Therefore, in our initial study we restrict our attention to the effects of SN feedback and defer an investigation of other feedback processes to future work.

## 2.6 Resolution

We use the system of mass refinement present in AREPO so that the resolution depends on the local density and temperature according to the following criteria. We use a base target cell mass of  $100 M_{\odot}$ . This means that no cells in the simulation fall below this resolution (i.e., no cell in the simulations can have mass larger than this) within a tolerance factor  $\sim 2$ . Then, we ensure that the Jeans length is locally resolved by at least four resolution elements according to the criterion of Truelove et al. (1997). We stop refining for densities above the sink creation threshold  $\rho_c$  (see Table 1 and discussion in Section 2.4). The resolution achieved in our simulation is displayed graphically in Figure 3.

## 2.7 Initial conditions

We initialise the density according to the following axisymmetric density distribution:

$$\rho(R, z) = \frac{\Sigma_0}{4z_d} \exp\left(-\frac{R_m}{R} - \frac{R}{R_d}\right) \text{sech}\left(\frac{z}{2z_d}\right)^2, \quad (9)$$

where  $(R, \phi, z)$  denote standard cylindrical coordinates,  $z_d = 85$  pc,  $R_d = 7$  kpc,  $R_m = 1.5$  kpc,  $\Sigma_0 = 50 M_{\odot} \text{ pc}^{-2}$ , and we cut the disc so that  $\rho = 0$  for  $R \geq 5$  kpc. This profile matches the observed radial distribution of gas in the Galaxy (Kalberla & Dedes 2008; Heyer & Dame 2015). The total initial gas mass in the simulation is  $\simeq 1.5 \times 10^9 M_{\odot}$ . The computational box has a total size of  $24 \times 24 \times 24$  kpc with periodic boundary conditions. The box is sufficiently large that the outer boundary has a negligible effect on the evolution of the simulated galaxy.

In order to avoid transients, we introduce the bar gradually, as is common practice in simulations of gas flow in barred potentials (e.g. Athanassoula 1992). We start with gas in equilibrium on circular orbits in an axisymmetrised potential and then we turn on the non-axisymmetric part of the potential linearly during the first 146 Myr (approximately one bar rotation) while keeping constant the total mass distribution which generates the underlying external potential. Therefore, only the simulation at  $t \geq 146$  Myr, when the bar is fully on, will be considered for the analysis in this paper.

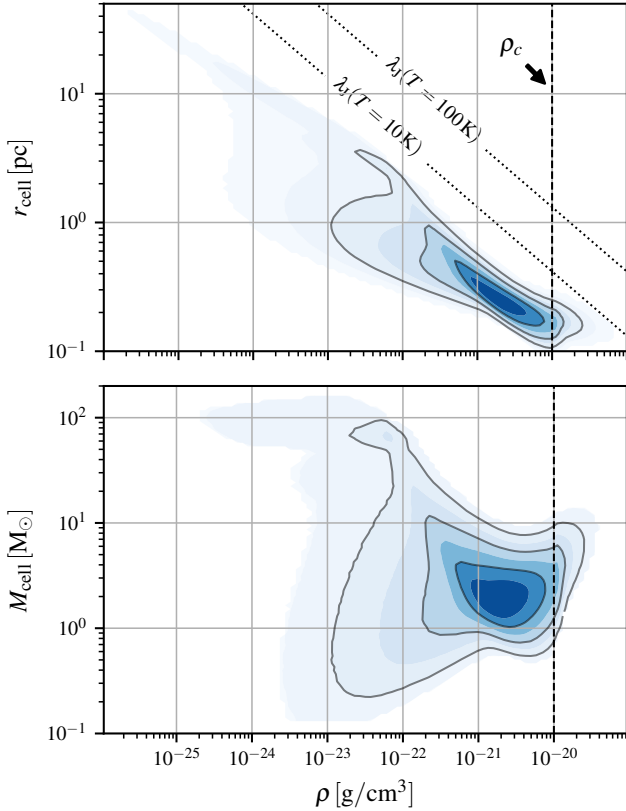


**Figure 3.** *Top:* spatial resolution as a function of density in our simulation.  $r_{\text{cell}}$  is the radius of a sphere with the same volume as the cell. *Bottom:* mass of the cells as a function of density. The black contours contain (25, 50, 75)% of the total number of cells. The dotted lines show the Jeans length  $\lambda_J$  at the indicated temperature. The vertical dashed line denotes the sink density formation threshold  $\rho_c$  (See Table 1).

### 3 GENERAL PROPERTIES OF THE GAS FLOWS

#### 3.1 Subdivision in three regions: CMZ, DLR, disc

In order to facilitate the analysis in the following sections, we subdivide our simulation into three spatial regions (see Figure 4):

- The *CMZ* is defined as the region within cylindrical radius  $R \leq 250$  pc.
- The *dust lane region (DLR)* is the elongated transition region between the CMZ and the Galactic disc, where highly non-circular gas motions caused by the bar are present.<sup>1</sup>
- The *disc* is defined as everything outside the DLR. In our simulation, the gaseous disc extends out to  $R \simeq 5$  kpc (see Section 2.7).

#### 3.2 Large-scale gas dynamics

Figure 5 shows the surface density of the gas at different times in the simulation and Figure 6 zooms onto the CMZ. The appendix

<sup>1</sup> The name “dust lane region” comes from the fact that this is the region where in observations of external barred galaxies such as NGC 1300 or NGC 5383 one can see “the presence of two dust lanes leaving the nucleus one on each side of the bar and extending into the spiral arms” (Sandage 1961). In the simulation, these correspond to the large-scale shocks which are clearly visible in Figure 4 (e.g. Athanassoula 1992).

provides further figures in different tracers. Figure 7 shows the instantaneous gas streamlines. These figures show that the large-scale gas flow approximately follows the  $x_1/x_2$  orbit<sup>2</sup> dynamics, similar to our previous non-self gravitating simulations (Sormani et al. 2018, 2019). This has been described in detail for example in Section 4.1 of Sormani et al. (2018) and references therein, and will not be repeated here.

#### 3.3 Morphology of the CMZ

The top and middle panels of Figure 8 show the time-averaged surface density of the gas. The time-averaged flow is very smooth and regular, and the CMZ shows up as a clearly defined ring. Comparing this figure with Figure 6 shows that while the time-averaged morphology is very regular and relatively simple, the instantaneous morphology of the CMZ is very rich in substructure that is transient in time. At any given time the CMZ can look very turbulent and irregular, to the point that the underlying regular structure is not obvious or even discernible. This illustrates that the most natural way to think of the current structure of the CMZ is as the sum of a regular, time-averaged structure and a set of highly transient perturbations superimposed on it.

These considerations are another manifestation of what is shown in Figure 12 of Sormani et al. (2018), where we display a typical molecular cloud orbiting in the CMZ at different times. We found that while the centre of mass of the cloud closely follows  $x_2$  orbits on average, on top of this underlying “guiding centre” motion there are often significant turbulent fluctuations.<sup>3</sup> These fluctuations can make the instantaneous observed kinematics of the cloud look very different from what we may naively expect from a regular  $x_2$  orbit. We continue the discussion on this point in Section 6.1

Comparison of the top and middle panels of Figure 8 shows that the CMZ morphology also depends on which tracer one is considering. The CMZ morphology in HI is more spiral-like, while in H<sub>2</sub> it is more ring-like. This is consistent with the fact that in external galaxies the morphologies of nuclear rings are complex, often showing both ring-like and spiral-like structures with a strong dependence on the tracer used (e.g. Izumi et al. 2013).

Figure 9 compares the present simulations (that include gas self-gravity and stellar feedback) to our previous simulations (which did not). One of the most notable differences is that in the former gas can be found at radii inside the main CMZ ring, while in the latter there was essentially no gas inside the CMZ ring. This suggests that self-gravity and stellar feedback may play a major role in driving the gas from the CMZ inwards, a currently important open question since it is related to the fuelling of the super-massive black hole SgrA\*. We investigate this in more detail in Section 5.2.

#### 3.4 Resolving individual molecular clouds

With this simulation we achieve resolutions that allow us to follow the formation of individual molecular clouds and start resolving their substructure. To illustrate this we show in Figure 10 a three-colour composite image of the CMZ with zoom-in panels onto individual cloud complexes. The dynamic nature of the complex en-

<sup>2</sup> This nomenclature has become standard in the literature after the work of Contopoulos & Grosbol (1989).

<sup>3</sup> In Sormani et al. (2018) these fluctuations were entirely due to the bar inflow, while in the present work they are due to both supernova feedback and the bar inflow.

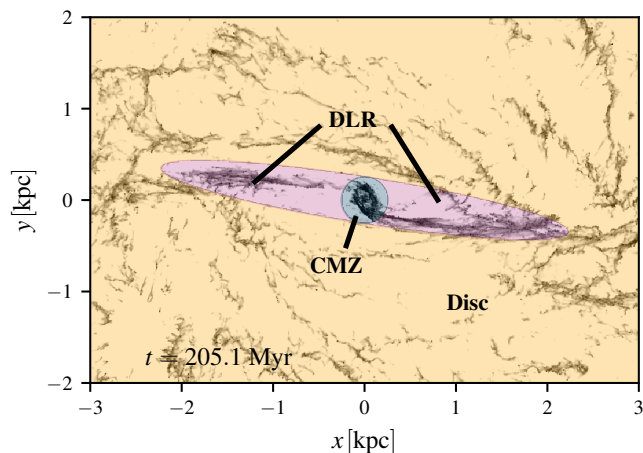


**Figure 4.** Definition of the three regions (CMZ, DLR, disc) into which we subdivide our simulated Galaxy for subsequent analysis. See Section 3.1 for more details.

environment in which the molecular clouds are embedded becomes clear from this figure. The clouds exhibit a complicated filamentary morphology, far from the idealised “spherical cloud” that is often used as a model. Clearly they cannot be idealised as individual and disconnected entities, but are part of a large interconnected network. Importantly, the clouds are part of and form self-consistently from the large-scale flow driven by the Galactic bar. Several processes unique to this environment shape their morphology, lifetime and evolution. Extreme shearing, stretching and compressive forces at the locations where clouds orbiting in the CMZ violently collide with the high velocity gas plunging in from the dust lanes produce dense and highly elongated structures around the apocentre (see Panels B and C of Figure 10). These clouds can grow extremely compact and massive while moving downstream of the apocentre due to their self-gravity (for instance Panel D of Figure 10), which will lead to intense star formation. Finally, supernova feedback leads to the formation of a filamentary gaseous disc in the innermost few tens of pc (Panel A of Figure 10), which is fed by the main CMZ ring (see Section 5.2). A more detailed analysis of the properties of the molecular cloud population will be presented in a future work.

## 4 THERMAL AND CHEMICAL PHASES OF THE ISM

### 4.1 A three-phase medium

The top panel in Figure 11 shows that the ISM in the simulation is a three phase medium. The cold component ( $T \leq 10^3$  K) is predominantly molecular and is well traced by  $\text{H}_2$  and CO. The warm component ( $10^3 < T < 10^{4.5}$  K) is well traced by H. The hot component ( $T \geq 10^{4.5}$  K) is produced by the SN feedback and is almost completely ionised. From the top panel in Figure 11 one can read off the typical densities of the three phases. The transition from warm (atomic) to cold (molecular) gas occurs around  $n \sim 10^2 \text{ cm}^{-3}$ , while the transition from warm to hot occurs around  $n \sim 10^{-2} \text{ cm}^{-3}$ . From Figure 12 one can see how the mass is distributed into the three phases. Globally, most of the mass is in the cold phase. The hot phase is the least massive phase, but as discussed below it has larger volume filling factors.

Figure 13 shows the volume filling factors of the cold, warm

and hot components in different regions. Most of the volume in the CMZ is occupied by the warm phase ( $\sim 70\%$ ), followed by the hot phase ( $\sim 25\%$ ), and by the cold phase ( $\sim 5\%$ ). These values are roughly consistent with the observational estimates of Oka et al. (2019) stating that the volume filling factor of the dense molecular gas is  $< 10\%$  and of Ferrière et al. (2007) who find that the filling factors of the cold molecular component is  $\sim 3.3\%$ . Figure 13 also shows that there is significant scatter in the filling factors at different locations within the same region, so they can be expected to vary from sightline to sightline in observations. In the DLR, the warm ( $\sim 65\%$ ) and hot ( $\sim 35\%$ ) volume filling factors are similar to those of the CMZ, but there is a higher volume fraction of molecular gas ( $\sim 10\%$ ) and it is possible to find 100 pc-wide regions with values reaching  $f_{\text{cold}} \sim 50\%$ . In the Disc, the warm phase does not dominate the volume contrary to the CMZ ( $\sim 35\%$ ), and most of the volume is occupied by the hot phase (60%). The filling factor of the cold phase remains small ( $\sim 5\%$ ) although it is still possible to find 100 pc-wide regions with high  $f_{\text{cold}}$ , similarly to the DLR. In the Halo, the hot phase becomes dominant ( $\sim 80\%$ ) while the cold phase is negligible ( $\lesssim 0.1\%$ ).

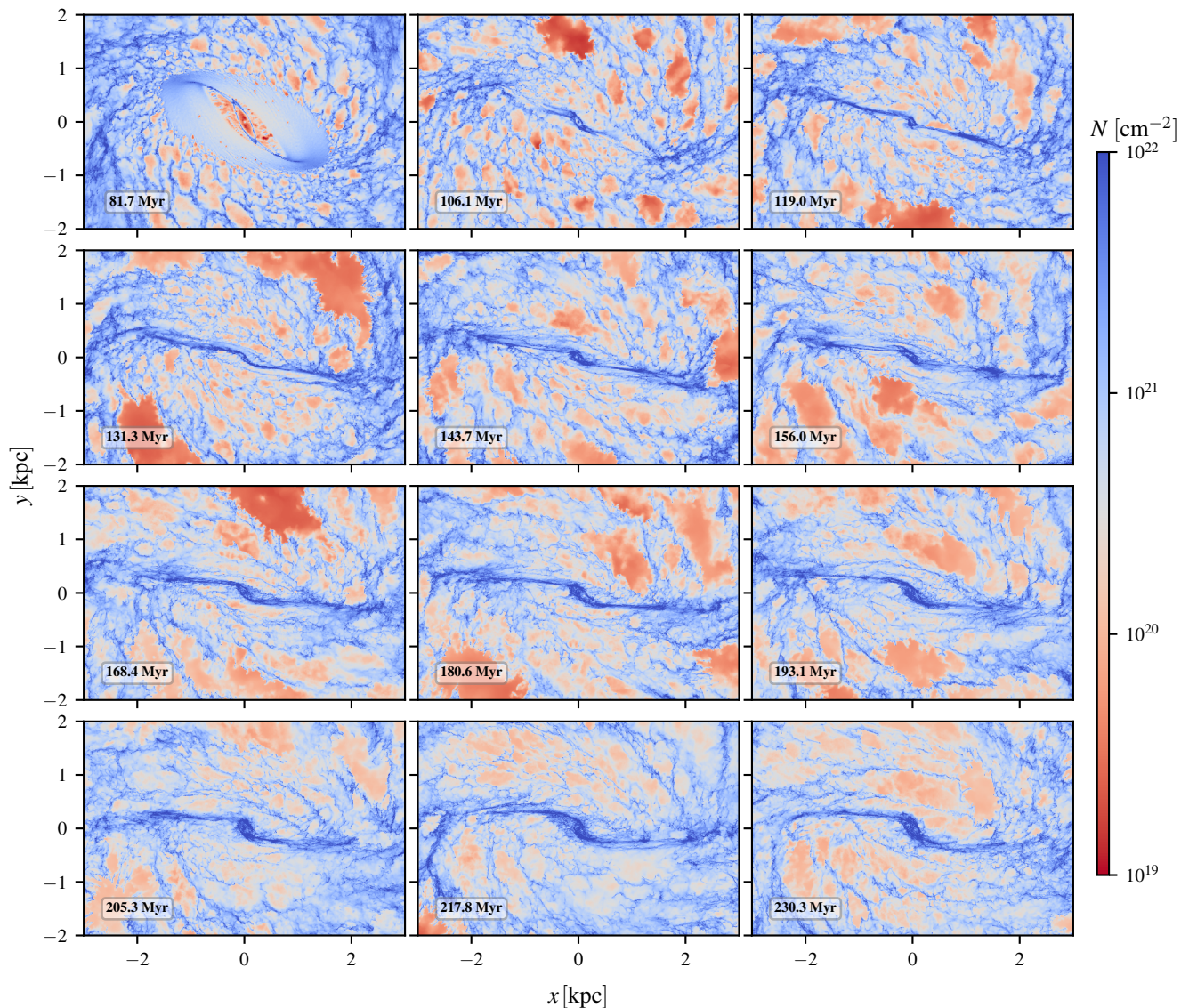
Figure 14 shows the time evolution of the various thermal and chemical components. From this plot, one can see that the amount of gas in each chemical/thermal phase is approximately constant in time in the second half of the simulation, indicating that a statistical steady state has been reached.

Figure 10 shows the spatial distribution and morphology of the three chemical phases relative to each other. Comparison between the different panels of Figure 15 allows us to study the spatial and morphological connection between the thermal and chemical phases. Comparing the left column with the middle column one can clearly see the spatial correlation between the cold phase and  $\text{H}_2$ , while comparing the left and right columns one can see the correlation between the warm phase and HI. The hot component is contained in large ionised cavities which are produced by the SN feedback.

Finally, we remark that the vertical dashed line in Figures 11-12 denotes the sink density formation threshold  $\rho_c$  (See Section 2.4). Above this density, gas in the simulation starts being converted into sink particles. This explains the decline in the PDF visible in the figures above this density.

### 4.2 CMZ vs disc

Figures 11-15 allow us to compare the gas properties in the CMZ with those in the Galactic disc. Comparing the two panels in Figure 11 we can see that the gas in the CMZ is much more predominantly cold/molecular than in the disc. The top panel in Figure 12 shows that the gas in the CMZ has considerably higher average densities than the gas in the disc, qualitatively consistent with what is observed in the real CMZ (e.g. Mills et al. 2018). Figure 12 also shows that our simulations underestimate the temperature of the cold gas compared to observations (e.g. Ginsburg et al. 2016; Krieger et al. 2017), which is expected given the low ISRF/CRIR and the absence of radiation feedback from massive stars in our numerical scheme (see Sections 2.3 and 2.5). Figure 14 indicates that the fraction of cold gas in the CMZ makes up  $\sim 90\%$  of its mass, compared to  $\sim 50\%$  in the disc, and that the mass fraction of hydrogen which is in molecular form is  $\sim 50\%$  in the CMZ vs  $\sim 20\%$  in the disc. These trends are also qualitatively similar to those observed in the real Galaxy (e.g. Morris & Serabyn 1996; Krieger et al. 2017).



**Figure 5.** Total gas surface density at different times in the simulation. The simulated CMZ is the dense ring at the centre (see Figure 6). The bar potential is gradually turning on for  $t < 146$  Myr (see Section 2.7). Hence, only the times  $t \geq 146$  Myr, when the bar is fully on, should be considered when analysing the morphology. In all panels, the bar major axis is horizontal.

## 5 INFLOWS AND OUTFLOWS

The purpose of this section is to investigate inflows and outflows in our simulation, and to compare with our previous simulations in Sormani et al. (2019), which were identical except for the lack of gas self-gravity and SN feedback (see Section 2 for more details).

Figure 16 shows the instantaneous radial mass flows. These are calculated as follows. Consider a spherical coordinate system  $(R, \theta, \phi)$  centred on the Galactic centre. Then the radial mass flux per unit area and per unit time is:

$$F(R, \theta, \phi) = \hat{\mathbf{e}}_R \cdot (\rho \mathbf{v}), \quad (10)$$

where  $\hat{\mathbf{e}}_R$  is the unit vector in the  $R$  direction,  $\rho$  is the gas volume density and  $\mathbf{v}$  is the gas velocity.  $F > 0$  indicates outflow, while  $F < 0$  indicates inflow.

The left panel of Figure 16 shows a face-on mass-weighted projection of the radial flows. At each instant, both radially inward

(red) and outward (blue) flows are present. The radially inward motions (red) are concentrated along the two “dust-lane features” which mediate the bar-driven accretion, while most of the radially outward motions (blue) occur after the gas has passed the point of closest approach to the centre along its orbit and is on its way to the apocentre.

It is interesting to note that embedded in the midst of the (red) dust lanes, some outflowing (blue) clouds can be spotted. These are clouds that are crashing against the dust lane after having moved in along the dust lanes on the opposite side and overshoot passing by the CMZ. Because they are going “against the current”, the hydrodynamic drag will cause them to decelerate and ultimately join the flow of the surrounding dust lane in which they are embedded.

The right panel in Figure 16 shows the instantaneous mass fluxes across the surfaces of two spheres of radii  $R_1 = 50$  pc and  $R_2 = 250$  pc. Because of the highly non-circular motions, there are

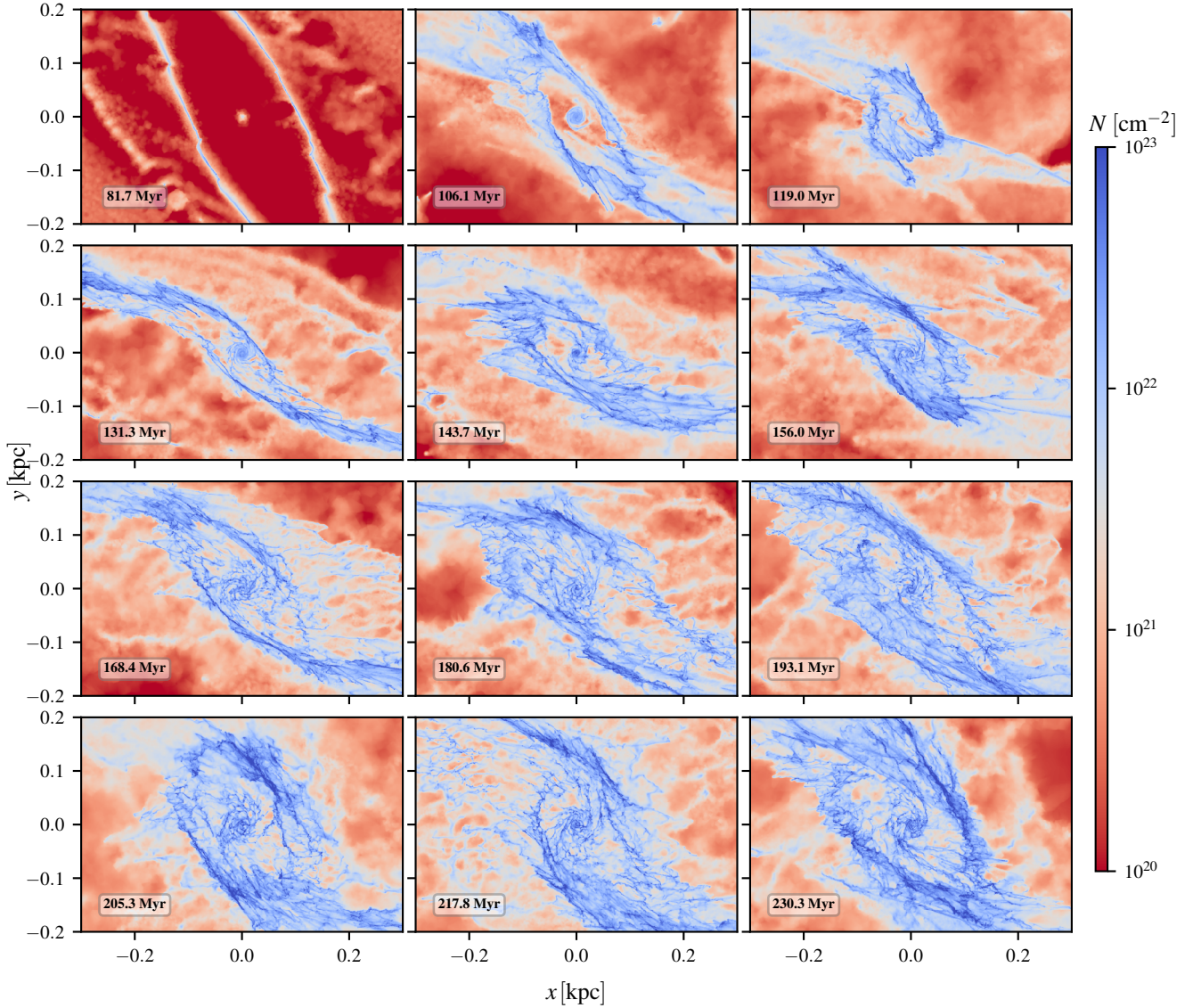


**Figure 6.** Zoom of Figure 5 onto the CMZ

both inflows and outflows, and some of the gas flows in and then back out. So it is not straightforward to tell whether the net flux is inwards or outwards. The instantaneous net fluxes for this particular snapshot, calculated by integrating over the surface of the spheres, are reported in Figure 16. However, the net fluxes are highly variable in time, as can be seen from Figure 17, which shows the net fluxes across the two spheres  $R_1$  and  $R_2$  as a function of time.

While it is instructive to look at the instantaneous fluxes, it is more meaningful to consider their time-averaged values. Figure 18 provides the time-averaged net fluxes across the two spheres defined in Figure 16. In contrast to the instantaneous fluxes, which can be either positive or negative depending on the particular instant that we choose to look at them, the time-averaged net contributions are always negative. The net inflow through  $R_1$  is much smaller than the net inflow through  $R_2$ . We now analyse in more detail the implications of this finding.

### 5.1 Bar inflow from the disc to the CMZ

It is well known that the Galactic bar is very efficient at driving the gas from large radii ( $R \simeq 4$  kpc) inwards along the dust lanes down to the CMZ ring at  $R \simeq 200$  pc. [Sormani & Barnes \(2019\)](#) use a simple geometrical model applied to CO data to provide an observational estimate of this bar-driven inflow. They report a mass inflow rate of  $2.7^{+1.5}_{-1.7} M_{\odot} \text{ yr}^{-1}$ . As they discuss in their Section 4.1.4, this value should be multiplied by an overshooting factor  $f \leq 1$  to take into account the fact that only part of the gas falling along the dust lanes accretes onto the CMZ, while partly misses it and ‘overshoots’, eventually hitting the dust lane on the opposite side. The value quoted in [Sormani & Barnes \(2019\)](#) assumed  $f = 1$  since at the time this paper was written the value of  $f$  was unknown. [Hatchfield et al.](#) (in preparation) has measured the value of  $f$  by adding tracer particles to the simulation of [Sormani et al. \(2019\)](#), and found  $f \simeq 50\%$ . This implies that the observationally determined value should be corrected to  $1.35^{+0.75}_{-0.85} M_{\odot} \text{ yr}^{-1}$ .

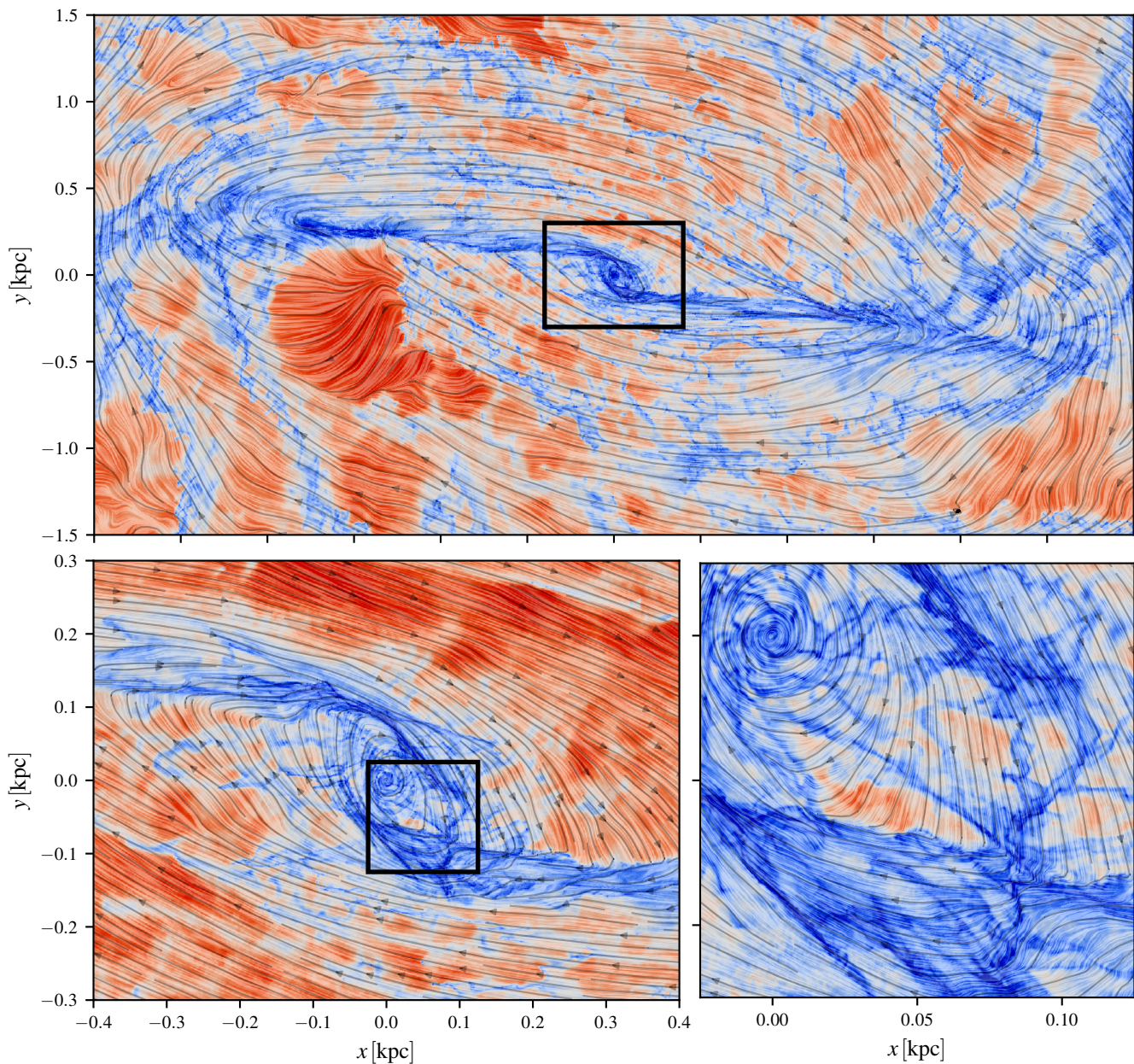


**Figure 7.** *Top:* Instantaneous gas streamlines superimposed on the total gas density for the snapshot at  $t = 161$  Myr. *Bottom:* zoom onto the simulated CMZ. The velocities are shown in the frame corotating with the bar.

The bar-driven inflow in our simulation is quantified by the net flux across  $R_2$  (see Figure 16). The time averaged net flux is  $\dot{M} = 0.987 M_{\odot} \text{ yr}^{-1}$  (Figure 18). This is consistent with the observationally determined inflow rate reported above. In addition to the average value, the time variability of the inflow in our simulation is also roughly consistent with the one inferred from observations (compare Figure 17 with Figure 3 in Sormani & Barnes 2019). Our inflow value is also consistent with the numerical result of Armillotta et al. (2019), which is  $\dot{M} = 1\text{--}3 M_{\odot} \text{ yr}^{-1}$ .

The blue lines in Figure 19 show the gaseous mass of the CMZ as a function of time, which grows according to the inflow rate determined above. The figure also shows that most of the mass in the CMZ is locked-up in the sinks, which is expected given that the average density of the CMZ is significantly higher than that of

the disc (see Figure 12), so that a larger fraction of the gas lies at densities above the sink formation threshold  $\rho_c$  (see Table 1). The total gas mass of the CMZ in the simulation at  $t > 146$  Myr (after the bar potential is fully on, see Section 2.7) is comparable to the observationally determined mass of  $\sim 5 \times 10^7 M_{\odot}$ .

Where does the gas go? Mass conservation requires that (see also Section 3.3 of Crocker 2012):

$$\dot{M}_{\text{inflow}} = \dot{M}_{\text{outflow}} + \text{SFR} + \dot{M}_{\text{CMZ}}. \quad (11)$$

In our simulation, the outflow rate is small (Section 5.3), and the total mass of the CMZ will continue to grow until the SFR approximately matches the bar-driven inflow rate or becomes high enough to power a more significant outflow rate (see discussion in the last paragraph in Section 3.1 of Paper II). However, in the real Galaxy

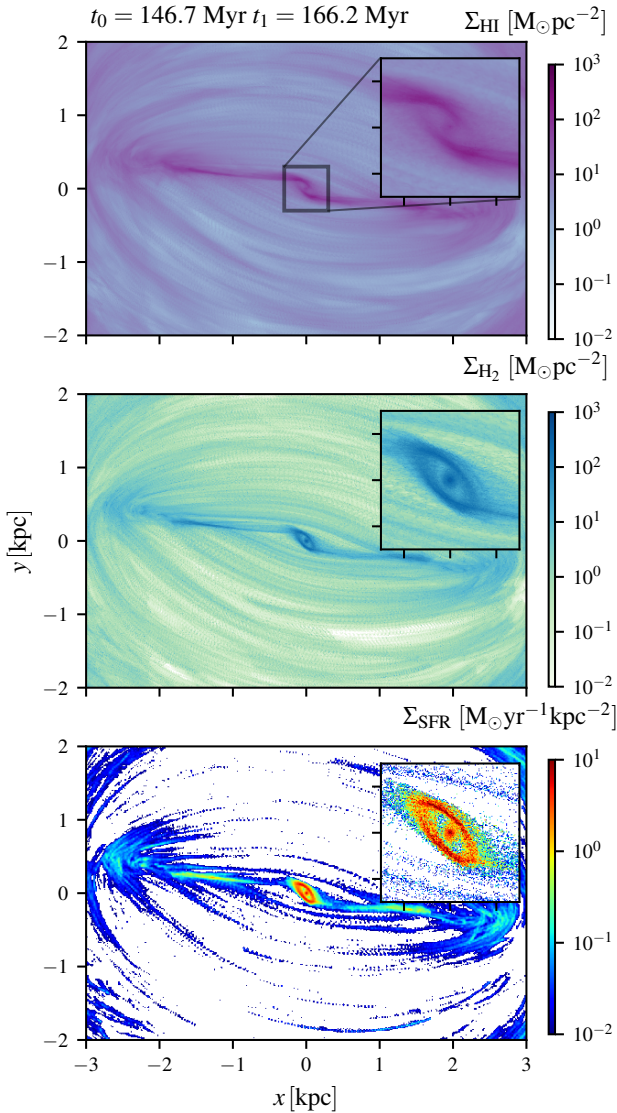


**Figure 8.** Time-averaged plot of *top*: H I surface density; *middle*: H<sub>2</sub> surface density; *bottom*: star formation rate (SFR) surface density. The average is calculated over the time period  $t = 146.7\text{--}166.2\text{ Myr}$ . A comparison with Figures 5 and 6 shows that while the time-averaged morphology is very regular, the instantaneous morphology displays a complex transient substructure. The SFR is calculated as a running average over the last 0.6 Myr and is analysed in more detail in Paper II.

it might be possible that the Galactic outflow efficiently removes the gas at a rate which is up to  $\sim 90\%$  of the inflow rate through high-energy processes that are not included in our simulation (see the discussion in Section 4.2 of Sormani & Barnes 2019).

The bar-driven inflow rate determined here is very similar ( $\simeq 1\text{ M}_{\odot}\text{ yr}^{-1}$ ) to the one that is obtained using our previous non-self gravitating simulations in Sormani et al. (2019). Recall that these are identical to those presented here except that they do not include gas self-gravity and stellar feedback (see Section 2). This result suggests that the inflow from the disc to the CMZ is driven by the non-axisymmetric potential of the Galactic bar, and not by the gas self-gravity and/or the SN feedback.

## 5.2 Feedback driven inflow from the CMZ inwards

As discussed in the previous section, the bar is very efficient in driving the gas from large radii ( $R \simeq 4\text{ kpc}$ ) inwards along the dust lanes down to the CMZ ring at  $R \simeq 200\text{ pc}$ . However, a long-standing and important open question is how the gas continues its journey from the CMZ inwards and how (and to what extent) these large-scale flows reach the supermassive black-hole (SgrA\*) at the centre of our Galaxy (e.g. Phinney 1994). Indeed, our previous simulations show that the bar is ineffective in driving the gas from the CMZ inwards: in the absence of any form of stellar feedback/magnetic fields, the gas just piles up in the CMZ ring and stalls there, without going further in (Sormani et al. 2018, 2019). Understanding how the gas flows from the CMZ inwards is key to understand the formation of the circum-nuclear disc (CND, e.g. Mills et al. 2013; Trani et al. 2018) and to learn more about the fuelling of SgrA\* (e.g. Ghez et al. 2008; Genzel et al. 2010; Gillessen et al. 2017).

One possibility to drive mass transport from the CMZ inwards is that stellar feedback associated with the intense CMZ SF activity could stochastically launch parcels of gas towards the centre (e.g. Davies et al. 2007). Given the right initial condition, a cloud might plunge almost undisturbed towards the centre, since the mean free path of molecular clouds is comparable to the radius of the CMZ (Sormani & Li 2020). The gas self-gravity can also play a role in driving an inflow by creating gravitational torques that are additional to those of the Galactic bar. The simulations presented here are ideal to test these hypotheses, because we can compare them with the previous non-self gravitating simulations in Sormani et al. (2019). Since the only difference between the current simulations and those in Sormani et al. (2019) (in which, as we have checked, there was essentially no net inflow from the CMZ inwards) is the presence of self-gravity and SN feedback (see Section 2), all the inflow present in the newer simulations can be attributed to these two ingredients.

As mentioned in Section 3.3, the difference between the old and new simulations is already evident from Figure 9. In the old simulation there is essentially no gas inside the CMZ ring, while in the new simulation a rich morphology is found inside the CMZ ring.

The inflow from the CMZ inwards can be quantified by the averaged net flux across  $R_1$  in Figure 16. This is highly variable in time (Figure 17), but there is a time averaged net inward flux of  $\dot{M} = 0.03\text{ M}_{\odot}\text{ yr}^{-1}$  (see Figure 18). While this is a factor of 30 smaller than the bar-driven inflow onto the CMZ (Section 5.1), it is quite significant. Observations show that at radii of  $1.5 \lesssim R \lesssim 10\text{ pc}$ , there is a concentration of molecular gas known as the circum-nuclear disc (CND) (e.g. Mills et al. 2013; Tsuboi et al. 2018). The CND has an estimated mass of  $M = 10^4\text{--}10^5\text{ M}_{\odot}$  (Requena-Torres et al. 2012), and is the closest large reservoir of molecular gas to SgrA\*, whose gravitational potential becomes dominant at  $R \lesssim 1\text{ pc}$  (Ghez et al. 2008; Genzel et al. 2010; Gillessen et al. 2017), and it is therefore critical in understanding its fuelling. Our determined inflow rate of  $\dot{M} = 0.03\text{ M}_{\odot}\text{ yr}^{-1}$  is significant because at this rate the CND would take only 0.3–3 Myr to build up, a relatively short time (see Section 3.2 of Paper II for a discussion of star formation associated with this inflow).

SN feedback is the dominant process in driving the nuclear inflow. Torques from the gas-self gravity appear to be negligible since we have checked that they are consistently one order of magnitude smaller than those from the Galactic bar at all radii. Note that although the Galactic bar alone is ineffective in driving the inflow in the absence of SN feedback, it still constitutes the ultimate “sink”

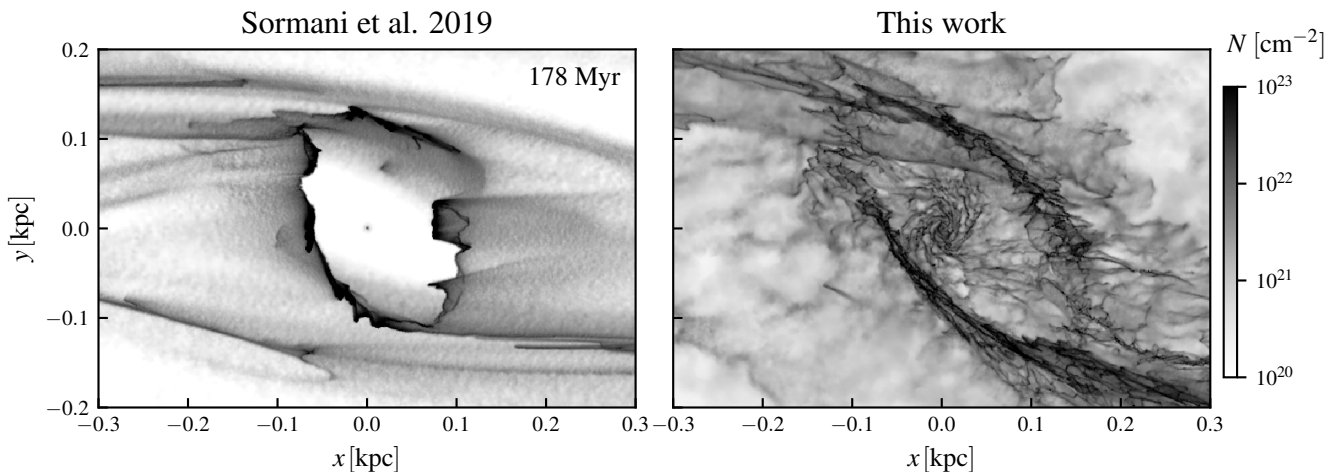


**Figure 9.** Comparison of the total gas surface density in the simulation from Sormani et al. (2019) (which did not include the gas self gravity) and in the one presented in this work (which includes self-gravity, star formation and supernova feedback). The two simulations employ exactly the same external MW barred potential and are shown at the same time,  $t = 178$  Myr.

of angular momentum even when the feedback is present. SN feedback cannot change the total amount of angular momentum, but can only redistribute it in such a way that it becomes available for removal by the bar. For example, a SN explosion in a CMZ cloud might send parts of it towards the centre, contributing to the inflow, and parts of it at larger radii, where the bar can then remove its angular momentum and eventually send it back to the CMZ.

We conclude that SN feedback is able to contribute  $\dot{M} \simeq 0.03 M_{\odot} \text{ yr}^{-1}$  to the inflow from the CMZ towards the CND. The question of how the gas migrates from the CND to SgrA\* cannot be addressed with the current simulations because the resolution is not sufficient to resolve the gas flows at  $R \leq 1$  pc.

### 5.3 Outflow

An interesting question is to what extent the supernova feedback is able to drive an outflow in the vertical direction. However, this cannot be studied from Figure 18 since the mass flux in this figure is dominated by motions in the plane  $z = 0$ . Hence, in order to investigate the presence of vertical outflows, we move from the spherical geometry of Figure 18 to a cylindrical geometry. Figure 20 shows the total inward and outward fluxes integrated across the lateral and the top/bottom surfaces of a cylinder with radius  $R = 250$  pc and  $z = \pm 100$  pc. The corresponding fluxes are obtained by integrating over all points with velocity vectors pointing inside and outside the cylinder respectively. From this figure it can be seen that the stellar feedback can drive a moderate outflow of about  $\sim 0.1 M_{\odot} \text{ yr}^{-1}$ , most of which falls back at a later time in a fountain flow, since its velocity is smaller than the escape velocity. This finding is similar to the predictions of the models of Crocker (2012) and Crocker et al. (2015) in the context of modelling the high-energy phenomenology of the inner Galaxy. The outflow is on average stronger at later ( $t > 190$  Myr) than at earlier ( $147 < t < 190$  Myr) times, indicative of a correlation with the SFR, which also increases at later times (see Figure 2 in Paper II). All these findings are similar to those obtained in the simulation of Armillotta et al. (2019); compare our Figure 20 with their Figure 10.

## 6 DISCUSSION

### 6.1 $x_2$ orbits vs open orbit: a false dichotomy?

We have seen in Sections 3.2 and 3.3 that clouds in CMZ roughly follow  $x_2$  orbits, as first proposed by Binney et al. (1991). However, Kruijssen et al. (2015) (hereafter KDL) report an inconsistency (see KDL Section 5.2.5) between their best-fitting open orbit and the  $x_2$  orbits. What is the relation between the present work and the KDL orbit? Are the two pictures really inconsistent? The purpose of this section is to show that the KDL open orbit scenario is not necessarily in contradiction with the Binney et al. (1991) picture. Instead, the KDL open orbit should be considered as one of the several possible ways to refine the Binney et al. (1991) model by taking into account epicyclic excursions around  $x_2$  orbits. Indeed, from a theoretical point of view, any open orbit like the best-fitting open orbit of KDL is most naturally understood as a libration around an underlying  $x_2$  orbit. In order to understand the theoretical arguments that lead to this conclusion, we need to digress a little bit to discuss the theory of orbits in barred potential.

In an *axisymmetric* potential, such as the one used by KDL, the only stable planar *closed* orbits are circular orbits. The typical (non-closed) orbit is a rosette (see for example Figure 3.1 in Binney & Tremaine 2008). Any rosette orbit is naturally described as the sum of the motion of a guiding centre which follows the circular orbit plus excursions around this circular orbit (Binney & Tremaine 2008). Indeed, the KDL orbit, if integrated forward or backwards in time for longer than shown in Figure 6 of KDL, would be a rosette which oscillates between the maximum and minimum radii of 59 pc and 121 pc respectively (see Figure 21 and KDL Table 1).

In the central regions of a *non-axisymmetric* rotating barred potential, such as the one of the MW, the typical orbit still looks like a rosette, but circular orbits are replaced by a family of mildly elongated stable *closed* orbits called  $x_2$  orbits. What do closed orbits look like in a sequence of potentials which start from an axisymmetric potential and then gradually become more barred? The answer to this question can be seen for example in Figure 6 of Sormani et al. (2015b): the circular orbits gradually morph into the  $x_2$  orbit. How can we understand *open* orbits (i.e., rosettes) in the central regions of a barred potential? Just as any rosette orbit in an

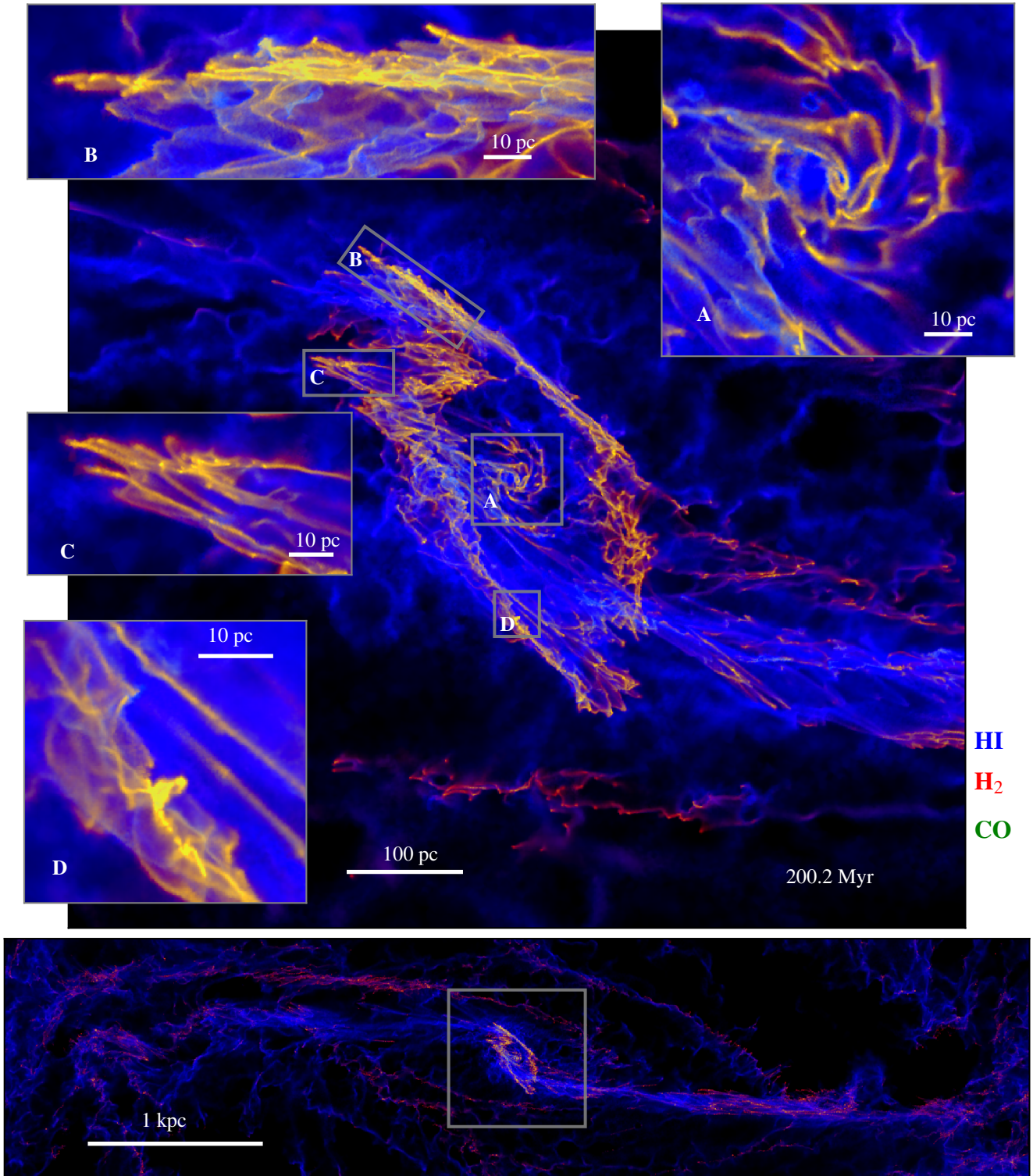


**Figure 10.** Three-colour composite showing the spatial relation of three chemical components: HI, H<sub>2</sub> and CO. The zoom-in panels show various cloud complexes in the CMZ. The resolution of our simulation allows us to resolve individual molecular clouds, which are formed self-consistently from the large-scale flow.

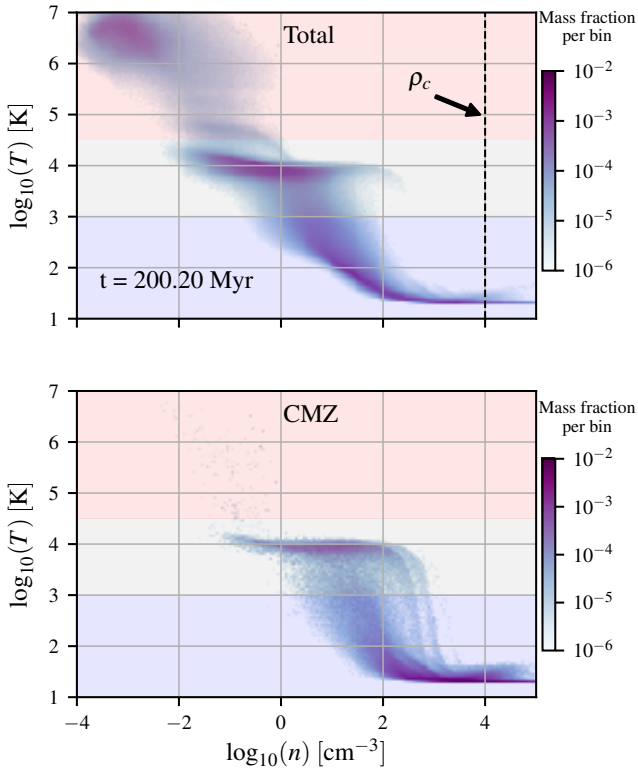


**Figure 11.** 2D histograms showing the mass distribution in the  $n$ - $T$  plane, where  $T$  is the gas temperature and  $n$  the gas number density. *Top*: for all gas in the simulation. *Bottom*: for the CMZ, defined as the region  $R \leq 250$  pc (see Figure 4). The vertical dashed line denotes the sink density formation threshold  $\rho_c$  (See Section 2.4 and Table 1). Shaded coloured areas indicate the three thermal phases (cold, warm, hot).

axisymmetric potential can be understood as a libration around a circular orbit, any rosette (non-closed) orbit in a bar potential can be understood as a libration around an underlying “parent”  $x_2$  orbit which acts as a guiding centre. The parent closed orbit can be identified through the use of surfaces of section (see e.g. Chapter 3 of Binney & Tremaine 2008). This is the most natural generalisation to non-axisymmetric potentials of axisymmetric framework described in the previous paragraph (Binney & Tremaine 2008).

Strictly speaking, since KDL have used an axisymmetric approximation to the real gravitational potential, their orbit should be considered as a libration around an underlying *circular* orbit. However, since the real gravitational potential of the Galaxy *is* barred, any open orbit which resembles the KDL orbit in the real galaxy has a parent  $x_2$  (not circular) orbit, and should be considered as an excursion around it. Therefore, *physically*, the KDL scenario says that the gas follows an open orbit with a specific type of excursion around an underlying  $x_2$  orbit. This is *not* in contradiction with the Binney et al. (1991) paper, because at the time the authors were only concerned with the *average* motion of the gas, i.e. with the guiding centre motions, which as we just argued is physically an  $x_2$  orbit even in the KDL scenario. Binney et al. (1991) were aware that there must be deviations from this average motion, but they were not attempting to describe it.

The excursions described by KDL model are not the only type of excursions possible, and there are other ways to generalise the Binney et al. (1991) picture by adding excursions around  $x_2$  orbits.

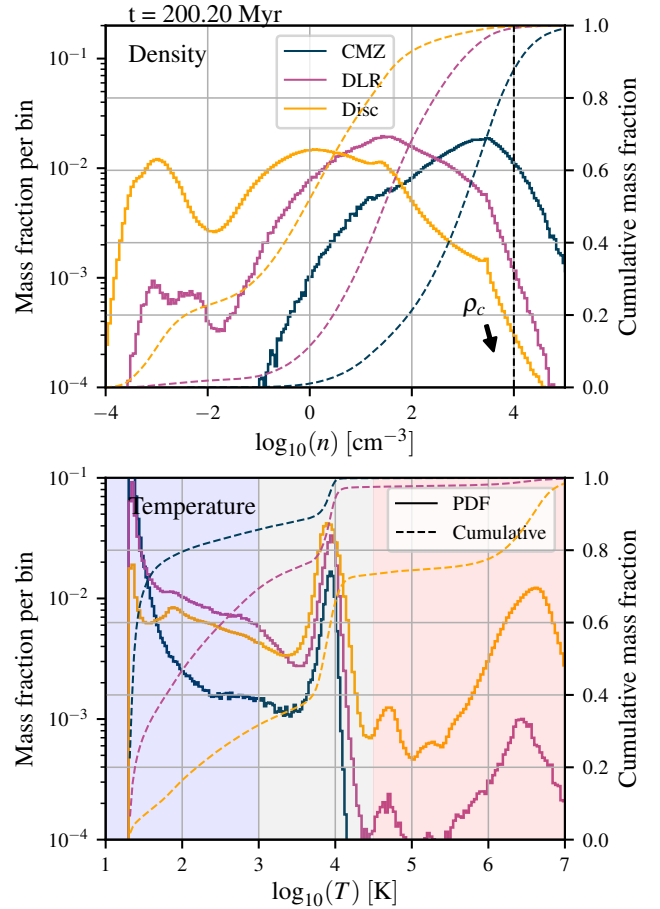


**Figure 12.** 1D histograms showing the mass distribution as a function of total number density  $n$  (*top*) and temperature  $T$  (*bottom*). Full lines are probability distribution functions (PDFs), while dashed lines are cumulative distributions. The three different colours of the lines denote the three different regions defined in Figure 4. The vertical dashed line denotes the sink density formation threshold  $\rho_c$  (See Section 2.4 and Table 1). Shaded coloured areas in the bottom panel indicate the three thermal phases (cold, warm, hot).

For example, in the isothermal simulations of Ridley et al. (2017) excursions around  $x_2$  orbits driven by gas pressure collectively give rise to nuclear spiral density waves. As another example, in the simulations of Sormani et al. (2018), stochastic excursions are driven by larger-scale turbulent flows. In the calculations presented in this paper, large excursions are driven by the large-scale flows as well as by the stellar feedback. Note that in all these simulations, the centres of mass of the clouds follow well  $x_2$  orbits on average (see e.g. Figure 12 of Sormani et al. 2018). This confirms that *the most natural theoretical framework* to think of orbital motions of gas in the CMZ is as the sum of the motion of a guiding centre which follows a closed  $x_2$  orbit plus excursions around this guiding centre (Sormani et al. 2018). The question of understanding the orbital dynamics of the CMZ is therefore reduced to understanding what kind of excursions around the underlying  $x_2$  orbits of the Galactic potential are present in the real CMZ, and what causes them.

KDL do not discuss the physical origin of the excursions in their model or how the gas ends up on their stream. Their is a phenomenological model obtained by fitting a ballistic orbit to the observed  $(l, b, v_{\text{los}})$  distribution of dense gas. In our simulations,

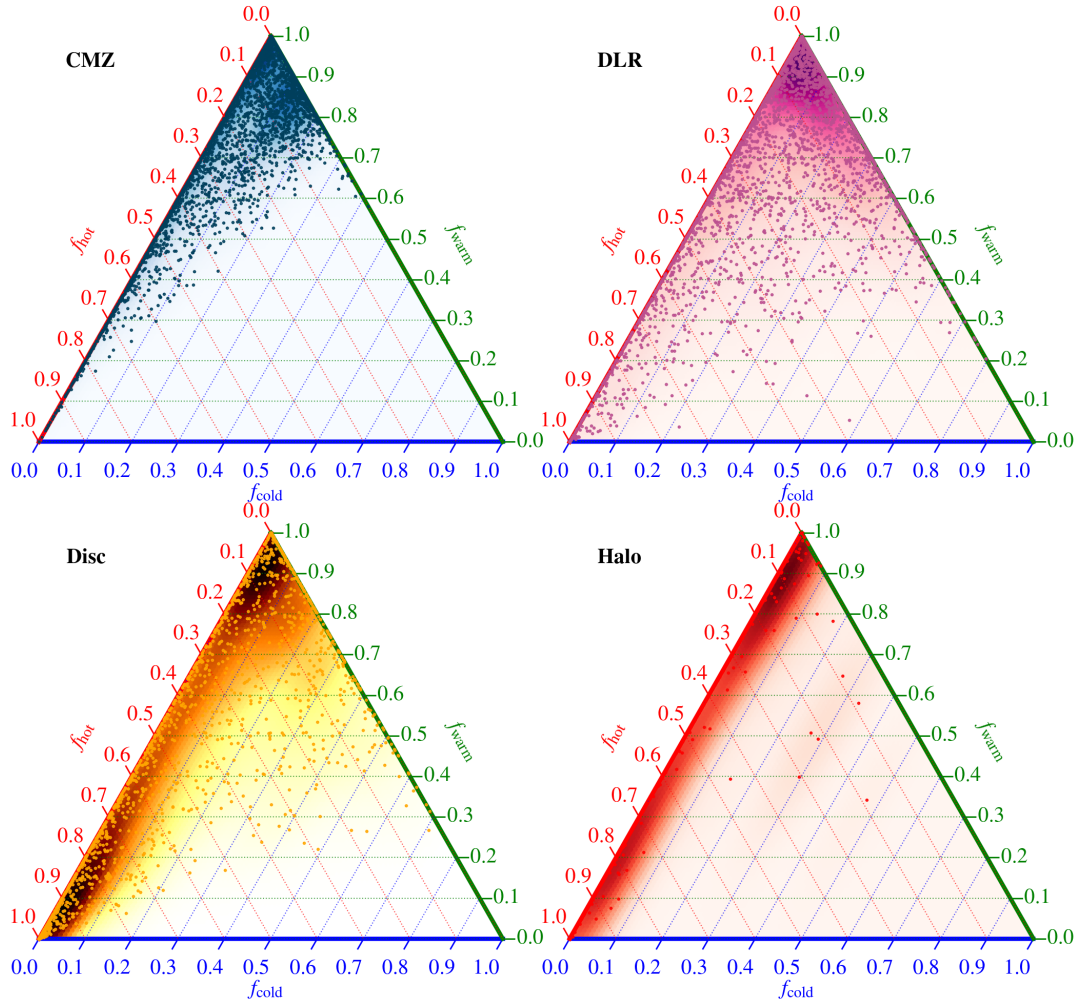


**Figure 13.** Triangle plot of the volume filling factors. “CMZ”, “DLR” and “Disc” refer to the three regions defined in Figure 4, while “Halo” is defined as the region  $|z| > 100$  pc. To construct the plot, we take 30 snapshots equally spaced in time between  $t = 175$  Myr and  $t = 250$  Myr, and for each snapshot we draw 100 random points within each region (CMZ, DLR, Disc, Halo). We thus have a total of  $30 \times 100$  points per region. We then measure the volume filling factor in a cube 100 pc on a side centred on these randomly selected points. Each dot in the plot represents one of these 100-pc cubes. The contour plot in background in each panel is obtained by a kernel density estimation of the dots. The three thermal phases (cold  $T < 10^3$  K; warm  $10^3 < T < 10^{4.5}$  K; hot  $T > 10^{4.5}$  K) are defined as in Section 4.1 and Figures 11–14, and satisfy the relation  $f_{\text{cold}} + f_{\text{warm}} + f_{\text{hot}} = 1$ .

we do not find gas streams with properties similar to the KDL orbit, because the hydrodynamical interactions with the bar inflow and/or stellar feedback typically disturb the coherence and ballistic nature of the stream in less than one orbital time (typically twice per orbit, when collisions with dust lane inflow happen). Moreover, reproducing the KDL orbit would require that a sequence of clouds are launched with exactly the same initial conditions from the same point in space during a time interval of 5 Myr, which is unlikely to happen given the stochastic nature of the perturbations. [Armillotta et al. \(2020\)](#) also report that they are unable to reproduce a stream with the characteristics of the KDL orbit in their simulations. At present, it remains to be shown that excursions compatible with the KDL orbit can occur in a self-consistent simulation of gas flow in a barred potential.

## 6.2 Is there an inner and outer CMZ?

In the model of [Krumholz & Kruijssen \(2015\)](#) material is deposited by the bar inflow at  $R \simeq 450$  pc, at the outer edge of what they call the “outer CMZ”, defined as the region  $120 \lesssim R \lesssim 450$  pc, and is then transported by acoustic instabilities to the “inner CMZ”, defined as the region  $0 \lesssim R \lesssim 120$  pc. In their model the distinction between the inner and outer CMZ has a physical meaning as the radius which separates the acoustically unstable region from the gravitationally unstable region. They argued that the distinction is necessary since the bar-driven inflow mediated by the dust lanes is only able to transport the gas down to  $R \simeq 450$  pc, not down to the inner CMZ. The same distinction between inner and outer CMZ is used in [Kruijssen et al. \(2015\)](#) and [Krumholz et al. \(2017\)](#).

In the model presented here, the distinction between outer and inner CMZ is not necessary. Instead, the CMZ is a star-forming ring at  $R \lesssim 200$  pc which is the natural continuation of the gas flow in a barred potential and is directly interacting with the dust lanes that

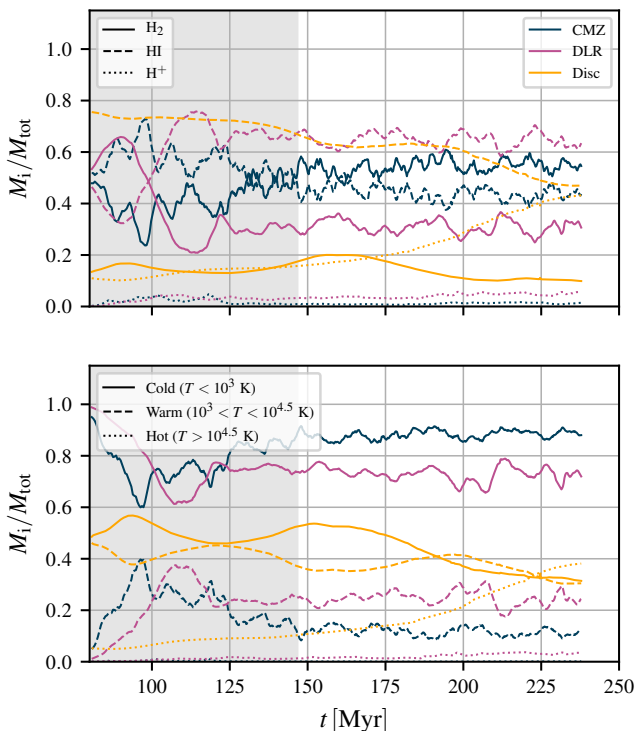


**Figure 14.** *Top:* mass in each chemical ( $\text{H}_2$ ,  $\text{HI}$ ,  $\text{H}^+$ ) component, normalised to the sum of the three components (the sum of three lines of the same colour is unity), as a function of time. *Bottom:* mass fraction in each thermal (cold, warm, hot) component as a function of time. In both panels, different colours indicate the three regions defined in Figure 4.

mediate the bar inflow, as schematically depicted in Figure 23. This view is supported by the following facts:

(i) Contrary to the scenario described in Krumholz & Kruijssen (2015), in the simulations presented here the gas is deposited by the bar dust lanes at  $R \simeq 200$  pc, where it interacts directly with the ring (see for example Figure 10). There is no axisymmetric disc outside this radius. Acoustic instabilities play no role in our model. Indeed, Sormani & Li (2020) show that acoustic instabilities are a spurious result and cannot drive turbulence in the ISM.<sup>4</sup>

<sup>4</sup> The “acoustic instability” was proposed by Montenegro et al. (1999), who studied the propagation of small perturbations in a differentially rotating fluid disc. These authors derived a dispersion relation (see their Equation 10) in the WKB approximation, similar to the classic Lin & Shu (1964) dispersion relation, but keeping one extra order when expanding in the small quantity  $1/|kR|$  (assumed small in the WKB approximation), where  $k$  is the radial wavenumber and  $R$  is the radius. In the axisymmetric case ( $m = 0$ ) the Montenegro et al. (1999) dispersion relation reduces to that of Lin & Shu (1964) and yields the standard Toomre (1964) criterion. In the non-axisymmetric case ( $m \neq 0$ ) their dispersion relation contains some extra terms and predicts new unstable modes that are absent in Lin & Shu (1964) and which were dubbed “acoustic” because they are driven by pressure rather than self-gravity. However, Sormani & Li (2020) used hydrodynamical simulations to show that modes that are predicted to be acoustically unstable by Montenegro et al. (1999) are actually stable. The physical reason is exactly the same reason as to why non-axisymmetric modes that are formally predicted to be unstable by the standard Lin & Shu (1964) dispersion relation turn out to be stable. As shown by Goldreich & Lynden-Bell (1965) and Julian & Toomre (1966) (see also footnote 6 at pg. 494 of Binney & Tremaine 2008), such non-axisymmetric disturbances in a fluid disc

(ii) In the observations, the dust lanes can be seen to reach down to at least  $l = 1.7^\circ$  on the positive side (see point C in Figure 1 of Sormani & Barnes 2019) and to  $l = -1.5^\circ$  on the negative longitude side (see point D in the same figure), which, assuming a Galactic centre distance of 8.2 kpc (Bland-Hawthorn & Gerhard 2016; Gravity Collaboration et al. 2019), correspond to projected radial distances of 240 pc and 210 pc respectively, in good agreement with our simulations. Moreover, the dust lanes can also be seen to interact directly with the dense gas in the CMZ at  $l \leq 1.5^\circ$ , in particular with the  $l = 1.3^\circ$  complex through one of the most prominent “extended velocity features” (EVF, see Figure 1 and Section 5.2 in Sormani et al. 2019).

(iii) In our simulation, copious star formation occurs as soon as the dust lanes touch the ring (see Paper II). If the dust lanes entered the CMZ at  $R \simeq 450$  pc, we should see widespread star formation at those radii, which is not seen in observations (Longmore et al. 2013).

(iv) The orbital model of KDL only fits gas in the “inner” CMZ and omits the widespread gas emission at higher longitudes than SgrB2 (i.e. it omits the  $1.3^\circ$  complex). In their picture, the  $1.3^\circ$  complex belongs to the outer CMZ and is physically disconnected from the inner CMZ which is fitted by their orbit. However, molecular gas observations indicate that the inner CMZ may be physically connected to the  $1.3^\circ$  complex. Figure 22 shows  $^{13}\text{CO}$  observations of the CMZ. The red ellipse highlights a feature in the  $1.3^\circ$  complex that appears to be continuously connected in  $(l, b, v_{\text{los}})$  space to the inner CMZ, and in particular to “Stream 1” in the notation of Figure 4 of KDL. This suggests that Stream 1 and the  $1.3^\circ$  complex are part of the same coherent structure, blurring the distinction between outer and inner CMZ. This connection cannot be explained in the KDL model. The orange line in Figure 22 shows the KDL orbit, and point A indicates its final point as provided by KDL. If integration is continued in time beyond this point, the orbit will turn back towards smaller longitudes, and will never reach the feature highlighted by the red ellipse.

(v) Other features at higher longitudes, such as Bania Clump 2  $\simeq 3.2^\circ$ , which might be seen as indicating the presence of an “outer CMZ”, can be more naturally interpreted as material that is crashing onto the dust lanes (Sormani et al. 2019). If this interpretation is correct, it makes the presence of an outer axisymmetric CMZ disc unnecessary, since no gas in the observations can be clearly attributed to it.

We conclude that both theory and observations support the view that the distinction between inner and outer CMZ is unnecessary. Instead, we argue that it is more useful to think of the CMZ as a ring-like structure which is interacting directly with the inflow along the dust lanes. This ring-like structure is surrounded for a few tens of parsecs by clumpy scattered material (see e.g. left panel in Figure 9), which is created partly by the  $\sim 50\%$  dust lane infall that overshoots the main CMZ ring, and partly from gas that is pushed out the CMZ ring via SN feedback. This scattered material will later fall back on the main CMZ ring, or get picked up by the opposite dust lane. In our interpretation, the  $1.3^\circ$  degree complex is part of the CMZ and represents an interaction region that is located at the intersection between the ring-like structure and the dust lanes,

wind up and propagate off to infinity, leaving behind a smooth disc. This is in hindsight not surprising, since the Montenegro et al. (1999) is just a refinement of the Lin & Shu (1964) dispersion relation. Hence the acoustic instability is a spurious result and cannot drive turbulence in the interstellar medium.

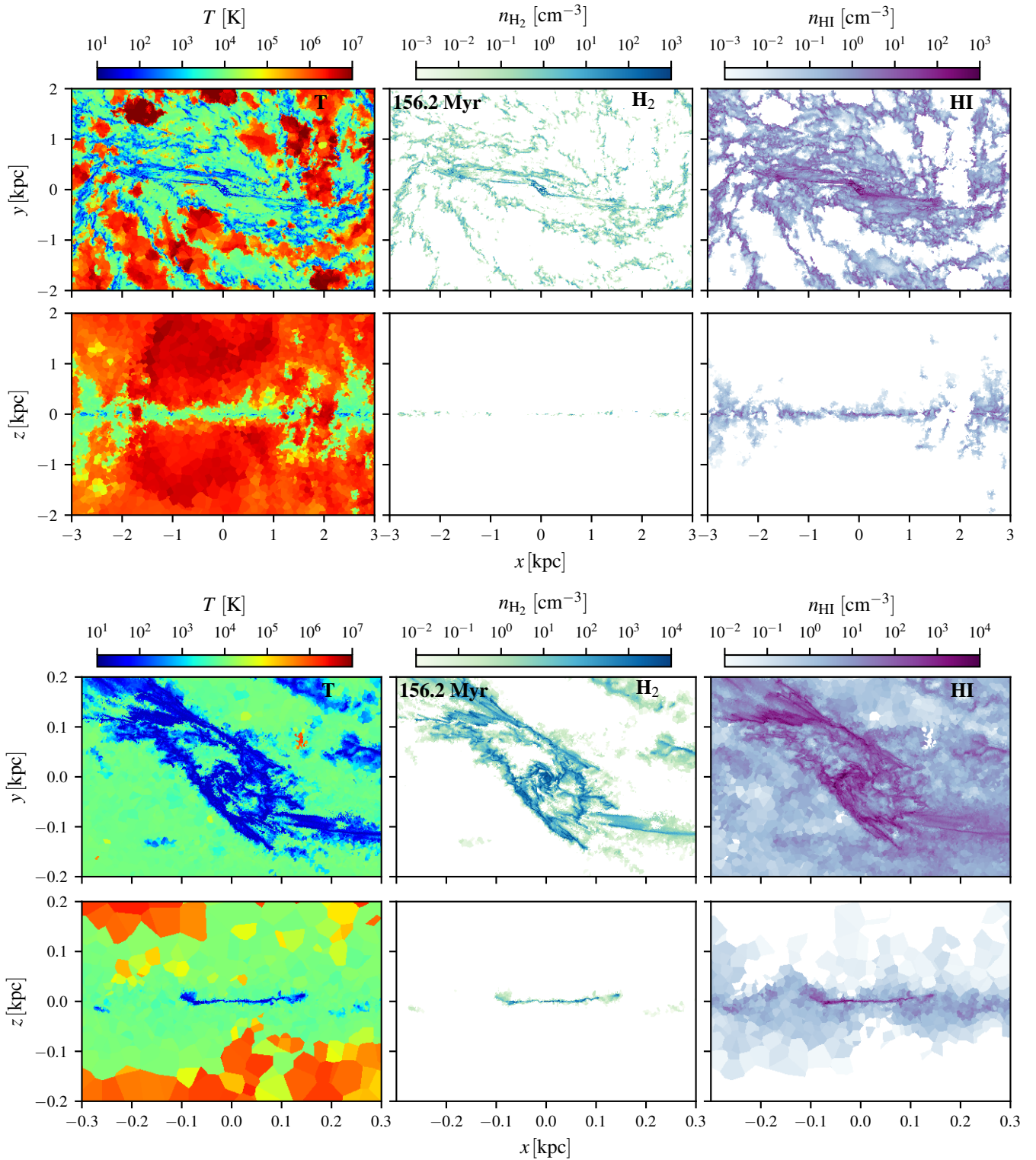


**Figure 15.** Temperature and density slices in the  $z = 0$  and  $y = 0$  planes. *Top two rows:* large scales. *Bottom two rows:* zoom on the CMZ. From this figure one can see that  $H_2$  and CO trace the coldest and densest gas. Note the different scaling of the colourbars in the top two and bottom two rows.

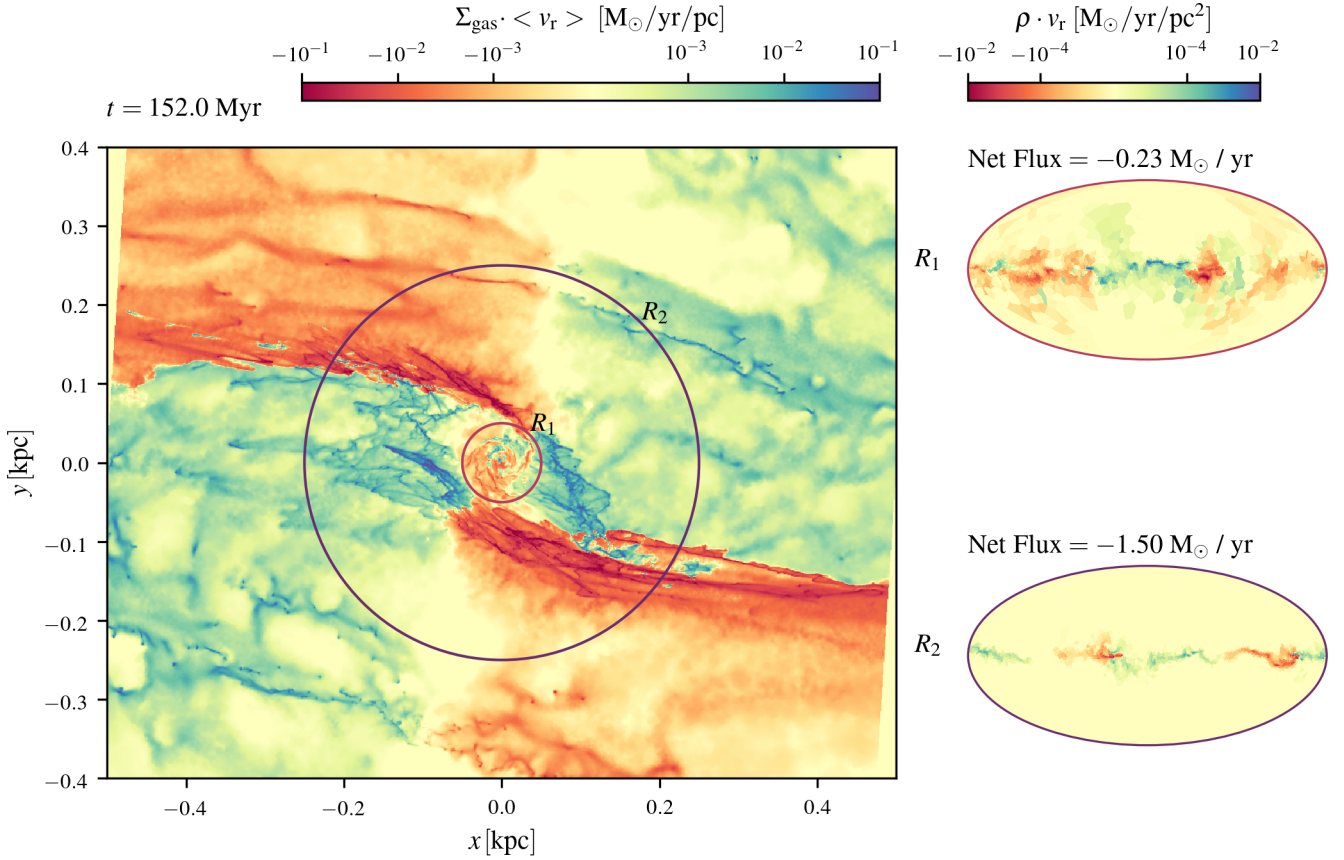


**Figure 16.** *Left:* instantaneous radial mass flows. Red indicates spherically inward motion (inflow) while blue indicates spherically outwards motion (outflow). Most of the inward-moving material (red) is concentrated in the two “dust-lane features” which mediate the bar-driven accretion. Embedded in the dust-lane features, some blue clouds can be spotted. These represent “overshooting” material which is moving outwards against the inward flow of the dust lane. These overshooting clouds are decelerating and eventually join the flow of the dust lanes (see text in Section 5 for more details). *Right:* instantaneous mass fluxes through two spheres of radius  $R_1 = 50$  pc and  $R_2 = 250$  pc in a Mollweide projection centred on the Galactic centre. Net flux indicates the instantaneous mass flow rate integrated over the surface of the sphere.

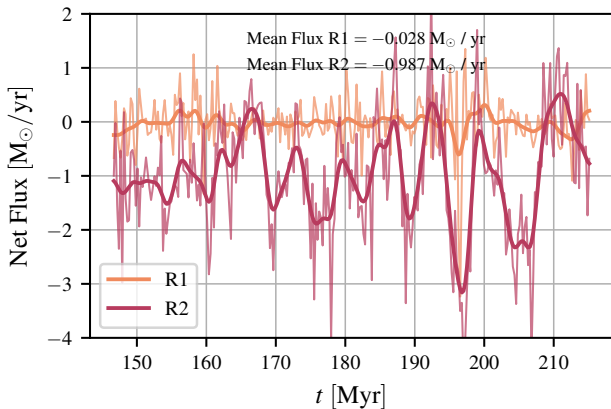


**Figure 17.** Mass flow rates integrated over the surface of the two spheres with radius  $R_1 = 50$  pc and  $R_2 = 250$  pc (see Figure 16) as a function of time. Thin lines are the instantaneous flows, while thick lines are the same lines smoothed with a gaussian filter of width 0.75 Myr. Mean flux indicates the mean over the period shown in the figure.

rather than being a structure which is physically separate from the CMZ.

### 6.3 The 20 and 50 km s<sup>-1</sup> clouds

The 20 and 50 km s<sup>-1</sup> clouds are two prominent ( $M \gtrsim 10^5 M_{\odot}$ ) molecular clouds located in projection close to SgrA\* ( $\simeq 12$  pc and  $\simeq 7$  pc respectively, see for example Figure 3 of Molinari et al. 2011). They take their names from their line of sight velocities.

In the orbital model of Kruijssen et al. (2015), these clouds are placed at  $R = 50$ -100 pc from the Galactic centre. This conclusion is based on the fact that the bulk emission of the two clouds is perfectly overlapping in  $(l, b, v_{\text{los}})$  space with one of the extended larger-scale streams that these authors fit with their orbit (compare black triangles and orange in Figure 9 of Henshaw et al. 2016b).

On the other hand, many authors agree in placing the 20 and 50 km s<sup>-1</sup> clouds close to SgrA\* ( $R \lesssim 20$  pc), based on the following lines of evidence:

- (i) They appear to be interacting with the SgrA East supernova remnant (Genzel et al. 1990; McGary et al. 2001; Hermstein & Ho 2005; Sjouwerman & Pihlström 2008; Lee et al. 2008)
- (ii) They appear to be morphologically and kinematically con-

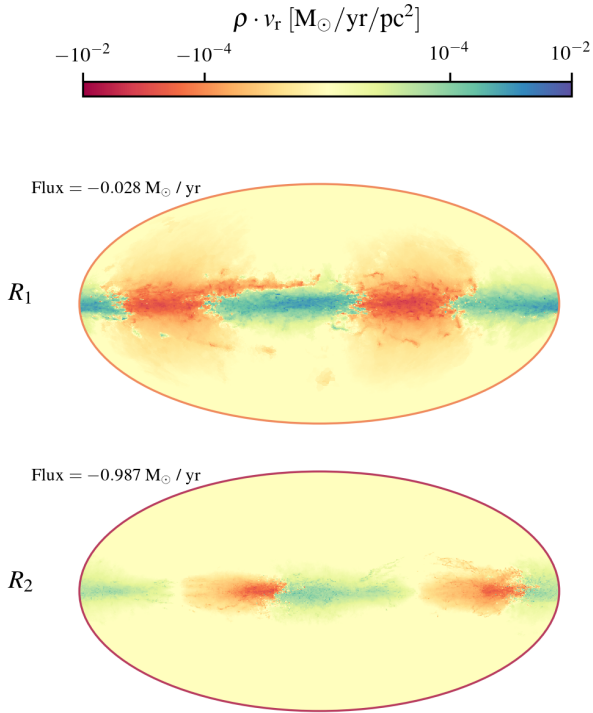


**Figure 18.** Time-averaged mass flow rates across the two spheres of radius  $R_1 = 50$  pc and  $R_2 = 250$  pc (see Figure 16). The time average is extended over the period  $147 \leq t \leq 215$  Myr. Flux indicates the total time-averaged flux integrated over the surface of the sphere (the same numbers are obtained by averaging the lines in Figure 17).

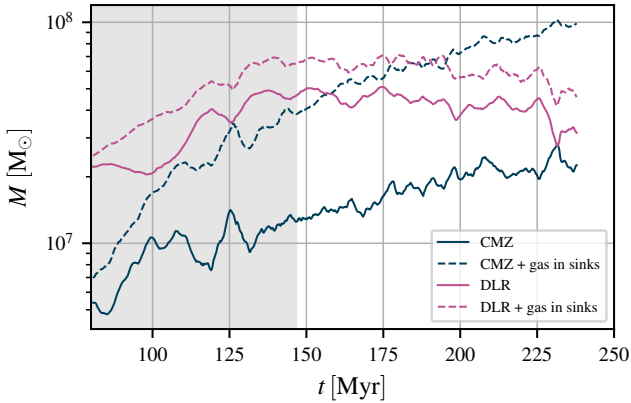


**Figure 19.** Total gas mass in the CMZ and in the DLR (defined in Figure 4) as a function of time.

nected to gaseous structures in the immediate vicinity SgrA\*, such as the circum-nuclear disc (Okumura et al. 1991; Coil & Ho 2000; Liu et al. 2012; Takekawa et al. 2017; Hsieh et al. 2017; Tsuboi et al. 2018; Ballone et al. 2019).

(iii) They have a comparable or larger column density than that of the Brick cloud (Longmore et al. 2012; Marsh et al. 2016; Lu et al. 2017; Barnes et al. 2017; Henshaw et al. 2019), however they are not seen as dark extinction features at 8 micron with Spitzer (GLIMPSE: Benjamin et al. 2003), whereas the Brick is a highly prominent infrared dark cloud (IRDC e.g. Longmore et al. 2012). It

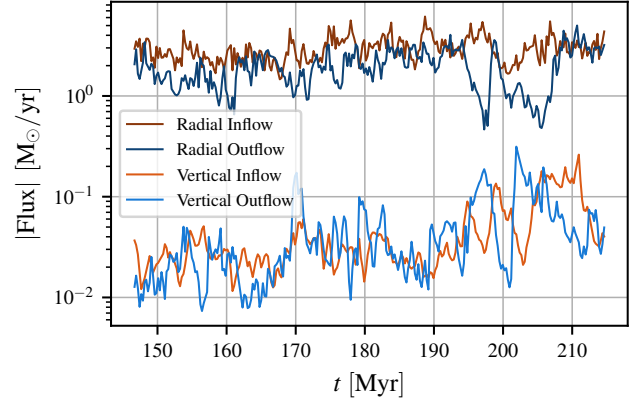


**Figure 20.** Inflowing and outflowing gas integrated across the lateral surface and the top/bottom surface of a cylinder of radius  $R = 250$  pc and  $z = \pm 100$  pc. The net flux is obtained by subtracting the two.

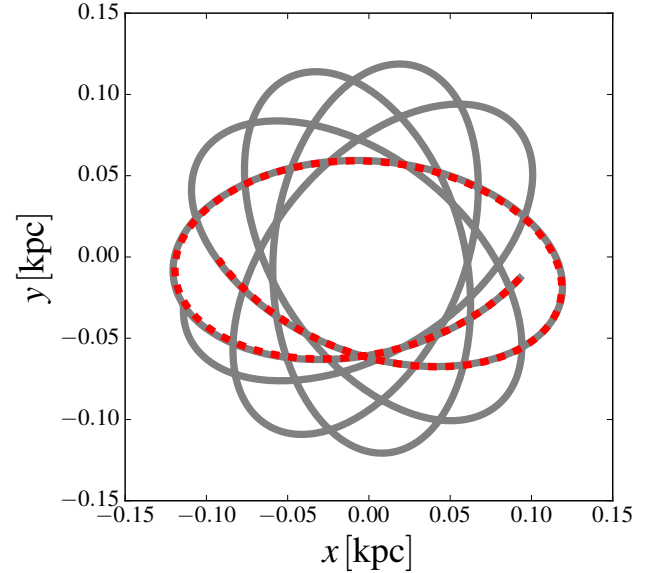


**Figure 21.** The best-fitting orbit of Kruijssen et al. (2015) (KDL) is a portion of a rosette. *Dashed red*: the best-fitting orbit of KDL, which is integrated for 5 Myr. *Gray solid*: continuation of the KDL orbit if it is integrated for further 15 Myr.

is thought that the Brick is such a prominent IRDC since it is a cold, dense cloud in front of the very bright Galactic centre background. Given this logic, if the 20 and 50  $\text{km s}^{-1}$  clouds were also 50-100 pc in front of the Galactic centre, as well as being very dense, they should also be seen as prominent extinction features. A straightforward solution to this problem would arise if these clouds were closer to SgrA\*, with more bright infrared Galactic centre emission in the foreground.

How can we reconcile the fact that the clouds seem to be connected to *both* to gas on the larger scale ( $\sim 100$  pc) stream and to gas close to SgrA\*? Our simulation suggests a way to reconcile these apparently contradictory observational facts. Figure 24 shows a snapshot of our simulation with a possible placement of the 20 and 50  $\text{km s}^{-1}$  clouds. The two clouds are placed where the line-of-

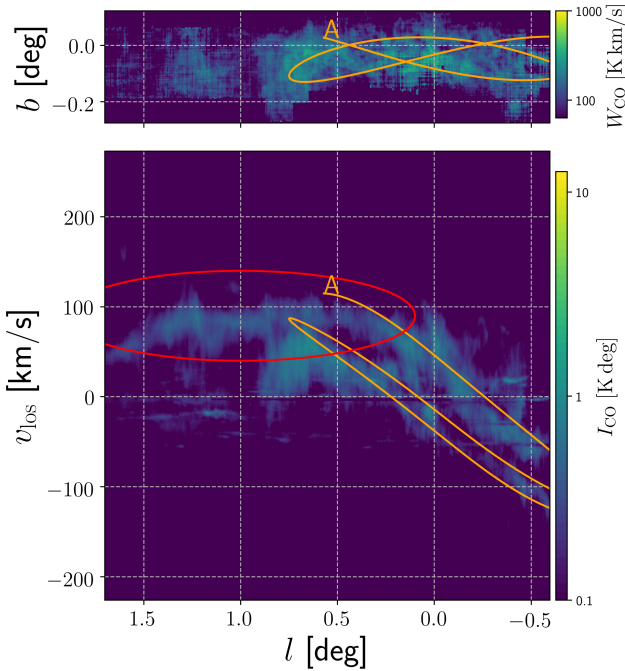


**Figure 22.** *Top:*  $^{13}\text{CO}$  2-1 longitude-latitude map of the CMZ, integrated over velocity, from the APEX CMZ SHFI-1 survey (Ginsburg et al. 2016, <https://doi.org/10.7910/DVN/27601>). *Bottom:* longitude-velocity map of the same data, integrated over latitude. The orange line shows the Kruijssen et al. (2015) (KDL) best-fitting orbit. Point A shows the ending point of the orbit as provided in KDL. The red ellipses highlights a feature that in  $(l, b, v)$  space appears to be continuously connected with stream 1 of KDL (see discussion in Section 6.2).

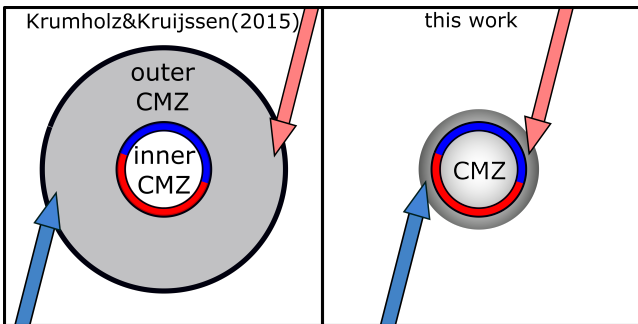


**Figure 23.** Schematic distinction between the scenarios in Krumholz & Kruijssen (2015) and the one presented here. In the former, the bar inflow mediated by the dust lanes deposits gas at the outer edge of the outer CMZ at  $R \simeq 450\text{pc}$ , while acoustic instabilities drive the gas down to the inner CMZ at  $R \simeq 100\text{pc}$ . In the latter, there is just a single structure called CMZ, defined as the region  $R \lesssim 200\text{pc}$ , and there is no distinction between outer and inner CMZ. The dust lanes deposit the gas at  $R \simeq 200\text{pc}$ , and acoustic instabilities play no role. See discussion in Section 6.2.

sight velocity in the simulation matches their observed one at their observed longitude values with respect to SgrA\*.<sup>5</sup> In the figure it can be seen that while the clouds are orbiting close to the centre

<sup>5</sup> We have assumed that SgrA\* coincides with the centre in our simulations and we have corrected for the fact that SgrA\* is not exactly at  $l = b = 0$ .

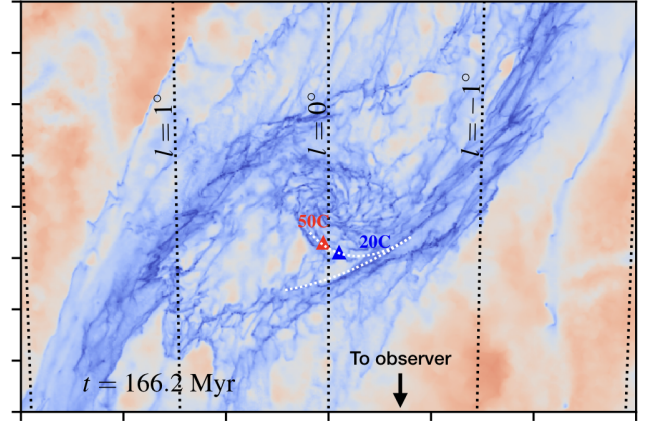


**Figure 24.** Placement of the 20 and 50  $\text{km s}^{-1}$  cloud according to our interpretation (see Section 6.3). The white dashed line indicates a bifurcation in the 100-pc stream.

( $R \lesssim 20\text{pc}$ ), at the same time they are also continuously connected to the large scale streams that form the CMZ ring at  $R \gtrsim 100\text{pc}$  in our simulation.

The fact that the 20 and 50  $\text{km s}^{-1}$  clouds in our simulation are connected to both the CMZ ring-like stream at  $R \simeq 100\text{pc}$  and to the gas in the immediate surrounding of SgrA\* as well is possible because the CMZ stream bifurcates into two branches (see white dashed line in Figure 24). One of the two branches connects to the 20 and 50  $\text{km s}^{-1}$  clouds, while the other continues its orbit along the main ring. A similar behaviour is found in the observations: when the 100-pc stream passes in front of the SgrA\* clouds, at the location of the 20 and 50  $\text{km s}^{-1}$  clouds, it appears to bifurcate into three independent velocity structures (at least one of which is presumably from gas on the far side). This bifurcation is not explained in the Kruijssen et al. (2015) model, who choose to fit only the two brightest velocity components and ignore the third one (see item iv in their Section 2.2). The bifurcation is instead naturally explained in our model.

Finally, we note that our interpretation is also supported by observations of external galaxies which often show gaseous “feathers” that emerge from inside the nuclear rings (e.g. NGC 4314, see Figure 1 in Benedict et al. 2002), consistent with being bifurcations similar to the one discussed above.

Our interpretation implies that the 3D geometry of the CMZ is even more complicated than previously suggested (e.g. Sofue 1995; Molinari et al. 2011; Kruijssen et al. 2015; Henshaw et al. 2016a; Ridley et al. 2017), and that we should take into account that gas in the CMZ ring is continuously connected through secondary branches to gas near SgrA\*.

#### 6.4 The tilt and the $\infty$ -shaped ring

In the orbital models of Molinari et al. (2011) and Kruijssen et al. (2015), the observed  $\infty$ -shape clearly visible in Figure 3 of Molinari et al. (2011) is explained as the result of a vertically oscillating orbit. An alternative explanation is provided by Ridley et al. (2017), who suggested that the  $\infty$ -shape is created by a tilted gas distribution (see their Figure 12). According to this interpretation, the gas rotates in a ring/disc whose rotation axis forms an angle with respect to the rotation axis of the Galaxy at large. The tilt angle required to explain observations in their model is  $\theta \simeq 5^\circ$ . In this

section we discuss whether a tilt is present in our simulations and the implications for observations.

The bottom row in Figure 15 shows a slice of the CMZ. It can be seen from this figure that the CMZ does not lie exactly in the plane  $z = 0$ , but is slightly tilted. We now analyse this in a more quantitative way. Following Ridley et al. (2017), we can specify the orientation of the normal to the disc  $\hat{n}$  with respect to a coordinate system  $xyz$  centred on the Galactic centre,

$$\hat{n} = \sin \theta \cos \phi \hat{x} + \sin \theta \sin \phi \hat{y} + \cos \theta \hat{z}, \quad (12)$$

where  $\hat{z}$  points towards the North Galactic Pole.

The three-dimensional orientation of the CMZ can be measured by diagonalising the moment of inertia  $I$  of the molecular gas distribution,

$$I_{ij} = \sum_c \rho_{\text{H}_2} x_c^i x_c^j, \quad (13)$$

where the sum is extended over all cells within the CMZ ( $R \leq 250$  pc). The direction  $\hat{n}$  normal to the CMZ disc will be the eigenvector of  $I_{ij}$  associated with the largest eigenvalue.

Figure 25 shows the tilt angle  $\theta$  as a function of time, measured using the procedure outlined above. The black line indicates the simulation presented in this work, while the red line compares with the previous non-self gravitating simulations of Sormani et al. (2019). The CMZ in the newer simulation shows a significant tilt which is typically of the order of  $\theta \simeq 2^\circ$  and can occasionally reach values of  $\theta \simeq 4\text{--}5^\circ$ . The latter values are marginally compatible with the value required by the model of Ridley et al. (2017). A similar tilt was also found in the hydrodynamical simulations of Shin et al. (2017).

What causes the CMZ tilt in the present simulations? Self-gravity and stellar feedback must play a role since these are the only differences from the previous simulations of Sormani et al. (2019), which did not show a tilt. However, if the SNe were directly responsible for creating the tilt, we would expect various parts of the orbit to be independently vertically displaced, because the supernovae randomly explode along the CMZ ring and only disturb the gas locally. In contrast, we often find that the tilt is coherent over the whole CMZ ring.

While we cannot rule out that SN feedback directly causes the tilt, closer inspection of the movies of the simulations suggests that the SNe may be causing the tilt in an indirect way. SN feedback creates turbulence and causes the gas layer in the disc outside the bar to be thicker than in previous non-self gravitating simulations. Therefore, the gas that enters the dust lanes typically does not do so at  $z = 0$ , but rather at some height above or below the Galactic plane. As the gas flows down along the dust lanes towards the CMZ, it acquires some vertical momentum. When this gas accretes onto the CMZ it transfers some of the momentum to it, causing the CMZ ring to wobble. Since the scale of the dust lanes is much larger (2-3 kpc) than the scale of the CMZ ring ( $\simeq 100$  pc), this mechanism causes oscillations that have more coherence than those that can be expected from direct supernovae driving. This suggests that the tilt can be caused by accretion-driven torques.

What do the observations say? Interestingly, the dust lanes are very clearly tilted. This is obvious from Figure 1 of Sormani & Barnes (2019) (see also Marshall et al. 2008). Referring to that figure, the near side dust lane shows a clear gradient towards negative latitudes in going from point C to point A, while the far side dust lane shows a gradient towards increasing latitude from point D to point B. We can use the geometrical model provided in Sormani & Barnes (2019) and schematically reproduced in Figure 26 to estimate the tilt angle. Both dust lanes have a length of

$l \simeq 3$  kpc. In going from where the near side dust lane touches the CMZ (point C) to its endpoint (point A) there is a  $\Delta b \simeq 1^\circ$ , and its endpoint is at a distance of  $d \simeq 5$  kpc from us. This implies a tilt of  $\theta_{\text{DL, near}} \simeq d\Delta b/l \simeq 2^\circ$  (see Figure 26 for the definition of this angle). For the far side dust lane,  $\Delta b \simeq 1^\circ$  and  $d \simeq 10$  kpc, which implies  $\theta_{\text{DL, far}} \simeq d\Delta b/l \simeq 3^\circ$ . These results are consistent with the dust lanes lying on a common tilted plane with average tilt  $\theta_{\text{DL}} \simeq 2.5^\circ$ .

We can estimate the time required for the torque<sup>6</sup> caused by the dust lane inflow to tilt the CMZ from  $\theta_i = 0$  to  $\theta_f = 5^\circ$ . The vertical momentum transferred from the dust lanes to the CMZ per unit time is  $\dot{p}_z = \dot{M}v \sin(\theta_{\text{DL}})$  where  $\dot{M} \simeq 1 M_\odot \text{ yr}^{-1}$  is the observationally determined bar-driven mass inflow rate (see discussion in Section 5.1) and  $v \simeq 250 \text{ km s}^{-1}$  is the speed of the gas in the dust lane as it enters the CMZ. The lever arm, which we can take to be the radius of the CMZ, is  $R \simeq 100$  pc. This gives a torque of  $\tau = \dot{M}vR \sin(\theta_{\text{DL}}) \simeq 1.1 M_\odot \text{ yr}^{-1} \text{ km s}^{-1} \text{ kpc}$ . The mass of the CMZ is  $M = 5 \times 10^7 M_\odot$  and its moment of inertia along an axis lying within the plane, assuming the CMZ mass can be approximated as distributed uniformly in a disc for the purposes of this estimation, is  $I = MR^2/4 \simeq 1.25 \times 10^5 M_\odot \text{ kpc}^2$ . The time required to generate the tilt is then  $t = \sqrt{2\theta_f I / \tau} \simeq 4 \text{ Myr}$ . This is a short time, comparable to the dynamical orbital time of the CMZ ring ( $\simeq 5 \text{ Myr}$ ). The tilt angle cannot grow more than a few degrees because as the gas moves away from the plane  $z = 0$ , the vertical restoring force of the Galactic potential brings it back to the plane (this restoring force is also what makes the CMZ wobble in a way similar to that of a coin spun on a table under the effect of the Earth's gravitational field). We conclude that the observed bar inflow should induce a significant and coherent tilt of the CMZ.

Although in our simulations the tilt in the dust lanes is driven by the SN feedback in the disc region outside the bar, we reckon this is unlikely to produce a tilt of both dust lanes along a common plane, because of the stochastic nature of the SN feedback. It is more likely that the dust lane tilt in the MW is produced by some other mechanism, perhaps the same mechanism that produces the warp of the outer HI layer (Ostriker & Binney 1989). This unidentified mechanism would act in addition to the SN feedback that is at work in our simulation. Regardless of what causes the origin of the dust lane tilt, our simulations show that the dust lane inflow is a viable mechanism for producing a tilt in the CMZ.

Summarising the discussion, we conclude that:

- Our simulations show that accretion through the dust lanes can induce a significant tilt in the CMZ.
- Observations show that both the MW dust lanes are currently tilted by an angle of  $\theta = 2\text{--}3^\circ$  along a roughly common plane. An order of magnitude calculation shows that this will induce a significant tilt of the CMZ within  $\sim 4 \text{ Myr}$  (roughly one orbital time).
- It is likely that the CMZ is currently tilted because of the bar-driven inflow. A CMZ tilted out of the Galactic plane may explain the  $\infty$ -shaped structure seen in the observations.

## 7 SUMMARY AND CONCLUSIONS

We have presented high-resolution hydrodynamical simulations of the Milky Way innermost 5 kpc, and have used these to investigate

<sup>6</sup> Note that this is a torque around an axis that lies within the plane of the Galaxy, not around the  $z$  axis. See “lateral view” in Figure 26.

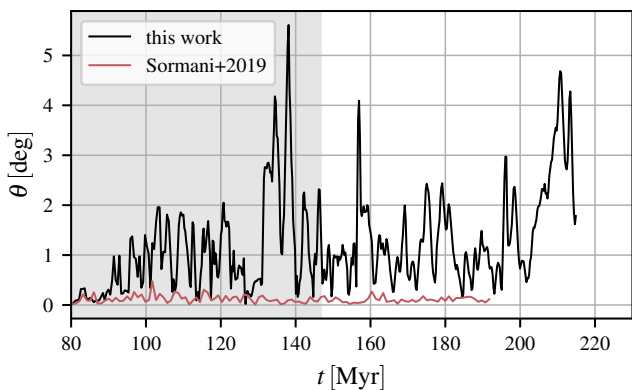


**Figure 25.** The tilt of the CMZ ring measured in the simulation presented in this paper (thick black line) and in the previous non-self gravitating simulations of Sormani et al. (2019) (thin red line). See discussion in Section 6.4.

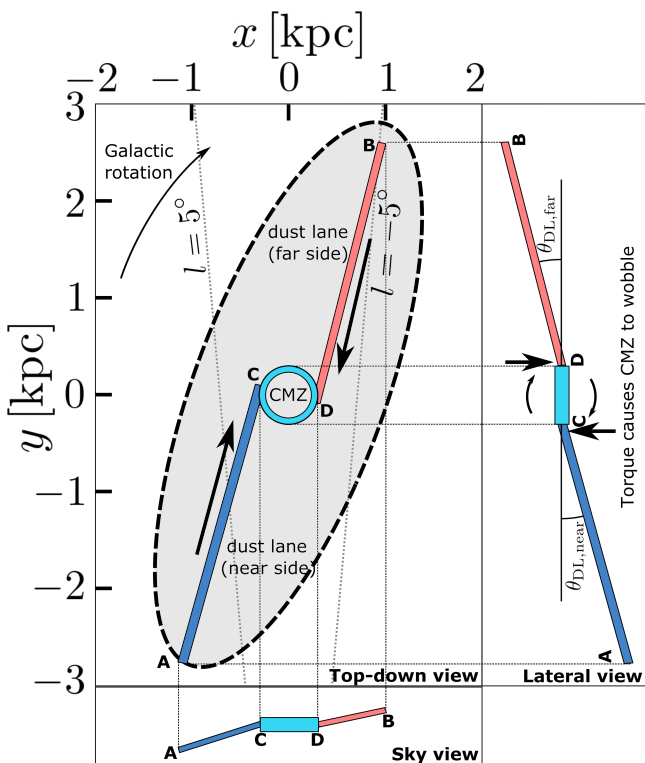


**Figure 26.** Schematic representation of how the dust lanes exert a torque on the CMZ along an axis that lies within the plane of the Galaxy, causing the CMZ to wobble. See discussion in Section 6.4.

gas dynamics in the central molecular zone (CMZ). The simulations include a realistic external barred potential, a time-dependent chemical network that keeps track of hydrogen and carbon chemistry (see Section 2.3), a physically motivated model for the formation of new stars using sink particles (see Section 2.4), and supernova feedback (see Section 2.5). The simulations allow us to follow the large-scale flow, which conforms to the usual  $x_1/x_2$  orbit dynamics (see Section 3.2), while at the same time reaching sub-parsec resolution in the dense regions (see Figure 3), thus allowing

us to resolve individual molecular clouds formed self-consistently from the large-scale flow.

Our main conclusions are as follows:

- The time-averaged morphology of the CMZ is very smooth and regular (Figure 8), while the instantaneous morphology of the CMZ is very rich in substructure that is transient in time (see Figure 6). The instantaneous CMZ morphology can depart significantly from the average morphology, to the point that the underlying regular structure is not obvious or even discernible (see Section 3.3). The CMZ morphology also depends on the tracer used: in HI it is more spiral-like, while in H<sub>2</sub> it is more ring-like (see Section 3.3). The CMZ dynamics is best understood as gas following  $x_2$  orbits plus librations (see Section 6.1).

- Molecular clouds exhibit a highly complex filamentary morphology and do not resemble idealised “spherical clouds”. They enter the CMZ already in this filamentary form, which suggests that the often-employed idealised idea of a roughly spherical cloud orbiting in the CMZ (e.g. Dale et al. 2019) may be an oversimplification which should be applied with care when studying the dynamical evolution of clouds in the Galactic centre environment (see Figure 10 and Section 3.4). This is consistent with the highly filamentary and almost fractal structure observed in the CMZ streams and in real molecular clouds (e.g. Jones et al. 2012; Rathborne et al. 2015; Henshaw et al. 2019).

- The bar efficiently drives an inflow from the Galactic disc ( $R \simeq 3$  kpc) down to the CMZ ( $R \simeq 200$  pc) of the order of  $1 M_{\odot} \text{ yr}^{-1}$ , consistent with observational determinations and previous theoretical findings (see Section 5.1)

- Stellar feedback can drive an inflow from the CMZ inwards towards the CND of  $\sim 0.03 M_{\odot} \text{ yr}^{-1}$  (see Section 5.2). This number is significant for the formation of the circum-nuclear disc (CND) since at this rate it would take only 0.3–3 Myr to reach its current mass. It is also important for understanding the fuelling of the supermassive black hole SgrA\* since the CND is its closest large reservoir of molecular gas.

- Both theory and observations support the view that there is no “outer CMZ” quasi-axisymmetric disc at radii  $120 \lesssim R \lesssim 450$  pc in between the CMZ 100-pc ring and the point where the dust lanes deposit the inflow. Instead, the dust lanes deposit the inflow almost directly into the ring, which in our interpretation extends to the  $1.3^{\circ}$  degree complex (see Section 6.2).

- We give a new interpretation for the 3D placement of the 20 and  $50 \text{ km s}^{-1}$  clouds, according to which they are close ( $R \lesssim 30$  pc) to SgrA\*, while at the same time being connected to the main gas streams orbiting in the CMZ ring-like structure at  $R \gtrsim 100$  pc (see Section 6.3).

- Accretion through the dust lanes can induce a significant tilt of the CMZ out of the Galactic plane. Observations show that the MW dust lanes are tilted by an angle of  $\theta = 2\text{--}3^{\circ}$ , and an order of magnitude calculation shows that this will induce a significant CMZ tilt within  $\simeq 4$  Myr. A CMZ tilted out of the Galactic plane may provide an alternative explanation to the  $\infty$ -shaped figure discovered by Molinari et al. (2011) (See Section 6.4).

## ACKNOWLEDGEMENTS

RGT and MCS both acknowledge contributing equally to this paper. We thank the anonymous referee for constructive comments that improved the paper. MCS thanks Ashley Barnes, Adam Ginsburg, Jonathan Henshaw, Zhi Li, Diederik Kruijssen and Elisabeth Mills for useful comments and discussions. RGT, MCS,

SCOG, and RSK acknowledge financial support from the German Research Foundation (DFG) via the collaborative research center (SFB 881, Project-ID 138713538) “The Milky Way System” (subprojects A1, B1, B2, and B8). CDB and HPH gratefully acknowledges support for this work from the National Science Foundation under Grant No. (1816715). PCC acknowledges support from the Science and Technology Facilities Council (under grant ST/K00926/1) and StarFormMapper, a project that has received funding from the European Union’s Horizon 2020 Research and Innovation Programme, under grant agreement no. 687528. HPH thanks the LSSTC Data Science Fellowship Program, which is funded by LSSTC, NSF Cybertraining Grant No. 1829740, the Brinson Foundation, and the Moore Foundation; his participation in the program has benefited this work. RJS gratefully acknowledges an STFC Ernest Rutherford fellowship (grant ST/N00485X/1) and HPC from the Durham DiRAC supercomputing facility (grants ST/P002293/1, ST/R002371/1, ST/S002502/1, and ST/R000832/1). RSK furthermore thanks for financial support from the European Research Council via the ERC Synergy Grant “ECOGAL – Understanding our Galactic ecosystem: from the disk of the Milky Way to the formation sites of stars and planets” (grant 855130). The authors acknowledge support by the state of Baden-Württemberg through bwHPC and the German Research Foundation (DFG) through grant INST 35/1134-1 FUGG. The authors gratefully acknowledge the data storage service SDS@hd supported by the Ministry of Science, Research and the Arts Baden-Württemberg (MWK) and the German Research Foundation (DFG) through grant INST 35/1314-1 FUGG.

## DATA AVAILABILITY

The data underlying this article will be shared on reasonable request to the corresponding author. Movies of the simulations can be found at the following link: <https://www.youtube.com/channel/UCwnzf0-xLxzRDz9XsexfPoQ>.

## REFERENCES

- Armillotta L., Krumholz M. R., Di Teodoro E. M., McClure-Griffiths N. M., 2019, *MNRAS*, **490**, 4401
- Armillotta L., Krumholz M. R., Di Teodoro E. M., 2020, *MNRAS*, **493**, 5273
- Athanassoula E., 1992, *MNRAS*, **259**, 345
- Balbus S. A., Hawley J. F., 1998, *Reviews of Modern Physics*, **70**, 1
- Ballone A., Mapelli M., Trani A. A., 2019, *MNRAS*, **488**, 5802
- Bally J., Stark A. A., Wilson R. W., Henkel C., 1988, *ApJ*, **324**, 223
- Barnes A. T., Longmore S. N., Battersby C., Bally J., Kruijssen J. M. D., Henshaw J. D., Walker D. L., 2017, *MNRAS*, **469**, 2263
- Bate M. R., Bonnell I. A., Price N. M., 1995, *MNRAS*, **277**, 362
- Benedict G. F., Howell D. A., Jørgensen I., Kenney J. D. P., Smith B. J., 2002, *AJ*, **123**, 1411
- Benjamin R. A., et al., 2003, *PASP*, **115**, 953
- Binney J., Tremaine S., 2008, *Galactic Dynamics: Second Edition*. Princeton University Press
- Binney J., Gerhard O. E., Stark A. A., Bally J., Uchida K. I., 1991, *MNRAS*, **252**, 210
- Bland-Hawthorn J., Gerhard O., 2016, *ARA&A*, **54**, 529
- Blondin J. M., Wright E. B., Borkowski K. J., Reynolds S. P., 1998, *ApJ*, **500**, 342
- Bordoloi R., et al., 2017, *ApJ*, **834**, 191
- Chevance M., et al., 2020, *MNRAS*, **493**, 2872
- Chuss D. T., Davidson J. A., Dotson J. L., Dowell C. D., Hildebrand R. H., Novak G., Vaillancourt J. E., 2003, *ApJ*, **599**, 1116
- Clark P. C., Glover S. C. O., Klessen R. S., 2012, *MNRAS*, **420**, 745
- Clark P. C., Glover S. C. O., Ragan S. E., Shetty R., Klessen R. S., 2013, *ApJ*, **768**, L34
- Coil A. L., Ho P. T. P., 2000, *ApJ*, **533**, 245
- Comerón S., Knapen J. H., Beckman J. E., Laurikainen E., Salo H., Martínez-Valpuesta I., Buta R. J., 2010, *MNRAS*, **402**, 2462
- Contopoulos G., Grosbol P., 1989, *Astronomy & Astrophysics Review*, **1**, 261
- Crocker R. M., 2012, *MNRAS*, **423**, 3512
- Crocker R. M., Jones D. I., Melia F., Ott J., Protheroe R. J., 2010, *Nature*, **463**, 65
- Crocker R. M., Bicknell G. V., Taylor A. M., Carretti E., 2015, *ApJ*, **808**, 107
- Dahme G., Huttemeister S., Wilson T. L., Mauersberger R., 1998, *A&A*, **331**, 959
- Dale J. E., Ngoumou J., Ercolano B., Bonnell I. A., 2014, *MNRAS*, **442**, 694
- Dale J. E., Kruijssen J. M. D., Longmore S. N., 2019, *MNRAS*, **486**, 3307
- Davies R. I., Müller Sánchez F., Genzel R., Tacconi L. J., Hicks E. K. S., Friedrich S., Sternberg A., 2007, *ApJ*, **671**, 1388
- Di Teodoro E. M., McClure-Griffiths N. M., Lockman F. J., Denbo S. R., Endsley R., Ford H. A., Harrington K., 2018, *ApJ*, **855**, 33
- Di Teodoro E. M., McClure-Griffiths N. M., Lockman F. J., Armillotta L., 2020, arXiv e-prints, p. [arXiv:2008.09121](https://arxiv.org/abs/2008.09121)
- Draine B. T., 1978, *ApJS*, **36**, 595
- Evans Neal J. I., Heiderman A., Vutisalchavakul N., 2014, *ApJ*, **782**, 114
- Federrath C., 2015, *MNRAS*, **450**, 4035
- Federrath C., Banerjee R., Clark P. C., Klessen R. S., 2010, *ApJ*, **713**, 269
- Federrath C., Sur S., Schleicher D. R. G., Banerjee R., Klessen R. S., 2011, *ApJ*, **731**, 62
- Federrath C., et al., 2016, *ApJ*, **832**, 143
- Ferrière K., Gillard W., Jean P., 2007, *A&A*, **467**, 611
- Fox A. J., et al., 2015, *ApJ*, **799**, L7
- Gatto A., et al., 2015, *MNRAS*, **449**, 1057
- Gatto A., et al., 2017, *MNRAS*, **466**, 1903
- Genzel R., Stacey G. J., Harris A. I., Townes C. H., Geis N., Graf U. U., Poglitsch A., Stutzki J., 1990, *ApJ*, **356**, 160
- Genzel R., Eisenhauer F., Gillessen S., 2010, *Rev. Mod. Phys.*, **82**, 3121
- Ghez A. M., et al., 2008, *ApJ*, **689**, 1044
- Gillessen S., et al., 2017, *ApJ*, **837**, 30
- Ginsburg A., et al., 2016, *A&A*, **586**, A50
- Girichidis P., Seifried D., Naab T., Peters T., Walch S., Wünsch R., Glover S. C. O., Klessen R. S., 2018, *MNRAS*, **480**, 3511
- Glover S. C. O., Clark P. C., 2012, *MNRAS*, **421**, 116
- Glover S. C. O., Mac Low M.-M., 2007a, *ApJS*, **169**, 239
- Glover S. C. O., Mac Low M.-M., 2007b, *ApJ*, **659**, 1317
- Glover S. C. O., Federrath C., Mac Low M.-M., Klessen R. S., 2010, *MNRAS*, **404**, 2
- Goldreich P., Lynden-Bell D., 1965, *MNRAS*, **130**, 125
- Goldsmith P. F., Langer W. D., 1978, *ApJ*, **222**, 881
- Gravity Collaboration et al., 2019, *A&A*, **625**, L10
- Henshaw J. D., et al., 2016a, *MNRAS*, **457**, 2675
- Henshaw J. D., et al., 2016b, *MNRAS*, **457**, 2675
- Henshaw J. D., et al., 2019, *MNRAS*, **485**, 2457
- Herrnstein R. M., Ho P. T. P., 2005, *ApJ*, **620**, 287
- Heyer M., Dame T. M., 2015, *ARA&A*, **53**, 583
- Hopkins P. F., Kereš D., Oñorbe J., Faucher-Giguère C.-A., Quataert E., Murray N., Bullock J. S., 2014, *MNRAS*, **445**, 581
- Hsieh P.-Y., Koch P. M., Ho P. T. P., Kim W.-T., Tang Y.-W., Wang H.-H., Yen H.-W., Hwang C.-Y., 2017, *ApJ*, **847**, 3
- Immer K., Schuller F., Omont A., Menten K. M., 2012, *A&A*, **537**, A121
- Immer K., Kauffmann J., Pillai T., Ginsburg A., Menten K. M., 2016, *A&A*, **595**, A94
- Inutsuka S.-i., Inoue T., Iwasaki K., Hosokawa T., 2015, *A&A*, **580**, A49
- Izumi T., et al., 2013, *PASJ*, **65**, 100
- Jones P. A., et al., 2012, *MNRAS*, **419**, 2961
- Julian W. H., Toomre A., 1966, *ApJ*, **146**, 810
- Kalberla P. M. W., Dedes L., 2008, *A&A*, **487**, 951

- Kataoka J., et al., 2013, *ApJ*, 779, 57
- Katz N., 1992, *ApJ*, 391, 502
- Katz N., Weinberg D. H., Hernquist L., 1996, *ApJS*, 105, 19
- Kauffmann J., Pillai T., Zhang Q., Menten K. M., Goldsmith P. F., Lu X., Guzmán A. E., Schmiedeke A., 2017a, *A&A*, 603, A90
- Kauffmann J., Goldsmith P. F., Melnick G., Tolls V., Guzman A., Menten K. M., 2017b, *A&A*, 605, L5
- Kennicutt Robert C. J., 1998, *ApJ*, 498, 541
- Kim C.-G., Ostriker E. C., 2015, *ApJ*, 802, 99
- Kim C.-G., Ostriker E. C., 2017, *ApJ*, 846, 133
- Kimm T., Cen R., 2014, *ApJ*, 788, 121
- Klessen R. S., Burkert A., 2000, *ApJS*, 128, 287
- Krieger N., et al., 2017, *ApJ*, 850, 77
- Kroupa P., 2001, *MNRAS*, 322, 231
- Kruijssen J. M. D., Dale J. E., Longmore S. N., 2015, *MNRAS*, 447, 1059
- Kruijssen J. M. D., et al., 2019a, *MNRAS*, 484, 5734
- Kruijssen J. M. D., et al., 2019b, *Nature*, 569, 519
- Krumholz M. R., Federrath C., 2019, *Frontiers in Astronomy and Space Sciences*, 6, 7
- Krumholz M. R., Kruijssen J. M. D., 2015, *MNRAS*, 453, 739
- Krumholz M. R., Dekel A., McKee C. F., 2012, *ApJ*, 745, 69
- Krumholz M. R., Kruijssen J. M. D., Crocker R. M., 2017, *MNRAS*, 466, 1213
- Le Petit F., Ruaud M., Bron E., Godard B., Roueff E., Languignon D., Le Bourlot J., 2016, *A&A*, 585, A105
- Lee S., et al., 2008, *ApJ*, 674, 247
- Li Z., Shen J., Schive H.-Y., 2020, *ApJ*, 889, 88
- Lin C. C., Shu F. H., 1964, *ApJ*, 140, 646
- Liu H. B., Hsieh P.-Y., Ho P. T. P., Su Y.-N., Wright M., Sun A.-L., Minh Y. C., 2012, *ApJ*, 756, 195
- Longmore S. N., et al., 2012, *ApJ*, 746, 117
- Longmore S. N., et al., 2013, *MNRAS*, 429, 987
- Longmore S. N., et al., 2017, *MNRAS*, 470, 1462
- Lu X., et al., 2017, *ApJ*, 839, 1
- Mac Low M.-M., Klessen R. S., 2004, *Reviews of Modern Physics*, 76, 125
- Maeder A., 2009, *Physics, Formation and Evolution of Rotating Stars*. Springer, Berlin Heidelberg, doi:10.1007/978-3-540-76949-1
- Mangilli A., et al., 2019, *A&A*, 630, A74
- Marsh K. A., Ragan S. E., Whitworth A. P., Clark P. C., 2016, *MNRAS*, 461, L16
- Marshall D. J., Fux R., Robin A. C., Reylé C., 2008, *A&A*, 477, L21
- Martizzi D., Faucher-Giguère C.-A., Quataert E., 2015, *MNRAS*, 450, 504
- McClure-Griffiths N. M., Green J. A., Hill A. S., Lockman F. J., Dickey J. M., Gaensler B. M., Green A. J., 2013, *ApJ*, 770, L4
- McGary R. S., Coil A. L., Ho P. T. P., 2001, *ApJ*, 559, 326
- Mills E. A. C., Güsten R., Requena-Torres M. A., Morris M. R., 2013, *ApJ*, 779, 47
- Mills E. A. C., Ginsburg A., Immer K., Barnes J. M., Wiesenfeld L., Faure A., Morris M. R., Requena-Torres M. A., 2018, *ApJ*, 868, 7
- Molinari S., et al., 2011, *ApJ*, 735, L33
- Montenegro L. E., Yuan C., Elmegreen B. G., 1999, *ApJ*, 520, 592
- Morris M. R., 2015, *Manifestations of the Galactic Center Magnetic Field*. Springer International Publishing, p. 391, doi:10.1007/978-3-319-10614-4\_32
- Morris M., Serabyn E., 1996, *ARA&A*, 34, 645
- Nakashima S., Koyama K., Wang Q. D., Enokiya R., 2019, *ApJ*, 875, 32
- Nelson R. P., Langer W. D., 1997, *ApJ*, 482, 796
- Offner S. S. R., Arce H. G., 2015, *ApJ*, 811, 146
- Oka T., Geballe T. R., Goto M., Usuda T., Benjamin McCall J., Indriolo N., 2019, *ApJ*, 883, 54
- Okumura S. K., Ishiguro M., Fomalont E. B., Hasegawa T., Kasuga T., Morita K.-I., Kawabe R., Kobayashi H., 1991, *ApJ*, 378, 127
- Ostriker E. C., Binney J. J., 1989, *MNRAS*, 237, 785
- Pakmor R., Springel V., 2013, *MNRAS*, 432, 176
- Phinney E. S., 1994, in Shlosman I., ed., *Mass-Transfer Induced Activity in Galaxies*. p. 1
- Pillai T., Kauffmann J., Tan J. C., Goldsmith P. F., Carey S. J., Menten K. M., 2015, *ApJ*, 799, 74
- Ponti G., et al., 2019, *Nature*, 567, 347
- Rahner D., Pellegrini E. W., Glover S. C. O., Klessen R. S., 2018, *MNRAS*, 473, L11
- Rahner D., Pellegrini E. W., Glover S. C. O., Klessen R. S., 2019, *MNRAS*, 483, 2547
- Rathborne J. M., et al., 2015, *ApJ*, 802, 125
- Requena-Torres M. A., et al., 2012, *A&A*, 542, L21
- Ridley M., Sormani M. C., Treß R. G., Magorrian J., Klessen R. S., 2017, *MNRAS*, 469, 2251
- Rosen A. L., Krumholz M. R., McKee C. F., Klein R. I., 2016, *MNRAS*, 463, 2553
- Sandage A., 1961, *The Hubble Atlas of Galaxies*. Carnegie Institution of Washington, Washington, D.C.
- Schmidt M., 1959, *ApJ*, 129, 243
- Shetty R., Beaumont C. N., Burton M. G., Kelly B. C., Klessen R. S., 2012, *MNRAS*, 425, 720
- Shin J., Kim S. S., Baba J., Saitoh T. R., Hwang J.-S., Chun K., Hozumi S., 2017, *ApJ*, 841, 74
- Simpson C. M., Bryan G. L., Hummels C., Ostriker J. P., 2015, *ApJ*, 809, 69
- Sjouwerman L. O., Pihlström Y. M., 2008, *ApJ*, 681, 1287
- Sofue Y., 1995, *PASJ*, 47, 527
- Sormani M. C., Barnes A. T., 2019, *MNRAS*, 484, 1213
- Sormani M. C., Li Z., 2020, *MNRAS*, 494, 6030
- Sormani M. C., Binney J., Magorrian J., 2015a, *MNRAS*, 449, 2421
- Sormani M. C., Binney J., Magorrian J., 2015b, *MNRAS*, 451, 3437
- Sormani M. C., Binney J., Magorrian J., 2015c, *MNRAS*, 454, 1818
- Sormani M. C., Treß R. G., Klessen R. S., Glover S. C. O., 2017, *MNRAS*, 466, 407
- Sormani M. C., Treß R. G., Ridley M., Glover S. C. O., Klessen R. S., Binney J., Magorrian J., Smith R., 2018, *MNRAS*, 475, 2383
- Sormani M. C., et al., 2019, *MNRAS*, 488, 4663
- Sormani M. C., Tress R. G., Glover S. C. O., Klessen R. S., Battersby C. D., Clark P. C., Hatchfield H. P., Smith R. J., 2020, *MNRAS*, 497, 5024 (Paper II)
- Springel V., 2005, *MNRAS*, 364, 1105
- Springel V., 2010, *MNRAS*, 401, 791
- Stinson G., Seth A., Katz N., Wadsley J., Governato F., Quinn T., 2006, *MNRAS*, 373, 1074
- Su M., Slatyer T. R., Finkbeiner D. P., 2010, *ApJ*, 724, 1044
- Takekawa S., Oka T., Tanaka K., 2017, *ApJ*, 834, 121
- Toomre A., 1964, *ApJ*, 139, 1217
- Trani A. A., Mapelli M., Ballone A., 2018, *ApJ*, 864, 17
- Tress R. G., Smith R. J., Sormani M. C., Glover S. C. O., Klessen R. S., Mac Low M.-M., Clark P. C., 2020, *MNRAS*, 492, 2973
- Truelove J. K., Klein R. I., McKee C. F., Holliman II J. H., Howell L. H., Greenough J. A., 1997, *ApJ*, 489, L179
- Tsuboi M., Kitamura Y., Uehara K., Tsutsumi T., Miyawaki R., Miyoshi M., Miyazaki A., 2018, *PASJ*, 70, 85
- Utomo D., et al., 2018, *ApJ*, 861, L18
- Walch S., et al., 2015, *MNRAS*, 454, 238
- Wang L., Wheeler J. C., 2008, *ARA&A*, 46, 433
- Weinberger R., Springel V., Pakmor R., 2020, *ApJS*, 248, 32

**APPENDIX A: IMAGES OF SURFACE DENSITIES IN  
VARIOUS TRACERS**

In this appendix, we show the time evolution of the gas surface densities in various tracers.

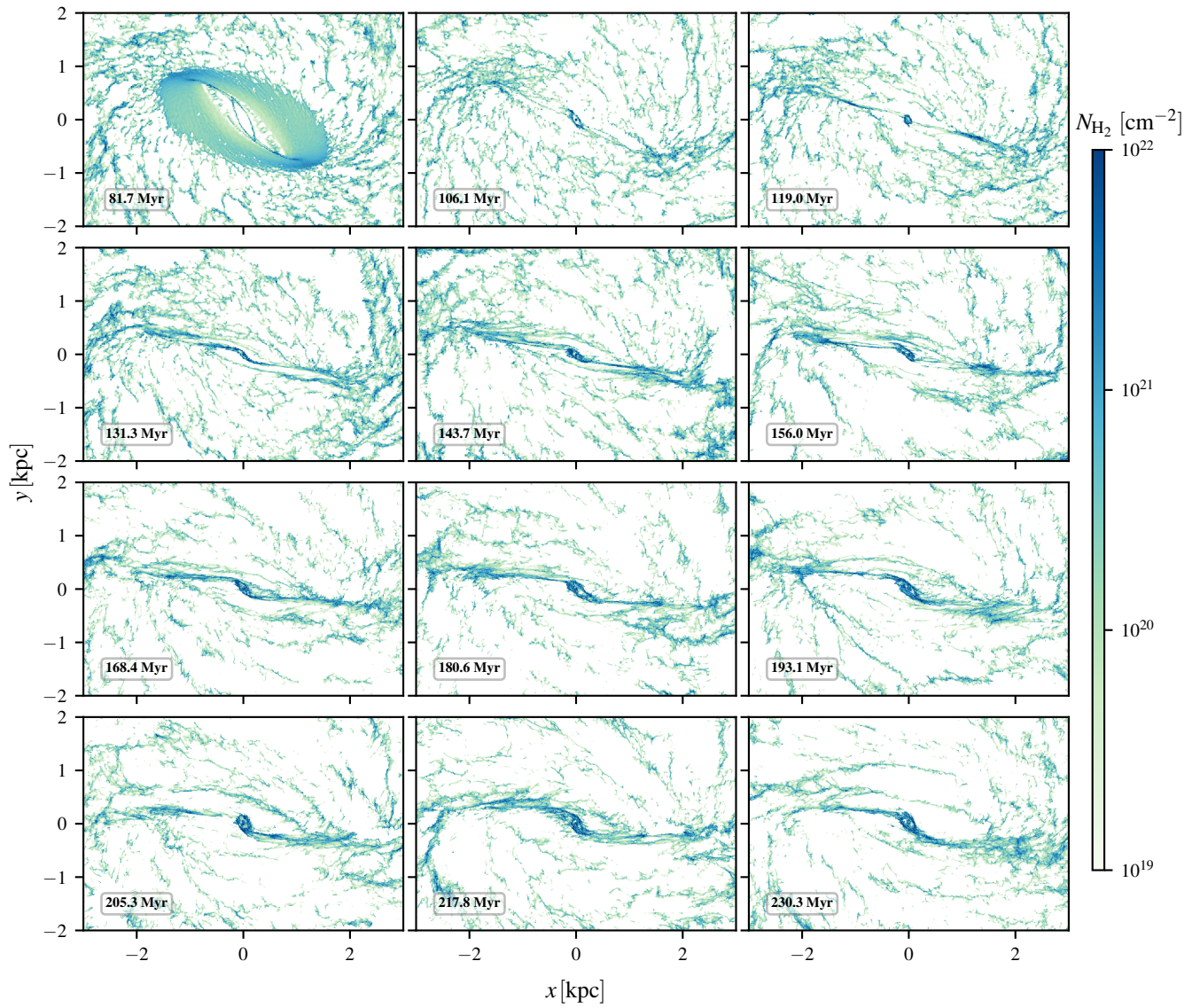


**Figure A1.**  $\text{H}_2$  gas surface density at different times in the simulation.

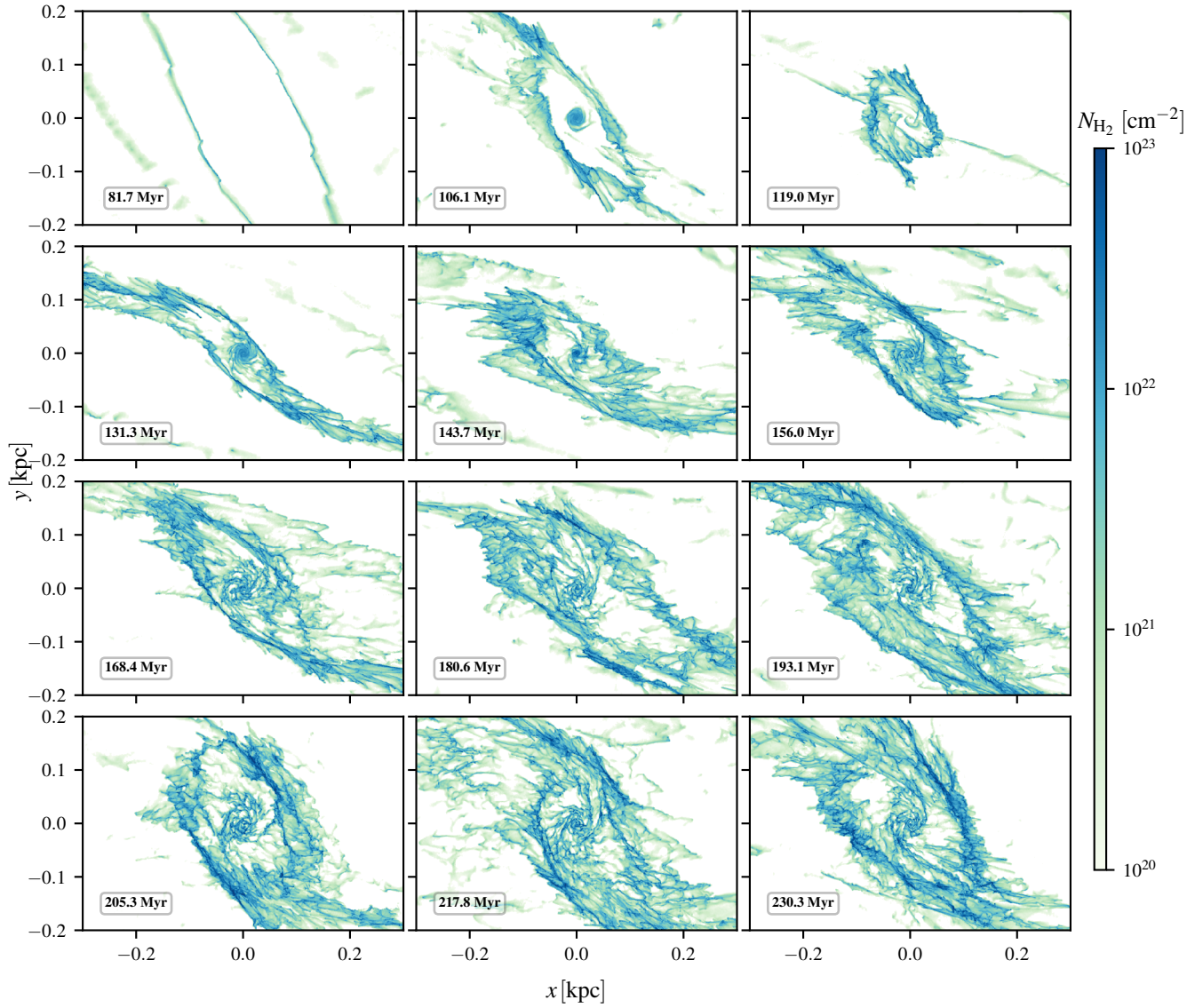


**Figure A2.** Zoom of Figure A1 onto the CMZ.

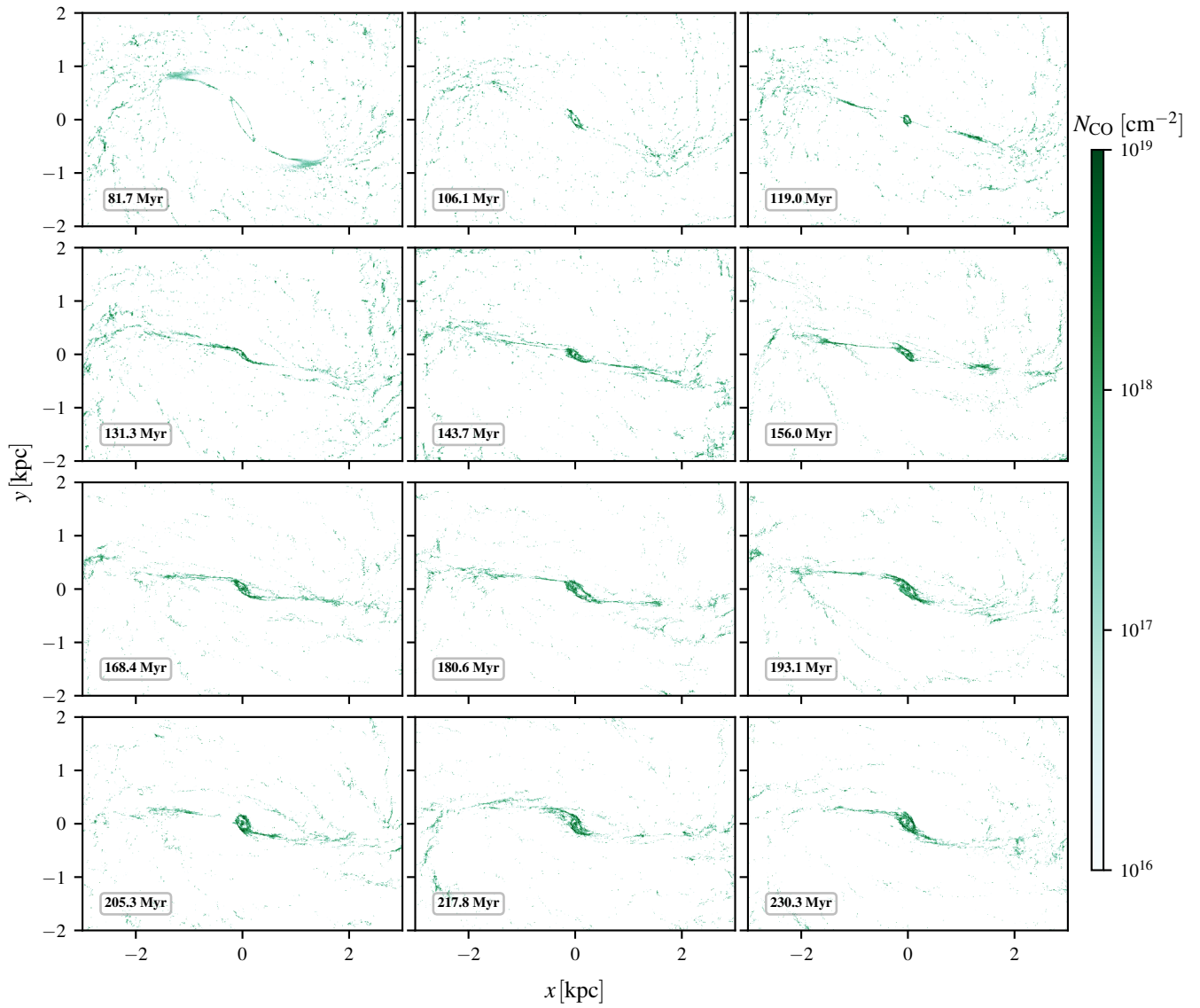


**Figure A3.** CO gas surface density at different times in the simulation.

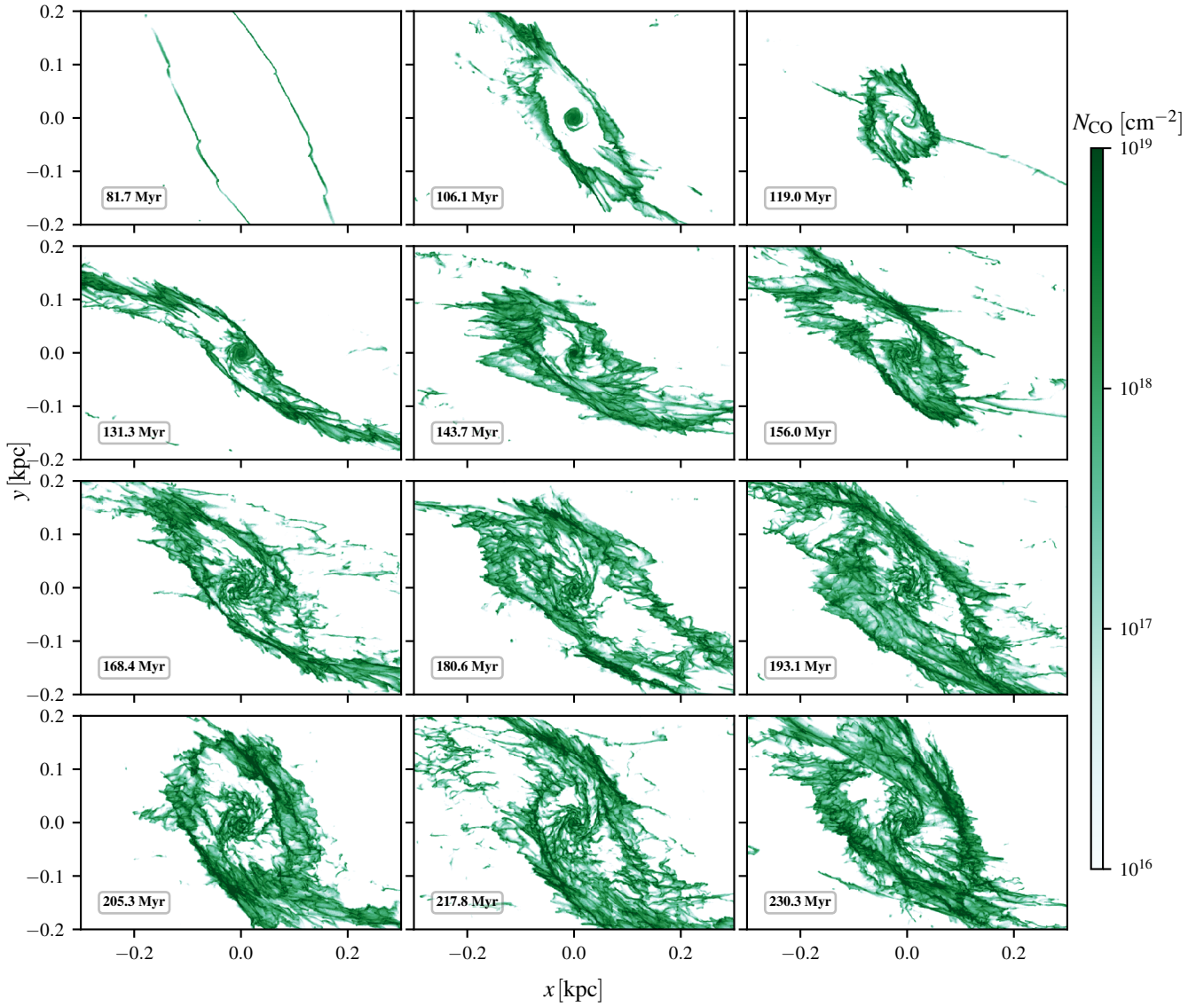


**Figure A4.** Zoom of Figure A3 onto the CMZ.

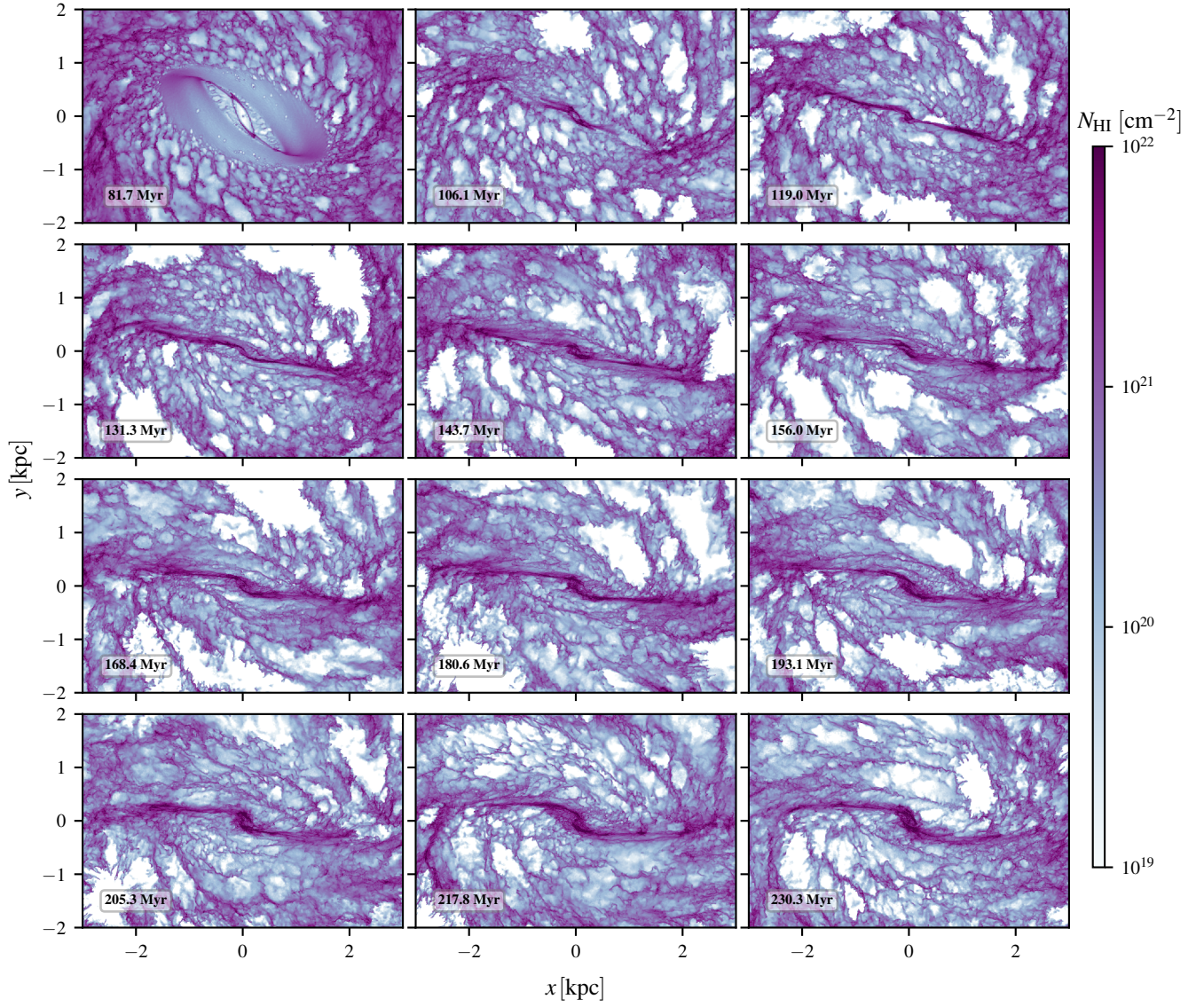


**Figure A5.** HI gas surface density at different times in the simulation.

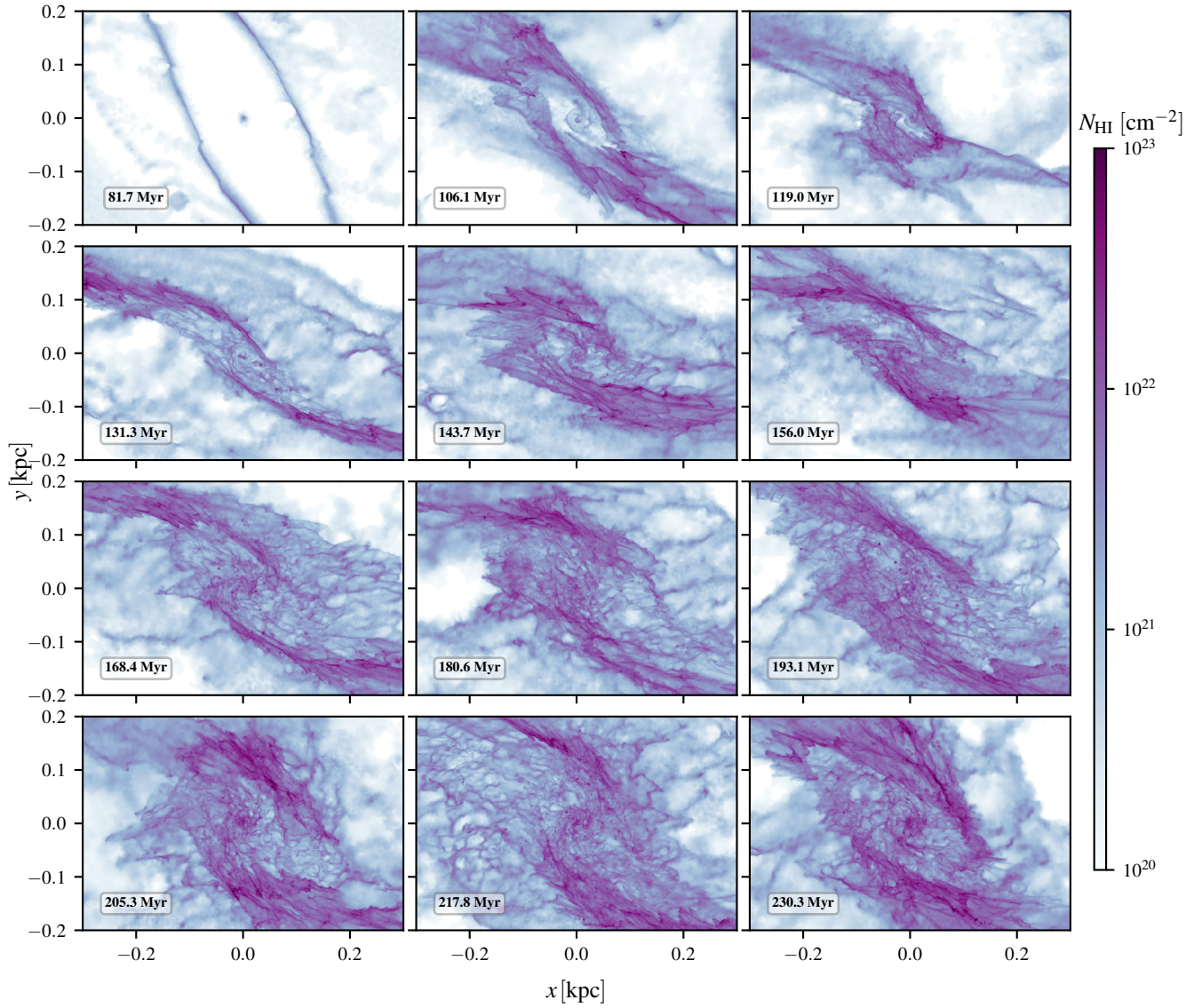


**Figure A6.** Zoom of Figure A5 onto the CMZ.

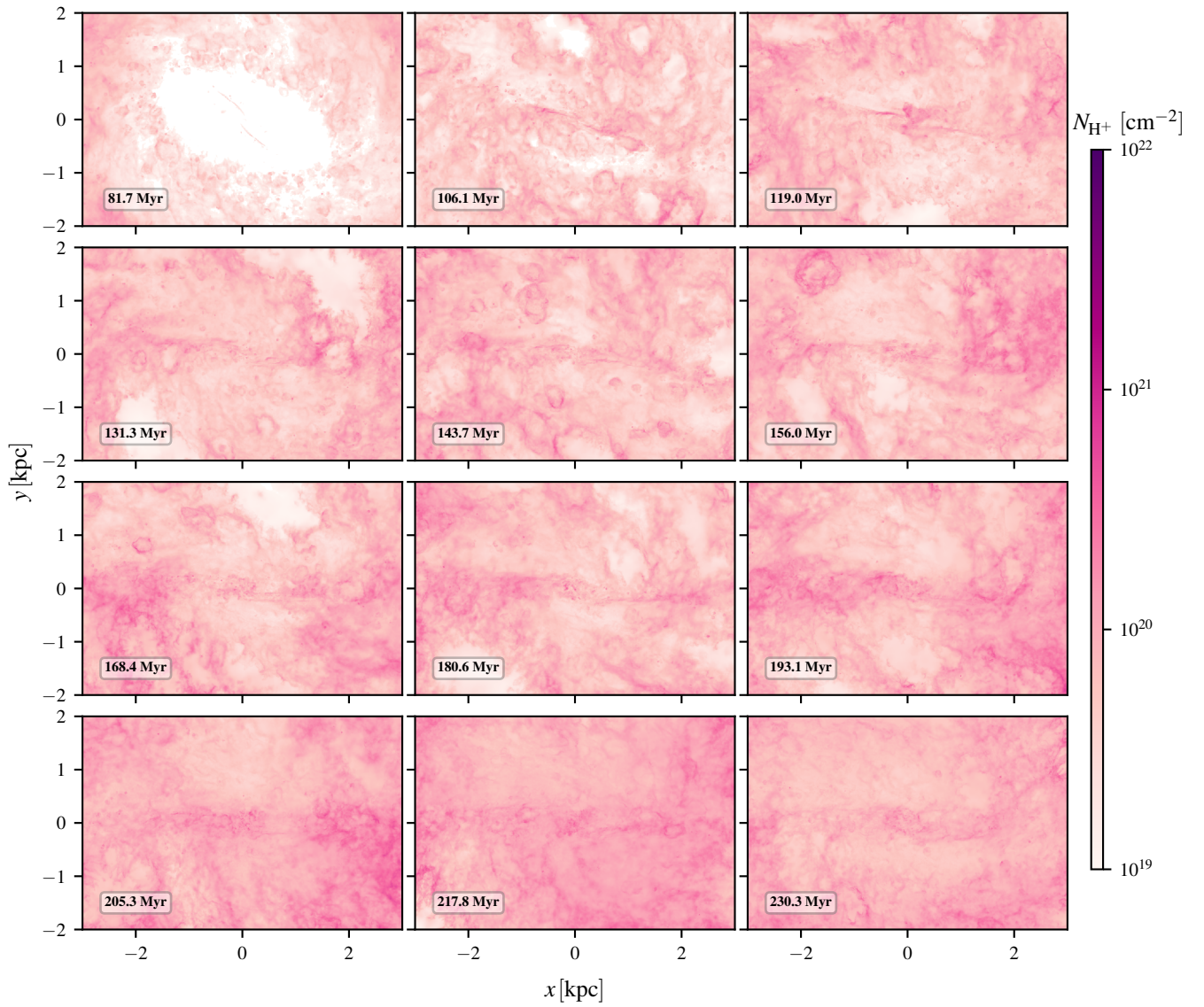


**Figure A7.**  $\text{H}^+$  gas surface density at different times in the simulation.

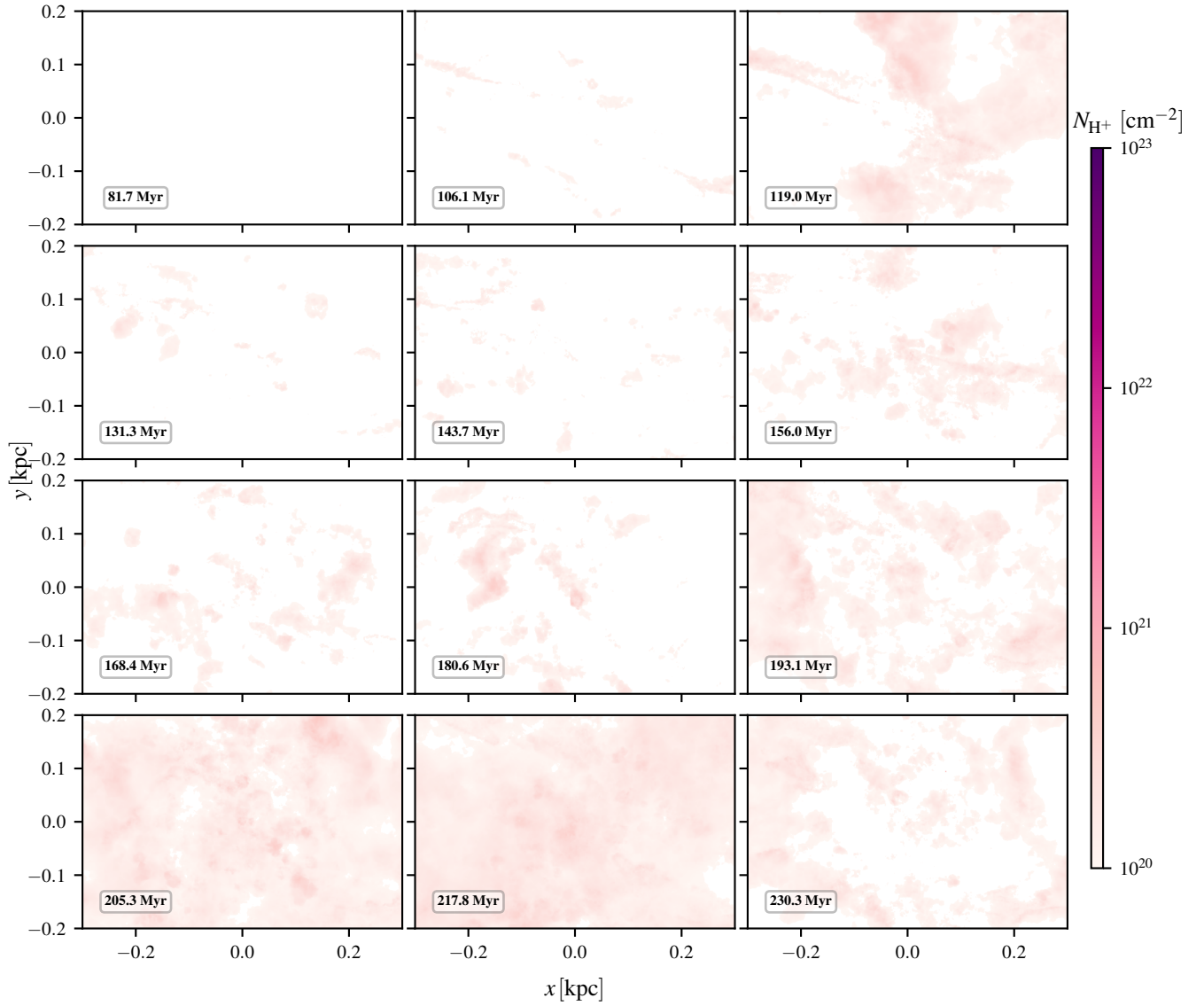


**Figure A8.** Zoom of Figure A7 onto the CMZ.

# Chapter 5

## Simulations of the Milky Way's central molecular zone - II. Star formation

### 5.1 Statement about my contribution

For this publication my contribution was equal to that of Dr. Mattia Sormani, the first author of the publication.

- **Simulations:** this publication relies on the same simulation data produced for the publication presented in Chapter 4. The workload regarding code development, simulation setup, running the simulations and physical model is therefore shared between the two scientific papers.
- **Analysis:** my contribution was central and equal to that of Dr. Mattia Sormani. Feedback from and discussion with our other collaborators was important as an iterative process during the analysis step as well as during the revision phase.
- **Figures:** my contribution was central. I produced most of the figures in the publication with major help and feedback from Dr. Mattia Sormani. I gave substantial feedback for the figures produced by Dr. Sormani instead.
- **Writing:** I have written large parts of the manuscript and gave feedback and contributions to the parts written by Dr. Mattia Sormani instead. The process was iterative and driven by feedback from our other collaborators.
- **Scientific discussion:** most collaborators contributed equally to the discussions, but Dr. Sormani and myself led the discussions and often proposed possible research

directions which were usually first considered in private meetings and then debated with our other collaborators.

# Simulations of the Milky Way’s central molecular zone - II. Star formation

Mattia C. Sormani<sup>1</sup>, Robin G. Tress<sup>1</sup>, Simon C.O. Glover<sup>1</sup>, Ralf S. Klessen<sup>1,2</sup>,  
Cara D. Battersby<sup>3</sup>, Paul C. Clark<sup>4</sup>, H Perry Hatchfield<sup>3</sup> and Rowan J. Smith<sup>5</sup>

<sup>1</sup>Universität Heidelberg, Zentrum für Astronomie, Institut für theoretische Astrophysik, Albert-Ueberle-Str. 2, 69120 Heidelberg, Germany

<sup>2</sup>Universität Heidelberg, Interdisziplinäres Zentrum für Wissenschaftliches Rechnen, Im Neuenheimer Feld 205, 69120 Heidelberg, Germany

<sup>3</sup>University of Connecticut, Department of Physics, 196 Auditorium Road, Unit 3046, Storrs, CT 06269, USA

<sup>4</sup>School of Physics and Astronomy, Queen’s Buildings, The Parade, Cardiff University, Cardiff, CF24 3AA, UK

<sup>5</sup>Jodrell Bank Centre for Astrophysics, School of Physics and Astronomy, University of Manchester, Oxford Road, Manchester M13 9PL, UK

## ABSTRACT

The Milky Way’s central molecular zone (CMZ) has emerged in recent years as a unique laboratory for the study of star formation. Here we use the simulations presented in Tress et al. 2020 to investigate star formation in the CMZ. These simulations resolve the structure of the interstellar medium at sub-parsec resolution while also including the large-scale flow in which the CMZ is embedded. Our main findings are as follows. (1) While most of the star formation happens in the CMZ ring at  $R \gtrsim 100$  pc, a significant amount also occurs closer to SgrA\* at  $R \lesssim 10$  pc. (2) Most of the star formation in the CMZ happens downstream of the apocentres, consistent with the “pearls-on-a-string” scenario, and in contrast to the notion that an absolute evolutionary timeline of star formation is triggered by pericentre passage. (3) Within the timescale of our simulations ( $\sim 100$  Myr), the depletion time of the CMZ is constant within a factor of  $\sim 2$ . This suggests that variations in the star formation rate are primarily driven by variations in the mass of the CMZ, caused for example by AGN feedback or externally-induced changes in the bar-driven inflow rate, and not by variations in the depletion time. (4) We study the trajectories of newly born stars in our simulations. We find several examples that have age and 3D velocity compatible with those of the Arches and Quintuplet clusters. Our simulations suggest that these prominent clusters originated near the collision sites where the bar-driven inflow accretes onto the CMZ, at symmetrical locations with respect to the Galactic centre, and that they have already decoupled from the gas in which they were born.

**Key words:** Galaxy: centre - Galaxy: kinematics and dynamics - ISM: kinematics and dynamics - ISM: clouds - ISM: evolution - stars: formation

## 1 INTRODUCTION

The central molecular zone (CMZ,  $R \lesssim 200$  pc) is the Milky Way’s counterpart of the star-forming nuclear rings that are commonly found in the central regions of external barred galaxies such as NGC 1300 (see for example the atlas of nuclear rings of Comerón et al. 2010). Being a hundred times closer than the nucleus of the next comparable galaxy, Andromeda, it offers us the possibility to study a nuclear ring in unique detail.

The CMZ has emerged in the last decade as a unique laboratory for the study of star formation (e.g. Molinari et al. 2011; Kruijssen et al. 2014; Armillotta et al. 2019). The main reason is that the environmental conditions in which stars are born are more extreme than anywhere else in the Galaxy. Indeed, the physical properties of the interstellar medium (ISM) in the CMZ are substantially different from those in the Galactic disc: average gas volume densities

(Guesten & Henkel 1983; Walmsley et al. 1986; Longmore et al. 2017; Mills et al. 2018), temperatures (Immer et al. 2016; Ginsburg et al. 2016; Krieger et al. 2017; Oka et al. 2019), velocity dispersions (Shetty et al. 2012; Federrath et al. 2016), and magnetic field strengths (Morris 2015; Mangilli et al. 2019) are all much higher than in the disc. The interstellar radiation field and higher cosmic ray ionisation rate (Clark et al. 2013; Ginsburg et al. 2016; Oka et al. 2019) are also much stronger. In addition, the CMZ region is characterised by the presence of Galactic outflows (Ponti et al. 2019), by the widespread presence of radio-emitting magnetised non-thermal filaments (Heywood et al. 2019), and by a strong hydrodynamical interaction with the larger-scale gas inflow driven by the Galactic bar (Sormani et al. 2018a). The star formation process, which is determined by the complex interplay of all these physical agents, is therefore expected to proceed differently in the CMZ.

Observations confirm this, by showing that the CMZ does not obey some star formation relations that are valid in the disc (Longmore et al. 2013a; Kauffmann et al. 2017a). Hence, understanding star formation in the CMZ is important for understanding the star formation process in extreme environments, as well as in general by probing a peculiar corner of parameter space.

In a companion paper (Tress et al. 2020, hereafter Paper I) we have presented sub-parsec resolution hydrodynamical simulations and have used them to study the gas dynamics in the CMZ. In this paper, we use the same simulations to investigate star formation.

Open questions that we address in the current work include:

- (i) What is the temporal distribution of star formation in the CMZ? (Section 3.1)
- (ii) What is spatial distribution of star formation in the CMZ? (Section 3.2)
- (iii) What is the impact of the orbital dynamics on star formation? Can we identify an absolute evolutionary timeline of star formation as suggested by Longmore et al. (2013b) and Kruijssen et al. (2015)? (Section 4.2)
- (iv) What drives the time variability of star formation in the CMZ? (Section 4.1)
- (v) Are the Arches and Quintuplet cluster on a common orbit with gas in the CMZ ring (Kruijssen et al. 2015) or are they on other types of orbits (Stolte et al. 2008)? (Section 4.4)

The paper is structured as follows. In Section 2 we give a brief summary of our numerical simulations. In Section 3 we study the temporal and spatial distribution of star formation and the trajectories of newly born stars. In Section 4 we discuss the implications of our results for some of the open questions raised above. We sum up in Section 5.

## 2 NUMERICAL METHODS

Our simulations have been presented in detail in Paper I. Hence we give here only a very brief overview, and refer to that paper for more details.

### 2.1 Overview

The simulations are similar to those we previously discussed in Sormani et al. (2018a, 2019), with the following differences: (i) inclusion of gas self-gravity; and (ii) inclusion of a sub-grid prescription for star formation and stellar feedback. In particular, we employ exactly the same externally-imposed rotating barred potential, the same chemical/thermal treatment of the gas, and the same initial conditions as in Sormani et al. (2019).

We use the moving-mesh code AREPO (Springel 2010; Weinberger et al. 2019). The simulations are three-dimensional and unmagnetised, and include a live chemical network that keeps track of hydrogen and carbon chemistry. The simulations comprise interstellar gas in the whole inner disc ( $R \leq 5$  kpc) of the Milky Way, which allows us to understand the CMZ in the context of the larger-scale flow, which is important since the CMZ strongly interacts with its surrounding through the bar inflow (Sormani et al. 2018a). The gas is assumed to flow in a multi-component external rotating barred potential  $\Phi_{\text{ext}}(\mathbf{x}, t)$  which is constructed to fit the properties of the Milky Way. The bar component rotates with a pattern speed  $\Omega_p = 40 \text{ km s}^{-1} \text{ kpc}^{-1}$ , consistent with the most recent determinations (e.g. Sormani et al. 2015; Portail et al. 2017; Sanders et al.

2019), which places the (only) inner Lindblad resonance (ILR) calculated in the epicyclic approximation at  $R_{\text{ILR}} = 1.1$  kpc and the corotation resonance at  $R_{\text{CR}} = 5.9$  kpc. The potential is identical to that used in Sormani et al. (2019) and is described in more detail in the appendix of that paper.

Gas self-gravity is included. The process of star formation and the consequent stellar feedback are modelled as follows (see Section 2 of Paper I for more details):

- (i) Gravitationally-collapsing gas that exceeds a density threshold  $\rho_c = 10^{-20} \text{ g cm}^{-3}$  is removed from the simulation and replaced with a non-gaseous sink particle, provided that it is unambiguously gravitationally bound and not within the accretion radius of an existing sink particle. The sink particle does not represent an individual star, but rather a small cluster which contains both gas and stars.
- (ii) Once a sink is created, a stellar population is assigned to it by drawing from an initial mass function (IMF) according to the Poisson stochastic method described in Sormani et al. (2017).
- (iii) Sink particles are allowed to accrete mass at later times, provided that the gas is within the sink accretion radius  $r_{\text{acc}} = 1$  pc and is gravitationally bound to the sink. The stellar population associated with a given sink is updated every time that that sink accretes additional mass.
- (iv) For each massive star ( $M \geq 8 M_{\odot}$ ) assigned to the sink, we produce a supernovae (SNe) event with a time delay which depends on the stellar mass. Each SNe event injects energy and/or momentum into the ISM and gives back to the environment part of the gas “locked-up” in the sink. Energy is injected only if the local resolution of the Voronoi mesh is high enough to resolve the supernova remnant at the end of its Sedov-Taylor phase; otherwise, an appropriate amount of momentum is injected instead. SNe feedback is the only type of feedback included in the simulation.
- (v) When all the SNe associated with a sink have exploded and all of its gas content has been given back to the environment, the sink is converted into a collisionless N-body star particle with a mass equal to the stellar mass of the sink. This N-body particle continues to exist indefinitely in the simulation and affects it through its gravitational potential, but, unlike a sink, it can no longer accrete new gas or form new stars.

When making projections onto the plane of the Sky, we assume an angle between the Sun-Galactic centre line and the bar major axis of  $\phi = 20^\circ$ , a Sun-Galactic centre distance of 8.2 kpc (Reid et al. 2019; Gravity Collaboration et al. 2019), and that the Sun is on a circular orbit at  $v_{\odot} = 235 \text{ km s}^{-1}$  (Schönrich et al. 2010; Reid et al. 2019), as in Paper I.

### 2.2 Subdivision in three regions: CMZ, DLR, disc

As in Paper I, we subdivide our simulation into three spatial regions in order to facilitate the subsequent analysis (see Figure 1):

- The *CMZ* is defined as the region within cylindrical radius  $R \leq 250$  pc.
- The *dust lane region (DLR)* is the elongated transition region between the CMZ and the Galactic disc, where highly non-circular gas motions caused by the bar are present.
- The *disc* is defined as everything outside the DLR.

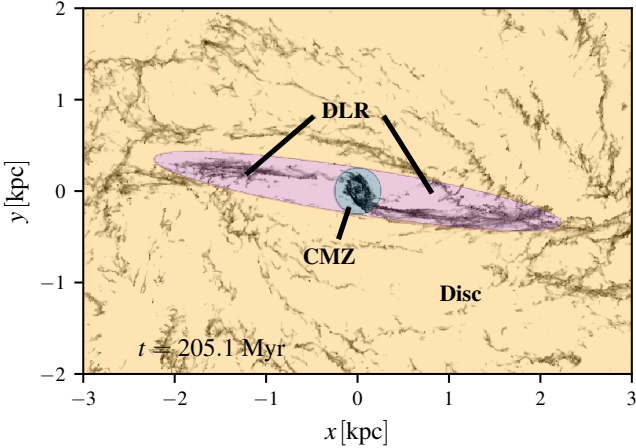


**Figure 1.** Definition of the three regions (CMZ, DLR, disc) into which we subdivide our simulated Galaxy for subsequent analysis. See Section 2.2 for more details.

### 3 STAR FORMATION

#### 3.1 Temporal distribution of star formation

Figure 2 shows the star formation rate (SFR) as a function of time in our simulation, calculated as a running average over the last 0.5 Myr. This corresponds to twice the timestep between consecutive simulation outputs, and has been chosen because we want to study where and when star formation is being triggered.<sup>1</sup> The thin blue line shows the total SFR in the entire simulation box (CMZ + DLR + disc). This is roughly constant at a value of approximately  $\sim 1 M_{\odot} \text{ yr}^{-1}$ , consistent with typically reported values of the MW total SFR derived from observations ( $\sim 2\text{--}3 M_{\odot} \text{ yr}^{-1}$ , e.g. Kennicutt & Evans 2012) when we take into account that our simulated disc only extends to  $R \simeq 5 \text{ kpc}$ , so the total gas mass in the simulation ( $\simeq 1.5 \times 10^9 M_{\odot}$ ) is only  $\sim 1/3$  of the total estimated mass in the MW gas disc.

The thick blue line shows the total SFR of the CMZ (defined as the region  $R \leq 250 \text{ pc}$ , see Figure 1). The insert panels correlate the SFR with the CMZ gas morphology at different times. At  $t = 146 \text{ Myr}$  (when the bar potential is fully turned on, see Section 2.7 in Paper I), the SFR in the CMZ has a value of  $\sim 0.1 M_{\odot} \text{ yr}^{-1}$ , consistent with observational estimates (see Yusef-Zadeh et al. 2009; Immer et al. 2012; Longmore et al. 2013a; Barnes et al. 2017 and Section 4.1), and the total gas mass of the CMZ is  $\sim 4 \times 10^7 M_{\odot}$ , which also agrees well with observational values ( $\sim 5 \times 10^7 M_{\odot}$ , Dahmen et al. 1998; Longmore et al. 2013a).

At later times ( $t > 146 \text{ Myr}$ ) the SFR of the CMZ slowly but steadily increases with time, with small fluctuations on short timescales ( $\sim 1 \text{ Myr}$ ) of a factor of  $\sim 2\text{--}3$ . This increase in the SFR is mirrored by an increase in the total gas mass of the CMZ (see blue lines in Figure 19 of Paper I). The depletion time, which is defined as the ratio between the mass and the SFR ( $\tau_{\text{depl}} = M/\text{SFR}$ ), is shown by the blue dashed line in Figure 3. It is approximately constant in time. Therefore, the SFR in the CMZ in our simulation

is roughly proportional to its total mass, and variations in the value of the SFR are determined by variations in the total mass.

Figure 3 also shows that the depletion time in the disc (yellow dashed line) is a factor of  $\sim 5$  higher than the depletion time in the CMZ (blue dashed line). Therefore, while the depletion time of each region is approximately constant in time, there are spatial variations when considering different portions of the Galaxy. The variations in the depletion times can be explained by the different stellar gravitational potential, whose vertical gradient is stronger in the CMZ than in the disc. This can be seen as follows. For a medium in which the turbulence is driven by supernovae feedback and assuming that the vertical force of the gravitational potential is balanced by the turbulent pressure (both conditions that are approximately verified in our simulations) the analytical model of Ostriker & Shetty (2011) predicts that (see their Equation 13):

$$\Sigma_{\text{SFR}} \propto (1 + \chi)\Sigma^2, \quad (1)$$

where  $\Sigma_{\text{SFR}}$  is the SFR surface density,  $\Sigma$  is the total gas surface density,  $\chi = 2C/(1 + \sqrt{1 + 4C})$ ,  $C = 8\zeta_{\text{d}}\rho_{\text{b}}\sigma_z^2/(3\pi G\Sigma^2)$ ,  $\sigma_z$  is the vertical velocity dispersion,  $\rho_{\text{b}}$  is the stellar midplane density (which is proportional to the strength of the gravitational potential),  $G$  is the gravitational constant and  $\zeta_{\text{d}} \simeq 1/3$  is a numerical factor (unimportant here). In the limit that the gravitational potential of the stars dominates over the gravitational potential of the gas disc, as is the case for the present simulations, we have  $C \gg 1$ ,  $\chi \simeq (2C)^{1/2}$  and therefore  $\Sigma_{\text{SFR}} \propto \rho_{\text{b}}^{1/2}\Sigma$ . The depletion time is then  $\tau_{\text{depl}} = \Sigma/\Sigma_{\text{SFR}} \propto \rho_{\text{b}}^{-1/2}$ . For the potential employed in our simulations, we find  $[\rho_{\text{b}}(R = 150 \text{ pc})/\rho_{\text{b}}(R = 3 \text{ kpc})]^{-1/2} \simeq 6$ , in good agreement with the results in Figure 3 considering the uncertainties present both in the simulations and in the simplifying assumptions on which the theory of Ostriker & Shetty (2011) is based. The agreement between our simulation and the theory of Ostriker & Shetty (2011) is consistent with the fact that the integrated properties of the CMZ follow well star formation relations based on the total or molecular gas surface density, such as the Schmidt-Kennicutt or the Bigiel et al. (2008) relation, and only become peculiar when considering the very dense gas (see Section 4.3).

Another factor that is likely to contribute to lowering the depletion time in the CMZ, and which is not accounted for in the vertical equilibrium theories of Ostriker et al. (2010) and Ostriker & Shetty (2011), is the increased number of shocks due to the large-scale bar flow, which cause local compressions and therefore enhanced star formation (Mac Low & Klessen 2004; Klessen & Glover 2016).

How would the CMZ mass/SFR evolve if we continue our simulation beyond the maximum time shown in Figure 2? Assuming that the depletion time remains constant at the value  $\tau_{\text{depl,CMZ}} \simeq 4 \times 10^8 \text{ yr}$  inferred from Figure 3, we might extrapolate that the mass of the CMZ would keep increasing until the SFR matches the bar-driven inflow rate. For an inflow rate of  $\dot{M} \simeq 1 M_{\odot} \text{ yr}^{-1}$  (see Paper I), the equilibrium CMZ mass would be  $\dot{M}\tau_{\text{depl,CMZ}} \simeq 4 \times 10^8 M_{\odot}$ . However, there are several factors that might invalidate this extrapolation: (i) at a mass  $\simeq 4 \times 10^8 M_{\odot}$ , the gravitational potential of the gas would become comparable to that of the stars, which would affect the depletion time (see discussion immediately after Equation 1 above); (ii) at a SFR of  $\simeq 1 M_{\odot} \text{ yr}^{-1}$ , the increased SN feedback rate might also change the depletion time; (iii) the bar-driven inflow rate will decrease once the reservoir at  $R \gtrsim 3 \text{ kpc}$  gets depleted as the simulation progresses. In the real Galaxy, additional processes not included in our simulation such as expulsion of gas

<sup>1</sup> Observationally determined rates are more often averaged over longer timescales ( $\sim 10 \text{ Myr}$ ). We will briefly discuss the distribution of older stars in Section 3.2, while we defer a more observationally oriented approach and synthetic observations to future work.

due to AGN feedback, Galactic winds and externally-driven variations in the bar-driven inflow rate are also likely to modify the mass of the CMZ on comparable or even shorter timescales (see also the discussion in Section 4.1).

### 3.2 Spatial distribution of star formation

Figures 4 and 5 show the spatial distribution of the SFR density in a typical simulation snapshot. As before, the SFR is calculated as the running average over the last 0.5 Myr. As expected, star formation occurs predominantly where gas is densest.

It is instructive to compare the “instantaneous” SFR density (Figures 4 and 5) with the time-averaged SFR density (bottom panel in Figure 6). This comparison shows very clearly that while the time-averaged distribution is smooth, the instantaneous SFR density can have complex and transient morphologies which deviate significantly from the averaged morphology. In particular, the time-averaged star formation in the CMZ is smoothly distributed along an elliptical ring, while looking at the instantaneous SFR does not always give the impression of a ring. The size of the ring is significantly smaller than the ILR calculated in the epicyclic approximation, consistent with previous studies (see for example Li et al. 2015; Sormani et al. 2015, 2018b). It is also worth noting that the points where overshooting<sup>2</sup> material crashes into the dust lanes, which in Sormani et al. (2019) we have interpreted as producing the observed extended velocity features (EVF), are sites of enhanced star formation. However, by the time this star formation is visible, these regions will have moved at high speed ( $\sim 200 \text{ km s}^{-1}$ ) inwards towards the CMZ. The time delay between sink formation in our model and the star formation actually becoming visible will depend on our choice of star formation rate tracer, but we would expect it to be at least  $\sim 0.4$  Myr (the free-fall time of the gas at the sink creation density). Star formation should become visible soon after this if observed with tracers that are insensitive to the dust extinction (e.g. radio recombination lines), or after a longer but poorly quantified period if observed with tracers such as  $\text{H}\alpha$  that are highly sensitive to dust obscuration. This is consistent with observations of Bania Clump 2 (one of the most prominent EVF), which despite containing dozen of 1.1 mm clumps, has been found to be deficient in near- and mid-infrared emission in the Spitzer images and has been suggested to be in a pre-stellar stage of cloud evolution by Bally et al. (2010). Our simulations therefore support the idea that Bania Clump 2 will shortly begin to form massive stars.

A noteworthy feature of the averaged as well as of the instantaneous SFR density distributions (bottom panel of Figure 6 and Figure 5) is that there is a site of star formation inside the CMZ ring radius, after a radial gap. Indeed, we noted in Sections 3.4 and 5.2 of Paper I that gas can be found inside the CMZ radius in these simulations (in contrast to our previous non self-gravitating simulations in Sormani et al. 2019, in which there was no gas inside the CMZ ring). This star formation might be associated with star formation occurring near SgrA\* ( $R \leq 10 \text{ pc}$ ). This would be consistent with claims of observational evidence for ongoing star formation in this region (Yusef-Zadeh et al. 2008, 2015), although we note that these claims are controversial at the moment (Mills et al. 2017).

<sup>2</sup> We use the term “overshooting” to denote material that, after plunging towards the CMZ along one of the dust lanes, passes close to the CMZ but does not stop and continues towards the dust lane on the opposite side. See for example Figure 4 in Sormani et al. (2019).

Such star formation might also be related to the formation of the nuclear stellar cluster (NSC, see for example Genzel et al. 2010; Schödel et al. 2014; Gallego-Cano et al. 2020) by providing in-situ newly born stars and, since such stars are rotating, it might contribute to its observed rotation (Feldmeier et al. 2014; Feldmeier-Krause et al. 2015; Chatzopoulos et al. 2015; Tsatsi et al. 2017; Neumayer et al. 2020).

Figure 7 analyses the radial distribution of  $\Sigma_{\text{gas}}$ ,  $\Sigma_{\text{SFR}}$  and of the depletion time. The lines show the time-averaged values, while the shaded regions show the scatter. This figure indicates that both  $\Sigma_{\text{gas}}$  and  $\Sigma_{\text{SFR}}$  increase considerably in the centre, while the ratio between the two, the depletion time, decreases by a factor of  $\sim 5$ , consistent with what we found in Section 3.1. Indeed, the minimum of the depletion time is reached in the CMZ ring.

Interestingly, the maximum of the depletion time as a function of radius is instead reached just outside the CMZ ring, at  $R \simeq 500 \text{ pc}$ , in the terminal part of the dust lanes. This is where gas reaches the highest bulk speeds (and observed line of sight velocities) over the entire MW disc, and may indicate that star formation is suppressed at these sites due to the very high shear, in line with the arguments presented in Renaud et al. (2015) and Emsellem et al. (2015). In order to check this, we plot in Figure 9 the quantity

$$\tau = \left[ \left( \frac{\partial V_x}{\partial y} + \frac{\partial V_y}{\partial x} \right)^2 + \left( \frac{\partial V_x}{\partial x} - \frac{\partial V_y}{\partial y} \right)^2 \right]^{1/2}, \quad (2)$$

where  $V_i = \int_{-\infty}^{\infty} \rho v_i dz / \int_{-\infty}^{\infty} \rho dz$  is the density-weighted projected velocity. The quantity  $\tau$  is a good indication of shear for a 2D flow, and has the desirable property of being invariant under rotations of the coordinates since it is the magnitude of the eigenvalues of the traceless shear tensor  $D_{ij} = [\partial_j V_i + \partial_i V_j - \delta_{ij} (\nabla \cdot \mathbf{V})] / 2$  (e.g. Maciejewski 2008). We estimate the derivatives  $\partial_i V_j$  using finite differences with a resolution  $\Delta x = 4 \text{ pc}$ , so any gradient on scales smaller than this is unresolved in the figure. Figure 9 shows that indeed terminal parts of the dust lanes are regions of particularly high density and high shear (see red arrow in the figure), confirming our interpretation.

A more detailed analysis of the spatial distribution of star formation can be performed by subdividing the newly born stars into different age ranges. The left column in Figure 8 performs this decomposition for an instantaneous snapshot, while the middle-right column shows the time-averaged version. One can see that the very young stars are well correlated with the dense gas, but they become increasingly decoupled as they age. Gas and stars have achieved significantly different spatial distributions by the time stars are  $\sim 5$  Myr old. The physical reason for the decoupling is as follows. Imagine a star and a gas element that are initially on the same orbit. In the CMZ, gas frequently collides with other gas (typically every 1-2 Myr and at least twice per orbit, when the CMZ gas collides with the dust-lane infall, see Paper I). In such a collision, the gas trajectory of the gas parcel will be strongly affected, while the star will simply fly through relatively undisturbed since it does not feel pressure forces according to its equations of motion. Therefore, after a few collisions the gas and the star will be on quite different trajectories. Renaud et al. (2013) also noted decoupling between the stellar and gaseous component within spiral arms in their simulation (see their Section 4.5). However, in their case the decoupling was caused by asymmetric drift, i.e. by a lag between stars and gas caused by the larger velocity dispersion of stars compared to the gas, which plays a minor role in our case since it is overshadowed by the frequent collisions in the CMZ (which were absent in the dynamically quieter region studied by Renaud et al. 2013).

Finally, we plot in Figure 10 the SFR as a function of longitude. The averaged distribution has a large central peak and two smaller lateral peaks on the sides at  $l \simeq 0.75^\circ$  and  $l = -1^\circ$  (lower panel), roughly consistent with observations which have peaks at the position of SgrB2 and SgrC (see for example Figure A1 of Barnes et al. 2017). Again, fluctuations of the instantaneous distribution around the averaged distribution can be quite large, and the peaks can be more or less evident in the instantaneous distributions depending on the particular snapshot chosen.

### 3.3 Trajectories of newly born stars

Once a sink particle is formed, it typically follows a different trajectory than the gas. As already noted in Section 3.2, this can be seen for example from Figure 8, which show how gas and stars in the CMZ quickly decouple and have achieved significantly different distribution within  $\sim 5$  Myr. As mentioned in that section, the main physical reason why stars and gas decouple is because gas trajectories are frequently disturbed by collisions, while stars continue on their path almost undisturbed.

Figure 11 investigates the trajectories of a sample of sink particles in more detail. The first panel shows stars that are born upstream along the dust lanes, while the gas is on its way towards the CMZ. These stars will have very elongated orbits that often pass close to the centre with very high speed (up to  $300 \text{ km s}^{-1}$ ), and after each passage reach several kpc out from the centre. The second panel shows stars that formed downstream along the dust lanes, where the gas is accreting onto the CMZ. These stars will overshoot a little bit and typically have elongated orbits which are a factor of 2-3 larger than the CMZ ring. Typical orbital speeds of these stars are larger ( $\sim 150 \text{ km s}^{-1}$ ) than gas in the CMZ ring ( $\sim 100\text{-}120 \text{ km s}^{-1}$ ). The third panel shows stars formed within the CMZ ring. These stars will stay within the ring and have typical orbital velocities comparable to the gas in the ring ( $\sim 100\text{-}120 \text{ km s}^{-1}$ ), but after a few Myr they will decouple from the gas. The accumulation of stars similar to those shown in the second and third panel is what forms the nuclear stellar disc over time (NSD, see for example Launhardt et al. 2002; Nishiyama et al. 2013; Schönrich et al. 2015; Baba & Kawata 2020). Finally, the last panel shows stars that have formed from gas inside the CMZ ring. These typically follow roughly circular orbits with moderate speeds ( $\sim 80 \text{ km s}^{-1}$ ), so they will remain inside the CMZ ring. As noted in Section 3.2, such star formation might also be related to the formation of the nuclear stellar cluster (NSC, see for example Genzel et al. 2010; Schödel et al. 2014; Gallego-Cano et al. 2020).

The trajectories of the sink particles in our simulation can be compared with the kinematics of star clusters and HII regions. In Section 4.4 we compare them with the Arches and Quintuplet clusters. In an upcoming paper (Anderson et al., in preparation) we will compare them with HII regions in the SgrE complex.

Finally, it is worth mentioning a limitation of our simulations. In the code, the gravitational force is calculated using a softening length, which for the gas is adaptive and depends on the cell size with a lower limit set at 0.1 pc, while for the sinks is constant at a value of 1 pc (see Section 2.2 in Paper I). The finite length of the gravitational softening will introduce biases in the binding of stellar structures. Thus, while we are able to retrieve the average motion of a small group of stars, we cannot properly retrieve the velocity distribution of individual stars.

## 4 DISCUSSION

### 4.1 What drives the time variability of the SFR in the CMZ?

The current global SFR in the CMZ (intended here as the region within  $R \lesssim 200 \text{ pc}$ , or  $|l| \lesssim 1.4^\circ$  assuming a distance to the Galactic centre of 8.2 kpc, e.g. Reid et al. 2019; Gravity Collaboration et al. 2019) is of the order of  $\simeq 0.1 M_\odot \text{ yr}^{-1}$  (e.g. Yusef-Zadeh et al. 2009; Immer et al. 2012; Longmore et al. 2013a; Barnes et al. 2017). This number is obtained by combining different independent methods, including direct counting of young stellar objects and integrated light measurements. All these methods agree with each other within a factor of two (see Table 3 in Barnes et al. 2017), and also agree with the number obtained from counts of supernovae remnants (see Section 8.9 in Ponti et al. 2015). Since these various methods trace SF over different timescales in the range 0.1-5 Myr, this also implies that the SFR in the CMZ has been roughly constant for the past  $\sim 5$  Myr (Barnes et al. 2017). Considering longer timescales, Nogueras-Lara et al. (2020) has recently studied the star formation history in the CMZ region by modelling the extinction-corrected K-band color-magnitude diagram as a superposition of star formation events at different times. They found that the SFR averaged over the past 30 Myr is  $0.2\text{-}0.8 M_\odot \text{ yr}^{-1}$ , i.e. a factor of a few higher than the rate averaged over the last 5 Myr. They also found that the SFR has been variable during the past Gyr, with periods of more intense activity ( $\sim 0.5 M_\odot \text{ yr}^{-1}$ ). This suggests that the SFR in the CMZ is not constant, but varies in time. Evidence for time variability in the star formation activity has also been found by Sarzi et al. (2007) for external galactic nuclei by analysing the star formation history of a sample of nuclear rings. It is therefore natural to ask: what drives the time variability in the SFR of the CMZ?

A possible explanation is that the CMZ goes through episodic starbursts driven by feedback instabilities (Krumholz & Kruijssen 2015; Krumholz et al. 2017; Torrey et al. 2017; Armillotta et al. 2019). In this scenario, the CMZ has a roughly constant gas mass but order-of-magnitude level variations in the SFR. The depletion time is not constant, but has large variations over time. The large scatter ( $\sim 1$  dex) in the depletion times observed in the centre of external barred galaxies (Leroy et al. 2013; Utomo et al. 2017) is explained by temporal fluctuations. Armillotta et al. (2019) run numerical hydrodynamical simulations of gas flowing in a barred potential which included star formation prescriptions that lend support to this scenario. In their simulation, the CMZ depletion time is not constant, and SFR variations are driven by variations in the depletion time rather than by variations in the mass of the CMZ.

Our simulations suggest an alternative scenario. Contrary to the findings of Armillotta et al. (2019), we do not find that the CMZ depletion time goes through strong oscillatory cycles. Instead, our simulation predicts that the depletion time is approximately constant in time (within a factor of two, see Section 3.1 and Figure 3), so that the SFR is roughly proportional to the total mass of the CMZ. This suggests that variations in the SFR reflect changes in the mass of the CMZ rather than changes in the depletion time/SF efficiency. Fluctuations in the mass of the CMZ could come from a variety of factors that are not included in our simulation. For example, the mass of the CMZ might drastically and suddenly decrease due to gas expulsion caused by AGN feedback. Perhaps, an AGN event associated with the Fermi Bubbles (Su et al. 2010) is what caused the observed drop in the SFR from the value  $0.2\text{-}0.8 M_\odot \text{ yr}^{-1} \sim 30$  Myr ago (Nogueras-Lara et al. 2020) to the value  $\sim 0.1 M_\odot \text{ yr}^{-1}$  inferred for the last 5 Myr (Barnes et al. 2017). This would be compatible with the currently estimated ages of the

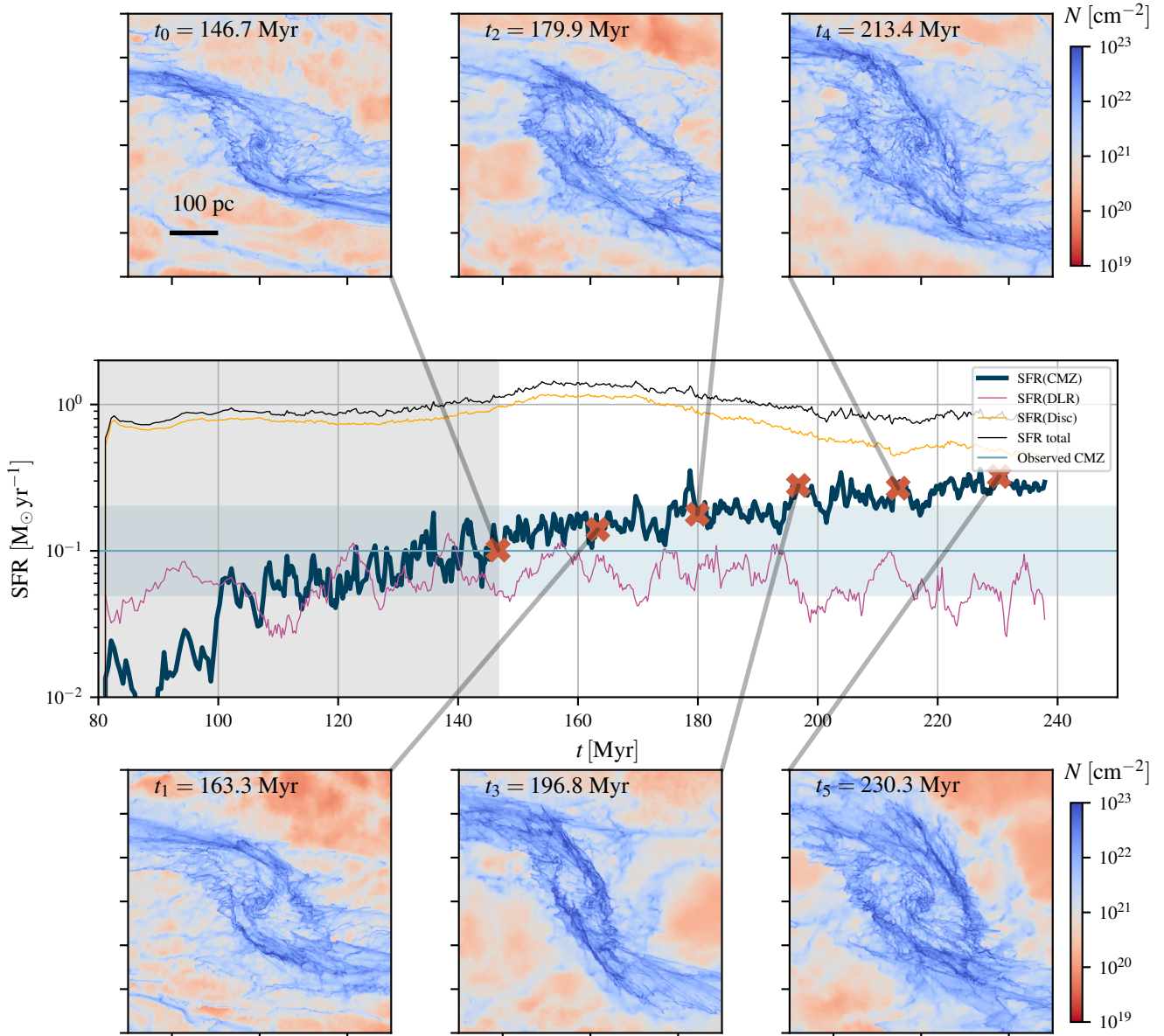


**Figure 2.** Star formation rate as a function of time in our simulation. The thick blue, thin pink and thin yellow lines are the SFR in the three different spatial regions (CMZ, DLR, disc) in which we have subdivided our simulation (see Figure 1). The thin black line is the total SFR (CMZ+DLR+disc). The insert panels show total gas surface density maps that allow us to correlate the SFR with the instantaneous CMZ morphology. The blue shaded horizontal region indicates the observed current SFR of the CMZ, taken to be in the conservative range  $0.05\text{--}0.2 M_{\odot} \text{yr}^{-1}$  (see references in Section 4.1). The grey shaded area indicates the times when the bar potential is still gradually turning on (see Section 2.7 in Paper I), which are excluded from the analysis.

Fermi Bubbles (see for example [Mou et al. 2018](#) and references therein). The mass of the CMZ could also change due to variations in the accretion rate, induced for example by an external perturbation such as a merger. We note that at the current estimated mass inflow rate of  $\sim 1 M_{\odot} \text{yr}^{-1}$  ([Sormani & Barnes 2019](#)), the entire current gas mass of the CMZ ( $\simeq 5 \times 10^7 M_{\odot}$ ) can be accumulated in just 50 Myr, so a change in this rate could potentially induce mass and SFR variability within the timescales required by observations. We also note that much higher accretion rates seem to be possible in barred galaxies: for example [Elmegreen et al. \(2009\)](#) reports a bar-driven inflow rate of  $40 M_{\odot} \text{yr}^{-1}$  in NGC 1365. Our scenario is

also supported by the work of [Seo et al. \(2019\)](#), who run hydrodynamical simulations of gas flowing in a live N-body barred potential and find that the SFR correlates well with the bar-inflow rate. In our scenario, the large scatter in the depletion times observed in the centre of external barred galaxies ([Leroy et al. 2013](#); [Utomo et al. 2017](#)) would be explained as due to different environmental conditions rather than to high time variability. For example, different strengths of the stellar gravitational potential might contribute to the scatter in the depletion times (see Equation 1 and related discussion). Note also that some of the scatter in these values may be driven by differences in the size of the CMZ-like region in different

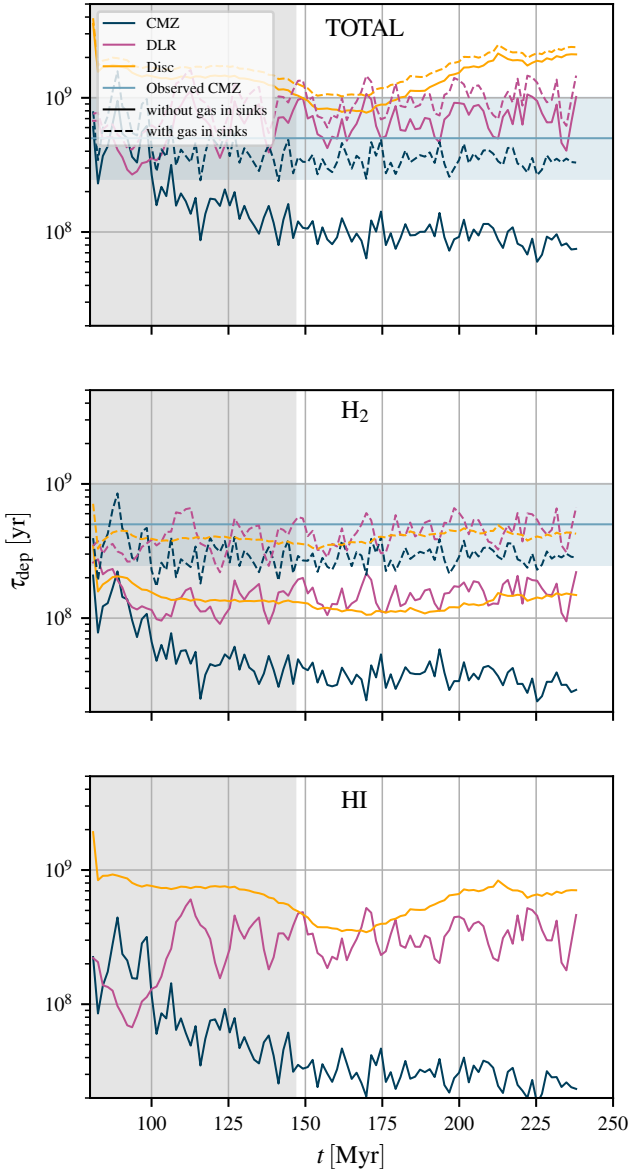


**Figure 3.** Depletion time ( $\tau_{\text{dep}}$ ) as a function of simulation time ( $t$ ) for the various regions defined in Figure 1. The blue shaded region indicates the observed depletion time of the CMZ, 0.25 – 1 Gyr, obtained by dividing the estimated total molecular mass of the CMZ ( $5 \times 10^7 M_{\odot}$ , see references in Section 3.1) by the observed SFR of the CMZ shown in Figure 2 ( $0.05\text{--}0.2 M_{\odot} \text{yr}^{-1}$ ). The grey shaded area indicates where the bar potential is gradually turning on, which are excluded from the analysis.

galaxies, since this region is typically not resolved in the kpc-scale molecular gas maps considered in Leroy et al. (2013) and Utomo et al. (2017).

What causes the differences between the results presented here and those in Armillotta et al. (2019)? There are several factors that could contribute to this and it is difficult to point to which one is most important. First, the two papers use significantly different treatments of ISM cooling. Armillotta et al. (2019) treat gas cooling using equilibrium cooling curves provided by the GRACKLE astrochemistry and cooling package (Smith et al. 2017), which potentially yield differences in behaviour compared to the fully non-

equilibrium treatment we use here. In addition, they treat photoelectric heating as a uniform heating process and do not account for variations in the heating rate due to changes in the fractional ionisation of the gas or its degree of dust shielding. Although the two treatments result in ISM phase diagrams that are qualitatively similar in many aspects (compare their Figure 5 with Figure 11 in Paper I), there are clear quantitative differences that may have some impact on the predicted star formation rates.

Second, the star formation prescription used in Armillotta et al. (2019) is also quite different from that used in our code. In their approach star particles are stochastically formed in gas denser than  $10^3 \text{cm}^{-3}$ , provided that it is gravitationally bound, cold and self-shielded. Compared to our scheme, the main differences are their choice of density threshold and the fact that in their scheme, significant quantities of dense gas can accumulate above the density threshold, something which is impossible by design in our scheme. Third, Armillotta et al. (2019) include the effects of photoionisation feedback as well as supernova feedback, while we concentrate here solely on the latter.

Finally, there is a substantial difference in the mass resolution achieved in dense gas in the two simulations. In our simulation, gas at densities around  $10^3 \text{cm}^{-3}$  is typically resolved with Voronoi cells with a mass of around  $2 M_{\odot}$  (see Figure 3 in Paper I). In contrast, the default particle mass in Armillotta et al. (2019) is  $2000 M_{\odot}$ , a factor of 1000 worse than we achieve here. Armillotta et al. (2019, 2020) also present results from a “high resolution” run with a particle mass of  $200 M_{\odot}$ , which they carried out for a much shorter period than their main run, but even this has a much worse resolution than our simulation. An important consequence of this difference in resolution is that in the Armillotta et al. (2019) simulation, the Sedov-Taylor phase following a supernova explosion is resolved only for supernovae exploding in low density gas with  $n < 1 \text{cm}^{-3}$ , whereas in our simulation it remains well-resolved even for supernovae exploding in gas with a density close to our sink creation threshold. Therefore, Armillotta et al. (2019) primarily inject momentum with their supernovae, since the associated thermal energy is rapidly radiated away, whereas we are able to follow the injection of both thermal energy and momentum in a more self-consistent fashion. This results in a clear difference in the morphology of the supernova-affected gas: in our simulation, supernova explosions produce large holes in the gas distribution, while corresponding features are rarely seen in the Armillotta et al. (2019) simulation.

In view of these significant differences in numerical approach, together with the fact that the results Armillotta et al. (2019) obtain for the star formation rate of the CMZ are clearly not numerically converged (see their Figure A2), and that the simulations span a quite different period in the life of the CMZ ( $\sim 100$  Myr after bar formation in our run vs. 500 Myr in their simulation), it is difficult to assess the reasons for the difference in results regarding the time variability of the SFR in the CMZ. This is an issue that we hope to address further in future work.

## 4.2 An evolutionary sequence of star formation?

Longmore et al. (2013b) and Kruijssen et al. (2015, 2019) suggested that star formation follows an evolutionary timeline as the gas clouds orbit the CMZ ring. In this scenario, star formation is triggered when the clouds are compressed during pericentre passage, i.e. when the clouds pass closest to the Galactic centre. This scenario is at variance with the two scenarios for star formation in nuclear rings that are more commonly discussed in the extra-

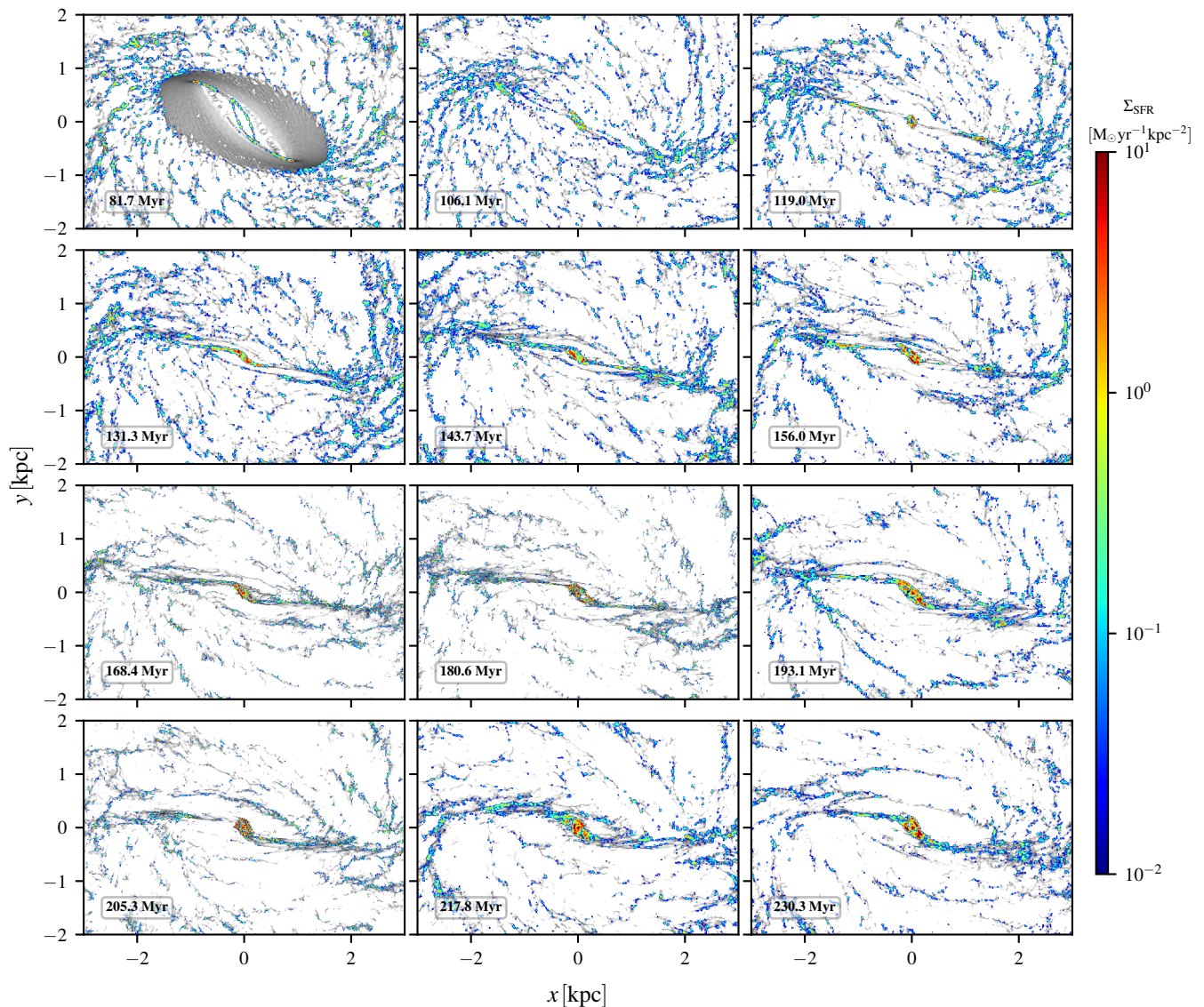


**Figure 4.** SFR density for various snapshots in our simulation. Shown is the very recent (0.5 Myr) star formation. The grey background shows the  $\text{H}_2$  surface density. Compare with the time-averaged SFR density shown in the bottom panel of Figure 6.

galactic context, namely the “popcorn” and the “pearls on a string” scenarios, which are schematically depicted in Figure 7 of [Böker et al. \(2008\)](#). In the “pearls on a string” scenario, star formation occurs prevalently at the contact point between the dust lanes and the gas ring, which typically coincides with the ring apocentre rather than with the pericentre. In the “popcorn” scenario, star formation occurs uniformly along the ring. The observational evidence for a clear evolutionary sequence as implied by the pericentre passage scenario is mixed ([Kauffmann et al. 2017a](#); [Krieger et al. 2017](#)), while the pearls on a string scenario has obtained some mild support from observations of nearby galaxies (see for example Section 4.1 in [Böker et al. 2008](#), see also [Mazzuca et al. 2008](#)).

These three scenarios make different predictions that can be tested with our simulations. The pericentre scenario predicts that star formation occurs predominantly after the pericentre passage. According to this scenario, very young stars should be found shortly after the passage, while stars of increasing age should be

found further downstream of the pericentre. The pearls on a string scenario predicts that star formation happens predominantly downstream of the contact point between the dust lanes and the CMZ ring, i.e. downstream of the apocentre. The popcorn scenario predicts that star formation is distributed uniformly along the ring, without preferred locations.

In order to test these predictions, we look at the time-averaged distribution of very young stars (age  $t \leq 0.25$  Myr), which is shown in the top row of Figure 8. These stars trace where the star formation is being triggered. The right panel in the top row shows the azimuthal distribution of stars in the CMZ. The apocentres of the CMZ ring are at  $\theta = 0^\circ$  and  $\theta = 180^\circ$ , and coincide with the contact points between dust lanes, while the pericentres are at  $\theta = 90^\circ$  and  $\theta = 270^\circ$ . This panel shows that the distribution of very young stars has a bi-periodic structure with two strong peaks at the apocentres, consistent with the prediction of the pearls on a string scenario.

The above analysis considers all the star formation within

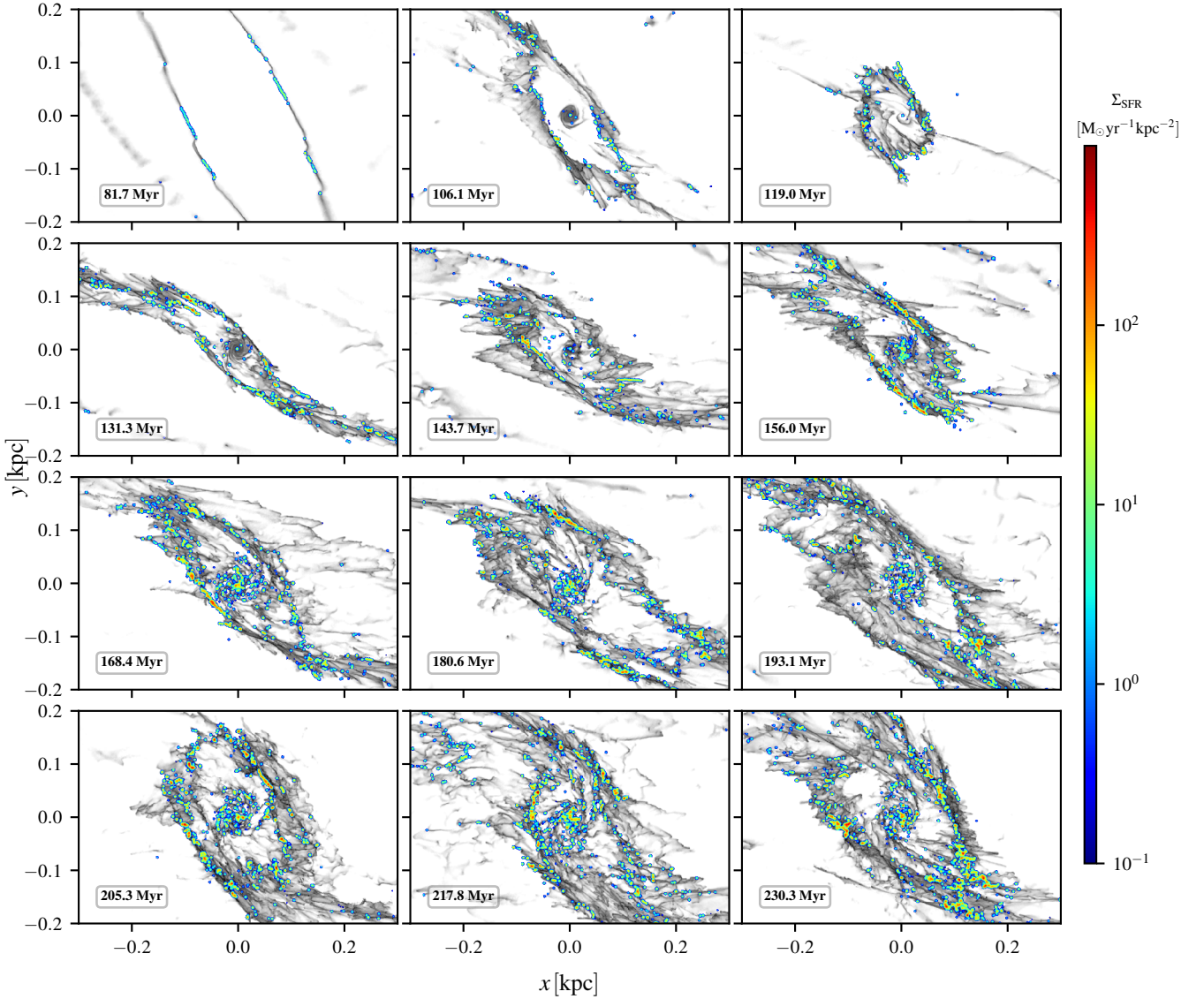


**Figure 5.** Same as Figure 4, but zooming onto the CMZ. Compare with the time-averaged SFR density shown in the bottom panel of Figure 6.

$R \leq 250$  pc, including some that strictly speaking is outside the “ring” structure. In order to investigate this aspect in more detail, we focus specifically on the ring in Figure 12. The right panel shows the time-averaged surface density<sup>3</sup> of very young stars ( $\Sigma_{YS}$ ) within the elliptical ring shown in the middle panel. It can be seen that most of the star formation occurs downstream of the apocentres, but before the pericentre passage. This is consistent with the prediction of the pearls on a string scenario, but not with the pericentre passage scenario. Note however that the maxima are quite broad, and star formation away from these maxima is not zero. Thus, while the maxima constitute a region of more intense star

<sup>3</sup> By plotting the *surface density* rather than a histogram of the mass distribution as a function of azimuth, we avoid any potential bias due to geometric effects caused by the area within the ellipse not being constant in each angular range. For example, if the surface density were constant along the ring, the azimuthal distribution of mass would not be constant, although the 2D face-on maps would look perfectly uniform.

formation, they are not the only regions where stellar birth takes place.

Let us now consider the distribution of older stars, which can be seen from Figure 8. For ages  $1 < t < 5$  Myr, the distribution of stars in the middle-right column exhibits a clear bi-polar structure. This is because stars accumulate close to the apocentre, where their orbital velocity slows down and where they therefore spend more time than in other parts of their orbit. As stars become older ( $t > 10$  Myr), the bipolar structure precesses as a consequence of the precession of the apocentres of the stellar orbit (which at their formation prevalently coincide with the contact point between ring and the dust lanes, but change at later times). The bipolar structure also becomes less pronounced, and the distribution more uniform, as stars mix in phase space

We remark that all our conclusions above come from analysing the *time-averaged* distributions. As discussed in Section 3.2, the instantaneous star formation distribution fluctuates strongly around the average (compare the left panels in Figure 8

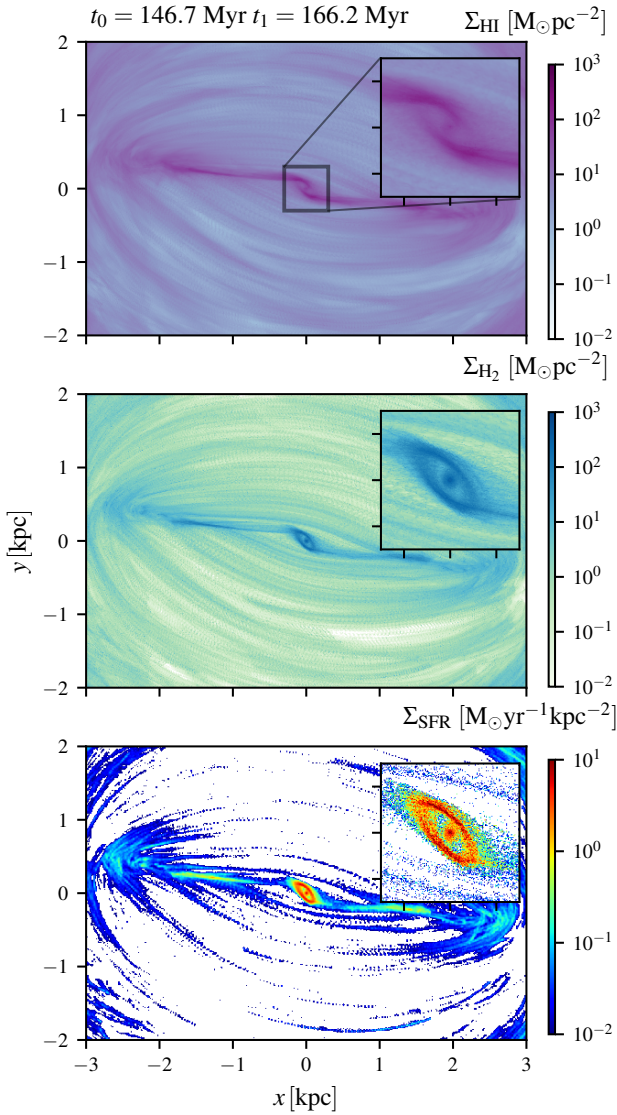


**Figure 6.** Time-averaged plot of *top*: H<sub>2</sub> surface density; *middle*: HI surface density; *bottom*: star formation rate (SFR) density. The average is calculated over the range  $t = 146.7$ - $166.2$  Myr. The “stripes” in the SFR rate originate from individual molecular clouds that form stars while following  $x_1$  orbits.

and the various panels in Figure 5 with the middle-right panels of Figure 8). Because of these fluctuations, it is much harder to tell whether our simulations are consistent with the pearls on a string scenario by looking just at a single snapshot. Moreover, while the time-averaged distributions favour the pearls on a string scenario, there is also significant star formation throughout the ring and away from the apocentres. These complications should be taken into account when analysing observations, which only constitute individual snapshots.

From a physical point of view, there are two reasons why enhanced star formation should be expected at the apocentres: (i) they are collisions sites where the gas from the dust lanes crashes into the ring (see e.g. the left panel in Figure 12); (ii) gas slows down at the apocentre of an orbit, causing it to pile up and become more dense. Our simulations suggest that these effects are dominant over the tidal compression at the pericentre proposed by [Krujissen et al.](#)

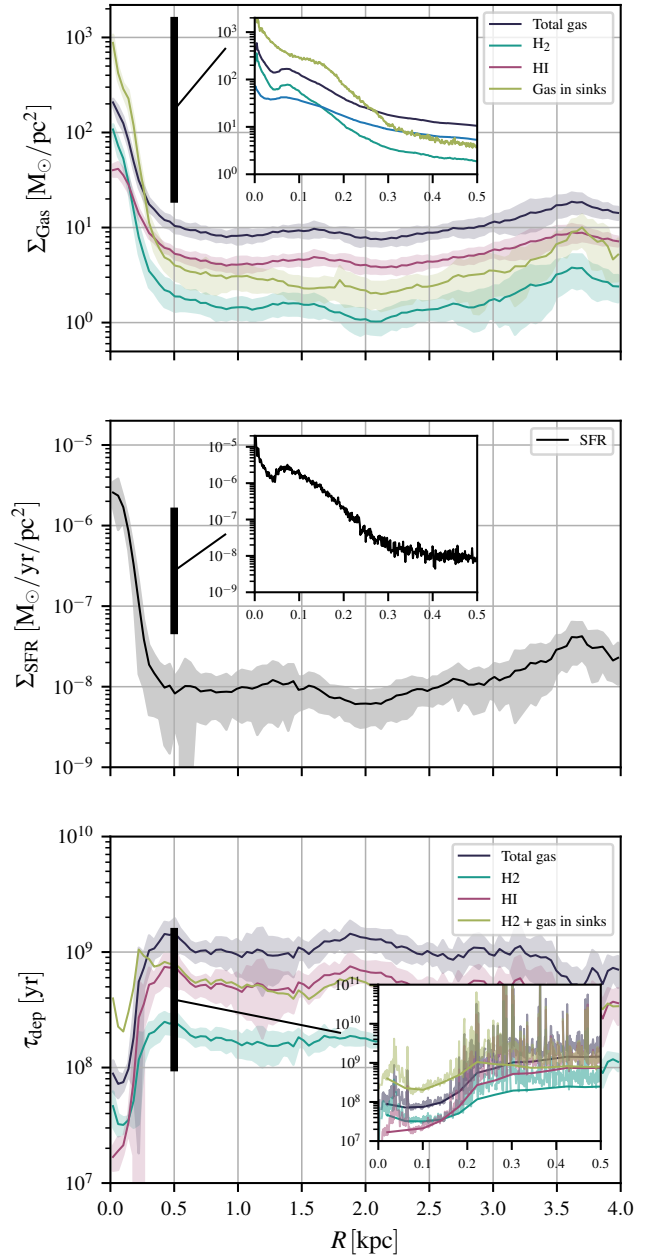


**Figure 7.** *Top*: time-averaged radial distribution of gas surface density. *Middle*: SFR density. *Bottom*: depletion times. Plots are averaged over time in the range  $t = (146.7, 175.8)$  Myr. Shaded areas show the 1-sigma scatter. The zoom-in inlays show the time-averaged quantities in the innermost 0.5 kpc with a finer radial binning.

(2015). Even neglecting these two dominant effects, there is evidence that the pericentre passage only has a minor role in triggering star formation events. We note that in the simulations of [Dale et al. \(2019\)](#) the pericentre has a rather weak effect in enhancing the SFR (compare the circular and non-circular orbits in Figures 3 and 9 of [Dale et al. 2019](#)). [Jefferson et al. \(2018\)](#) also estimates that only a small fraction ( $\sim 20\%$ ) of the star formation events might be triggered by pericentre passage. Their estimate neglects the two dominant mechanisms mentioned above, i.e. cloud collisions at the dust lanes and gas slowing down at the apocentre, so it is likely that

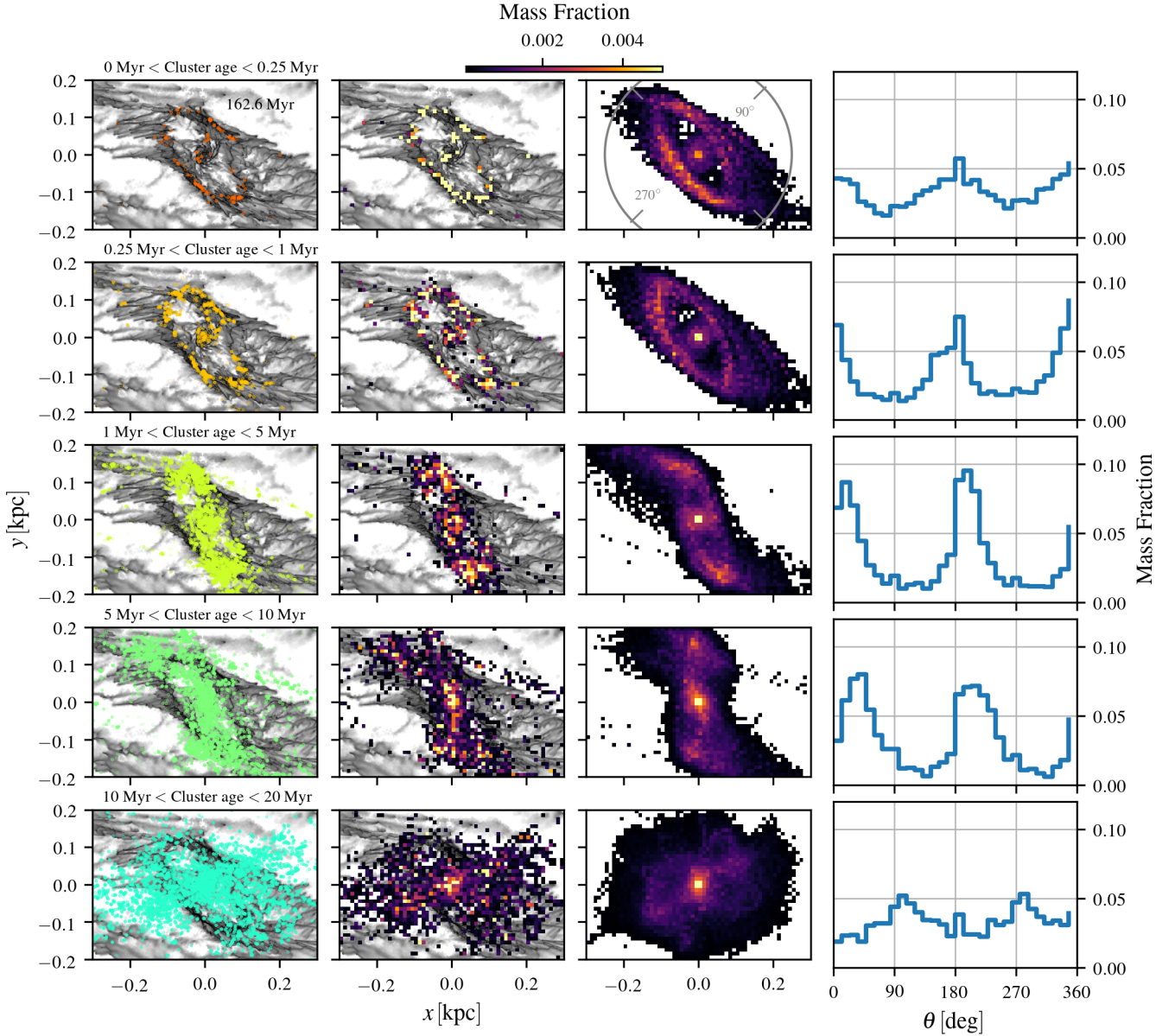


**Figure 8.** *Left column:* instantaneous spatial distribution of stars with age in the given range, for a typical snapshot of our simulation. This is a scatter plot. *Middle-left column:* same as the left panel, but binned in a 2D histogram weighted by mass. *Middle-right column:* time-averaged spatial distribution of stars by age, i.e. obtained by time-averaging the middle-left column. The time averaged is taken over  $t = (160, 180)$ . *Right column:* azimuthal distribution of stars with age in the given range in the CMZ ( $R \leq 250$ pc), obtained by looking at the azimuthal distribution of the histograms in the middle-right column. This shows that the stars are not distributed uniformly through azimuth, but have distinct peaks whose azimuthal position depends on the age range of the stars considered.

the actual number is significantly lower than this. Finally, [Kruijssen et al. \(2019\)](#) also acknowledge that star formation might be triggered by accretion, similarly to the pearls-on-a-string scenario. However, in their discussion the accumulation of gas in the CMZ takes place within the context of the [Krumholz & Kruijssen \(2015\)](#) model rather than from direct accretion from the dust lanes. As we have argued in Section 6.2 of Paper I, the theoretical framework of [Krumholz & Kruijssen \(2015\)](#) and [Krumholz et al. \(2017\)](#) does not capture well the physics of the CMZ since it predicts the existence of a quasi-axisymmetric outer CMZ extending out to  $R \simeq 450$ pc, which is not supported by either observations or simulations. More-

over, [Sormani & Li \(2020\)](#) have shown that the acoustic instability on which these models are based is a spurious result which cannot drive turbulence and mass transport in the interstellar medium.

We conclude that our simulation supports a scenario which is a mixture of the pearls on a string and of the popcorn scenarios. Most of the star formation happens downstream of the apocentres, but a significant amount of star formation also takes place distributed along the ring. Our results do not support the pericentre passage scenario.

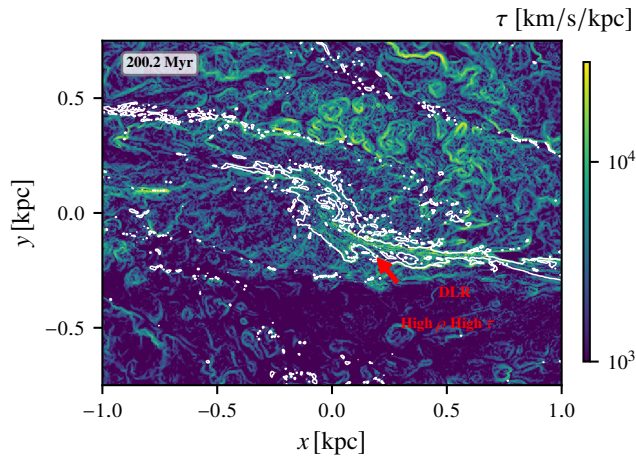


**Figure 9.** Shear map for the snapshot at  $t = 200.2$  Myr. The colours show the quantity  $\tau$  defined in Equation (2), which is a good indication of shear for a 2D flow. The white contour indicates where the total surface density of the gas is  $N = 5 \times 10^{21} \text{ cm}^{-2}$ . The red arrow indicates the terminal part of the dust lane, a region of high density and high shear, where the maximum of the depletion time as a function of Galactocentric radius is reached (see bottom panel in Figure 7 and discussion in Section 3.2). The map also shows that high shear occurs predominantly in the dust lanes and in expanding SN shells.

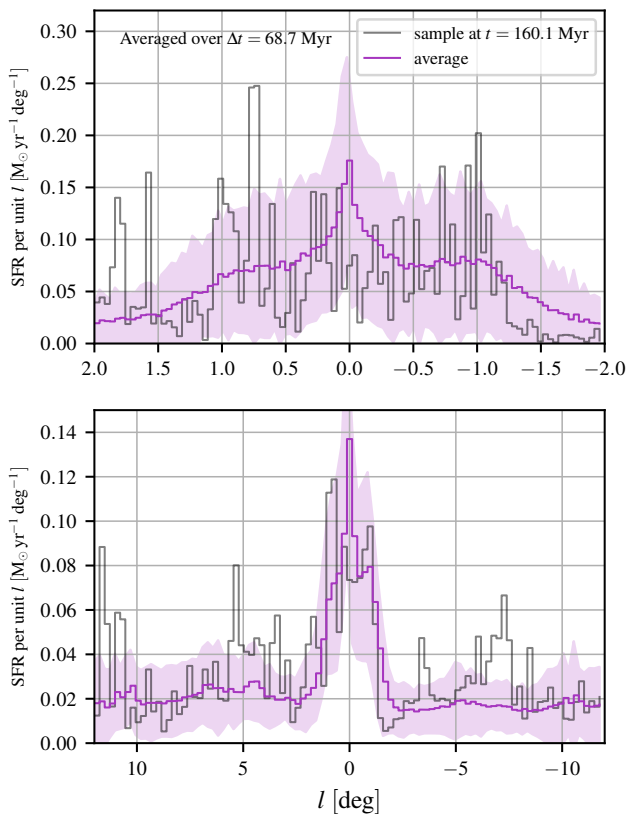


**Figure 10.** Star formation rate as a function of Galactic longitude in our simulation. The magenta line shows the time-averaged distribution, while the grey line shows the instantaneous distribution at  $t = 160.1$  Myr. Shaded area shows the typical scatter. The time averages are calculated over the time range  $t = (146.7, 215.4)$  Myr.

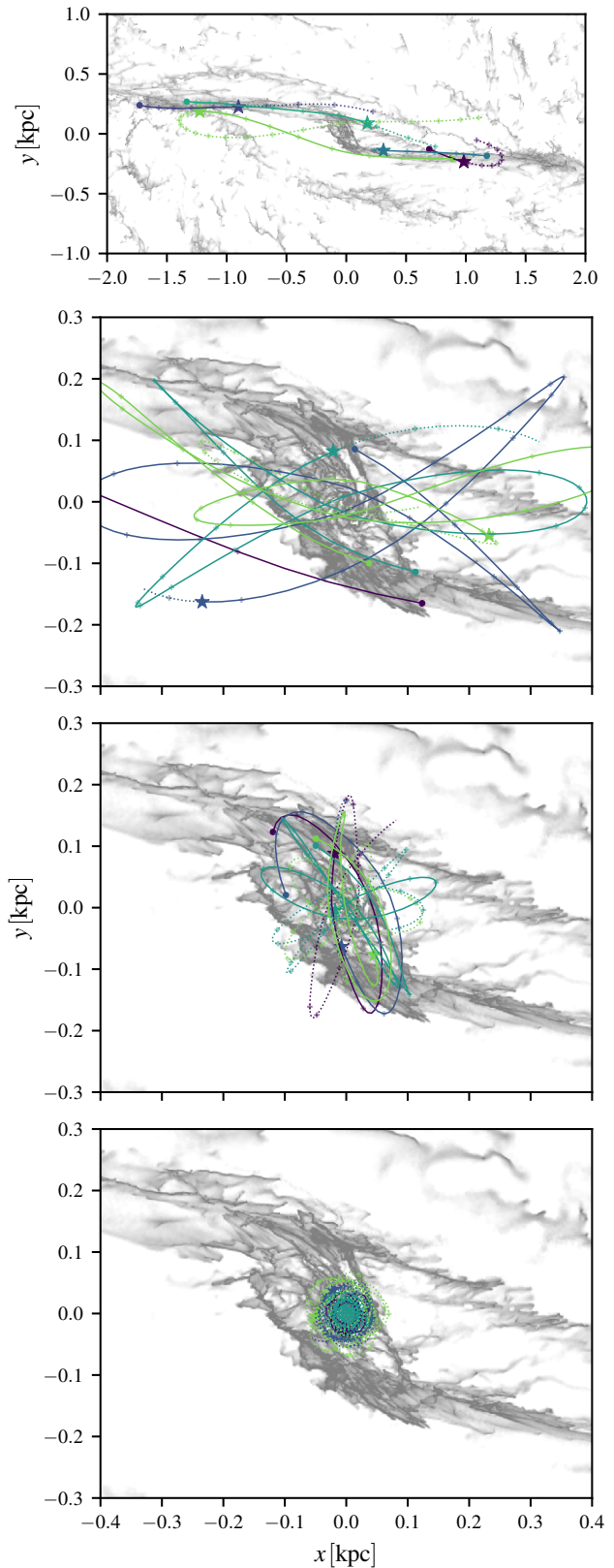


**Figure 11.** Typical trajectories of newly born stars in our simulations. *Top panel:* for stars formed upstream along the dust lane. *Middle-top panel:* for stars formed downstream along the dust lanes. *Middle-bottom panel:* for stars formed from gas orbiting in the CMZ ring. *Bottom panel:* for stars formed at radii smaller than the CMZ ring. Star markers indicate the current position of the stars. Round markers indicate the location where they formed. Full lines indicate the past trajectories, while dashed lines indicate the future trajectories. Cross markers log the position of the stars at equal time intervals of  $\Delta t = 1$  Myr. Grey shows the  $\text{H}_2$  surface density at current time.

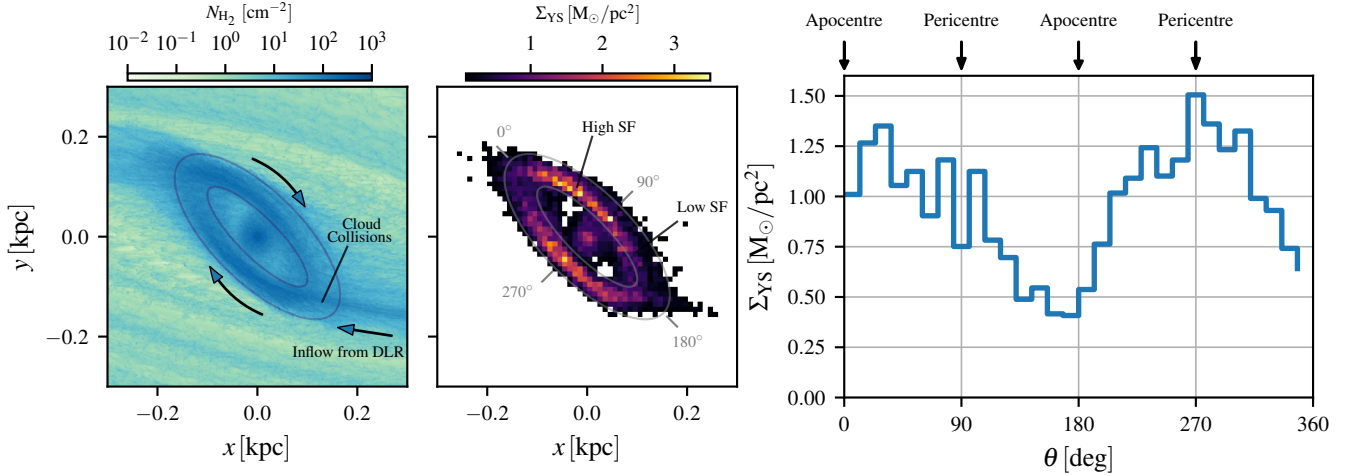


**Figure 12.** *Left:* time-averaged  $H_2$  surface density. *Middle:* time-averaged surface density of the very young stars (age  $t \leq 0.25$  Myr) formed in our simulation. *Right:* time-averaged surface density of very young stars (age  $t \leq 0.25$  Myr) as a function of azimuth along the elliptical ring shown in the middle panel. The time averages are calculated over the time range  $t = (146.7, 168.7)$  Myr.

### 4.3 Star formation relations

Star formation relations are empirical correlations between the SFR and properties of the interstellar medium (ISM) from which stars are born. It has been extensively discussed in the literature that the CMZ follows some star formation relations but not all of them (e.g. Yusef-Zadeh et al. 2009; Longmore et al. 2013a; Kruijssen et al. 2014; Kauffmann et al. 2017b,a). In particular, it has been shown that the *global* SFR of the CMZ is consistent with the Schmidt-Kennicutt density relation (Schmidt 1959; Kennicutt 1998), with the Bigiel et al. (2008) molecular gas relation, and with the Bacchini et al. (2019a,b) volumetric star formation relation (Bacchini, private communication). However, the global SFR of the CMZ is not consistent with the SFR-dense gas relation observed by e.g. Gao & Solomon (2004), Wu et al. (2005) and Lada et al. (2010, 2012). This is a linear relation between the quantity of dense gas (as traced by HCN emission or high dust extinction) and the SFR. It has been shown to work well both for the total (integrated) properties of external galaxies, and for local molecular clouds in the MW, which made it apparently valid over an impressive 9 orders of magnitude (although with a gap in the middle, see Figure 2 in Lada et al. 2012). This generated the expectation that the same law should be valid for the CMZ, but the data shows that it is not (see Longmore et al. 2013a; Kruijssen et al. 2014 and Figure 1 in Kauffmann et al. 2017a). This expectation, and the universality of the SFR-dense gas relation, is also challenged by observations that suggest that the centres of nearby galaxies lie on average below the Lada et al. 2012 relation (see Gallagher et al. 2018; Jiménez-Donaire et al. 2019 and in particular Figure 13 in the latter).

Figure 13 shows that the CMZ in our simulation follows the Schmidt-Kennicutt relation (Schmidt 1959; Kennicutt 1998) and the Bigiel et al. (2008) molecular gas relation, consistent with observational findings. This reassures us that our numerical star formation subgrid model is working correctly. Unfortunately, our simulations do not have the resolution to probe the dense-gas star formation relations, which the CMZ has been shown to be not consistent with (e.g. Longmore et al. 2013a; Kruijssen et al. 2014; Kauffmann et al. 2017b,a). To do that, we would need to increase the sink formation density threshold  $\rho_c$  (see Appendix A) to densities

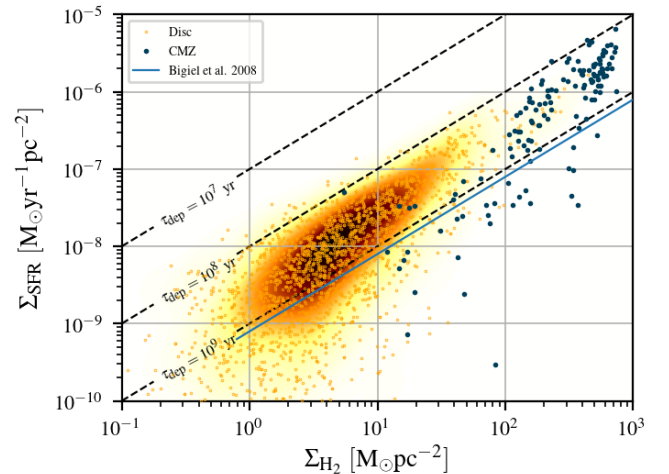


**Figure 13.** Schmidt-Kennicutt plot for our simulation. We bin face-on  $H_2$  and SFR surface densities with a grid size of 100 pc. Each point in this graph represents one such bin. The points are coloured based on the position of the centre of the bin. The underlying distribution is obtained by Gaussian kernel density estimation of the points associated to the disc. To increase statistics especially for the CMZ we include surface densities of eight different consecutive snapshots i.e. over a time of approximately 2 Myr. The CMZ approximately follows the SK as well as the Bigiel et al. (2008) relation, as found in observations (e.g. Figure 2 in Kruijssen et al. 2014).

of  $n \simeq 10^7 \text{ cm}^{-3}$ , which is the dense gas formation threshold in the CMZ estimated by Kruijssen et al. (2014) and Kauffmann et al. (2017a). This is impractical with our current simulations owing to the very high computational expense, but is a worthwhile direction for future investigations.

### 4.4 The Arches and Quintuplet clusters

The Arches and Quintuplet clusters are two young massive ( $M \gtrsim 10^4 M_\odot$ ) clusters found close to the Galactic centre ( $\simeq 30 \text{ pc}$  in projected distance). They have estimated ages of  $3.5 \pm 0.7 \text{ Myr}$

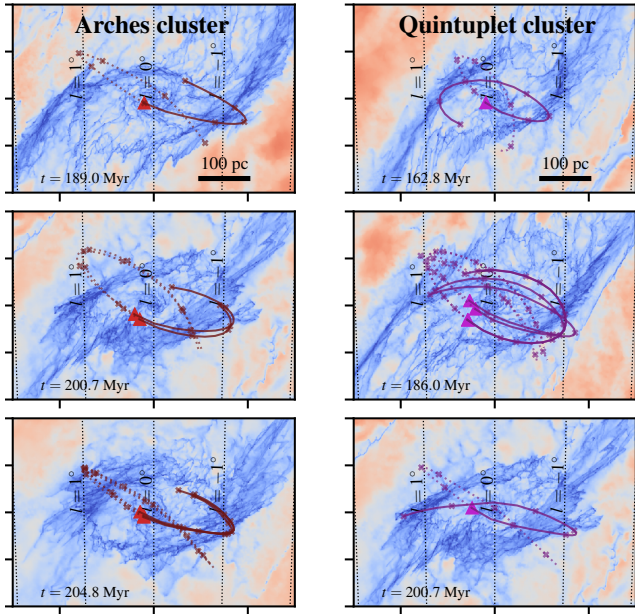


**Figure 14.** Sink particles in our simulations with properties (age, line-of-sight velocity, proper motion velocity) within the observational constraints of the Arches (*left panels*) and the Quintuplet (*right panels*) clusters. Red/violet triangles denote the present day position, while solid and dotted lines show the past (from the birth site to the current position) and the future trajectories (for the next 5 Myr) respectively. The crosses log the position of the cluster at equal time intervals of 1 Myr. The background shows the gas total density distribution at the time when the clusters are at their present day position.

and  $4.8 \pm 1.1$  Myr respectively (Schneider et al. 2014). The Arches cluster has a line-of-sight velocity of  $v_{\text{los}} = 95 \pm 8 \text{ km s}^{-1}$  (Figer et al. 2002) and a proper motion velocity of  $v_{\text{pm}} = 172 \pm 15 \text{ km s}^{-1}$  (Clarkson et al. 2012), which yields a 3D orbital velocity of  $v_{3\text{D}} = 196 \pm 17 \text{ km s}^{-1}$  in the direction of increasing longitude (Clarkson et al. 2012). The Quintuplet cluster has a line-of-sight velocity of  $v_{\text{los}} = 102 \pm 2 \text{ km s}^{-1}$  and a proper motion velocity of  $v_{\text{pm}} = 132 \pm 15 \text{ km s}^{-1}$ , which yields a 3D orbital velocity of  $v_{3\text{D}} = 167 \pm 15 \text{ km s}^{-1}$ , also in the direction of increasing longitude (Stolte et al. 2014).

The observed motions of the Arches and Quintuplet clusters can be compared with the trajectories of our sink particles discussed in Section 3.3. We have searched in our simulations for sink particles that are within 30 pc of the Galactic centre (in projected distance) on the positive longitude side and that have age, line-of-sight velocity and proper motion velocities compatible with those of the observed clusters within the observational uncertainties given above. Figure 14 shows trajectories for a sample of sinks which are found according to this procedure. This figure suggests that (i) the Arches cluster (left panels) formed from gas that is colliding into the far side dust lane at negative longitudes while orbiting in the CMZ. All the clusters in our simulation compatible with the above observational constraints are consistent with this picture. (ii) The Quintuplet cluster formed either in a similar scenario as the Arches cluster, but from gas colliding onto the near side dust lane (top-right panel), or more probably by gas in the terminal part of the dust lanes which is just entering the CMZ (middle- and lower-right

panels). Occurrences of the second type are more frequent (roughly by a factor of  $\sim 5$ ).

Comparing with other works, the scenario described here is in some respects similar to the one proposed by Stolte et al. (2008, 2014), according to which the clusters are formed on a transitional trajectory between  $x_1$  and  $x_2$  orbits, since this transition happens at the contact point between the dust lanes (compare Figure 14 with Figure 12 in Stolte et al. 2014). Kruijssen et al. (2015) have proposed that the clusters originated on the same orbit that they use to fit dense gas data. However, we find that sink particles with properties compatible with the observed kinematics of the clusters have typically decoupled from the gas in which they are born by the time the clusters have reached their present age. Moreover, the gas orbiting in the CMZ ring has typically lower absolute 3D velocities than those of the clusters. Therefore, the scenario proposed by Kruijssen et al. (2015) seems to be inconsistent with the result of the present simulation.

## 5 SUMMARY AND CONCLUSIONS

We have used the high-resolution hydrodynamical simulations presented in Paper I to study star formation in the CMZ. These include a realistic Milky Way external barred potential, a time-dependent chemical network that keeps track of hydrogen and carbon chemistry, a physically motivated model for the formation of new stars using sink particles, and supernovae feedback. The simulations reach sub-parsec resolution in the dense regions and allow us to resolve individual molecular clouds which are formed self-consistently from the large-scale flow.

Our main conclusions are as follows:

- We have studied the temporal distribution of star formation. We find that the depletion time in the CMZ is approximately constant in time. This implies that variations in the SFR of the CMZ are primarily driven by variations in its mass, caused for example by changes in the bar-driven inflow rate, AGN events or other external factors, while the observed scatter in the depletion time of external galactic centres is interpreted as variations in the environmental factors (e.g. the stellar surface density, Jiménez-Donaire et al. 2019). Contrary to the findings of Armillotta et al. (2019), we do not find that the depletion time in the CMZ goes through strong oscillatory cycles, at least within the timescale of our simulation ( $\sim 100$  Myr, see Sections 3.1 and 4.1).

- We have studied the spatial distribution of star formation. Most of the star formation happens in the CMZ ring at  $R \gtrsim 100$  pc, but a significant amount of star formation also occurs closer to SgrA\* ( $R \leq 10$  pc, see Section 3.2 and Figure 5). While the time-averaged spatial distribution of the SFR is typically smooth, the instantaneous distribution can have complex and transient fluctuations which deviate significantly from the average morphology (compare the bottom panel in Figure 6 with Figures 4 and 5). Molecular clouds formed self-consistently from the large-scale flow, and their embedded star formation, exhibit complicated filamentary morphologies and do not resemble the idealised “spherical clouds” that are often used as a model to understand star formation. We have also investigated how the spatial distribution changes when we consider stars in different age ranges, and found that a bi-polar structure persists even for stars with age 10–20 Myr (see Section 3.2 and Figure 8).

- We tested the predictions of the three main scenarios that have been put forward to explain the spatial and temporal distribution of star formation in the centre of barred galaxies, namely the “pearls

on a string", the "popcorn" and the "pericentre passage" scenarios. We found that our simulations are consistent with a mixture of the pearls on a string and popcorn scenarios, while they are inconsistent with the pericentre passage scenario (see Section 4.2).

- We have studied the trajectories of newly born stars (see Figure 11). We find that gas and stars typically decouple within at most 2-3 Myr (see Sections 3.2 and 3.3).

- We have used the trajectories of newly born stars to provide a detailed analysis of the origin of the Arches and Quintuplet clusters. Our simulation favour a scenario in which the Arches cluster is formed from gas that crashed into the far side dust lane at negative longitudes while orbiting in the CMZ, while the Quintuplet cluster is either formed in a similar event but with the roles of the near/far sides the Galaxy reversed, or more likely by gas in the terminal part of the near side dust lane which was just entering the CMZ (see Figure 14 and Section 4.4).

## ACKNOWLEDGEMENTS

We thank the anonymous referee for constructive comments that improved the paper. MCS thanks Ashley Barnes, Adam Ginsburg, Jonathan Henshaw, Zhi Li, Diederik Kruijssen, Alessandra Mastrobuono-Battisti, Elisabeth Mills, Nadine Neumayer, Francisco Nogueras-Lara, Ralph Schoenrich and Alessandro Trani for useful comments and discussions. MCS and RGT both acknowledge contributing equally to this paper. MCS, RGT, SCOG, and RSK acknowledge financial support from the German Research Foundation (DFG) via the collaborative research center (SFB 881, Project-ID 138713538) "The Milky Way System" (sub-projects A1, B1, B2, and B8). CDB and HPH gratefully acknowledges support for this work from the National Science Foundation under Grant No. (1816715). PCC acknowledges support from the Science and Technology Facilities Council (under grant ST/K00926/1) and StarFormMapper, a project that has received funding from the European Union's Horizon 2020 Research and Innovation Programme, under grant agreement no. 687528. HPH thanks the LSSTC Data Science Fellowship Program, which is funded by LSSTC, NSF Cybertraining Grant No. 1829740, the Brinson Foundation, and the Moore Foundation; his participation in the program has benefited this work. RJS gratefully acknowledges an STFC Ernest Rutherford fellowship (grant ST/N00485X/1) and HPC from the Durham DiRAC supercomputing facility (grants ST/P002293/1, ST/R002371/1, ST/S002502/1, and ST/R000832/1). The authors acknowledge support by the state of Baden-Württemberg through bwHPC and the German Research Foundation (DFG) through grant INST 35/1134-1 FUGG. The authors gratefully acknowledge the data storage service SDS@hd supported by the Ministry of Science, Research and the Arts Baden-Württemberg (MWK) and the German Research Foundation (DFG) through grant INST 35/1314-1 FUGG.

## DATA AVAILABILITY

The data underlying this article will be shared on reasonable request to the corresponding author. Movies of the simulations can be found at the following link: <https://www.youtube.com/channel/UCwnzf0-xLxzRDz9XsexfPoQ>.

## REFERENCES

- Armillotta L., Krumholz M. R., Di Teodoro E. M., McClure-Griffiths N. M., 2019, *MNRAS*, **490**, 4401
- Armillotta L., Krumholz M. R., Di Teodoro E. M., 2020, *MNRAS*, **493**, 5273
- Baba J., Kawata D., 2020, *MNRAS*, **492**, 4500
- Bacchini C., Fraternali F., Iorio G., Pezzulli G., 2019a, *A&A*, **622**, A64
- Bacchini C., Fraternali F., Pezzulli G., Marasco A., Iorio G., Nipoti C., 2019b, *A&A*, **632**, A127
- Bally J., et al., 2010, *ApJ*, **721**, 137
- Barnes A. T., Longmore S. N., Battersby C., Bally J., Kruijssen J. M. D., Henshaw J. D., Walker D. L., 2017, *MNRAS*, **469**, 2263
- Bigiel F., Leroy A., Walter F., Brinks E., de Blok W. J. G., Madore B., Thornley M. D., 2008, *AJ*, **136**, 2846
- Böker T., Falcón-Barroso J., Schinnerer E., Knapen J. H., Ryder S., 2008, *AJ*, **135**, 479
- Chatzopoulos S., Fritz T. K., Gerhard O., Gillessen S., Wegg C., Genzel R., Pfühl O., 2015, *MNRAS*, **447**, 948
- Clark P. C., Glover S. C. O., Ragan S. E., Shetty R., Klessen R. S., 2013, *ApJ*, **768**, L34
- Clarkson W. I., Ghez A. M., Morris M. R., Lu J. R., Stolte A., McCrady N., Do T., Yelda S., 2012, *ApJ*, **751**, 132
- Comerón S., Knapen J. H., Beckman J. E., Laurikainen E., Salo H., Martínez-Valpuesta I., Buta R. J., 2010, *MNRAS*, **402**, 2462
- Dahmen G., Huttemeister S., Wilson T. L., Mauersberger R., 1998, *A&A*, **331**, 959
- Dale J. E., Kruijssen J. M. D., Longmore S. N., 2019, *MNRAS*, **486**, 3307
- Elmegreen B. G., Galliano E., Alloin D., 2009, *ApJ*, **703**, 1297
- Emsellem E., Renaud F., Bournaud F., Elmegreen B., Combes F., Gabor J. M., 2015, *MNRAS*, **446**, 2468
- Federrath C., et al., 2016, *ApJ*, **832**, 143
- Feldmeier-Krause A., et al., 2015, *A&A*, **584**, A2
- Feldmeier A., et al., 2014, *A&A*, **570**, A2
- Figier D. F., et al., 2002, *ApJ*, **581**, 258
- Gallagher M. J., et al., 2018, *ApJ*, **858**, 90
- Gallego-Cano E., Schödel R., Nogueras-Lara F., Dong H., Shahzamanian B., Fritz T. K., Gallego-Calvente A. T., Neumayer N., 2020, *A&A*, **634**, A71
- Gao Y., Solomon P. M., 2004, *ApJ*, **606**, 271
- Genzel R., Eisenhauer F., Gillessen S., 2010, *Reviews of Modern Physics*, **82**, 3121
- Ginsburg A., et al., 2016, *A&A*, **586**, A50
- Gravity Collaboration et al., 2019, *A&A*, **625**, L10
- Guesten R., Henkel C., 1983, *A&A*, **125**, 136
- Heywood I., et al., 2019, *Nature*, **573**, 235
- Immer K., Schuller F., Omont A., Menten K. M., 2012, *A&A*, **537**, A121
- Immer K., Kauffmann J., Pillai T., Ginsburg A., Menten K. M., 2016, *A&A*, **595**, A94
- Jefferson S. M. R., Kruijssen J. M. D., Krumholz M. R., Longmore S. N., 2018, *MNRAS*, **478**, 3380
- Jiménez-Donaire M. J., et al., 2019, *ApJ*, **880**, 127
- Kauffmann J., Pillai T., Zhang Q., Menten K. M., Goldsmith P. F., Lu X., Guzmán A. E., Schmiedeke A., 2017a, *A&A*, **603**, A90
- Kauffmann J., Goldsmith P. F., Melnick G., Tolls V., Guzman A., Menten K. M., 2017b, *A&A*, **605**, L5
- Kennicutt Robert C. J., 1998, *ApJ*, **498**, 541
- Kennicutt R. C., Evans N. J., 2012, *ARA&A*, **50**, 531
- Klessen R. S., Glover S. C. O., 2016, in: *Star Formation in Galaxy Evolution: Connecting Numerical Models to Reality*, Saas-Fee Advanced Course, **43**, 85
- Krieger N., et al., 2017, *ApJ*, **850**, 77
- Kruijssen J. M. D., Longmore S. N., Elmegreen B. G., Murray N., Bally J., Testi L., Kennicutt R. C., 2014, *MNRAS*, **440**, 3370
- Kruijssen J. M. D., Dale J. E., Longmore S. N., 2015, *MNRAS*, **447**, 1059
- Kruijssen J. M. D., et al., 2019, *MNRAS*, **484**, 5734
- Krumholz M. R., Kruijssen J. M. D., 2015, *MNRAS*, **453**, 739

- Krumholz M. R., Kruijssen J. M. D., Crocker R. M., 2017, *MNRAS*, **466**, 1213
- Lada C. J., Lombardi M., Alves J. F., 2010, *ApJ*, **724**, 687
- Lada C. J., Forbrich J., Lombardi M., Alves J. F., 2012, *ApJ*, **745**, 190
- Launhardt R., Zylka R., Mezger P. G., 2002, *A&A*, **384**, 112
- Leroy A. K., et al., 2013, *AJ*, **146**, 19
- Li Z., Shen J., Kim W.-T., 2015, *ApJ*, **806**, 150
- Longmore S. N., et al., 2013a, *MNRAS*, **429**, 987
- Longmore S. N., et al., 2013b, *MNRAS*, **433**, L15
- Longmore S. N., et al., 2017, *MNRAS*, **470**, 1462
- Mac Low M.-M., Klessen R. S., 2004, *Reviews of Modern Physics*, **76**, 125
- Maciejewski W., 2008, in Bureau M., Athanassoula E., Barbu B., eds, IAU Symposium Vol. 245, Formation and Evolution of Galaxy Bulges. pp 161–164 ([arXiv:0709.3959](https://arxiv.org/abs/0709.3959)), doi:10.1017/S1743921308017547
- Mangilli A., et al., 2019, *A&A*, **630**, A74
- Mazzuca L. M., Knapen J. H., Veilleux S., Regan M. W., 2008, *ApJS*, **174**, 337
- Mills E. A. C., Togi A., Kaufman M., 2017, *ApJ*, **850**, 192
- Mills E. A. C., Ginsburg A., Immer K., Barnes J. M., Wiesenfeld L., Faure A., Morris M. R., Requena-Torres M. A., 2018, *ApJ*, **868**, 7
- Molinari S., et al., 2011, *ApJ*, **735**, L33
- Morris M. R., 2015, Manifestations of the Galactic Center Magnetic Field. Springer International Publishing, p. 391, doi:10.1007/978-3-319-10614-4\_32
- Mou G., Sun D., Xie F., 2018, *ApJ*, **869**, L20
- Neumayer N., Seth A., Boeker T., 2020, arXiv e-prints, p. [arXiv:2001.03626](https://arxiv.org/abs/2001.03626)
- Nishiyama S., et al., 2013, *ApJ*, **769**, L28
- Nogueras-Lara F., et al., 2020, *Nature Astronomy*, **4**, 377
- Oka T., Geballe T. R., Goto M., Usuda T., Benjamin McCall J., Indriolo N., 2019, *ApJ*, **883**, 54
- Ostriker E. C., Shetty R., 2011, *ApJ*, **731**, 41
- Ostriker E. C., McKee C. F., Leroy A. K., 2010, *ApJ*, **721**, 975
- Ponti G., et al., 2015, *MNRAS*, **453**, 172
- Ponti G., et al., 2019, *Nature*, **567**, 347
- Portail M., Gerhard O., Wegg C., Ness M., 2017, *MNRAS*, **465**, 1621
- Reid M. J., et al., 2019, *ApJ*, **885**, 131
- Renaud F., et al., 2013, *MNRAS*, **436**, 1836
- Renaud F., et al., 2015, *MNRAS*, **454**, 3299
- Sanders J. L., Smith L., Evans N. W., 2019, arXiv e-prints 1903.02009,
- Sarzi M., Allard E. L., Knapen J. H., Mazzuca L. M., 2007, *MNRAS*, **380**, 949
- Schmidt M., 1959, *ApJ*, **129**, 243
- Schneider F. R. N., et al., 2014, *ApJ*, **780**, 117
- Schödel R., Feldmeier A., Künneriath D., Stolovy S., Neumayer N., Amaro-Seoane P., Nishiyama S., 2014, *A&A*, **566**, A47
- Schönrich R., Binney J., Dehnen W., 2010, *MNRAS*, **403**, 1829
- Schönrich R., Aumer M., Sale S. E., 2015, *ApJ*, **812**, L21
- Seo W.-Y., Kim W.-T., Kwak S., Hsieh P.-Y., Han C., Hopkins P. F., 2019, *ApJ*, **872**, 5
- Shetty R., Beaumont C. N., Burton M. G., Kelly B. C., Klessen R. S., 2012, *MNRAS*, **425**, 720
- Smith B. D., et al., 2017, *MNRAS*, **466**, 2217
- Sormani M. C., Barnes A. T., 2019, *MNRAS*, **484**, 1213
- Sormani M. C., Li Z., 2020, *MNRAS*, **494**, 6030
- Sormani M. C., Binney J., Magorrian J., 2015, *MNRAS*, **454**, 1818
- Sormani M. C., Treß R. G., Klessen R. S., Glover S. C. O., 2017, *MNRAS*, **466**, 407
- Sormani M. C., Treß R. G., Ridley M., Glover S. C. O., Klessen R. S., Binney J., Magorrian J., Smith R., 2018a, *MNRAS*, **475**, 2383
- Sormani M. C., Sobacchi E., Fragkoudi F., Ridley M., Treß R. G., Glover S. C. O., Klessen R. S., 2018b, *MNRAS*, **481**, 2
- Sormani M. C., et al., 2019, *MNRAS*, **488**, 4663
- Springel V., 2010, *MNRAS*, **401**, 791
- Stolte A., Ghez A. M., Morris M., Lu J. R., Brandner W., Matthews K., 2008, *ApJ*, **675**, 1278
- Stolte A., et al., 2014, *ApJ*, **789**, 115
- Su M., Slatyer T. R., Finkbeiner D. P., 2010, *ApJ*, **724**, 1044
- Torrey P., Hopkins P. F., Faucher-Giguère C.-A., Vogelsberger M., Quataert E., Kereš D., Murray N., 2017, *MNRAS*, **467**, 2301
- Tress R. G., Sormani M. C., Glover S. C. O., Klessen R. S., Battersby C. D., Clark P. C., Hatchfield H. P., Smith R. J., 2020, *Paper I (submitted)*,
- Tsatsi A., Mastrobuono-Battisti A., van de Ven G., Perets H. B., Bianchini P., Neumayer N., 2017, *MNRAS*, **464**, 3720
- Utomo D., et al., 2017, *ApJ*, **849**, 26
- Walmsley C. M., Guesten R., Angerhofer P., Churchwell E., Mundy L., 1986, *A&A*, **155**, 129
- Weinberger R., Springel V., Pakmor R., 2019, arXiv e-prints; [arXiv:1909.04667](https://arxiv.org/abs/1909.04667),
- Wu J., Evans Neal J. I., Gao Y., Solomon P. M., Shirley Y. L., Vanden Bout P. A., 2005, *ApJ*, **635**, L173
- Yusef-Zadeh F., Braatz J., Wardle M., Roberts D., 2008, *ApJ*, **683**, L147
- Yusef-Zadeh F., et al., 2009, *ApJ*, **702**, 178
- Yusef-Zadeh F., et al., 2015, *ApJ*, **808**, 97

## APPENDIX A: RESOLUTION STUDY

In this appendix we show the results of a resolution study that we have conducted in order to assess the impact of varying the resolution and the sink particle creation threshold  $\rho_c$  (see Section 2.4 of Paper I). We consider 4 simulations, whose properties are summarised in Table A.1.

The simulations differ for two parameters: the base target cell mass  $M$ , and the sink particle formation density threshold  $\rho_c$ . The fiducial simulation (m100densc1e4) has both the smallest  $M$  (highest resolution) and the highest  $\rho_c$ . The simulation m100densc1e3 has the same  $M$  but lower  $\rho_c$ . This allows us to assess the impact of having lower resolution in the high density regions where the gravitational collapse is happening, which is important in the context of star formation. Then we consider a simulation with a higher  $M$  (i.e., lower resolution), m300densc1e3, in order to assess how a different base mass resolution affects the various phases of the ISM. Finally, we consider a very low resolution simulation, m1000densc1e2, as a general benchmark. Figure A1 shows the mass resolution of the four simulations as a function of density.

Figure A2 shows the behaviour of various quantities as a function of time for the four simulations considered in the resolution study. From this figure we see that the largest difference between the different simulations is seen in the chemical mass fraction: at higher resolution there is roughly a factor of 2 more gas in molecular form ( $H_2$ ) than in lower resolution simulations (see second panel from top to bottom). This induces a similar difference in the  $H_2$  depletion times. The SFR and the total gas depletion times does not appear to change substantially between the different simulations. While this is encouraging and gives us confidence in the results of our main simulation, we caution against drawing too many conclusions about convergence from this. We cannot rule out that a further increase in resolution may show major differences, since the star formation process is not resolved in our simulations.

name	$M_{\text{base}} [M_{\odot}]$	$\rho_c [\text{g cm}^{-3}]$
m1000densc1e2	1000	$10^{-22}$
m300densc1e3	300	$10^{-21}$
m100densc1e3	100	$10^{-21}$
m100densc1e4 (fiducial)	100	$10^{-20}$

**Table A1.** Summary of the simulations considered in the resolution study.  $M_{\text{base}}$  is the base target cell mass. No cells in the simulations are allowed to fall below this resolution (i.e., no cells can have mass higher than  $M_{\text{base}}$ ).  $\rho_c$  is the sink particle formation threshold (see Section 2.4 of Paper I). m100densc1e4 is the fiducial simulation considered for analysis in the main text of this paper and of Paper I.

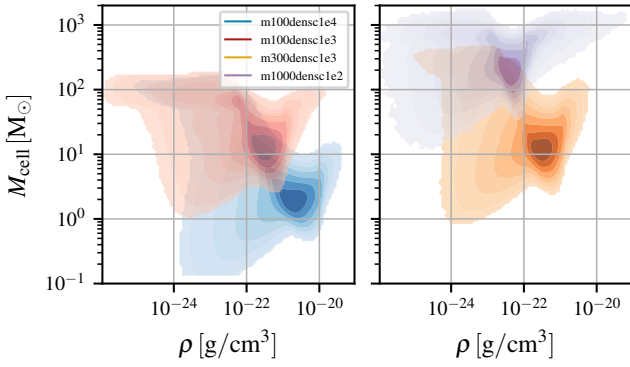


**Figure A1.** Mass resolution of the four simulation considered in the resolution study. The histogram shows the distribution of number of cells in the  $(M_{\text{cell}}, \rho)$  plane.

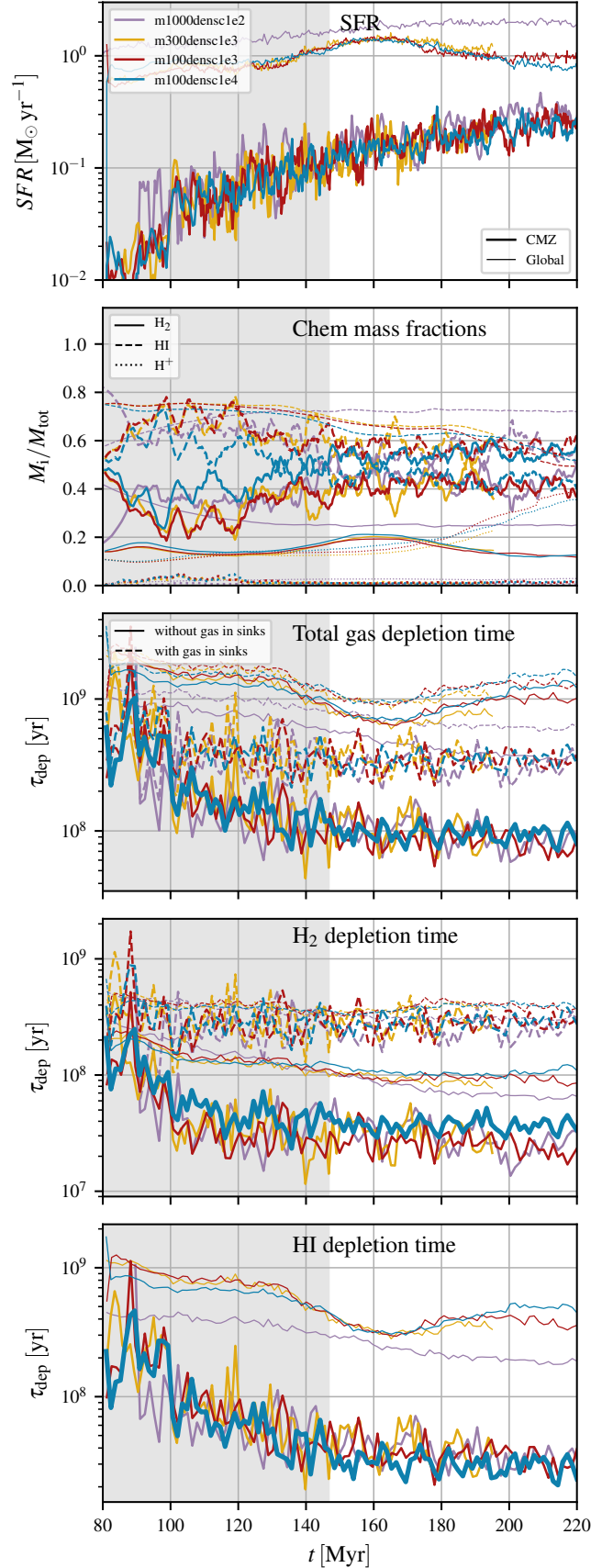


**Figure A2.** Various quantities as a function of time for the four simulations considered in our resolution study. Different colours indicate different simulation (see Table A1). Thick lines indicate the CMZ, defined as the region within  $R \leq 250$  pc, while thin lines indicate all the simulated box.



# Chapter 6

## Conclusions

### 6.1 Summary

For this dissertation we investigated the properties and the dynamics of the ISM in the context of a complex galactic environment with the help of high-resolution hydrodynamic simulations. In particular our focus was towards the densest parts of the ISM to better understand GMCs in the galactic context and to pinpoint the environmental conditions that lead to star formation.

We perform high-resolution hydrodynamic simulations of the ISM in the context of a galaxy. We use the moving-mesh code AREPO coupled to a detailed non-equilibrium and time-dependent chemical network which is able to model hydrogen and CO chemistry. This is essential for the proper formation and evolution of a cold molecular phase in the simulated ISM towards which our analysis is geared. We therefore also model the local shielding from the background photodissociating ISRF to properly follow the formation and destruction of H<sub>2</sub> and CO. We account for the gas self-gravity and follow the collapse up to densities of  $n \sim 10^3 \text{ cm}^{-3}$  in chapter 2 and 3 and  $n \sim 10^4 \text{ cm}^{-3}$  in chapter 4 and 5. After this threshold the last stages of the star formation process are abstracted from the simulation by employing collisionless sink particles. Sub-parsec resolution is achieved in the GMC density regime. We account for SN feedback coupled to the local star formation which are the main energy source responsible for destroying GMCs in our simulation. Magnetic fields and early-type feedback is ignored in this initial set of simulations.

We then applied the model to two astronomically interesting targets, namely the M51 interacting galaxy pair and the dynamically complex but compelling environment which is the Galactic bar of our Milky Way. In the former case we use a live stellar and DM potential, while in the case of the Milky Way we evolve the ISM in an externally imposed background potential fine-tuned to comply with the observational constraints of the MW

potential.

With this model we are able to get reasonably well-resolved GMCs down to scales of a few parsec while still retaining the larger scale context. Moreover we have a high dynamic range in environmental conditions which enables us to study the ISM in a statistically broad set of gas conditions.

The main scientific driver for the development of these models was to improve our understanding of the molecular gas in a galaxy. These models are however detailed and broad enough such that we can use them to generally describe the gas response to galactic dynamics. Such a description will then draw the framework to better understand the properties of the cold molecular phase and in particular of GMCs in this context. In this respect in chapter 2 we focused our attention to the ISM structure as a whole and how the interaction of a galaxy with a companion affects the ISM. When we then analyse GMC properties in this system in chapter 3 we can put our findings into context, better understanding the results.

Likewise, for the CMZ and the Galactic bar our analysis was not limited to the molecular phase for which these models were designed for, but we exploited the power of these type of simulations to get a clearer picture of the general gas flow and ISM properties in this extreme environment. Since particular attention was devoted to get an accurate model of the MW central region, we used our simulations to understand certain observed features characteristic of the CMZ, coming closer to disentangle the true 3D morphology of the real CMZ. For instance, we were able to interpret in our picture the 3D position of two prominent observed clouds (the 20 and 50 km/s clouds) based on their line-of-sight velocity information; we explained the tilt of the observed CMZ; we refined our vision about the large-scale structure of the CMZ arguing that an outer CMZ is inconsistent with the model and observations; and we were able to trace back the origin of two observed young stellar clusters, namely the Arches and the Quintuplet cluster.

Another important application of these simulations, is the comparison to previous models which did not include SN feedback and SF which were performed using the same gravitational potential. In this way by analysing the gas flows in this updated model, we can assess the importance of these elements in producing certain features. We found that SNe are responsible for driving gas flows from the CMZ towards the centre of the MW feeding the CND. This mechanism is not limited to the MW case, but could potentially act in analogous barred galaxies as well, describing thus an efficient mechanism to push gas to smaller galactic radii where it could eventually be available to trigger and sustain AGN activity.

We made substantial progress in our task to study the dynamics of the cold molecular gas in the CMZ and the conditions that lead to SF here. We highlighted the complexity of

the GMCs in this region which are highly filamentary, and shaped by frequent interactions with clouds rotating in the x2 ring and with clouds accreting at high velocities from the dust-lanes. We confirmed with this ISM model that the mass in the central few hundred parsecs is dominated by the molecular phase and mean densities are much higher compared to disc-like conditions as showed by density PDFs. Even with all these complex dynamics, the conditions that lead to SF still support a scenario where the depletion-time of the molecular phase over the CMZ is roughly constant for the time simulated. This constant depletion time would imply that the observed variability in SF is driven by variations in the accretion from the dust-lanes onto the CMZ instead. Moreover we find that the SF is not evenly distributed along the x2 orbit, but more pronounced close to the regions that directly interact with the inflowing gas from the dust-lanes. Cloud collisions trigger SF here, although SF still stays high across the entire orbit.

While for the CMZ-simulations a systematic analysis of GMC statistics is still lacking, we performed such a study in the case of the M51-like models (see chapter 3). For this galaxy model we invested less attention into getting an exact reproduction of the actual astrophysical system, and hence the results will have to be viewed in more general terms of how such an interaction can affect the ISM. We found that molecular cloud properties were less sensitive to the presence of spiral arms, and instead exhibited a more systematic shift as a function of galactic radius. In our simulations the spiral arms did not induce a major increase in the stellar surface densities, which instead was seen for increasing galactic radii. GMCs are therefore more sensitive to these environmental conditions than the specific presence of a spiral arm structure, which acted more as a snow-plow gathering pre-existing clouds rather than triggering new molecular gas formation. This result was in line with the general ISM analysis where we found that the interaction was not very efficient in driving significant changes in the relative fraction of gas in the ISM phases and changes in the SF compared to the galaxy in isolation. While this result might not be generally applicable to any galaxy interaction, it is still illuminating since it is generally implied that an encounter and/or the presence of spiral arms correspond to triggered GMC- and star-formation.

The GMC analysis performed in chapter 3 is also extremely useful to better understand the dynamical state of clouds as they are self-consistently formed in a galactic context. We found that clouds cannot be viewed in terms of quasi-equilibrium objects, their virial parameters, instead, exhibit a wide range of values. While at a density regime where the gas becomes CO-bright the structures would prefer  $\alpha_{\text{vir}} \sim 1$ , the molecular ISM disclosed a smooth transition of  $\alpha_{\text{vir}}$  in its hierarchy of density levels; from highly unbound structures if the diffuse CO-dark envelopes were considered to strongly bound in the highest density regimes.

## 6.2 Open questions

We just discussed the power of the simulations performed for this work where clouds are able to self-consistently form and evolve in a galactic environment of the size of several kpc. The major drawbacks which are restricting the realism of such models are related to the limited resolution, the lack of other important physical ingredients and the necessity to abstract the final stages of star formation employing a sub grid model.

Even though we reach excellent resolution in the dense part of the ISM compared to galaxy evolution models and cosmological simulations in general, we still had to make compromises since we were interested in the self-consistent evolution of GMCs in the larger galactic context. A workaround would be to produce a small high-resolution region within the galactic simulation. In this way statistical information would be lost and an evolution of the system for secular time-scales would be unfeasible, but nonetheless this technique would be a valuable supplement to the type of simulations presented in this dissertation. See Smith et al. (2020) where this method was performed on a cloud in a Solar-neighborhood environment.

We performed resolution tests to probe the robustness of our results. However, due to the high costs in terms of computing resources and time, we could not push the resolution of these expensive simulations further. Some of our results, even though qualitatively robust, might therefore not be fully converged and will adapt slightly once higher resolutions can be reached. Ever increasing power in computational resources will enable us to address this issue with our planned next generation models.

The current resolution also precludes us to properly address certain issues which are of considerable interest, such as substructure of GMCs (clumps and filaments) and how this is related to the SF. This is a central point of debate in the scientific community today and most relations are either purely empirical or based on rather idealised models. Testing these theories in a more dynamical simulated environment where clouds form self-consistently and having a wide range of different galactic conditions, is therefore of great interest.

A consequence of the limited resolution is the necessity to use a sub-grid model for star formation. Here we decided to employ accreting sink particles. As discussed previously, these particles are comprised of a gas part and a stellar part. The gas trapped in sink particles is one of the main sources of uncertainty in our analysis, since its state (density, temperature etc...) cannot be known but has to be assumed. Eventually the feedback will return this trapped material to the gas phase where it is then self consistently evolved through the hydro equations by the code. However, since it is reinjected with the SNe associated to the sink, it can sometimes take several Myr to free up this material again

and for some molecular clouds this gas is considerable and not negligible. This introduces great uncertainties in values such as mass fractions in the different thermal phases or molecular gas fractions. Future simulations should deal with this problem in a better way.

The ISM is a rich and complex system with many physical ingredients all energetically important. However, due to limited computing resources and time for development and testing, we decided to limit the ingredients added to the simulations presented to strictly the most important ones necessary to get a proper and active ISM cycle. Namely GMC physics, star formation with self-gravity and some type of feedback which can dissipate GMCs. We chose SNe as our source of feedback since it is energetically one of the dominant sources<sup>1</sup>, easily implemented and not too costly computationally. SNe, if coupled to the local star formation, will contribute to generate an ISM with roughly the appropriate mass fractions in the different phases; moreover GMC life-times are reasonable for the bulk of the clouds if SNe are considered, and the properties of the resulting cloud population are well-behaved. However, the lack of early feedback generates some extreme cases which are referred throughout the text as pathological clouds. These have very long life-times since they are unable to be disrupted by SN feedback alone and can grow extensively in mass. These clouds could dynamically affect large parts of the ISM in the galaxy once the massive cluster which forms in these situations decouples from the cloud. The numerous SNe associated to these stellar clusters will in fact then be injected into a low-density environment, generating huge expanding superbubbles. The addition of early-type feedback will presumably solve this issue. Moreover, considering only SN feedback, precludes us from analysing late stages of GMC evolution and cloud destruction since here other type of feedback is dynamically very important.

Having a limited amount of physical ingredients included in the simulations, has however also some benefits. A system with more and more ingredients becomes also more difficult to study and to assess the importance of certain type of phenomena in shaping the ISM and the clouds. Therefore it is necessary to approach the problem incrementally and in this way being able to compare models with different ingredients. But then when a comparison to real observational data is performed, these caveats have to be always kept in mind.

Another important limitation of our simulations is the lack of magnetic fields which in the real ISM might play an important role. In particular the effect of the galactic interaction on the ISM could be more pronounced since some of the gas might then be kept from becoming molecular by magnetic pressure forces. The compression induced

---

<sup>1</sup>although other type of feedback can be at least equally important for certain parameters of the natal cloud.

by the interaction could then be sufficient to overcome this force and induce more cloud formation than compared to the isolated case. In addition, in the CMZ it is believed that there are intense magnetic fields which produce peculiar features. It is interesting to see how the molecular gas is affected if we introduce such high B field here.

With the work summarised in this dissertation we pushed our understanding of gas dynamics, and in particular of the cold molecular gas, in the larger scale galactic context. But of course we just scratched the surface in terms of analysis to fully grasp the dynamics at play. Additional effort needs to be devoted to the dynamical state of GMCs. We argued that the gravitational equilibrium picture of clouds is rather simplistic, but this statement still needs further assessment and a proper understanding of how the scaling relations of clouds arise is needed. We further noted that the effect of galaxy dynamics on GMCs is non-trivial, but how exactly galactic dynamics is shaping cloud properties and what are the most important large-scale parameters in controlling these properties needs to be further investigated.

In terms of GMC physics, a highly interesting still open question which can be addressed with our simulation is about the formation of clouds in a galactic context. A study is in program about statistical information on the preferred formation channel of GMCs as a function of galactic environment.

Further attention is also needed on our study about the CMZ. Major points that still need explanation are for instance about the true 3D morphology of the CMZ. Our model is geared to reproduce the observational constraints of the central regions, but it is of course highly stochastic and finding an exact instance that is able to explain all the observed features is very difficult. Moreover the inclusion of other physical ingredients in new simulations might change this picture once more. It has to be said, however, that our type of CMZ modelling will never suit for a chi-square-type analysis with observations due to the inevitably stochastic nature of the simulations. Its strengths are to qualitatively explain observed features and gas dynamics in a self-consistent way, where the small GMC scales are connected with the large galactic scales encompassing the entire barred region.

We also just scratched the surface about GMCs in the CMZ. A systematic analysis is needed of the properties, formation and evolution of clouds in the CMZ. The driving question would be to understand in what sense the CMZ is special in terms of star formation and molecular gas and why we observe an abundance of dense gas relative to the actual SF in the region. Moreover an exploration about how scaling relations are affected in this extreme environment would give us hints on the complex interplay between clouds and the bar.

We were able to explain how the gas is driven from the CMZ towards the central CND,

but how the material bridges the last few parsec until it accretes onto the central SMBH is still not clear. An analysis could help in this regard, following the time-evolution of the accretion onto the central BH to get an idea about how much material is accreted given our model and about the time variability of the accretion.

Finally we want to stress that with the current setup the origin of the Fermi bubbles remains unexplained, it will be exiting to see how this changes with the inclusion of additional stellar feedback and magnetic fields. Moreover, the study about BH accretion could give us a hint on the expected AGN activity of our MW and if this is energetically compatible with the Fermi bubbles.

## 6.3 Future steps

### 6.3.1 Planned simulations

Having in mind what we just described in the previous section where we explained the limitations of our current models and the most compelling still open questions, it is quite clear what path to follow for future investigations.

In particular, we plan to produce next generation simulations where we fix the problems that the current models had and improve in terms of resolution and physical ingredients. We are working already to introduce magnetic fields into the code and we already made preliminary progress (Reissl et al., 2020). We also produced a simple radiation feedback scheme with a Stromgren sphere approximation. This code still needs optimization but it will be ready to be used on whole galaxy simulations for future models. Ideally the radiation feedback should be performed properly with a radiative transfer code like SPRAI developed by Jaura et al. (2018, 2020), this is already tested and implemented but needs to be coupled to the relevant chemical network for the present-day star formation case. Moreover, this is computationally more expensive and probably such a simulation will be achievable only for a few tens of Myr. Implementation of winds is simple but will probably be difficult to achieve for larger time-scales since it is very computationally demanding. Jets, on the other hand, are energetically not dominating in most circumstances and so their implementation and study has lowest priority. Another interesting question is about the feedback coming from the central black hole, if we could couple it to the local accretion we could address the issue of the Fermi bubbles, other than being able to study how BH feedback affects the surrounding gas.

We plan to address the problem of the sink particles by varying the type of particles created. We will employ stellar particles which are spawned stochastically in collapsing regions with a fixed stellar mass. These particles will only have a stellar component

and therefore we will not have the problem of gas phase trapped inside sink particles. Moreover, these star particles can interact and smooth the large gravitational cusp that we are seeing with a single sink particle. The problem is that they are not predictive like sinks but stochastic. For very high resolution studies it is therefore good to not fully abandon sink particles and so being able to follow gas accretion onto star forming regions within the cloud.

In terms of resolution we have to adapt our model based on the computing resources available. One possibility is to increase the resolution throughout the simulation domain, and/or to improve resolution in regions of interest. In particular we plan to increase resolution in the central few hundred parsec of the MW simulations around the CMZ. We plan to use sink formation density thresholds of  $10^6 \text{ cm}^{-3}$  which is necessary to increase the robustness of our results since in the CMZ the average density is at  $10^4 \text{ cm}^{-3}$ . In this way we can better address high density gas fractions, star formation and GMC properties there. Another way to go is to increase considerably the resolution around a single molecular cloud and follow it for its lifetime. This is currently done in the *cloud factory* simulations (Izquierdo et al., 2021; Smith et al., 2020) and we plan to apply this to the CMZ as well. Another demand is to raise the number of cells required to resolve a Jeans-length since with our current model it is set to 4 which is the minimum number of cells necessary to not get artificial fragmentation. A more robust requirement would be to use 8 or 16 resolution elements per Jeans-length.

We further plan to perform improvements in our Galaxy model. In the CMZ we are looking to create a new model, first with an external improved gravitational potential which includes all the latest findings about the Galactic potential (e.g. to include a peanut shaped bulge, proper spiral arms, etc...) and then also to experiment with a live-stellar-potential which is unstable in regard to the formation of a stellar bar. This latter project will likely move us away from the true 3D structure of the actual CMZ since the parameters in such a model are even more difficult to control given the dynamic evolution of the stellar system, but they can give us better valuable insight on the behaviour of clouds in a more dynamic environment.

We also plan to apply our ISM model using different galaxies altogether. Interesting targets would be dwarf galaxies of the way of the Magellanic Clouds, or other specific targets which have detailed observations of the molecular gas.

### 6.3.2 planned analysis

We will try to further improve our understanding of the molecular gas and its connection to the larger-scale galactic environment. The next step will be to study GMC formation. Suggested theories for cloud formation include converging gas flows, agglomeration of

smaller cloudlets, gravitational and thermal instability. But the relative importance in function of the local galactic conditions is largely unexplored. To do this we will add tracer particles to our simulations being then able to follow in time a given GMC selected at a given snapshot time. The evolution of the properties of this gas can then give us hints on the formation scenario which we can then relate to environmental parameters such as surface density, shear, location etc... This can be done for a statistically significant sample of clouds in different environmental conditions. With the help of tracer particles we can also understand from where spatially the gas comprising a cloud is coming from, which can help us to study metal diffusion problems. Besides, timescales of the formation process can be extracted and analysed. We then could further use this type of analysis to study the dependence on cloud mass of the formation scenario.

With the simulations that we have at hand plus the ones that we are planning we are in the best position to address these questions.

Another subsequent step is to study cloud populations in the CMZ. We can then compare what was found in chapter 3 with clouds in a more extreme environment such as the CMZ. Differences in properties could translate also to differences in scaling relations as higher shear and more frequent collisions would drive higher turbulence in clouds of a given mass range. We can then try to understand and describe how the differences arise. It is also important to follow the time evolution of clouds in this extreme environment.

Moreover it is worth exploring whether and to what extent the differences in GMC properties can be fully explained by different global environmental conditions such as higher surface densities and shearing forces or if the particular history of the gas that formed the cloud is more important in shaping the cloud properties. For instance a collision of high velocity gas coming from the dust lane will produce particular type of objects regardless of the local surface density. The specific morphology and kinematics of the bar region is then more important than the global environmental parameters.

We are currently performing additional analysis on the cloud catalog which was extracted from a snapshot of the M51-like galaxy in chapter 3. In particular we are analysing the shapes of clouds and relate them to the local shear. Moreover we study the shape of clouds as a function of GMC properties and environment. In this way we can understand, resolution permitting, at what regime the cloud prefers a more elongated/filament-like shape and when instead the cloud exhibits a more spherical-like configuration.

Given that the next generation models will include magnetic fields and photoionization feedback, we can properly address the question of the dynamical state of GMCs and what physical processes are controlling it. It is still actively debated if clouds are generally collapsing structures, or if they are in virial equilibrium or if they instead do not actually have a preferred binding energy. We have seen in chapter 3 that the virial equilibrium

picture is disfavoured, but the addition of magnetic fields could change this result. We can additionally study in more detail how environment enters the equation. To understand the dynamical state of clouds a virial analysis might not be sufficient. We want to employ also a more detailed analysis where we evaluate whether a cloud is collapsing given the actual velocity structure of the gas comprising the cloud. But also the time evolution and the actual star formation efficiency of the cloud in the next few snapshots can give us hints on its dynamical state in function of time. By further studying the magnetic pressures we can get the magnetic support. By performing a systematic comparison between the thermal and magnetic pressure we can then address the role of  $B$  in the support of clouds.

## Bibliography

Izquierdo A. F., et al., 2021, MNRAS, 500, 5268

Jaura O., Glover S. C. O., Klessen R. S., Paardekooper J. P., 2018, MNRAS, 475, 2822

Jaura O., Magg M., Glover S. C. O., Klessen R. S., 2020, MNRAS, 499, 3594

Reissl S., et al., 2020, A&A, 642, A201

Smith R. J., et al., 2020, MNRAS, 492, 1594

# Acronyms

**CMZ** Central Molecular Zone.

**CND** Circum-Nuclear Disc.

**CNM** Cold Neutral Medium.

**GMCs** Giant Molecular Clouds.

**HIM** Hot Ionised Medium.

**ISM** Interstellar Medium.

**ISRF** Interstellar Radiation Field.

**MHD** Magneto Hydrodynamic.

**MW** Milky Way.

**SF** Star Formation.

**SMBH** Super-Massive Black Hole.

**SN** Supernova.

**SPH** Smoothed Particle Hydrodynamics.

**WIM** Warm Ionised Medium.

**WNM** Warm Neutral Medium.



## Acknowledgements

First of all I thank my supervisors Ralf Klessen and Simon Glover. I am grateful for their patience and their trust throughout these years. But also and not least for their human aspect, which in my opinion is a substantial ingredient to allow for good research to be produced.

Among my major collaborators and people I had the pleasure to meet, learn from and work with I would like to thank especially Mordecai Mac Low and Rowan Smith.

A further thank goes to my informal supervisor, collaborator and dearest friend Mattia Sormani. The researcher I grew up to be during these years is greatly influenced by his shared knowledge and analytic and pragmatic way of approaching problems.

I am extremely grateful for the cheerful and friendly working environment at the ITA. On a scientific and a personal level I would like to thank the many interesting people I had the pleasure to meet there, discuss with, laugh with and complain and despair together over the many problems encountered in a PhD life. A non exhaustive list includes Mattis Magg, Mattia Sormani (again), Eric Pellegrini, Maria Jimenez, Bhaskar Agarwal, Ondrej Jaura, Maximilian Disch, Daniel Rahner, Raul Dominguez, Toni Peter, Peter Rodenkrich, Melanie Kaasinen, Loke Loennblad Ohlin, Sacha Hony, Dimitrios Gouliermis.

An honorable mention goes to the pizza evenings, bouldering sessions, boardgame events, barbecues, Christmas karaoke parties and many more events we shared at ITA that helped to ease the sometimes hard PhD life.

This thesis has been completed in a very difficult and challenging period of my life. While the covid-19 pandemic was raging, my father was being consumed by a terrible brain tumour. I thank all the people, too many to list, who gave me strength and support to pursue with my dreams and goals nonetheless.

A special mention goes of course to my mother, but my biggest thank is of course dedicated to my soon-to-be wife Cinthia who supported me in so many subtle yet surprisingly substantial and game-changing ways. The everyday small things are those who matter most even though we do not realise it at the moment.